Technical Physics, Vol. 49, No. 7, 2004, pp. 805–809. Translated from Zhurnal Tekhnicheskoĭ Fiziki, Vol. 74, No. 7, 2004, pp. 1–5.
Original Russian Text Copyright © 2004 by Vladimirov, Shtraukh.

THEORETICAL AND MATHEMATICAL PHYSICS

Entropy Control in Discrete- and Continuous-Time Dynamic Systems

S. N. Vladimirov* and A. A. Shtraukh

Tomsk State University, Tomsk, 634050 Russia

**e-mail: vsn@re.tsu.ru, vsn@ic.tru.ru*

Received August 14, 2003; in final form, December 22, 2003

Abstract—The dynamics of a modified logistic mapping are considered for a system with the order parameter modulated by an external signal. It is shown that the Kolmogorov–Sinay entropy changes with changing modulation depth, while the harmonic signals and white noise can be used as a modulating signal. The conditions for the excitation of regular and strange nonchaotic attractors in the phase space are established. *© 2004 MAIK “Nauka/Interperiodica”.*

INTRODUCTION

At present, random oscillations have been observed in a great variety of objects, starting with crude mechanical systems and ending with highly organized biological systems. In the theoretical and applied studies of determinate chaos, one can distinguish a number of priorities such as the elaboration of new scenarios for the transition from regular to chaotic motion, methods of generating dynamic chaos, the study of the interactions between chaotic systems and the possible types of their collective behavior, unconventional dynamics and informational processes, and entropy control in continuous- and discrete-time dynamic systems. The latter area is caused by the needs for both the excitation and suppression of chaotic oscillations in the same dynamic system [1–6].

Apart from the purely theoretical interest, the control of the degree of motion ordering is also of great applied importance. Dynamic systems with chaotic oscillations can be used in the design of systems for radio camouflage and electronic countermeasures, noise radiolocation systems, confidential communication systems, and systems for nonstandard action on biological objects [7–9]. However, in some cases, the appearance and development of the determinate chaos regime are highly undesirable.

The purpose of this work is to examine one of the possible methods of controlling the degree of motion ordering, namely, through the modulation of the order parameter by an external signal in the form of a harmonic oscillation or white noise.

MATHEMATICAL MODEL AND ITS ANALYTIC INVESTIGATION

As the object for investigation, we chose a discrete-time system representing a modified logistic mapping [10]. After the addition of a multiplier describing the modulation of the order parameter, this mapping takes the form

$$x_{n+1} = \Phi(x_n),\ \mathrm{mod}\ 1,$$
$$\Phi(x_n) = 1 - \alpha_0\left[1 + m\sin\left(\frac{2\pi}{T}n + \varphi_0\right)\right]|x_n|. \tag{1}$$

Here, $\alpha_0 \ge 1$ is the order parameter; $0 \le m \le 1$ is the order-parameter modulation depth (control parameter); T and φ_0 are, respectively, the period and initial phase of the external force; and $n = 0, 1, 2, \ldots, N$ is the discrete time. Mapping (1) models a nonautonomous dynamic system subjected to the parametric action of an external periodic force. In the autonomous case $m = 0$, the order parameter α_0 determines the degree of randomness of the motion $\{x_n\}$, when the Kolmogorov– Sinay entropy can be calculated exactly to give $K = \log_2\alpha_0$ [10].

Piecewise linear mapping (1) represents two rays that emanate from the point ($x = 0$, $\Phi(x) = 1$) at the angle θ and go to $-\infty$. As the discrete time n varies at fixed α_0 and m, the angle θ varies from $\theta_{\min} = \pi - 2\arctan[\alpha_0(1 + m)]$ to $\theta_{\max} = \pi - 2\arctan[\alpha_0(1 - m)]$ with the period T, resulting in a periodic variation of the Lyapunov characteristic index.

Indeed, the local Lyapunov index λ_n is calculated analytically according to the relation

$$\lambda_n = \log_2\left|\frac{d\Phi(x_n)}{dx_n}\right|$$
$$= \log_2\alpha_0\left[1 + m\sin\left(\frac{2\pi}{T}n + \varphi_0\right)\right], \tag{2}$$

whence it follows that it is a 2π-periodic function of the discrete phase $\tau_n = 2\pi n/T + \varphi_0$. During the action of the external force, λ_n takes both positive and negative values. Consequently, a strong dependence on the initial conditions for different τ_n values may either take place or be absent; i.e., the phase trajectories may either mix or not.

Due to the periodicity of λ_n, the Lyapunov characteristic index Λ defined as its mean along the time realization of $\{x_n\}$,

$$\Lambda = \frac{1}{N}\sum_{n=1}^{N}\lambda_n, \tag{3}$$

may be calculated only on the interval [0–2π]. Passing from the discrete to a continuous τ_n phase, one gets

$$\Lambda = \frac{1}{2\pi}\int_0^{2\pi}\lambda(\tau)d\tau = \log_2\alpha_0 + \frac{1}{2\pi}\int_0^{2\pi}\log_2(1+m\sin\tau)d\tau = \log_2\frac{\alpha_0}{2}(1+\sqrt{1-m^2}). \tag{4}$$

If $\Lambda < 0$, the motion in the attractor is, on average, ordered and, conversely, it is chaotic if $\Lambda > 0$. For this reason, by setting the right-hand side of expression (4) equal to zero, one can determine the critical value $\hat{m}$ that separates the chaotic and nonchaotic regimes,

$$\hat{m} = \frac{2}{\alpha_0}\sqrt{\alpha_0 - 1}. \tag{5}$$

It is significant that neither the period of the external force nor its initial phase appears in this relation. Because of this, the motion type in the system is determined only by the parameters α_0 and m. This implies that only the force and energetic relations play the dominant part. The external action does not affect the crudeness property that is inherent in an autonomous system [10], and, hence, the main properties of model (1) do not change if the variations of its parameters are small.

According to the familiar theorem in [11], the Kolmogorov–Sinay entropy (hereinafter entropy) for mapping (1) is defined by the relation

$$K = \int_0^{\infty}\rho(x)\Lambda(x)dx,$$

where $\rho(x)$ is the invariant probability measure of a dynamic system. Since the dynamics of the mapping under consideration proceed in a restricted phase-space domain, the probability measure always exists for the time series generated by this mapping [12]. In our case, Λ is independent of x, so that, with allowance for the normalization condition, $K \equiv \Lambda$. In what follows, we will not distinguish between these two notions and identify the Lyapunov characteristic index of model (1) with its entropy.

So far, we dealt with the properties of a discrete-time system, and nothing was said about the way of constructing model (1). At the same time, it is well known that many of the discrete-time systems can be related to a certain flow system, and this applies, in full measure, to the mapping of interest. Model (1) can identically be transformed to a set of two autonomous mappings

$$\begin{cases} x_{n+1} = 1 - \alpha_0(1+m\sin 2\pi\psi_n)|x_n|, \quad \mod 1, \\ \psi_{n+1} = \psi_n + \dfrac{1}{T}, \quad \mod 1, \end{cases} \tag{6}$$

which now describe the dynamics of a nonlinear continuous-time system subjected to an external biharmonic excitation with periods T_1 and T.

Indeed, the first of the equations in (6) is obtained from the stroboscopic sections (with the period T_1) of the motion of the original flow system, while the first action by itself is excluded. One iteration in the discrete time n corresponds to the period T_1 of the first harmonic action.

Since the relation

$$\psi_n = \psi_0 + \frac{1}{T}n, \quad \mod 1$$

holds for the phase of eternal action, the rotation number Θ is defined as

$$\Theta = \lim_{n\to\infty}\frac{\psi_n - \psi_0}{2\pi n} = \frac{1}{T}. \tag{7}$$

If T is an irrational number, the external action is quasi-periodic; otherwise it is periodic. Thus, the results obtained for model (1) can be extended in full measure to continuous-time systems of the indicated type.

This completes the analytic study of models (1) and (6). In the subsequent sections, the results of numerical experiments are presented.

HARMONIC EXTERNAL ACTION

In this section, we analyze the influence of the control parameter m on the dynamics of models (1) and (6) with various values of the order parameter α_0. Calculations were carried out by formula (4) and numerically using algorithm [13] with quite a long realization of the time series $\{x_n\}$. Both methods gave identical results (Fig. 1a). For any value of the order parameter, there exists the $\hat{m}$ value which separates the chaotic and nonchaotic oscillation types. Since the function $\Lambda(m, \alpha_0)$ decreases monotonically, one can assert that the control parameter "smoothly" changes the entropy of the system and, hence, the degree of motion ordering in it. The character of the motion is fundamentally different for rational and irrational, even if close, rotation numbers. If the modulation period is rational, the time series is periodic (Fig. 1b), otherwise the periodicity is absent (Fig. 1c). At the same time, one can see that the motions share some common traits. At the instants the local

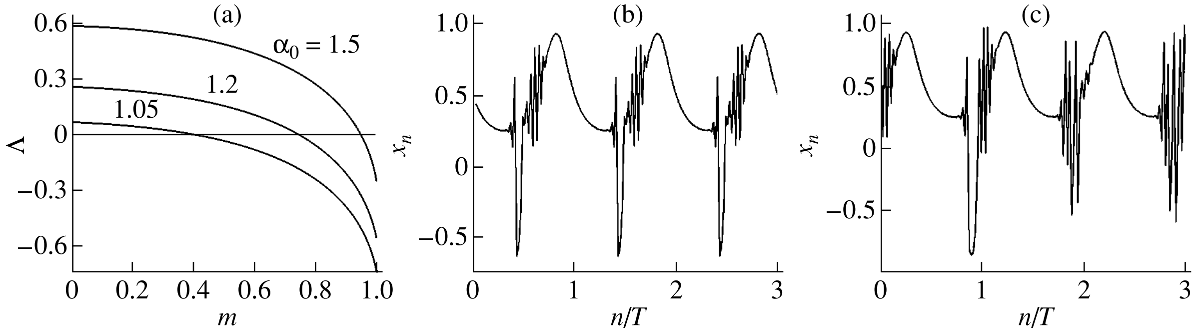

Fig. 1. (a) The Lyapunov characteristic index Λ as a function of the controlling parameter m for different values of order parameters α_0 of system (1). (b, c) The fragments of time realizations of x_n calculated for $m = 0.95$. The period of modulating signal is (b) rational, $T = 50$, and (c) irrational, $T = 20/(\sqrt{2} - 1) \approx 48.284271$.

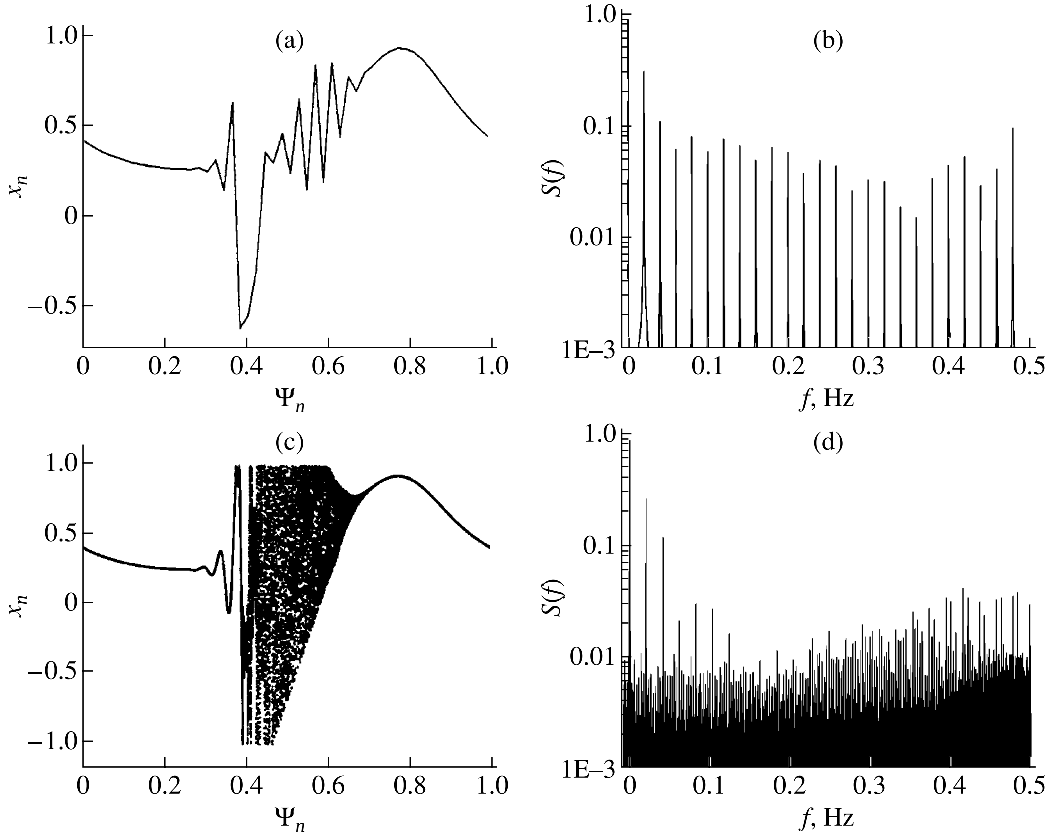

Fig. 2. (a) Phase portrait and (b) Fourier spectrum of system (6) calculated for $\alpha_0 = 1.5$, $m = 0.95$, and rational rotation number $\Theta = 0.02$. (c) Phase portrait and (d) Fourier spectrum calculated for the same values of α_0 and $m = 0.95$, but irrational rotation number $\Theta = (\sqrt{2} - 1)/20 \approx 0.020711$. The attractor dimensions were as follows: attractor capacity (fractal dimension) $D_C \approx 1.478$, informational dimension $D_I \approx 1.251$, and correlational dimension $D_{\mathrm{cor}} \approx 1.077$.

Lyapunov index is negative, the variable x_n is a smooth function with a period coinciding with the modulation period. If the local Lyapunov index becomes positive, the character of the motion changes qualitatively; its characteristic time scale no longer correlates with the period of the external field, the local phase trajectories diverge exponentially, although, on average, no mixing occurs at the attractor.

A more comprehensive idea of the character of motion at $m > \hat{m}$ can be obtained by analyzing its phase portraits and Fourier spectra (Fig. 2). The phase portraits were constructed on a unit square with equal

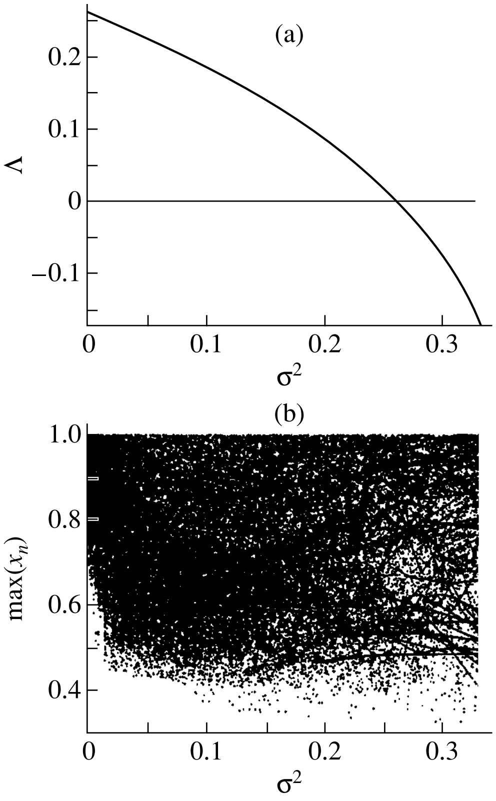

Fig. 3. (a) The Lyapunov characteristic index Λ as a function of the white-noise variance σ^2 for system (8) and (b) the bifurcation diagram, as calculated for $\alpha_0 = 1.2$. The critical value of the variance separating the chaotic and regular motions is $\hat{\sigma}^2 \cong 0.275$.

sides, which is topologically equivalent to a two-dimensional torus.

For a rational value of the external force, the trajectory is an unsmooth closed curve (Fig. 2a), indicating that the motion is periodic. The unsmooth character of the trajectory is due to the unsmooth character of the generating mapping. The line Fourier spectrum consisting of a set of equidistant harmonics separated by the frequency interval $\Delta f = 1/T$ is also indicative of the motion periodicity.

For an irrational rotation number, the mapping attractor is qualitatively different from the preceding case (Fig. 2c). The dimensions calculated by algorithm [14, 15] proved to be fractional values. The noninteger dimensions, in conjunction with the negative Lyapunov index, are evidence for the presence of a strange nonchaotic attractor. In this case, the motion in the system is rather intricate and aperiodic; although the geometric structure of the attractor is irregular, the motion is asymptotically stable. The disparity between the dimensions is caused by the fact that the attractor capacity is a purely geometric measure, whereas the informational dimension takes into account the frequency with which the points $\{x_n\}$ visit different sections of the attractor. The Fourier spectrum (Fig. 2d) has a line continuous character; i.e., it is intermediate between discrete and continuous spectra. The components at the frequency of external action and its harmonics are seen against a continuous background. In addition, the spectrum contains many harmonic components whose frequencies are unrelated to the external action, which is quite typical of strange nonchaotic attractors [16].

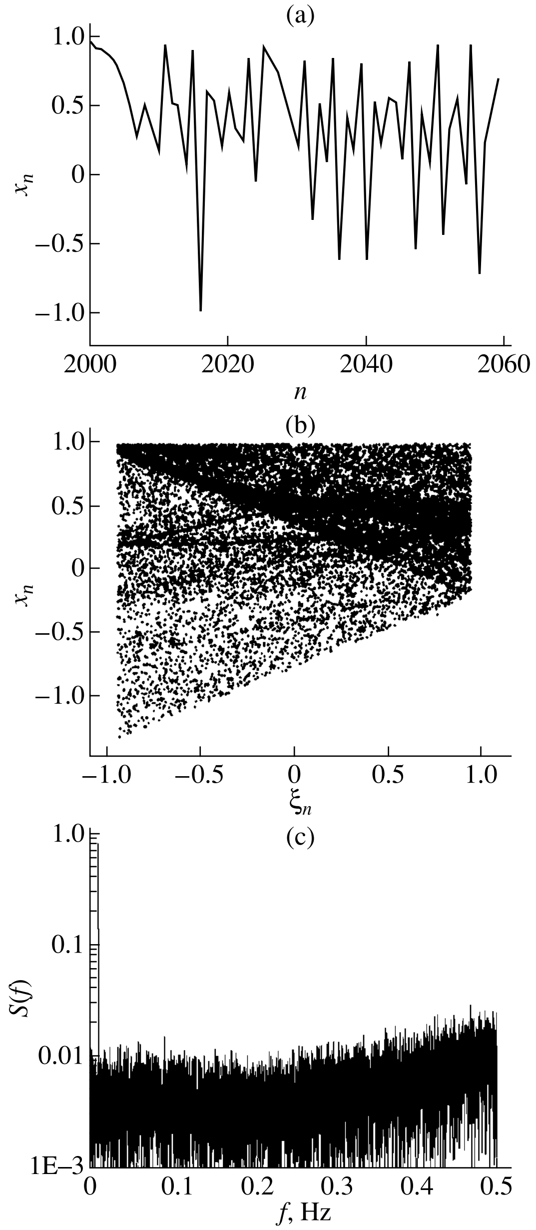

Fig. 4. (a) Fragment of the time realization of x_n, (b) the phase portrait, and (c) the Fourier spectrum, as calculated for $\alpha_0 = 1.2$ and $\sigma^2 = 0.3$. The attractor capacity $D_C \approx 1.839$, the informational dimension is $D_I \approx 1.837$, and correlational dimension $D_{\rm cor} \approx 1.744$.

In closing this section, we note that the origination of a strange nonchaotic attractor upon quasi-harmonic excitation was observed earlier only in smooth dynamic systems, such as circle mapping, Eno mapping, logistic mapping, and Grebogy–Pelican–York mapping. Our study allows the results of previous works to be extended to unsmooth systems.

WHITE NOISE ACTION

It is pertinent to pose the nontrivial question of the possibility of entropy control in a dynamic system subjected to random external action and, specifically, to its limiting form of white noise. To answer this question, we consider the dynamic system

$$x_{n+1} = 1 - \alpha_0(1+\xi_n)|x_n|, \qquad (8)$$

where ξ_n is white noise with a smooth and symmetric distribution about the point $x = 0$, zero mean, and variance σ^2; the white-noise variance is chosen as the controlling parameter.

First we examine how the controlling parameter influences the dynamics of the model. The results of calculation are shown in Fig. 3. Analysis of this figure suggests that the entropy of the system changes with changing σ^2; it decreases with increasing variance (Fig. 3a) and becomes negative at a certain critical value of $\hat{\sigma}^2$. The disorder creates order. The critical value of the variance cannot be determined visually from the bifurcation diagram (Fig. 3b). Consequently, the geometric structure of the attractor changes only slightly in the vicinity of $\hat{\sigma}^2$.

As in the case of harmonic external action, we analyze below the dynamics and Fourier spectrum of the model, restricting ourselves to the case $\sigma^2 > \hat{\sigma}^2$. The computational results are presented in Fig. 4. The time realization of $\{x_n\}$ (Fig. 4a) is a finite aperiodic process with a complex geometric structure in the phase space (Fig. 4b). The fractal and informational dimensions are larger than in the case of harmonic external action and approach their limiting possible value of 2. The negative Lyapunov index and the fractional dimensions are evidence that white noise excites a strange nonchaotic attractor in the system. The Fourier spectrum (Fig. 4c) is smooth, and its structure is close to the white noise spectrum and has no regular harmonic components, except for a constant component. This overturns the usual ideas about the line continuous spectrum inherent in the strange nonchaotic attractor. That is why we spoke above about the typical character of this spectrum rather than about its universality.

CONCLUSIONS

In this work, nonautonomous discrete- and continuous-time dynamic systems have been considered. It has been shown that the Kolmogorov–Sinay entropy of these systems and the degree of their motional ordering can be controlled not only by a harmonic action but also by white noise. Since action of the first type is regular, while that of the second type is completely disordered, the results obtained are quite general. It has been demonstrated for the first time that the strange nonchaotic attractor can also be excited in smooth dynamic systems in the absence of a quasi-periodic action.

ACKNOWLEDGMENTS

We are grateful to Prof. T.E. Vadivasova (Saratov State University) for clarifying some questions associated with the preparation of this work and to Prof. J.J. Sarraille (University of California) for providing the program for calculating the fractal dimensions and for valuable advice on the interpretation of the obtained results.

REFERENCES

1. H. D. Abarbanel, L. Korzinov, A. I. Mees, and I. M. Starobinets, Syst. Control Lett. **31**, 263 (1997).
2. C. Grebogi and Y. C. Lai, Syst. Control Lett. **31**, 307 (1997).
3. B. P. Bezruchko, R. N. Ivanov, and V. I. Ponomarenko, Pis'ma Zh. Tekh. Fiz. **25** (4), 61 (1999) [Tech. Phys. Lett. **25**, 151 (1999)].
4. A. A. Alexeyev and V. D. Shalfeev, Int. J. Bifurcation Chaos Appl. Sci. Eng. **5**, 551 (1995).
5. T. Vincent and J. Yu, Dyn. Control **1**, 35 (1991).
6. A. M. Dolov and S. P. Kuznetsov, Zh. Tekh. Fiz. **73** (8), 139 (2003) [Tech. Phys. **48**, 1074 (2003)].
7. V. Ya. Kislov, Radiotekh. Élektron. (Moscow) **38**, 1783 (1993).
8. S. N. Vladimirov, S. V. Zolotov, V. V. Negrul', *et al.*, Élektron. Promyshlennost, Nos. 2–3, 154 (2002).
9. M. Hasler, Int. J. Bifurcation Chaos Appl. Sci. Eng. **8**, 647 (1998).
10. S. N. Vladimirov and V. V. Negrul', Izv. Vyssh. Uchebn. Zaved. Prikl. Nelineinaya Din. **8** (6), 53 (2000).
11. Ya. B. Pesin, Usp. Mat. Nauk **32** (4), 55 (1977).
12. N. S. Krylov, *Publications on the Statistical Physics Substantiation* (Izd. Akad. Nauk SSSR, Moscow, 1950).
13. G. Benettin, L. Galgani, and J.-M. Strelcyn, Phys. Rev. A **14**, 2338 (1976).
14. S. Liebovitch and T. Toth, Phys. Lett. A **141**, 386 (1989).
15. J. J. Sarraille and L. S. Myers, Educ. Psychol. Meas. **54**, 94 (1994).
16. V. S. Anishchenko, Izv. Vyssh. Uchebn. Zaved. Prikl. Nelineinaya Din. **5** (1), 109 (1997).

Translated by V. Sakun

Technical Physics, Vol. 49, No. 7, 2004, pp. 810–817. Translated from Zhurnal Tekhnicheskoĭ Fiziki, Vol. 74, No. 7, 2004, pp. 6–12.
Original Russian Text Copyright © 2004 by Vladimirov, Perfil'ev.

THEORETICAL AND MATHEMATICAL PHYSICS

Nonlinear Parametric Effects and Dynamic Chaos in a Nonautonomous Oscillating System with a Nonlinear Capacitance

S. N. Vladimirov and V. I. Perfil'ev
Tomsk State University, Tomsk, 634050 Russia
e-mail: vsn@re.tsu.ru, vsn@ic.tsu.ru

Received September 15, 2003

Abstract—A mathematical model is constructed of a nonautonomous dynamic system containing a nonlinear capacitance and possessing a four-dimensional phase space. A numerical investigation is performed of branching processes and phenomena accompanying variations in the frequency and amplitude of an external force. The existence of complex dynamic processes that are a combination of a nonlinear force resonance and a parametric resonance is demonstrated. It is found that both a strange chaotic and a strange nonchaotic attractor exist in the phase space. It is shown that, in the case of a single-frequency external force, the latter attractor exhibits the property of roughness. The results of numerical calculations are confirmed by the results of laboratory experiments. *© 2004 MAIK "Nauka/Interperiodica".*

INTRODUCTION

In the classical theory of nonlinear oscillations, the treatment of a nonlinear force resonance is usually artificially separated from that of a nonlinear parametric resonance [1–3]. From the methodological standpoint, such a separation seems to be quite natural and reasonable, because it enables one to employ simple means for a mathematical description of models and to analyze these models self-consistently. In this way, the basic characteristic features of nonlinear systems and their fundamental distinctions from linear systems were revealed. This is quite sufficient for the formation of a scientific paradigm for those beginning to study the theory of oscillations.

However, this approach involves a number of problems. One of these problems was very clearly outlined by Migulin *et al.* [2]: "It is not quite correct to treat the case of a direct force action without simultaneously affecting the system parameters; if we take into account the fact that a forced periodic process caused by a direct action in turn causes periodic variations in the parameters of a nonlinear system, then it becomes clear that the resultant resonance phenomena may have a very complex pattern; this fact rules out the possibility of a complete separation of the above two types of resonance phenomena for nonlinear systems." We also note that, if the motion in an oscillating system is far from periodic, then the difficulties increase manyfold.

No less an important problem is that the classical theory of nonlinear oscillations deals with motions that occur, as a rule, in dynamic systems with a small dimension of the phase space. The motion in these systems is usually close to periodic. The present-day theory of oscillations is characterized by the ever increasing interest in stochastic (for Hamiltonian systems) and chaotic (for dissipative systems) motion. By now it has become evident that such motions of dynamic systems are as natural as, e.g., the state of rest or limiting cycles. Note that the study of deterministic chaos not only attracts researchers from the standpoint of obtaining new theoretical results, it is also becoming more and more applied [4–6].

Another interesting problem is that of identifying attractors of dynamic systems exhibiting nonconventional behavior. The concept of the strange attractor was first introduced by Ruelle and Takens [7] and has been repeatedly refined since that time (see, e.g., [8]). Special interest is aroused by a strange nonchaotic attractor. Some researchers believe that processes similar to the processes of evolution and data processing may occur at the boundary between regular and chaotic motion [9]. As a rule, the presence of a strange nonchaotic attractor is identified with the biharmonic effect produced by oscillations with an irrational frequency ratio.

The objective of this study is to construct and numerically investigate a mathematical model of a dynamic system with a small number of degrees of freedom and continuous time, in which all of the phenomena and processes listed above could be observed when varying the system parameters. The model should be physically feasible and, furthermore, should represent a reasonable combination of components traditionally employed in radiophysics and electronics. The results of numerical experiments should be compared with those of laboratory experiments.

1. CONSTRUCTION OF A GENERAL MATHEMATICAL MODEL

Let us consider the nonautonomous nonlinear electric circuit shown in Fig. 1. The circuit contains a source of an external harmonic signal of the form $A\cos pt$; linear dissipative elements R_1, R_2, and R_S; a nonlinear capacitance C_N; two linear inductances L_1 and L_2; and a source of the bias voltage E. The elements serve the following functions: The dissipative elements R_1, R_2, and R_S determine the losses of energy in the reactive elements L_1, L_2, and C_N, respectively; the inductance L_1, along with the nonlinear capacitance, serves to tune the circuit to resonance with the frequency of the external signal p; and the inductance L_2 forms the bias circuit of the nonlinear capacitance.

We use Kirchhoff's laws to write the set of equations for the currents and voltages in the circuit under study:

$$\begin{cases} L_1\dfrac{di_1}{dt} = A\cos pt - R_1 i_1 - R_S(i_1 - i_2) - u_C \\ L_2\dfrac{di_2}{dt} = u_C + R_S(i_1 - i_2) - R_2 i_2 \\ \dfrac{d}{dt}(C_N u_C) = i_1 - i_2. \end{cases} \quad (1)$$

This set of equations is of the third order. The presence of an external force increases the order by unity; therefore, the resultant dimension of the phase space is 4, which proves to be sufficient to ensure a highly diverse dynamics of the model.

The last equation in the set of Eqs. (1) may be rewritten as

$$C_D\frac{du_C}{dt} = \left(C_N + u_C\frac{dC_N}{du_C}\right)\frac{du_C}{dt} = i_1 - i_2, \quad (2)$$

where C_D is the dynamic capacitance of the nonlinear element.

Let us specify the volt–farad characteristic of the nonlinear capacitance. We will take this characteristic to be as close as possible to the respective characteristic of real varicaps with an abrupt *p–n* junction [10],

$$C_N = C_0\sqrt{\frac{g}{g - u_C}}, \quad g = E + \varphi_0. \quad (3)$$

Here, E is the bias voltage, φ_0 is the contact potential difference, and C_0 is the capacitance of the junction at the working point with the bias E.

After the performing necessary transformations, we will write Eq. (2), in view of the chosen form of nonlinearity (3), in the form

$$C_0 m(u_C)\frac{du_C}{dt} = i_1 - i_2, \quad (4)$$

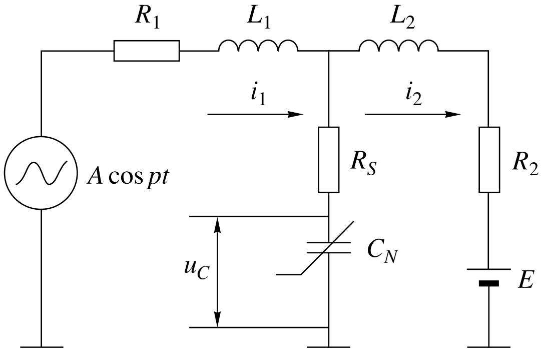

Fig. 1. Schematic diagram of a nonautonomous electric circuit with a nonlinear capacitance.

where the factor

$$m(u_C) = \sqrt{\frac{g}{g - u_C}}\,\frac{g - 0.5u_C}{g - u_C} \quad (5)$$

is the modulation factor of the nonlinear capacitance at the working point.

The model described by Eqs. (1), (4), and (5) is suitable for numerical analysis with arbitrary values of the parameters of dissipative and reactive elements, provided that the only additional inequality $u_C < g$ is valid. The branching phenomena and processes observed during variations in these parameters are so multiple and diverse that it does not appear possible to examine them within a single journal paper. Therefore, we will restrict ourselves to treating the resonance case.

2. MATHEMATICAL MODEL IN THE RESONANCE CASE

Let, in the low-signal case ($m(u_C) \approx 1$), the dynamic system under study have a resonance frequency ω_0 on the side of the pump oscillator. This enables one to introduce the dimensionless time $\tau = \omega_0 t$ and, because $d/dt = \omega_0 d/d\tau$, to transform the set of Eqs. (1) into the form

$$\begin{cases} X_1\dfrac{di_1}{d\tau} = A\cos\Omega\tau - R_1 i_1 - R_S(i_1 - i_2) - u_C \\ X_2\dfrac{di_2}{d\tau} = u_C + R_S(i_1 - i_2) - R_2 i_2 \\ Y_C m(u_C)\dfrac{du_C}{d\tau} = i_1 - i_2, \end{cases} \quad (6)$$

where $X_1 = \omega_0 L_1$ and $X_2 = \omega_0 L_2$ are the reactances of the inductive elements, $Y_C = \omega_0 C_0$ is the static conductivity of a varicap at the low-signal resonance frequency, and $\Omega = p/\omega_0$ is the normalized frequency of the external signal. Since Y_C, as well as R_S, is a rated quantity for a given type of varicap, it makes sense to find convenient expressions for the remaining reactances by expressing them in terms of this particular quantity.

Let us write the expression for the circuit impedance at the frequency ω_0 on the side of the pump oscillator,

$$Z(j\omega_0) = R_1 + jX_1 + \frac{R_2R_S + X_2X_C + j(R_SX_2 - R_2X_C)}{R_2 + R_S + j(X_2 - X_C)}, \qquad X_C = \frac{1}{Y_C}, \quad j = \sqrt{-1}. \tag{7}$$

The losses in reactive elements are usually insignificant and may be ignored in a first approximation. This approximation is further justified for the reason that the anharmonic and nonisochronous properties of a nonlinear system will necessarily show up as the amplitude of the external signal increases, so that the resonance frequency will inevitably change. In our case, the nonlinearity of C_N is "soft"; hence, one can expect a leftward slope of the resonance curve and a decrease in the resonance frequency [2]. As a result, expression (7) may be simplified to

$$Z(j\omega_0) = j\frac{X_1X_2 - X_C(X_1 + X_2)}{X_2 - X_C}. \tag{8}$$

It is clear that the efficient utilization of the pumping voltage with a frequency $p \approx \omega_0$ requires the absence of a pole of decay at this frequency. Therefore, we will assume that $X_2 \neq X_C$ and set $X_2 = \alpha X_C$ $(\alpha \neq 1)$. In addition, in view of the condition that the imaginary part $Z(j\omega_0)$ is equal to zero, it follows from Eq. (8) that $X_1 = \alpha X_C/(\alpha - 1)$ $(\alpha > 1)$. From this, we derive the sought correlations between the parameters of the set of Eqs. (6),

$$X_1 = \alpha\frac{1}{Y_C}, \quad X_2 = \frac{\alpha}{\alpha - 1}\frac{1}{Y_C}. \tag{9}$$

The parameter α has a simple physical meaning. In a low-loss approximation, an analysis of the behavior of the impedance $Z(j\omega)$ in a certain frequency range (we omit the latter as being irrelevant to the problem under consideration), has revealed that, in addition to the resonance frequency $\omega_0 = \sqrt{(L_1 + L_2)/C_0L_1L_2}$, there is a pole of decay at the frequency $\omega_\infty = 1/\sqrt{C_0L_2}$. These frequencies are related through the parameter α as follows: $\alpha = (\omega_0/\omega_\infty)^2$.

Now, the set of Eqs. (6) complemented with relations (9) enables one to finally formulate the mathematical model:

$$\begin{cases} \dfrac{di_1}{d\tau} = \dfrac{\alpha - 1}{\alpha}Y_C[A\cos\Omega\tau - R_1i_1 - R_S(i_1 - i_2) - u_C] \\ \dfrac{di_2}{d\tau} = \dfrac{Y_C}{\alpha}[u_C + R_S(i_1 - i_2) - R_2i_2] \\ \dfrac{du_C}{d\tau} = \dfrac{1}{m(u_C)Y_C}(i_1 - i_2). \end{cases} \tag{10}$$

The results of numerical analysis of this model are given in the next section. In conclusion of this section, we will prove the existence of an attractor for flow (10), i.e., a limiting attracting set in phase space. The attractor exists if and only if the flow divergence D is negative. Indeed, in this case any initial volume of phase space V_0 behaves with time τ as

$$V(\tau) = V_0\exp(D\tau). \tag{11}$$

This means that, if $D < 0$, then all phase trajectories that start from V_0 "settle" with time on a closed attracting set of zero volume, i.e., an attractor [1, 11].

For flow (10), the phase flow divergence (Lie derivative) has the form

$$\begin{aligned} D &= \frac{\partial}{\partial i_1}\left(\frac{di_1}{d\tau}\right) + \frac{\partial}{\partial i_2}\left(\frac{di_2}{d\tau}\right) + \frac{\partial}{\partial u_C}\left(\frac{du_C}{d\tau}\right) \\ &= D_1 + D_2(i_1 - i_2), \\ D_1 &= -\frac{Y_C}{\alpha}[(\alpha - 1)(R_1 + R_2) + R_2 + R_S], \\ D_2 &= \frac{1}{Y_C}\sqrt{1 - \frac{u_C}{g}}\frac{u_C - 4g}{(2g - u_C)^2}. \end{aligned} \tag{12}$$

In these expressions, the term D_1 is negative for any values of the quantities entering in it, and the factor D_2 is always positive. In the general case, the term $D_2(i_1 - i_2)$ is alternating-sign, is a function of time, and is obviously limited (if only by virtue of the finite power of the pumping source). Therefore, $V(\tau) = V_0\exp(D_1\tau)\exp[D_2(i_1 - i_2)\tau] \longrightarrow 0$ as $\tau \longrightarrow \infty$, which proves the existence of an attractor for flow (10). However, the properties and structure of this attractor may only be judged by the results of numerical analysis and laboratory experiments.

3. RESULTS OF NUMERICAL ANALYSIS

The set of differential equations (10) was integrated by the eighth-order Dorman–Prince method with automatic control of the integration step [12]. The local error of integration in numerical experiments was no larger than 10^{-8}; in some special cases (e.g., when investigating the vicinity of a branching point), this error was decreased to 10^{-12}. The resultant time series were stored and then processed. The maximum characteristic Lyapunov exponent was calculated by the algorithm suggested by Benettin *et al.* [13]. The attractor capacity and the informational and correlational dimensions of the attractors were estimated using the approaches described in [14, 15].

The results given in this section were obtained for the following values of the parameters of model (10): $E = 6$ V, $\varphi_0 = 0.8$ V, $R_1 = 1\ \Omega$, $R_2 = 2\ \Omega$, $R_3 = 0.2\ \Omega$, $Y_C = 2 \times 10^{-3}$ S, and $\alpha = 10$.

We will start with the construction of a one-parameter bifurcation diagram that enables one to qualitatively estimate the types of motion and their transformations while using simple means. In the general case, the bifurcation diagram represents the dependence of the maxima of some process on the control parameter. If the process under analysis exhibits a harmonic behavior, then its maxima are periodically repeated and the bifurcation diagram is a point when the control parameter has a fixed value and it is a line when this parameter varies. However, if the diagram lines are diffuse or the points fill up entire regions of the diagram, the process exhibits a limited aperiodic behavior, and it is quite safe to talk about the strangeness of the attractor of the dynamic system under study.

The bifurcation diagram presented in Fig. 2 shows the dependence of the current maxima i_1 on the relative frequency of the external signal $\Omega = p/\omega_0$ for a normalized pumping amplitude $B = A/g$ of 0.5. Eight nonlinear resonances numbered from 1 to 8 are observed in the chosen frequency range of the external signal. The frequency is varied from low to high values, hysteretic phenomena are observed in the vicinities of the resonance frequencies, and the resonance curves are inclined to the left. When the frequency of the external signal is varied from high to low values, the pattern of the diagram is qualitatively the same; however, the hysteresis phenomena are observed at lower frequencies than in the previous case. We will regard the half-sum of the frequencies at which hysteretic jumps in the current amplitude i_1 take place as nonlinear resonance frequencies. These frequencies are $\Omega_1 \approx 0.228$, $\Omega_2 \approx 0.304$, $\Omega_3 \approx 0.373$, $\Omega_4 \approx 0.42$, $\Omega_5 \approx 0.593$, $\Omega_6 \approx 0.757$, $\Omega_7 \approx 1.446$, and $\Omega_8 \approx 1.877$.

It is known from the classical theory of nonlinear oscillations [2, 3] that the frequencies of nonlinear force resonances are defined by relations of the form $\Omega_n = 1/n$, and the frequencies of nonlinear parametric resonances, by relations $\Omega_m = 2/m$ (where n and m are integers). In addition, higher order force resonances are possible [1] at frequencies of $\Omega_{nm} = n/m$.

The first and seventh resonances observed in the bifurcation diagram may be identified with the fifth-order nonlinear force resonances at $n/m = 1/4$ and $n/m = 3/2$, respectively. The third, fifth, and eighth resonances are manifestations of the nonlinear parametric resonances with $m = 5$, 3, and 2. Finally, the second ($n = 3$, $m = 6$), fourth ($n = 2$, $m = 4$), and sixth ($n = 1$, $m = 2$) resonances are results of the simultaneous manifestation of force and parametric phenomena. We note that force resonances at the frequencies $\Omega_n = 1/n$ do not show up in pure form and are always accompanied by nonlinear parametric resonances, because $\Omega_m = 2\Omega_n$, with $n = m$.

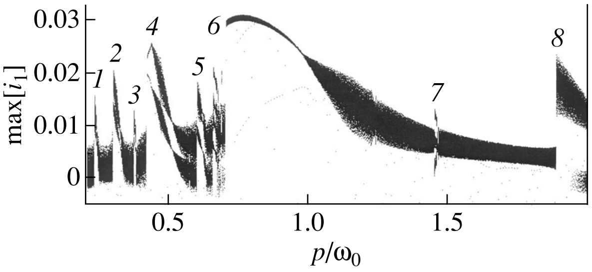

Fig. 2. Bifurcation diagram: maxima of i_1 vs. external signal frequency.

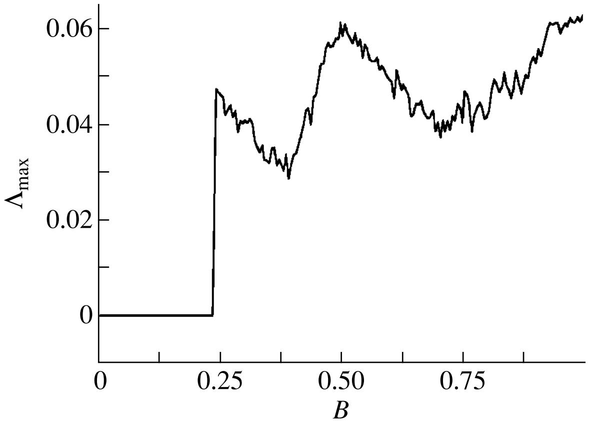

Fig. 3. The highest Lyapunov exponent as a function of the external force amplitude. The bifurcation value of the external force is $\hat{B} = 0.2358\ldots$.

Note the blurriness of the lines in the bifurcation diagram. As was mentioned above, this corresponds to the complex internal dynamics at the chosen amplitude of the pumping voltage. It is interesting to investigate how the system properties depend on this amplitude. We will fix the frequency of the external force in the vicinity of the most pronounced (sixth) resonance assuming that $\Omega = 0.8$ and use B as a control parameter. The behavior of the highest characteristic Lyapunov exponent $\Lambda_{\max}$ as a function of the external force amplitude is shown in Fig. 3. It follows from this figure that there exists the critical (bifurcation) value of the pumping voltage amplitude $\hat{B} = 0.2358\ldots$, which separates qualitatively different types of motion. At $B < \hat{B}$, the highest Lyapunov exponent is negative, $\Lambda_{\max} \approx -4.4 \times 10^{-5}$, which indicates that the system is insensitive to

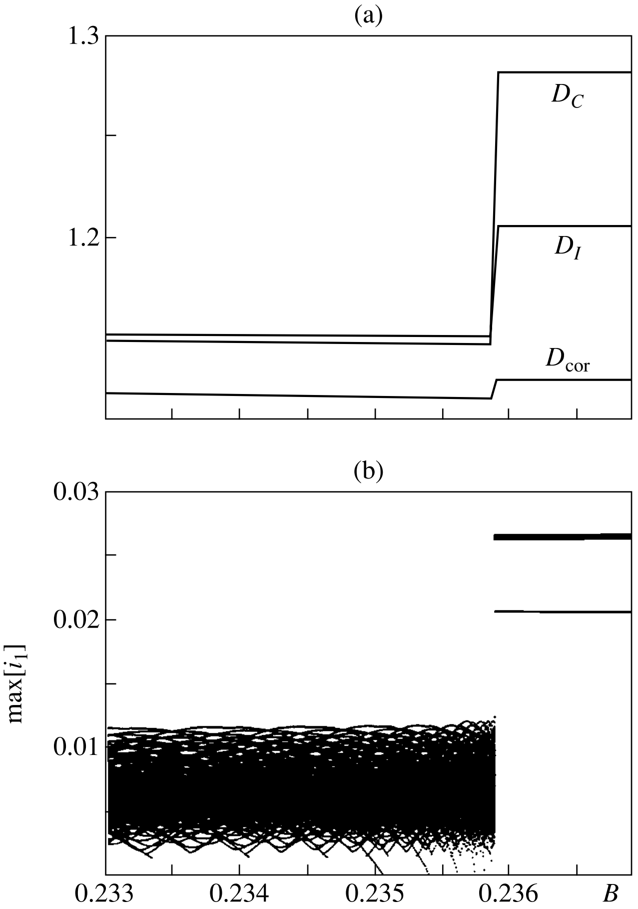

Fig. 4. (a) Attractor capacity D_C and its informational, D_I, and correlational, D_{cor}, dimensions as functions of the external force amplitude; (b) a fragment of the bifurcation diagram plotted in the vicinity of the bifurcation point.

initial conditions and that the mixing of trajectories in phase space is absent.

It is expedient to clarify what is meant by the highest Lyapunov exponent. An N-dimensional dynamic system possesses N Lyapunov exponents. Their signs make up the so-called signature of the exponent spectrum, which is conventionally written as $\langle +, +, \ldots, 0, -, - \rangle$. The presence of a zero exponent in flow (10) is obligatory and is caused by the effect of an external periodic force. Indeed, the set of Eqs. (10) may be transformed into a fourth-order autonomous system by adding the equation $d\phi/d\tau = \Omega$, which is equivalent to the introduction of a new variable $\phi = \Omega\tau$. It is obvious that the variations in the distances between trajectories in phase space are zero along the ϕ axis, which results in the emergence of the zero exponent in the signature. This fact is rigorously proven by the well-known Haken theorem [16]. The exponent that is defined only by the internal dynamics of a system, even when it is less than zero, will be referred to as the highest Lyapunov exponent.

When the pumping amplitude exceeds the critical value, the highest Lyapunov exponent changes its sign and assumes a value of $\Lambda_{\max} \approx 4.8 \times 10^{-2}$. As a result, a mode corresponding to dynamic chaos arises. The modes change stepwise; in thermodynamic systems, this corresponds to a first-order phase transition. The highest Lyapunov exponent increases nonmonotonically as B increases further, and no regularity windows are present. The latter means that, at $B > \hat{B}$, a single chaotic attractor exists, which does not contain stable regular attractors and retains its properties as the control parameter varies. According to the existing classification, such an attractor must be assigned to the quasi-hyperbolic type [8].

Let us investigate the fractal properties of the attractor in the vicinity of the bifurcation point. We will turn to Fig. 4a, which presents the attractor capacity (fractal dimension) D_C and the informational D_I and correlational D_{cor} dimensions as functions of the external force amplitude. These dimensions differ from one another, with the necessary relations $D_{\mathrm{cor}} \le D_I \le D_C$ retained, and undergo a greater or smaller jump at the point of transition to the chaotic mode. The fractal dimension increases by approximately 11%, and the informational and correlational dimensions increase by approximately 5 and 0.8%, respectively. It is especially important that all the dimensions are fractional both before and after bifurcation. Consequently, a strange nonchaotic attractor exists in the system before the bifurcation point, and a strange chaotic one exists after the bifurcation point. At present, the existence of a strange chaotic attractor appears to be as usual as the existence of, e.g., a limiting cycle. Up to now, it was believed that the external action of two harmonic signals with an irrational frequency relation was an obligatory condition for the existence of a strange nonchaotic attractor in a dynamic system [17, 18]. It was demonstrated in [19] that it is not necessary that the frequency ratio be always irrational, and it has now become clear that sometimes even a one-frequency external action is sufficient. The results obtained indicate that the strange nonchaotic attractor mode is not a rare and exotic phenomenon but is a fairly typical manifestation of the nonlinear properties of dynamic systems.

Let us now turn to Fig. 4b, which shows a fragment of a one-parameter bifurcation diagram plotted in the vicinity of the parameter region where the characteristic Lyapunov exponent changes its sign. To the right of point $\hat{B}$, the attractor is arranged rather simply and represents a closed, weakly diffuse double-turn curve. To the left of point $\hat{B}$, in spite of the fact that the highest Lyapunov exponent is negative, the bifurcation diagram is much more complicated. Here, a nonperiodic oscillatory mode with a rather complicated geometric structure (strangeness) is realized, but without both the exponential divergence and mixing of phase trajectories (the absence of chaos), which is determined by the negative sign of the Lyapunov exponent. It is these properties that are typical of strange nonchaotic attractors.

It is no less important that the observed strange nonchaotic attractor is structurally stable, because its dimension and bifurcation diagram remain almost the same as the external force amplitude varies within a fairly wide range. Consequently, this attractor retains its structure in the presence of perturbations.

In conclusion of this section, we will consider another important problem associated with the possibility of estimating the fractal dimension of an attractor by the calculated Lyapunov dimension. This problem is nontrivial and has long been under discussion in the literature. For example, the results of tests performed for Eno, Kaplan-Yorke, and Zaslavskii mappings and for the Rabinovich–Fabrikant equations showed that the Lyapunov dimension is very close to the fractal one [20]; however, for higher order mappings and flow systems, this is generally not the case. At present, a number of examples are known that point to an overestimated value of the dimension obtained by the Kaplan–Yorke procedure [21].

Young [22] rigorously proved the validity of the relation

$$k_+ \le D_C \le D_L, \tag{13}$$

which relates the number of the positive Lyapunov exponents k_+ and the fractal and Lyapunov (D_L) dimensions. Therefore, the Lyapunov dimension is the upper limit of the possible values of the attractor capacity. However, the question remains open as to the closeness of this limit to the fractal dimension for each particular dynamic system. We will try to find an answer to this question for flow (10).

The concept of the Lyapunov dimension originates from the hypothesis of Kaplan–Yorke [21], who proposed to use D_L to calculate the informational dimension of attractors of dynamic systems. The calculation algorithm is as follows:

$$D_L = k + \frac{\sum_{i=1}^{k} \Lambda_i}{|\Lambda_{k+1}|}. \tag{14}$$

Here, k is an integer for which the relations $\Lambda_1 + \Lambda_2 + \ldots + \Lambda_k > 0$ are valid, but $\Lambda_1 + \Lambda_2 + \ldots + \Lambda_{k+1} < 0$. In principle, two signatures of the Lyapunov spectrum are possible for flow (10) at $B > \hat{B}$, namely, $\langle +, 0, -, - \rangle$ and $\langle +, +, 0, - \rangle$. No other signatures are possible, because the sum of the Lyapunov exponents of a dissipative system must be negative. Note that, in the case of a signature with two positive exponents, the attractor dimension cannot be less than 3 according to relation (14), which contradicts the results of numerical calculations (Fig. 4). Therefore, for the parameters used in our numerical experiment, the hyperchaotic mode cannot occur and a signature of the form $\langle +, 0, -, - \rangle$ must take place. However, for this signature too, k as a function of the absolute value of Λ_3 may assume values of 2 or 3. Therefore, in the most favorable case (k = 2), the Lyapunov dimension cannot be less than 2, which exceeds the fractal dimension by almost 60% and the informational dimension by 66%.

Thus, it has been found that neither the informational dimension nor the attractor capacity can be even approximately estimated using the Lyapunov dimension for flow (10).

4. LABORATORY EXPERIMENT

In order to check the results of numerical analysis and the agreement between the constructed mathematical model and real physical systems, we carried out a laboratory experiment. To eliminate various side effects, the experiment was performed at low frequencies.

The experimental setup was designed in accordance with the basic diagram given in Fig. 1, except for two modifications that did not affect the operation of the device. These unimportant modifications consisted in the fact that the elements L_1 and R_1 were interchanged, and the common wire was connected to the junction between the elements R_1 and L_2. This modification made it possible to use R_1 as a sensor of the current i_1; however, this involved the need for galvanic decoupling of the pumping source from the experimental setup. For this reason, the pumping source was provided with a standard-signal generator, to the output of which a matching source voltage follower and a wideband transformer were additionally connected.

The nonlinear capacitance consisted of ten varicaps connected in parallel (the experimental development of the Research Institute of Semiconductor Devices, Tomsk), each having a capacitance at the working point C_0 of about 500 pF. In view of the condition of reaching a value of $Y_C = \omega_0 C_0 = 2 \times 10^{-3}$ S, employed in the numerical experiment, the low-signal resonance frequency $f_0 = \omega_0/2\pi$ was chosen to be $f_0 \approx 65$ kHz. We performed a series of experiments with this setup; however, in this section, we present only the results pertaining to the subject of this paper.

First of all, the resonance characteristic of the device (i.e., the dependence of the mean-square value of the current i_1 on the pumping frequency) was measured. With a varicap bias voltage of $E = 6$ V and a pumping voltage amplitude of $A \approx 3.5$ V, the resonance characteristic corresponded to the bifurcation diagram shown in Fig. 2 with a high degree of accuracy. The second (19.6 kHz), third (23.4 kHz), fourth (26 kHz), fifth (39 kHz), sixth (50 kHz), and eighth (120.2 kHz) resonances were reliably observed. Since the resonance peaks were curved, the resonance frequencies were

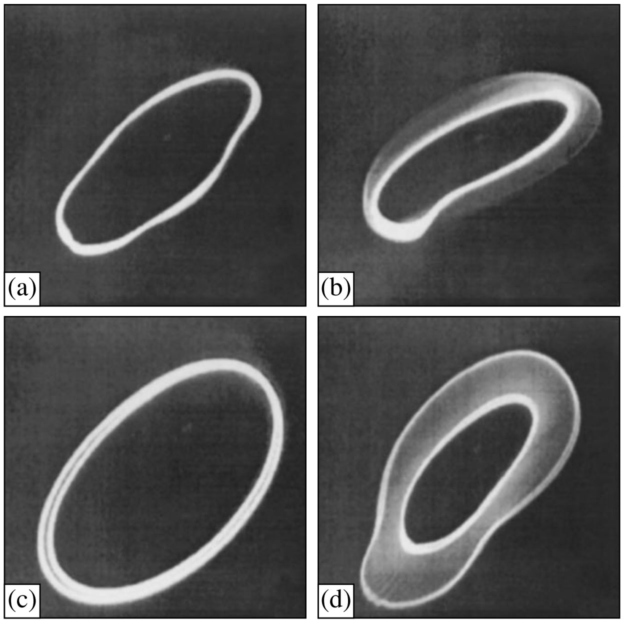

Fig. 5. The sequence of transformations of the attractor of the system under investigation on the (i_1, u_C) plane, observed in the laboratory experiment with an increasing amplitude of the external force.

determined as the half-sums of the frequencies at which hysteretic phenomena corresponding to the change of the variation direction of the pumping frequency were observed. The first and seventh resonances were not observed experimentally; this fact may be associated with a certain difference between the volt–farad characteristics of the employed varicaps and the adopted approximation (3).

The shape of the current i_1 was observed on the oscilloscope display. At the resonance frequencies, this current had the shape of a diffuse strip that was not synchronized with the oscilloscope scan signal; this points to the random character of the system behavior.

Phase portraits on the (i_1, u_C) plane were investigated at the frequency of the main nonlinear parametric force resonance (50 kHz). This made it possible to judge the structure of attractors of a nonlinear system. These portraits are presented in Fig. 5. At low pumping amplitudes on the order of fractions of a volt, the limiting cycle is the attractor (Fig. 5a). As the pumping amplitude increases, the attractor assumes a diffuse shape (Fig. 5b). The results of the numerical analysis allow us to conclude that this is a strange nonchaotic attractor. The first bifurcation occurs at $A \approx 1.65$ V. At this point, the attractor abruptly transforms into the form shown in Fig. 5c. Now, the attractor shape resembles a double-turn limiting cycle; however, its blurriness points to the random character of motion (cf. Fig. 4b). As the pumping amplitude increases further, the attractor assumes a form close to a flat strip (Fig. 5d), which agrees well with the fractal dimension calculated in the numerical experiment.

Thus, the results of laboratory experiments are in good agreement with the results of numerical analysis. This indicates that the constructed model (10) fits actual physical systems well.

CONCLUSIONS

The proposed mathematical model of a dynamic system makes it possible to investigate complicated dynamic modes that arise when nonlinear force and parametric resonances manifest themselves simultaneously. The increase in the phase space dimension to 4 significantly enriches the system dynamics and makes it possible to observe various types of motion such as deterministic chaos and the excitation of a strange nonchaotic attractor by a single-frequency external force.

We have investigated the effect of the external force amplitude on the value of the highest Lyapunov exponent and different types of attractor dimensions.

Using the system studied as a prototype, we are now completing the development of a source of broadband noiselike signals in the eight-millimeter wavelength range.

ACKNOWLEDGMENTS

We are grateful to Prof. J. Sarraille of the University of California for providing us with computer codes for calculating the fractal dimensions and for valuable advice on interpreting the results obtained.

REFERENCES

1. M. I. Rabinovich and D. I. Trubetskov, *Introduction to the Theory of Oscillations and Waves* (Nauka, Moscow, 1984; Kluwer, Dordrecht, 1989).
2. V. V. Migulin, V. I. Medvedev, E. R. Mustel', and V. N. Parygin, *Fundamentals of the Vibration Theory* (Nauka, Moscow, 1978).
3. V. S. Andreev, *Theory of Nonlinear Electric Circuits* (Svyaz', Moscow, 1972).
4. M. Hasler, Int. J. Bifurcation Chaos **8**, 647 (1998).
5. S. N. Vladimirov and V. V. Negrul, in *Proceedings of the International Symposium on Antennas and Propagation ISAP-2000, Fukuoka, 2000*, Vol. 3, pp. 1403–1406.
6. S. N. Vladimirov and V. V. Negrul, J. Bifurcation Chaos **12**, 819 (2002).
7. D. Ruelle and F. Takens, Commun. Math. Phys. **20**, 167 (1971).
8. V. S. Anishchenko, Izv. Vyssh. Uchebn. Zaved. Prikl. Nelineinaya Din. **5** (1), 109 (1997).
9. A. S. Dmitriev, Komp'yuterra, Issue 47 (1998).

10. V. I. Kaganov, *Transistor Transmitters* (Énergiya, Moscow, 1976).
11. V. S. Anishchenko, T. E. Vadivasova, and V. V. Astakhov, *Nonlinear Dynamics of Chaotic and Stochastic Systems* (Izd. Saratovsk. Univ., Saratov, 1999).
12. E. Hairer, S. Nörsett, and G. Wanner, *Solving Ordinary Differential Equations*, Vol. 1: *Nonstiff Problems* (Springer-Verlag, Heidelberg, 1987; Mir, Moscow, 1990).
13. G. Benettin, L. Galgani, and J. M. Strelkyn, Phys. Rev. A **14**, 2338 (1976).
14. S. Leibovitch and T. Toth, Phys. Lett. A **141**, 386 (1989).
15. J. J. Sarraille and L. S. Myers, Educ. Psychol. Meas. **54**, 94 (1994).
16. H. Haken, *Advanced Synergetics: Instability Hierarchies of Self-Organizing Systems and Devices* (Springer-Verlag, New York, 1983; Mir, Moscow, 1985).
17. C. Grebogi, E. Ott, and J. A. Yorke, Phys. D **13**, 261 (1984).
18. I. A. Khovanov, N. A. Khovanova, V. S. Anishchenko, and W. E. McClintock, Zh. Tekh. Fiz. **70** (5), 112 (2000) [Tech. Phys. **45**, 633 (2000)].
19. S. N. Vladimirov and A. A. Shtraukh, Zh. Tekh. Fiz. **74** (7), 1 (2004) [Tech. Phys. **49**, 805 (2004)].
20. Yu. I. Neĭmark and P. S. Landa, *Stochastic and Chaotic Oscillations* (Nauka, Moscow, 1987; Kluwer, Dordrecht, 1992).
21. J. L. Kaplan and J. A. Yorke, Lect. Notes Math., No. 730, 204 (1979).
22. L. S. Young, Ergodic Theory Dyn. System **2**, 109 (1982).

Translated by A. Bronshteĭn

Technical Physics, Vol. 49, No. 7, 2004, pp. 818–823. Translated from Zhurnal Tekhnicheskoĭ Fiziki, Vol. 74, No. 7, 2004, pp. 13–18.
Original Russian Text Copyright © 2004 by Yalamov, Khassanov.

GASES AND LIQUIDS

Thermophoresis of Sublimating Aerosol Particles with Inhomogeneous Thermal Conductivity

Yu. I. Yalamov and A. S. Khassanov
Moscow State Region University, Moscow, 105005 Russia
e-mail: rectorat@mgou.ru

Received December 4, 2003

Abstract—The theory of thermophoresis of a large solid spherical sublimating aerosol particle with a coordinate-dependent thermal conductivity is elaborated. The expression for the thermophoresis rate is derived and analyzed. *© 2004 MAIK “Nauka/Interperiodica”.*

FORMULATION OF THE PROBLEM

Let us consider a large solid spherical aerosol particle suspended in a one-component gas where a constant temperature gradient is sustained far from the particle. The phase transition that takes place on the surface of the particle in the form of evaporation (sublimation) of the the particle material leads to the formation of a viscous binary mixture around the particle. The interaction between the binary mixture and the nonuniformly heated particle surface results in thermal slip of the mixture over the surface. It is known that the appearance of a local inhomogeneity in the concentration of a binary mixture entails diffusion slip of the gas mixture over the particle surface. These conditions generate a momentum acting on the particle and propelling its accelerated motion. Simultaneously, the particle experiences the action of the viscous resistance of the binary mixture. When the resultant of these forces turns to zero, the particle begins to move in a straight line at a constant velocity, which we intend to determine and analyze in this study.

Let us take the coordinate system with the origin at the center of the particle. Thus, we have a problem on the flow past a sphere with velocity $\mathbf{v}_\infty$ that is constant in magnitude and direction at infinity. The positive direction of the x axis is chosen along the temperature gradient $(\nabla T_e)_\infty$, which is also constant at infinity. If the velocity of the particle relative to the center of gravity of the external medium is denoted by $\mathbf{U}$, we have $\mathbf{v}_\infty = -\mathbf{U} = U\mathbf{i}$, where U is the length of vector $\mathbf{U}$. Turning to the spherical coordinate system, where the angle θ is measured from the positive direction of the x axis, and considering the steady-state motion of the binary mixture relative to the particle at small Reynolds numbers in the absence of the external forces, we obtain [1] the following equations of motion and the boundary conditions at infinity:

$$\eta\nabla^2\mathbf{v} = \nabla p, \quad \operatorname{div}\mathbf{v} = 0, \tag{1}$$

$$v_r = U\cos\theta, \quad v_\theta = -U\sin\theta, \quad p = p_\infty \quad \text{at} \quad r \longrightarrow \infty, \tag{2}$$

where η is the dynamic viscosity of the binary mixture; $\mathbf{v}$ and p describe the distributions of velocity and pressure, respectively; p_∞ is a constant; and $v_\varphi = 0$.

Let n_1 and n_2 be the numbers of molecules of the first component (evaporating particle substance) and the second component (one-component gas) of the binary mixture per unit volume, respectively; c_1 and c_2 represent their respective relative concentrations; and $n = n_1 + n_2$. Then,

$$c_1 = \frac{n_1}{n}, \quad c_2 = \frac{n_2}{n}, \quad c_1 + c_2 = 1. \tag{3}$$

As follows from (3), it is sufficient to find c_1. Since we are dealing with low velocities (the Reynolds number $\mathrm{Re} \ll 1$), function c_1 satisfies [1] the following equation and the condition at infinity:

$$\nabla^2 c_1 = 0, \quad c_1 = c_\infty, \tag{4), (5}$$

where c_∞ is a constant.

From this point on, we will express the boundary conditions in terms of quantities n_{01}, n_{02}, n_0, ρ_0, T_{0e}, and T_{0i}. The point is that, strictly speaking, the values of n_1, n_2, n, ρ, T_e, and T_i (ρ and T_e are the density and the temperature of the binary mixture, respectively, and T_i is the temperature inside the particle) depend on r and θ. However, an external perturbation induced by the temperature gradient $(\nabla T_e)_\infty$ is only a small addition to the unperturbed parameters [1]: $n_1 = n_{01} + n_1'$, $n_2 = n_{02} + n_2'$, $n = n_0 + n'$, $\rho = \rho_0 + \rho'$, $T_e = T_{0e} + T_e'$, and $T_i = T_{0i} + T_i'$, where the first terms on the right-hand sides are equal to the corresponding unperturbed values of the corresponding quantities and the second terms are the deviations from the mean values due to the presence of the temperature gradient $(\nabla T_e)_\infty$. In our case, these deviations are small as compared to the mean values [1] and are disregarded in the boundary conditions (i.e., the boundary conditions are linearized).

The surface of a drop is assumed to be impermeable for the second component of the binary mixture [1]:

$$n_{02}v_r - D\beta_1\frac{\partial c_2}{\partial r} = 0 \quad \text{at} \quad r = a, \tag{6}$$

where

$$\beta_1 = n_0^2\frac{m_1}{\rho_0}, \tag{7}$$

a is the particle radius, m_1 is the molecular mass of the evaporating substance, and D is the coefficient of interdiffusion of the mixture components.

Using formulas (3), we can rewrite condition (6) in the form

$$v_r = -\frac{D\beta_1}{n_{02}}\frac{\partial c_1}{\partial r} \quad \text{at} \quad r = a. \tag{8}$$

Taking into account the thermal and diffusion slip of the binary mixture over the particle surface yields the following condition for the velocity v_θ [1]:

$$v_\theta = \frac{K_{Tsl}^{(e)}}{aT_{0e}}\frac{\partial T_e}{\partial\theta} + \frac{K_{sl}D}{a}\frac{\partial c_1}{\partial\theta} \quad \text{at} \quad r = a, \tag{9}$$

where $K_{Tsl}^{(e)}$ and K_{sl} are the thermal and the diffusion slip factors of the binary mixture, respectively.

We now consider heat transfer in the system including the particle and the medium. Let us assume that this process is quasi-stationary. If the distribution of temperature T in a nonuniformly heated medium is maintained only by external heat sources that are constant in time, the heat conduction equation appears as [2]

$$\rho c_p(\mathbf{v}, \nabla T) = \mathrm{div}(\kappa\nabla T), \tag{10}$$

where ρ is the density, c_p is the heat capacity at constant pressure, $\mathbf{v}$ is the velocity, and κ is the thermal conductivity.

In our case, Eq. (10) becomes [1, 2]

$$\nabla^2 T_e = 0, \tag{11}$$

$$\mathrm{div}(\kappa_i\nabla T_i) = 0, \tag{12}$$

where T_i and κ_i are the temperature and the thermal conductivity inside the particle, respectively.

The temperature T_e meets the following condition at infinity [1]:

$$T_e = T_{0e} + |(\nabla T_e)_\infty| r\cos\theta \quad \text{at} \quad r \longrightarrow \infty. \tag{13}$$

We consider that the thermal conductivity κ_e of the external medium is constant [1] and the thermal conductivity κ_i at each point inside the particle is a function of the radius vector of this point. It is assumed that the particle radius is much larger than the free paths of the molecules of the binary mixture components (the Knudsen number is small) and the following condition is met at the particle surface (the corrections proportional to the Knudsen number are neglected) [1]:

$$T_e = T_i \quad \text{at} \quad r = a. \tag{14}$$

Phase transition occurring on the particle surface provides for the boundary conditions in the form [1]

$$n_{01}v_r - D\beta_2\frac{\partial c_1}{\partial r} = n_0\alpha\nu(s_1 - c_1) \quad \text{at} \quad r = a, \tag{15}$$

$$-\kappa_e\frac{\partial T_e}{\partial r} + \kappa_i\frac{\partial T_i}{\partial r} = -Lm_1 n_0\alpha\nu(s_1 - c_1) \quad \text{at} \quad r = a, \tag{16}$$

where

$$\beta_2 = n_0^2\frac{m_2}{\rho_0}; \tag{17}$$

m_2 being the molecular mass of the second component; α is the evaporation coefficient ($\alpha \in [0, 1]$); and $\nu = \sqrt{kT_{0e}/(2\pi m_1)}$, s_1, and L are one-fourth of the absolute thermal velocity of the evaporating molecules (k is the Boltzmann constant), the saturating relative concentration, and the specific heat of the phase transition of the first component of the binary mixture, respectively.

Based on expressions (8), (15), and $n_{01}m_1 + n_{02}m_2 = \rho_0$, we obtain Eq. (16) in the form

$$-\kappa_e\frac{\partial T_e}{\partial r} + \kappa_i\frac{\partial T_i}{\partial r} = \frac{Lm_1 Dn_0^2}{n_{02}}\frac{\partial c_1}{\partial r} \quad \text{at} \quad r = a, \tag{18}$$

where $s_1(T_i) = s + \delta(T_i - T_{0i})$ at

$$T_i - T_{0i} = \frac{c_1 - s}{\delta} - \frac{Dn_0}{n_{02}\alpha\nu\delta}\frac{\partial c_1}{\partial r} \quad \text{at} \quad r = a, \tag{19}$$

$$s = s_1 \quad \text{at} \quad T_i = T_{0i}, \tag{20}$$

$$\delta = \frac{\partial s_1}{\partial T_i} \quad \text{at} \quad T_i = T_{0i}. \tag{21}$$

From the equations and boundary conditions listed above, we must find T_i, T_e, and c_1 (thermal and diffusion parts); $\mathbf{v}$ and p (hydrodynamic part); and the velocity $\mathbf{U}$.

SOLUTION TO THE THERMAL AND DIFFUSION PARTS OF THE PROBLEM

Let us pass from the variables r and θ to the variables R and θ such that

$$R = r/a. \tag{22}$$

Since $r = a(r/a)$, we can consider κ_i as a function of R:

$$\kappa_i = f\left(\frac{r}{a}\right) = f(R). \tag{23}$$

Assume that

$$T_1 = |(\nabla T_e)_\infty| a, \tag{24}$$

$$g_e(R, \theta) = (T_e - T_{0e} - T_1 R\cos\theta)/T_1, \tag{25}$$

$$g_i(R, \theta) = (T_i - T_{0i})/T_i, \tag{26}$$

$$c_1(R, \theta) = (c_1 - c_\infty)/(\delta T_1). \tag{27}$$

Then, Eqs. (12), (11), (4), (14), (18), (19), (13), and (5) correspond to the following conditions:

$$\nabla^2 g_i = -\frac{f'}{f} g_i', \tag{28}$$

$$\nabla^2 g_e = 0, \tag{29}$$

$$\nabla^2 c_1 = 0, \tag{30}$$

$$g_i - g_e = \cos\theta + (T_{0e} - T_{0i})/T_1 \quad \text{at} \quad R = 1, \tag{31}$$

$$\frac{\kappa_{i1}}{\kappa_e} g_i' - g_e' - k_2 c_1' = \cos\theta \quad \text{at} \quad R = 1, \tag{32}$$

$$c_1 - k_1 c_1' - g_i = (s - c_\infty)/(\delta T_1) \quad \text{at} \quad R = 1, \tag{33}$$

$$g_e = 0 \quad \text{at} \quad R \longrightarrow \infty, \tag{34}$$

$$c_1 = 0 \quad \text{at} \quad R \longrightarrow \infty, \tag{35}$$

where κ_{i1} is the value of κ_i on the particle surface; f', g_i', g_e', and c_1' are the derivatives with respect to R (in Laplacians $\nabla^2 g_i$, $\nabla^2 g_e$, and $\nabla^2 c_1$, the variable r is also replaced by R); and the dimensionless constants k_1 and k_2 are defined by

$$k_1 = \frac{Dn_0}{\alpha \nu n_{02} a}, \tag{36}$$

$$k_2 = \frac{L m_1 D n_0^2 \delta}{n_{02} \kappa_e}. \tag{37}$$

We begin from Eq. (28). Let us seek the function $g_i(R, \theta)$ in the form

$$g_i(R, \theta) = M(R)\cos\theta. \tag{38}$$

Then function $M(R)$ can be derived from the differential equation

$$R^2 M'' + \left(2 + R\frac{f'}{f}\right) R M' - 2M = 0. \tag{39}$$

We assume that the function $f(R)$ is given and can be represented in terms of the power series

$$f(R) = \sum_{t=0}^{\infty} f_t R^t, \tag{40}$$

where f_t is the expansion coefficient.

From the expansion of function $f(R)$, one can gain the coefficients of expansion of function $2 + Rf'/f$, for example, by the method of undetermined coefficients. Let us suppose that

$$2 + R\frac{f'}{f} = \sum_{t=0}^{\infty} b_t R^t, \tag{41}$$

where b_t are undetermined coefficients.

To find these coefficients, note that

$$b_0 = 2 \tag{42}$$

($\kappa_i = f(R) > 0$ for $R \le 1$).

Deriving from (40) that

$$f'(R) = \sum_{t=1}^{\infty} t f_t R^{t-1}, \tag{43}$$

and using expressions (42) and (43), we can represent Eq. (41) as

$$\sum_{t=1}^{\infty} t f_t R^t = \left(\sum_{t=0}^{\infty} f_t R^t\right)\left(\sum_{t=1}^{\infty} b_t R^t\right). \tag{44}$$

Multiplying the series in the right-hand part of Eq. (44) and comparing the coefficients at the same powers of R, we obtain

$$b_1 = \frac{f_1}{f_0}, \tag{45}$$

$$b_t = \frac{t f_t - \sum_{j=1}^{t-1} f_j b_{t-j}}{f_0}, \tag{46}$$

where $t \ge 2$.

Now, when the coefficients b_t are determined, Eq. (39) becomes

$$R^2 M'' + \left(\sum_{t=0}^{\infty} b_t R^t\right) R M' - 2M = 0. \tag{47}$$

We seek the particular solution M_1 of this equation in the form [3]

$$M_1 = R^\rho \sum_{t=0}^{\infty} \alpha_t R^t, \tag{48}$$

where ρ is an undetermined exponent.

Since we seek a particular solution, we may take $\alpha_0 = 1$. It follows from (48) that

$$RM_1' = \sum_{t=0}^{\infty} \alpha_t (\rho + t) R^{\rho + t}, \tag{49}$$

$$R^2 M_1'' = \sum_{t=0}^{\infty} \alpha_t (\rho + t)(\rho + t - 1) R^{\rho + t}. \tag{50}$$

Substituting formulas (48)–(50) into Eq. (47), we have

$$\sum_{t=0}^{\infty} \Biggl[(\rho + t)(\rho + t - 1)\alpha_t + \sum_{j=0}^{t} (\rho + t - j)\alpha_{t-j} b_j - 2\alpha_t \Biggr] R^{\rho + t} = 0. \tag{51}$$

This relation suggests that, at any $t \geq 0$,

$$(\rho + t)(\rho + t - 1)\alpha_t + \sum_{j=0}^{t} (\rho + t - j)\alpha_{t-j} b_j - 2\alpha_t = 0. \tag{52}$$

Since $\alpha_0 = 1$ and $b_0 = 2$, Eq. (52) at $t = 0$ yields the following equation with respect to ρ:

$$\rho(\rho - 1) + 2\rho - 2 = 0. \tag{53}$$

From two roots of this equation, only the root $\rho = 1$ is valid. Let us suppose that $t \geq 1$. We write Eq. (52) in the form

$$(\rho + t)(\rho + t - 1)\alpha_t + (\rho + t)\alpha_t b_0 - 2\alpha_t + \sum_{j=1}^{t} (\rho + t - j)\alpha_{t-j} b_j = 0. \tag{54}$$

Since $\rho = 1$, it follows from Eq. (54) that coefficients α_t can be found for any $t \geq 1$ by using the recurrent formula

$$\alpha_t = -\frac{\sum_{j=1}^{t} (t + 1 - j)\alpha_{t-j} b_j}{t(t + 3)}, \tag{55}$$

where $\alpha_0 = 1$.

Thus, we have obtained a particular solution $M_1(R)$ to Eq. (39). It is known [3] that, from a particular solution $y_1(x)$ to the differential equation

$$y'' + p(x)y' + q(x)y = 0, \tag{56}$$

we can construct another solution, which is linearly independent of the first one, by the formula

$$y_2(x) = y_1(x) \int \exp\left(-\int_{x_0}^{x} p(\tau) d\tau \right) \frac{dx}{y_1^2(x)}. \tag{57}$$

Equation (39) can be readily reduced to the form (56). With the use of formula (57), we derive the second particular solution M_2 to Eq. (39):

$$M_2(R) = M_1(R) \int_1^R \frac{dt}{t^2 f(t) M_1^2(t)}. \tag{58}$$

Thus, the general solution to Eq. (39) has the form

$$M = C_1 M_1(R) + C_2 M_1(R) \int_1^R \frac{dt}{t^2 f(t) M_1^2(t)}, \tag{59}$$

where C_1 and C_2 are indeterminate coefficients.

It is easy to see that, in the case under study, we must choose $C_2 = 0$. Therefore, $M(R) = C_1 M_1(R)$ and, on the strength of Eq. (38),

$$g_i(R, \theta) = C_1 M_1(R) \cos\theta. \tag{60}$$

In general, function $M_1(R)$ is constructed on the basis of the recurrent formulas presented above; however, in two limiting cases, this function can be found directly from differential equation (39). If the thermal conductivity varies only slightly (i.e., $\kappa_i = \text{const}$), then $f(R) = \text{const}$ and the sought particular solution to Eq. (39) can be readily found:

$$M_1 = R. \tag{61}$$

In the opposite case of a strongly varying thermal conductivity, for example,

$$\kappa_i = C \exp(kR), \tag{62}$$

where C and k are certain constants, the desired particular solution to Eq. (39) is given by the function

$$M_1(R) = -\frac{6}{k^3 R^2} \left(\exp(-kR) - 1 + kR - \frac{k^2 R^2}{2} \right). \tag{63}$$

Let us turn to Eqs. (29) and (30) and seek functions g_e and c_1 in the form

$$g_e = \frac{\mu_1}{R^2} \cos\theta + \frac{\varphi}{R^2}, \tag{64}$$

$$c_1 = \frac{\mu_2}{R^2} \cos\theta, \tag{65}$$

where μ_1, φ, and μ_2 are indeterminate coefficients.

From conditions (31)–(33), one obtains six equations for the four coefficients C_1, μ_1, φ, and μ_2 and the two quantities T_{0e} and c_∞. Solving this system, we find T_e, T_i, and c_1. We write only the expression for μ_2:

$$\mu_2 = 3\left[2(1 + 2k_1) + 2k_2 + (1 + 2k_1) \frac{\kappa_{i1}}{\kappa_e} \frac{M_1'(1)}{M_1(1)} \right]^{-1}. \tag{66}$$

SOLUTION TO THE HYDRODYNAMIC PART OF THE PROBLEM

As in [1], we look for a solution to the Stocks equation in the form

$$v_r = \left(\frac{A_e}{R^3} + \frac{B_e}{R} + 1\right) U \cos\theta, \tag{67}$$

$$v_\theta = \left(\frac{A_e}{2R^3} - \frac{B_e}{2R} - 1\right) U \sin\theta, \tag{68}$$

$$p = p_\infty + \eta \frac{U}{a} \frac{B_e}{R^2} \cos\theta. \tag{69}$$

From boundary conditions (8) and (9), one finds A_e and B_e. Here, we present only the expression for B_e:

$$B_e = -\frac{3}{2} + \frac{D\delta T_1}{aU}\left[\frac{\beta_1}{n_{02}} + \frac{K_{Tsl}^{(e)}(1+2k_1)}{\delta T_{0e} D} + K_{sl}\right]\mu_2. \tag{70}$$

Substituting the values of A_e and B_e into Eqs. (67)–(69), we obtain the expressions for v_r, v_θ, and p. The flow exerts on a particle the force [1]

$$\mathbf{F} = \left(\iint\limits_S (p_{rr}\cos\theta - p_{r\theta}\sin\theta)\,ds\right)\mathbf{i}, \tag{71}$$

where p_{rr} and $p_{r\theta}$ are the components of the stress tensor on the particle surface S.

Calculating integral (71) yields the following expression for force **F**:

$$\mathbf{F} = -4\pi\eta U a B_e \mathbf{i}. \tag{72}$$

In order to find the velocity of rectilinear and uniform motion, we impose the condition

$$\mathbf{F} = 0. \tag{73}$$

Hence, it follows that $B_e = 0$. Using formulas (70) and (66), we arrive at

$$\begin{gathered}\mathbf{U} = -\left[\frac{2K_{Tsl}^{(e)}}{T_{0e}} + \frac{2D\delta}{1+2k_1}\left(\frac{\beta_1}{n_{02}} + K_{sl}\right)\right] \\ \times\left[2 + \frac{2k_2}{1+2k_1} + \frac{\kappa_{i1}}{\kappa_e}\frac{M_1'(1)}{M_1(1)}\right]^{-1}(\nabla T_e)_\infty.\end{gathered} \tag{74}$$

DISCUSSION

In what follows, we consider some particular cases of formula (74). The absence of a phase transition at the surface of a particle implies that $\alpha = 0$, $k_1 = \infty$ (see formula (36)), and $K_{Tsl}^{(e)} = K_{Tsl}\eta/\rho$ [1], where K_{Tsl}, η, and ρ are the coefficient of thermal slip, the dynamic viscosity, and the density of the one-component gas, respectively. In this case, formula (74) becomes [4]

$$\mathbf{U} = -\frac{K_{Tsl}\eta}{\rho T_{0e}} 2\kappa_e \left[2\kappa_e + \kappa_{i1}\frac{M_1'(1)}{M_1(1)}\right]^{-1}(\nabla T_e)_\infty. \tag{75}$$

If, in addition, the particle is homogeneous in thermal conductivity, then $\kappa_i \equiv$ const, $M_1(R) = R$ (see formula (61)), and $M_1'(1)/M_1(1) = 1$, and expression (75) in its turn is transformed into a well-known expression for the rate of thermophoresis [1].

In the case when the phase transition does occur on the surface of a particle and the particle is homogeneous in thermal conductivity, $\kappa_i \equiv$ const, $M_1(R) = R$, and $M_1'(1)/M_1(1) = 1$, and we derive from (74) the expression [5]

$$\begin{gathered}\mathbf{U}_0 = -\left[\frac{2K_{Tsl}^{(e)}}{T_{0e}} + \frac{2D\delta}{1+2k_1}\left(\frac{\beta_1}{n_{02}} + K_{sl}\right)\right] \\ \times\left[2 + \frac{2k_2}{1+2k_1} + \frac{\kappa_{i1}}{\kappa_e}\right]^{-1}(\nabla T_e)_\infty.\end{gathered} \tag{76}$$

Using formula (76), we can write (74) in the form

$$\begin{gathered}\mathbf{U} = \mathbf{U}_0\left\{1 + \left(\frac{M_1'(1)}{M_1(1)} - 1\right)\right. \\ \left.\times\left[1 + \frac{2\kappa_e}{\kappa_{i1}}\left(1 + \frac{k_2}{1+2k_1}\right)\right]^{-1}\right\}^{-1}.\end{gathered} \tag{77}$$

The second multiplier on the right-hand side of expression (77) is a correction factor and depends on both the evaporation factor and the inhomogeneity in thermal conductivity. It is reasonable to consider the case when the first multiplier in formula (77) depends on the evaporation factor and the second multiplier is almost independent of the evaporation factor and characterizes only the influence of the varying conductivity. Let us denote

$$\gamma_1 = 1 + \frac{2\kappa_e}{\kappa_{i1}}\left(1 + \frac{k_2}{1+2k_1}\right), \tag{78}$$

$$\gamma_2 = \frac{M_1'(1)}{M_1(1)}. \tag{79}$$

Formula (78) suggests that

$$1 \le \gamma_1 \le 1 + \frac{2\kappa_e}{\kappa_{i1}}(1 + k_2). \tag{80}$$

The latter expression indicates that, if the value of $2\kappa_e(1 + k_2)/\kappa_{i1}$ is small, the correction factor in Eq. (77) only slightly depends on the evaporation factor α and closely approximates the effect of varying conductivity on the rate of thermophoresis. By way of illustration, let the ice on the particle surface melt and evaporate into the air. Since [6] $\kappa_e = 2.38 \times 10^{-4}$ W/(m deg) and $\kappa_{i1} =$

5.69×10^{-1} W/(m deg), we have $2\kappa_e/\kappa_{i1} = 8.36 \times 10^{-4}$. The coefficient k_2 can be calculated from (37). The specific heat of the phase transition of the first component in the binary mixture is determined as the sum $L = q + r$, where q is the specific heat of the ice melting and r is the specific heat of evaporation: $q = 3.4 \times 10^5$ J/kg, $r = 2.50 \times 10^6$ J/kg, and $L = 2.84 \times 10^6$ J/kg. The value of n_{02} is approximately equal to n_0, and $n_0 = 2.65 \times 10^{25}$ 1/m^3. The remaining values required for the calculation of k_2 are as follows: $m_1 = 2.99 \times 10^{-26}$ kg, $D = 2.5 \times 10^{-5}$ m^2/s, and $\delta = 1.67 \times 10^{-3}$ 1/deg. Hence, the calculation results in $k_2 = 3.95$ and $2\kappa_e(1 + k_2)/\kappa_{i1} = 4.14 \times 10^{-3}$. Therefore, the correction factor on the right-hand side of (77) only slightly depends on α. This particular dependence on α can be easily plotted for $a = 10^{-5}$ m ($k = 1.38 \times 10^{-23}$ J/deg, $T_{0e} = 273$ K, $m_1 = 2.99 \times 10^{-26}$ kg, and $\nu = 1.42 \times 10^2$ m/s):

$$\mathbf{U} = \mathbf{U}_0\left[1 + (\gamma_2 - 1)\frac{100\alpha + 352}{100.4\alpha + 352.3}\right]^{-1}. \qquad (81)$$

To reveal the influence of changes in thermal conductivity on the motion of a sublimating particle, it is reasonable to consider particles with strongly pronounced inhomogeneity, i.e., particles with an appreciable difference in the thermal conductivities at the center and on the surface. For example, we take as the model the exponential function (62),

$$\kappa_i(R) = \kappa_i(0)\exp(kR). \qquad (82)$$

Assume that a change in $\kappa_i(R)$ (variation within one particle radius) is subjected to the condition

$$0.1 \le \frac{\kappa_1(1)}{\kappa_i(0)} \le 10. \qquad (83)$$

From inequality (83), we obtain

$$-2.3 \le k \le 2.3. \qquad (84)$$

As was mentioned above, if $\kappa_i(R)$ is defined by formula (82), then $M_1(R)$ is defined by (63). From (63), it follows that

$$\frac{M_1'(1)}{M_1(1)} = -2 - k\frac{\exp(-k) - 1 + k}{\exp(-k) - 1 + k - 0.5k^2}. \qquad (85)$$

The latter expression together with condition (84) yields γ_2 in the range [0.59, 1.81]. Since the correction factor in (81) is almost independent of α, it varies from 0.6 to 1.6 when γ_2 changes from 0.59 to 1.81. This example indicates that the inhomogeneity in the thermal conductivity of a sublimating particle can produce a substantial effect on its velocity irrespective of the value of the evaporation factor α.

REFERENCES

1. V. S. Galoyan and Yu. I. Yalamov, *Dynamics of Drops in Inhomogeneous Viscous Media* (Luǐs, Yerevan, 1985).
2. L. D. Landau and E. M. Lifshitz, *Course of Theoretical Physics*, Vol. 6: *Fluid Mechanics* (Nauka, Moscow, 1988; Pergamon, New York, 1987).
3. V. I. Smirnov, *A Course of Higher Mathematics* (Nauka, Moscow, 1967; Addison-Wesley, Reading, 1964), Vol. 2.
4. Yu. I. Yalamov and A. S. Khasanov, Teplofiz. Vys. Temp. **34**, 929 (1996).
5. G. Yu. Yalamov, Vestn. Mosk. Gos. Otkr. Univ., Ser.: Fiz. Khim. Geogr., No. 1, 26 (2003).
6. N. B. Vargaftik, *Tables of Thermophysical Properties of Liquids and Gases* (Nauka, Moscow, 1972; Halsted Press, New York, 1975).

Translated by A. Sidorova

Technical Physics, Vol. 49, No. 7, 2004, pp. 824–832. Translated from Zhurnal Tekhnicheskoĭ Fiziki, Vol. 74, No. 7, 2004, pp. 19–26.
Original Russian Text Copyright © 2004 by Zharov, Shiryaeva, Grigor'ev.

GASES AND LIQUIDS

On Nonlinear Corrections to the Frequencies of Oscillations of a Charged Drop in an External Incompressible Medium

A. N. Zharov, S. O. Shiryaeva, and A. I. Grigor'ev
Yaroslavl State University, Yaroslavl, 150000 Russia
e-mail: grig@uniyar.ac.ru

Received November 4, 2003

Abstract—Analytical expressions are derived for the shape generatrix of an ideally conducting drop immersed in an incompressible dielectric medium as well as for nonlinear corrections to the frequencies of the oscillations of the drop. The solutions are obtained in an approximation of the third order of smallness with respect to the amplitude of the initial deformation of the equilibrium spherical shape of the drop. It is shown that the presence of the ambient liquid results in a reduction of the absolute magnitudes of corrections both to the oscillation frequencies and the self-charge critical for the development of instability of the drop. © *2004 MAIK "Nauka/Interperiodica".*

1. The problem of nonlinear oscillations of a charged drop in an ambient dielectric medium is of interest in connection with numerous scientific, technical, and technological applications [1, 2]. Therefore, this problem has already become a subject of theoretical analysis in the second order of smallness both in the cases of incompressible [3] and compressible ambient media [4]. However, the issue of nonlinear corrections to the oscillation frequencies, manifesting themselves only in the third order of smallness, has remained beyond the scope of research [5–7]. The present study is performed in connection with the above.

2. Let us consider a spherical drop of an ideal incompressible and ideally conducting liquid with a density $\rho_{(i)}$ and surface tension coefficient σ. The drop having a radius R and bearing a charge Q is immersed in an ideal incompressible liquid with a density $\rho_{(e)}$ and permittivity ε_d under the zero-gravity condition. The liquid motion both inside the drop and in the ambient medium is assumed to be potential with velocity potentials $\psi_{(i)}$ and $\psi_{(e)}$, respectively. Denote the electric field potential in the drop vicinity by ϕ. The drop shape will be assumed to be axisymmetric both at the initial instant and at all subsequent ones. The interface equation in nondimensional variables such that $\rho_{(i)} = 1$, $R = 1$, and $\sigma = 1$ at any time instant t can be written in the form

$$r = 1 + \xi(\vartheta, t), \tag{1}$$

where ϑ is the polar angle of a spherical coordinate system. The initial deformation of the spherical surface of the drop we take in the form

$$t = 0:\ \xi = \xi_0 P_0(\cos\vartheta) + \varepsilon \sum_{m \in \Omega} h_m P_m(\cos\vartheta) \tag{2}$$

with the additional condition

$$t = 0:\ \partial_t \xi = 0, \tag{3}$$

where ε is an arbitrary small parameter characterizing the amplitude of the initial perturbation; $P_m(\cos\vartheta)$ is the Legendre polynomial of the mth order; ξ_0 is a constant chosen in such a way that the volume of the drop at the initial instant coincides with the volume of the equilibrium sphere; ∂_t means a partial derivative with respect to variable t; Ω is the set of indices of modes initially excited; h_m are constants allowing for the contribution of the mth mode to formation of the initial shape of the drop such that $\sum_{m \in \Omega} h_m = 1$. The complete mathematical formulation of the problem on capillary oscillations of a charged drop, in addition to the drop surface equation (1) and boundary conditions (2) and (3), includes the Laplace equations for the potentials of the liquid velocity and electric field,

$$\Delta\psi_{(i)} = 0; \quad \Delta\psi_{(e)} = 0; \quad \Delta\phi = 0; \tag{4}$$

conditions of boundedness of the potentials,

$$r \longrightarrow 0:\ \psi_{(i)} \longrightarrow 0; \tag{5}$$

$$r \longrightarrow +\infty:\ \psi_{(e)} \longrightarrow 0; \quad \nabla\phi \longrightarrow 0; \tag{6}$$

the kinematic and dynamic boundary conditions,

$$\begin{aligned} r = 1 + \xi(\vartheta, t):\ \partial_t \xi &= \partial_r \psi_{(i)} - \frac{1}{r^2}\partial_\vartheta \psi_{(i)} \partial_\vartheta \xi \\ &= \partial_r \psi_{(e)} - \frac{1}{r^2}\partial_\vartheta \psi_{(e)} \partial_\vartheta \xi, \end{aligned} \tag{7}$$

$$\begin{aligned} \partial_t \psi_{(i)} + \frac{1}{2}(\nabla\psi_{(i)})^2 - \rho_{(e)}\left(\partial_t \psi_{(e)} + \frac{1}{2}(\nabla\psi_{(e)})^2\right) \\ = p_0 - p_\infty + p_q - p_\sigma; \end{aligned} \tag{8}$$

1063-7842/04/4907-0824$26.00 © 2004 MAIK "Nauka/Interperiodica"

the condition of invariability of the volume of the drop,

$$\int_V r^2 \sin\vartheta \, dr d\vartheta d\varphi = \frac{4\pi}{3}, \tag{9}$$

where

$$V = \{r, \vartheta, \varphi | 0 \le r \le 1 + \xi;\ 0 \le \vartheta \le \pi;\ 0 \le \varphi \le 2\pi\};$$

the condition of constancy of the total charge,

$$\int_V \mathbf{n} \cdot \nabla \phi dS = -4\pi Q, \tag{10}$$

where

$$S = \{r, \vartheta, \varphi | r = 1 + \xi;\ 0 \le \vartheta \le \pi;\ 0 \le \varphi \le 2\pi\};$$

and the condition of constancy of the electric potential over the interface between the drop and ambient liquid,

$$r = 1 + \xi(\vartheta, t):\ \phi = \phi_S(t). \tag{11}$$

In expressions (4)–(11), p_∞, p_0, p_q, and p_σ are the pressures of the ambient medium at infinity, of the liquid at the center of the drop, of the electric field, and the capillary pressure, respectively; **n** is a unit vector normal to the surface of the drop; and ϕ_S is the electric potential of the surface of the drop.

3. We solve the problem (1)–(11) by a multiscale method [8, 9]. In particular, all potentials and the equation of the generatrix of the drop's surface we assume to be functions of three time scales $T_m = \varepsilon^m t$; $m = 0, 1, 2$, and present them in the form of series with respect to small parameter ε,

$$\phi(r, \vartheta, t) = \sum_{m=0}^{3} \varepsilon^m \phi^{(m)}(r, \vartheta, T_0, T_1, T_2) + O(\varepsilon^4); \tag{12}$$

$$\phi_S(r, t) = \sum_{m=0}^{3} \varepsilon^m \phi_S^{(m)}(r, T_0, T_1, T_2) + O(\varepsilon^4); \tag{13}$$

$$\psi_{(i)}(r, \vartheta, t) = \sum_{m=1}^{3} \varepsilon^m \psi_{(i)}^{(m)}(r, \vartheta, T_0, T_1, T_2) + O(\varepsilon^4); \tag{14}$$

$$\psi_{(e)}(r, \vartheta, t) = \sum_{m=1}^{3} \varepsilon^m \psi_{(e)}^{(m)}(r, \vartheta, T_0, T_1, T_2) + O(\varepsilon^4); \tag{15}$$

$$\xi(\vartheta, t) = \sum_{m=1}^{3} \varepsilon^m \xi^{(m)}(\vartheta, T_0, T_1, T_2) + O(\varepsilon^4); \tag{16}$$

where $\phi^{(0)} = Q/(\varepsilon_d r)$ and $\phi_S^{(0)} = Q/\varepsilon_d$ are the solutions of the problem of the zeroth order of smallness, that is, for an equilibrium spherical surface of the drop. Substituting expressions (12)–(16) into Eqs. (1)–(11) gives problems of different orders of smallness that, for the sake of briefness here, are presented in Appendix A. Since the Laplace equation (4) is linear, the potentials of the liquid velocity and electric field in each order of smallness are solutions of Laplace equations (1A), (10A), and (19A). Solutions of these equations with regard for the boundedness conditions (2A), (3A), (11A), (12A), (20A), and (21A) can be written in the form

$$\psi_{(i)}^{(m)}(r, \vartheta, T_0, T_1, T_2) = \sum_{n=1}^{\infty} r^n D_{(i)n}^{(m)}(T_0, T_1, T_2) P_n(\cos\vartheta); \tag{17}$$

$$m = 1, 2, 3;$$

$$\psi_{(e)}^{(m)}(r, \vartheta, T_0, T_1, T_2) = \sum_{n=0}^{\infty} \frac{D_{(e)n}^{(m)}}{r^{n+1}}(T_0, T_1, T_2) P_n(\cos\vartheta); \tag{18}$$

$$m = 1, 2, 3;$$

$$\phi^{(m)}(r, \vartheta, T_0, T_1, T_2) = \sum_{n=0}^{\infty} \frac{F_n^{(m)}(T_0, T_1, T_2)}{r^{n+1}} P_n(\cos\vartheta); \tag{19}$$

$$m = 1, 2, 3.$$

Note that in expression (17), the summation begins at $n = 1$ because the potential is determined to an accuracy of an arbitrary function of time which allows one to set $D_{(i)0}^{(m)} = 0$. A function describing the deviation of the drop's surface from a spherical shape we represent in the form of an expansion in the Legendre polynomials,

$$\xi^{(m)}(\vartheta, T_0, T_1, T_2) = \sum_{n=0}^{\infty} M_n^{(m)}(T_0, T_1, T_2) P_n(\cos\vartheta); \tag{20}$$

$$m = 1, 2, 3.$$

Note that the solution of the problem formulated in the third order of smallness in ε allows one to reveal the dependencies of coefficients of the first order of smallness ($m = 1$) in expansions (17)–(20) on three time scales, T_0, T_1, and T_2; coefficients of the second order of smallness ($m = 2$) on two time scales, T_0 and T_1; and coefficients of the third order of smallness ($m = 3$) only on time scale T_0. Substituting expressions (17)–(20) into Eqs. (4A)–(9A), we find the explicit dependencies of all coefficients of the first order of smallness on time scale T_0:

$$M_n^{(1)}(T_0, T_1, T_2) = a_n^{(1)}(T_1, T_2) \cos(\omega_n T_0 + \tau_n^{(1)}(T_1, T_2)); \tag{21}$$

$$D_{(i)n}^{(1)}(T_0, T_1, T_2) = \partial_{T_0} M_n^{(1)}(T_0, T_1, T_2)/n; \tag{22}$$

$$D^{(1)}_{(e)n}(T_0, T_1, T_2) = -\partial_{T_0} M^{(1)}_n(T_0, T_1, T_2)/(n+1); \quad (23)$$

$$F^{(1)}_n(T_0, T_1, T_2) = QM^{(1)}_n(T_0, T_1, T_2). \quad (24)$$

In expression (21), functions $a^{(1)}_n(T_1, T_2)$ and $\tau^{(1)}_n(T_1, T_2)$ depend only on time scales T_1 and T_2 and meet initial conditions (9A),

$$t = 0: a^{(1)}_n = h_n\delta_{n,m}, \quad \tau^{(1)}_n = 0, \quad m \in \Omega, \quad (25)$$

where $\delta_{n,m}$ is Kronecher's delta. Substituting expansions (17)–(20) and solutions (21)–(24) into Eqs. (13A)–(18A) and eliminating secular terms, we find that functions $a^{(1)}_n(T_1, T_2)$ and $\tau^{(1)}_n(T_1, T_2)$ are independent of time scale T_1 and depend only on time scale T_2. The explicit dependencies of coefficients $D^{(2)}_{(i)n}$, $D^{(2)}_{(e)n}$, $F^{(2)}_n$, and $M^{(2)}_n$ in expansions (17)–(20) on time scale T_0 subject to conditions (25) can be written in the form

$$M^{(2)}_0(T_0) = -\sum_{m \in \Omega} \frac{(a^{(1)}_m)^2 \cos^2(\omega_m T_0)}{2m+1};$$

$$\begin{aligned} M^{(2)}_n(T_0, T_1) &= a^{(2)}_n(T_1)\cos(\omega_n T_0 + \tau^{(2)}_n(T_1)) \\ &+ \sum_{l,m \in \Omega} \frac{a^{(1)}_l a^{(2)}_m}{2}(\lambda^{(+)}_{lmn}\cos((\omega_l + \omega_m)T_0) \qquad (26) \\ &+ \lambda^{(-)}_{lmn}\cos((\omega_l - \omega_m)T_0)), \quad n \geq 1, \end{aligned}$$

$$\begin{aligned} F^{(2)}_0 = 0: F^{(2)}_n(T_0, T_1) &= QM^{(2)}_n(T_0, T_1) \qquad (27) \\ &+ Q\sum_{l,m \in \Omega} lK_{lmn}a^{(1)}_l a^{(1)}_m \cos(\omega_l T_0)\cos(\omega_m T_0); \end{aligned}$$

$$\begin{aligned} D^{(2)}_{(i)n}(T_0, T_1) &= \frac{1}{n}\Bigg\{\partial_{T_0} M^{(2)}_n(T_0, T_1) \\ &+ \sum_{l,m \in \Omega}\left((l-1)K_{lmn} - \frac{\alpha_{lmn}}{l}\right)\omega_l a^{(1)}_l a^{(1)}_m \qquad (28) \\ &\times \sin(\omega_l T_0)\cos(\omega_m T_0)\Bigg\}, \quad n \geq 1; \end{aligned}$$

$$\begin{aligned} D^{(2)}_{(e)n}(T_0, T_1) &= -\frac{1}{(n+1)}\Bigg\{\partial_{T_0} M^{(2)}_n(T_0, T_1) \\ &+ \sum_{l,m \in \Omega}(\alpha_{lmn}/(l+1) - (l+2)K_{lmn})\omega_l a^{(1)}_l a^{(1)}_m \qquad (29) \\ &\times \sin(\omega_l T_0)\cos(\omega_m T_0)\Bigg\}, \quad n \geq 0, \end{aligned}$$

where $\lambda^{(+)}_{lmn}$, $\lambda^{(-)}_{lmn}$, K_{lmn}, and α_{lmn} are the coefficients defined in Appendix B, and $a^{(2)}_n(T_1)$ and $\tau^{(2)}_n(T_1)$ are functions of time scale T_1 meeting initial conditions (18A),

$$t = 0: a^{(2)}_n = -\sum_{l,m \in \Omega} \frac{h_l h_m}{2}(\lambda^{(+)}_{lmn} + \lambda^{(-)}_{lmn}), \quad \tau^{(2)}_n = 0. \quad (30)$$

Substituting expressions (17)–(20) and solutions (21)–(24), (26)–(29) into the set of equations (22A)–(27A) and eliminating secular terms from it, we find that functions $a^{(1)}_n(T_2)$, $a^{(2)}_n(T_1)$, and $\tau^{(2)}_n(T_1)$ are independent of time scales T_1 and T_2; therefore, their magnitudes are entirely determined by initial conditions (25) and (30), and for function $\tau^{(1)}_n(T_2)$ the following expression is true:

$$\begin{aligned} \tau^{(1)}_n(T_2) = T_2 b_n &= \frac{T_2}{2\omega_n}\Bigg\{\frac{h^2_n(\Xi^0_n + 2\omega^2_n(\Xi^1_n - 2\Xi^2_n))}{4(2n+1)} \\ &+ \sum_{k \in \Omega}\frac{h^2_k \Xi^0_n}{2(2k+1)} - \sum_{k \in \Omega}\frac{h^2_k}{4}[H^{1(-)(+)}_{nkkn} + H^{2(+)(+)}_{knkn} \qquad (31) \\ &+ H^{2(-)(-)}_{knkn} + (1-\delta_{kn})(H^{1(-)(+)}_{kknn} + H^{2(+)(+)}_{kknn} + H^{2(-)(-)}_{nkkn})]\Bigg\}. \end{aligned}$$

Coefficients $D^{(3)}_{(i)n}$, $D^{(3)}_{(e)n}$, $F^{(3)}_n$, and $M^{(3)}_n$ of expansions (17)–(20) are defined by the expressions

$$\begin{aligned} M^{(3)}_0(T_0) &= -\sum_{k \in \Omega}\frac{2M^{(2)}_k(T_0)}{2k+1}h_k\cos(\omega_k T_0) \\ &- \sum_{k,m,l \in \Omega}\frac{K_{kml}h_k h_m h_l}{3(2l+1)}\cos(\omega_k T_0)\cos(\omega_m T_0)\cos(\omega_l T_0); \end{aligned}$$

$$\begin{aligned} M^{(3)}_n(T_0) &= -\sum_{k \in \Omega}\frac{h_n h^2_k(\Xi^0_n - 2\Xi^1_n\omega_n\omega_k - 4\Xi^2_n\omega^2_k)}{8(2k+1)\omega_k(\omega_n + \omega_k)} \\ &\times \sin((\omega_n + \omega_k)T_0)\sin(\omega_k T_0) \\ &- \sum_{k \in \Omega}\frac{h_n h^2_k(1-\delta_{nk})(\Xi^0_n + 2\Xi^1_n\omega_n\omega_k - 4\Xi^2_n\omega^2_k)}{8(2k+1)\omega_k(\omega_n - \omega_k)} \\ &\times \sin((\omega_n - \omega_k)T_0)\sin(\omega_k T_0) \end{aligned}$$

$$\begin{aligned}
&-\sum_{g=1}^{\infty}\sum_{k,m,l\in\Omega}\frac{h_kh_mh_l(\lambda_{lmg}^{(+)}+\lambda_{lmg}^{(-)})}{4}\\
&\times\left\{\frac{H_{kgn}^{0(+)}(\cos((\omega_k+\omega_g)T_0)-\cos(\omega_nT_0))}{\omega_n^2-(\omega_k+\omega_g)^2}\right.\\
&\left.+\frac{H_{kgn}^{0(-)}(\cos((\omega_k-\omega_g)T_0)-\cos(\omega_nT_0))}{\omega_n^2-(\omega_k-\omega_g)^2}\right\}\\
&+\sum_{k,m,l\in\Omega}\frac{h_kh_mh_l}{4}\left\{\frac{H_{kmln}^{1(+)(-)}(\cos(\psi_{klm}^{(+)(+)}T_0)-\cos(\omega_nT_0))}{\omega_n^2-(\omega_k+\omega_l+\omega_m)^2}\right.\\
&+\frac{H_{kmln}^{1(-)(+)}D_{lm}^{kn}D_{km}^{ln}(\cos(\psi_{klm}^{(+)(-)}T_0)-\cos(\omega_nT_0))}{\omega_n^2-(\omega_k+\omega_l-\omega_m)^2}\\
&+\frac{H_{kmln}^{2(+)(+)}D_{kl}^{mn}D_{km}^{ln}(\cos(\psi_{klm}^{(-)(-)}T_0)-\cos(\omega_nT_0))}{\omega_n^2-(\omega_k-\omega_l-\omega_m)^2}\\
&\left.+\frac{H_{kmln}^{2(-)(-)}D_{kl}^{mn}D_{ml}^{kn}(\cos(\psi_{klm}^{(+)(-)}T_0)-\cos(\omega_nT_0))}{\omega_n^2-(\omega_k-\omega_l+\omega_m)^2}\right\},\\
&n\ge1;
\end{aligned}\tag{32}$$

$$\begin{aligned}
F_0^{(3)}(T_0)&=Q\sum_{k,m,l\in\Omega}\frac{k+1}{2l+1}\left(\alpha_{kml}-\frac{k(k+1)}{2}K_{kml}\right)\\
&\times h_kh_mh_l\cos(\omega_kT_0)\cos(\omega_mT_0)\cos(\omega_lT_0);\\
F_0^{(3)}(T_0)&=QM_n^{(3)}(T_0)\\
&+\sum_{m\in\Omega}\sum_{k=1}^{\infty}(k+1)K_{kmn}F_k^{(2)}(T_0)h_m\cos(\omega_mT_0)\\
&+Q\sum_{k\in\Omega}\sum_{m=0}^{\infty}(k-1)K_{kmn}M_m^{(2)}(T_0)h_k\cos(\omega_kT_0)\\
&-Q\sum_{g=0}^{\infty}\sum_{k,m,l\in\Omega}\frac{k(k+3)}{2}K_{kmg}K_{gln}h_kh_mh_l\\
&\times\cos(\omega_kT_0)\cos(\omega_mT_0)\cos(\omega_lT_0),\quad n\ge1;
\end{aligned}\tag{33}$$

$$\begin{aligned}
D_{(i)n}^{(3)}(T_0)&=\frac{1}{n}\partial_{T_0}M_n^{(3)}(T_0)-\frac{1-\delta_{1n}}{n}h_nb_n\sin(\omega_nT_0)\\
&-\frac{1}{n}\sum_{m\in\Omega}\sum_{k=1}^{\infty}(k(k-1)K_{kmn}-\alpha_{kmn})D_k^{(2)}(T_0)h_m\cos(\omega_mT_0)\\
&+\frac{1}{n}\sum_{k\in\Omega}\sum_{m=0}^{\infty}(k(k-1)-\alpha_{kmn})M_m^{(2)}(T_0)\omega_kh_k\sin(\omega_kT_0)\\
&+\frac{1}{n}\sum_{k,m,l\in\Omega}\sum_{g=0}^{\infty}\left(\frac{k(k-1)}{2}K_{kmg}-\alpha_{kmg}\right)(k-2)\\
&\times K_{gln}\omega_kh_kh_mh_l\sin(\omega_kT_0)\cos(\omega_mT_0)\cos(\omega_lT_0),\quad n\ge1;
\end{aligned}\tag{34}$$

$$\begin{aligned}
D_{(e)n}^{(3)}(T_0)&=-\frac{1}{n+1}\partial_{T_0}M_n^{(3)}(T_0)\\
&+\frac{(1-\delta_{0n})(1-\delta_{1n})}{n+1}h_nb_n\sin(\omega_nT_0)\\
&+\frac{1}{n+1}\sum_{k\in\Omega}\sum_{m=0}^{\infty}\left((k+2)K_{kmn}-\frac{\alpha_{kmn}}{k+1}\right)M_m^{(2)}\omega_kh_k\sin(\omega_kT_0)\\
&-\frac{1}{n+1}\sum_{k\in\Omega}\sum_{m=0}^{\infty}(\alpha_{kmn}-(m+1)(m+2)K_{kmn})D_m^{(2)}h_k\\
&\times\cos\omega_k(T_0)+\frac{1}{n+1}\sum_{k,m,l\in\Omega}\sum_{g=0}^{\infty}\left(\frac{\alpha_{kmg}}{k+1}-\frac{k+2}{2}K_{kmg}\right)(k+3)\\
&\times K_{gln}\omega_kh_kh_mh_l\sin(\omega_kT_0)\cos(\omega_mT_0)\cos(\omega_lT_0),\\
&n\ge0;
\end{aligned}\tag{35}$$

where Ξ_n^0, ξ_n^1, Ξ_n^2, $\beta_{kmgln}^{1(\pm)}$, $\beta_{kmgln}^{2(\pm)}$, $H_{kgn}^{0(\pm)}$, $H_{kmln}^{1(\pm)(\pm)}$, $H_{kmln}^{2(\pm)(\pm)}$, $\psi_{kml}^{(\pm)(\pm)}$, and D_{lm}^{kn} are the coefficients given in Appendix B; δ_{kn} is Kronecher's delta. Substituting relation (20) into Eq. (1), we obtain an expression for the generatrix of the drop's shape in the form

$$\begin{aligned}
r(\vartheta,T_0,T_2)&=1+\varepsilon\sum_{n\in\Omega}M_n^{(1)}(T_0,T_2)P_n(\cos(\vartheta))\\
&+\varepsilon^2\sum_{n=0}^{\infty}(M_n^{(2)}(T_0)+\varepsilon M_n^{(3)}(T_0))P_n(\cos(\vartheta)).
\end{aligned}\tag{36}$$

4. Analyzing expressions (26), (32), and (36), we note that the amplitudes of deviation of the drop's shape from spherical in the second and third orders of smallness, similar to the case with no ambient medium, are proportional to the expressions

$$M_g^2\sim\sum_{k,m\in\Omega}K_{kmg},\quad M_n^{(3)}\sim\sum_{g=0}^{\infty}\sum_{k,m,l\in\Omega}K_{kmg}K_{gln},$$

where coefficients K_{kmg} differ from zero only if $|k-m|\le g\le|k+m|$ and $k+m+g$ is an even number. Thus, the presence of the ambient does not result in broadening of the spectrum of the modes forming the surface of a charged drop. From expressions (21) and (31) it is seen that any initially excited mode of the first order of smallness has a frequency shift proportional to the square of amplitude ε^2 of the initial perturbation of the drop's surface. This frequency shift depends appreciably on set Ω of the initially excited modes and on the ambient density $\rho_{(e)}$. From (36), it is seen that correc-

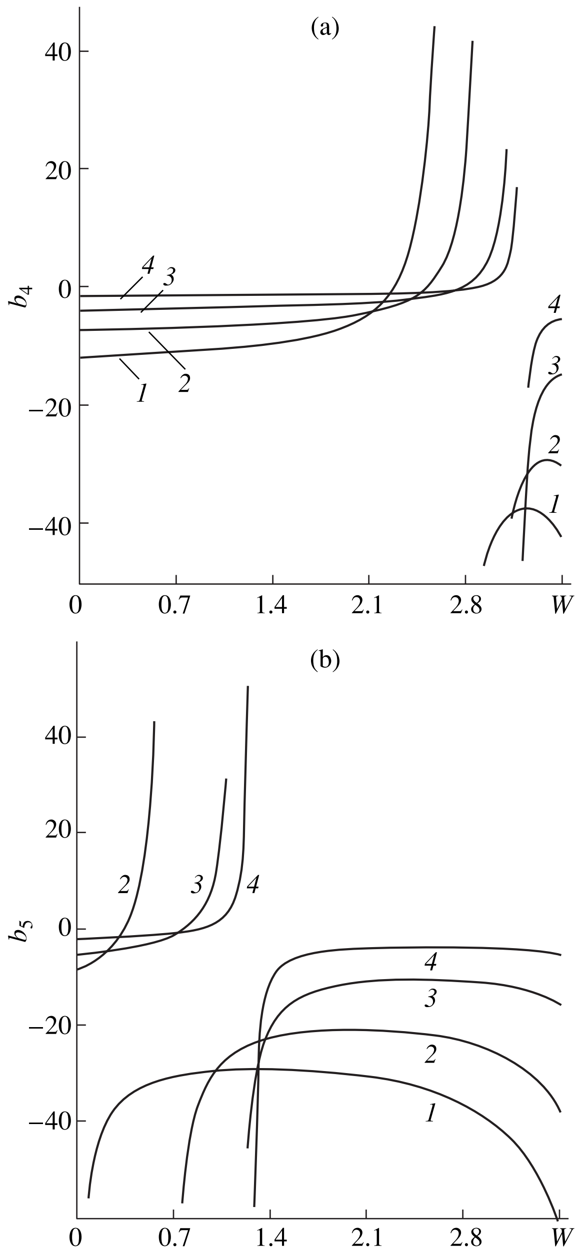

Fig. 1. Coefficient b_n characterizing the frequency shift of the nth mode as a function of the Rayleigh parameter W at the initial excitation of this mode for different density magnitudes of the ambient liquid. $\rho_{(e)}$: (*1*) 0, (*2*) 1, (*3*) 10, (*4*) 100; n: (a) 4, (b) 5.

tions to the frequencies proportional to b_n are of the second order of smallness in ε, and the denominators in the expressions for these corrections include factors becoming zeros for certain ratios between the frequencies of various modes (in such cases, the resonant character of the corresponding corrections [9] is usually assumed). For example, when the fourth mode is excited at the initial instant, a correction to the frequency corresponds to the resonance at $\omega_6^2 - 4\omega_4^2 = 0$, while when the fifth mode is excited, the resonance is realized at $\omega_8^2 - 4\omega_5^2 = 0$. Away from the resonant positions, the corrections $b_n\varepsilon^2$ to the frequencies decrease in absolute magnitudes with increasing density $\rho_{(e)}$ of the ambient liquid (see Fig. 1). Making allowance for corrections to the frequencies of capillary drop oscillations results in a change in the critical Rayleigh parameter W_{cr} at which instability of the nth mode with respect to the self-charge is realized [6]. The instability condition for the nth mode subject to the nonlinear correction to the frequency can be written in the form

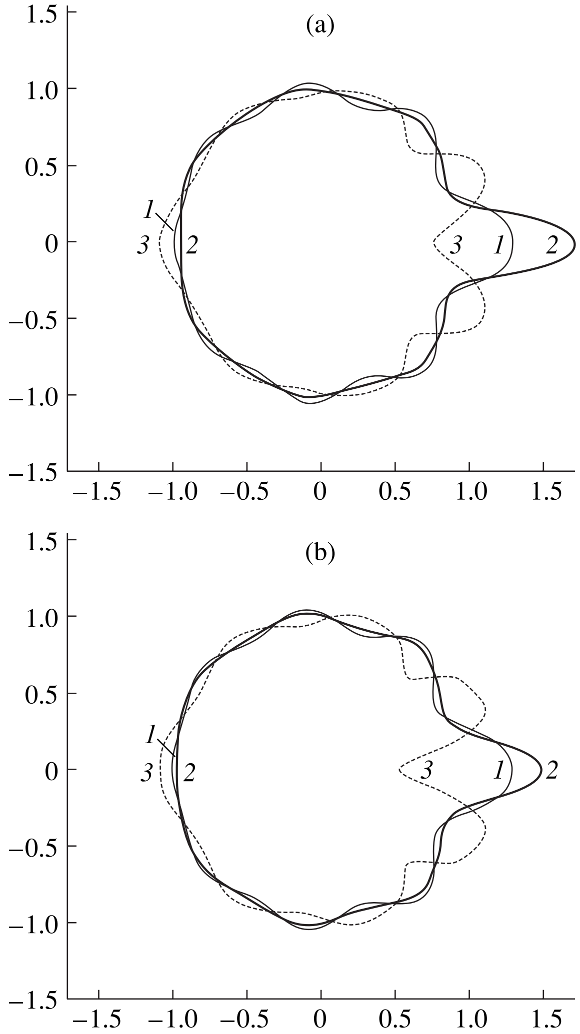

Fig. 2. The generatrix contour of a drop at the initial excitation of the seventh and eighth modes when $h_7 = h_8 = 0.5$, $W = 3$, $\varepsilon = 0.3$. (a) $\rho_{(e)} = 0$; t: (*1*) 0.01, (*2*) 0.075, (*3*) 0.22; (b) $\rho_{(e)} = 5$; t: (*1*) 0.02, (*2*) 0.14, (*3*) 0.525.

$$(\omega_n + \varepsilon^2 b_n)^2 = \omega_n^2 + 2\varepsilon^2\omega_n b_n + O(\varepsilon^4) = 0.$$

The influence of the ambient medium on the critical instability conditions manifests itself in an insignificant increase in the critical Rayleigh parameter with increasing density of the ambient liquid $\rho_{(e)}$ (due to a decrease in coefficient b_n in absolute magnitude) [7] and in a very noticeable reduction of the interphase surface tension coefficient compared with the surface tension coefficient of a drop in vacuum [10]. Eventually, in the presence of the ambient medium, the critical self-charge magnitude from the standpoint of the instability development decreases. The mode amplitudes of the second, $M_n^{(2)}$, and third, $M_n^{(3)}$, orders are also dependent on the density of the ambient liquid, which results in a certain change in the surface shape of a drop (local decrease of its surface curvature) when the drop is in the ambient medium as compared with a drop in vacuum (see Fig. 2). The presence of the ambient medium influences the surface shape of the drop most noticeably in the vicinity of points moving at the greatest velocity.

CONCLUSION

Magnitudes of nonlinear corrections to the oscillation frequencies of a charged drop of an ideal incompressible conducting liquid immersed in a dielectric incompressible ambient medium appreciably depend on the ratio between the densities of the media and decrease with increasing density of the ambient medium. The influence of the ambient medium (which is assumed to be incompressible) on the stability of the drop with respect to the self-charge manifests itself in two ways: on the one hand, the nonlinear oscillation frequency shift leads to a weak growth of the critical charge; on the other hand, an appreciable decrease in the interphase surface tension coefficient (as compared with a drop in vacuum) causes a very noticeable decrease in the critical charge.

APPENDIX A

Division of the Problems according to the Order of Smallness

The problem of the first order of smallness obtained after substitution of relations (12)–(16) into Eqs. (1)–(11) has the form

$$\Delta\psi_{(i)}^{(1)} = 0; \quad \Delta\psi_{(e)}^{(1)} = 0; \quad \Delta\phi^{(1)} = 0; \tag{1A}$$

$$r \longrightarrow 0:\ \psi_{(i)}^{(1)} \longrightarrow 0; \tag{2A}$$

$$r \longrightarrow +\infty:\ \psi_{(e)}^{(1)} \longrightarrow 0; \quad \nabla\phi^{(1)} \longrightarrow 0; \tag{3A}$$

$$r = 1:\ \partial_{T_0}\xi^{(1)} = \partial_r\psi_{(i)}^{(1)} = \partial_r\psi_{(e)}^{(1)}; \tag{4A}$$

$$\partial_{T_0}\psi^{(1)} - \rho_{(e)}\partial_{T_0}\psi_{(e)}^{(1)} = \frac{1}{4\pi\varepsilon_d}\partial_r\phi^{(0)} \times(\partial_r\phi^{(1)} + \xi^{(1)}\partial_{rr}\phi^{(0)}) + 2\xi^{(1)} + \Delta_\Omega\xi^{(1)}; \tag{5A}$$

$$\int_{-1}^{1}\xi^{(1)}d(\cos\vartheta) = 0; \tag{6A}$$

$$\int_{-1}^{1}\{\partial_r\phi^{(1)} + \xi^{(1)}(\partial_{rr}\phi^{(0)} + 2\partial_r\phi^{(0)})\}d(\cos\vartheta) = 0; \tag{7A}$$

$$\phi^{(1)} + \xi^{(1)}\partial_r\phi^{(0)} = \phi_S^{(1)}(t); \tag{8A}$$

$$t = 0:\ \xi^{(1)} = \varepsilon\sum_{m\in\Omega}h_mP_m(\cos\vartheta); \quad \partial_{T_0}\xi^{(1)} = 0. \tag{9A}$$

The problem of the second order of smallness has the form

$$\Delta\psi_{(i)}^{(2)} = 0; \quad \Delta\psi_{(e)}^{(2)} = 0; \quad \Delta\phi^{(2)} = 0; \tag{10A}$$

$$r \longrightarrow 0:\ \psi_{(i)}^{(2)} \longrightarrow 0; \tag{11A}$$

$$r \longrightarrow +\infty:\ \psi_{(e)}^{(2)} \longrightarrow 0; \quad \nabla\phi^{(2)} \longrightarrow 0; \tag{12A}$$

$$r = 1:\ \partial_{T_0}\xi^{(2)} + \partial_{T_1}\xi^{(1)} = \partial_r\psi_{(i)}^{(2)} + \xi^{(1)}\partial_{rr}\psi_{(i)}^{(1)} - \partial_\vartheta\xi^{(1)}\partial_\vartheta\psi_{(i)}^{(1)} = \partial_r\psi_{(e)}^{(2)} + \xi^{(1)}\partial_{rr}\psi_{(e)}^{(1)} - \partial_\vartheta\xi^{(1)}\partial_\vartheta\psi_{(e)}^{(1)}; \tag{13A}$$

$$\begin{aligned}&\partial_{T_0}\psi_{(i)}^{(2)} + \partial_{T_1}\psi_{(i)}^{(1)} + \xi^{(1)}\partial_{rT_0}\psi_{(i)}^{(1)} + \frac{1}{2}(\partial_r\psi_{(i)}^{(1)})^2 \\ &+ \frac{1}{2}(\partial_\vartheta\psi_{(i)}^{(1)})^2 - \rho_{(e)}\Big(\partial_{T_0}\psi_{(e)}^{(2)} + \partial_{T_1}\psi_{(e)}^{(1)} + \xi^{(1)}\partial_{rT_0}\psi_{(e)}^{(1)} \\ &+ \frac{1}{2}(\partial_r\psi_{(e)}^{(1)})^2 + \frac{1}{2}(\partial_\vartheta\psi_{(e)}^{(1)})^2\Big) = \frac{1}{8\pi\varepsilon_d}\{2\xi^{(2)}\partial_r\phi^{(0)}\partial_{rr}\phi^{(0)} \\ &+ (\xi^{(1)})^2((\partial_{rr}\phi^{(0)})^2 + \partial_{rrr}\phi^{(0)}\partial_r\phi^{(0)}) \\ &+ (\partial_\vartheta\phi^{(1)})^2 + (\partial_r\phi^{(1)})^2 + 2\partial_r\phi^{(2)}\partial_r\phi^{(0)} \\ &+ 2\xi^{(1)}(\partial_{rr}\phi^{(0)}\partial_r\phi^{(1)} + \partial_{rr}\phi^{(1)}\partial_r\phi^{(0)})\} \\ &+ 2\xi^{(2)} + \Delta_\Omega\xi^{(2)} - 2(\xi^{(1)})^2 - 2\xi^{(1)}\Delta_\Omega\xi^{(1)};\end{aligned} \tag{14A}$$

$$\int_{-1}^{1}(\xi^{(2)} + (\xi^{(1)})^2)d(\cos\vartheta) = 0; \tag{15A}$$

$$\begin{aligned}\int_{-1}^{1}\Big\{&\partial_r\phi^{(2)} + \xi^{(1)}(\partial_{rr}\phi^{(1)} + 2\partial_r\phi^{(1)}) + \xi^{(2)}(\partial_{rr}\phi^{(0)} + 2\partial_r\phi^{(0)}) \\ &+ (\xi^{(1)})^2\Big(\frac{1}{2}\partial_{rrr}\phi^{(0)} + 2\partial_{rr}\phi^{(0)} + \partial_r\phi^{(0)}\Big) \\ &- \partial_\vartheta\xi^{(1)}\partial_\vartheta\phi^{(1)}\Big\}d(\cos\vartheta) = 0;\end{aligned} \tag{16A}$$

$$\phi^{(2)} + \xi^{(1)}\partial_r\phi^{(1)} + \xi^{(2)}\partial_r\phi^{(0)} + \frac{1}{2}(\xi^{(1)})^2\partial_{rr}\phi^{(0)} = \phi_S^{(2)}(t); \tag{17A}$$

$$t = 0\colon \xi^{(2)} = -\sum_{m\in\Omega}\frac{h_m P_0(\cos\vartheta)}{2m+1}; \quad \partial_{T_0}\xi^{(2)} + \partial_{T_1}\xi^{(1)} = 0. \tag{18A}$$

The problem of the third order of smallness has the form

$$\Delta\psi_{(i)}^{(3)} = 0; \quad \Delta\psi_{(e)}^{(3)} = 0; \quad \Delta\phi^{(3)} = 0; \tag{19A}$$

$$r \longrightarrow 0\colon \psi_{(i)}^{(3)} \longrightarrow 0; \tag{20A}$$

$$r \longrightarrow +\infty\colon \psi_{(e)}^{(3)} \longrightarrow 0; \quad \nabla\phi^{(3)} \longrightarrow 0; \tag{21A}$$

$$\begin{gathered} r = 1\colon \partial_{T_0}\xi^{(3)} + \partial_{T_1}\xi^{(2)} + \partial_{T_2}\xi^{(1)} = \partial_r\psi_{(i)}^{(3)} \\ - \partial_\vartheta\xi^{(2)}\partial_\vartheta\psi_{(i)}^{(1)} - \partial_\vartheta\xi^{(1)}\partial_\vartheta\psi_{(i)}^{(2)} + \xi^{(2)}\partial_{rr}\psi_{(i)}^{(1)} \\ + \xi^{(1)}(\partial_\vartheta\xi^{(1)}(2\partial_\vartheta\psi_{(i)}^{(1)} - \partial_{r\vartheta}\psi_{(i)}^{(1)}) + \partial_{rr}\psi_{(i)}^{(2)}) \\ + \frac{1}{2}(\xi^{(1)})^2\partial_{rrr}\psi_{(i)}^{(1)} = \partial_r\psi_{(e)}^{(3)} - \partial_\vartheta\xi^{(2)}\partial_\vartheta\psi_{(e)}^{(1)} \\ - \partial_\vartheta\xi^{(1)}\partial_\vartheta\psi_{(e)}^{(2)} + \xi^{(2)}\partial_{rr}\psi_{(e)}^{(1)} \\ + \xi^{(1)}(\partial_\vartheta\xi^{(1)}(2\partial_\vartheta\psi_{(e)}^{(1)} - \partial_{r\vartheta}\psi_{(e)}^{(1)}) + \partial_{rr}\psi_{(e)}^{(2)}) \\ + \frac{1}{2}(\xi^{(1)})^2\partial_{rrr}\psi_{(e)}^{(1)}; \end{gathered} \tag{22A}$$

$$\begin{gathered} \partial_{T_0}\psi_{(i)}^{(3)} + \partial_{T_2}\psi_{(i)}^{(1)} + \partial_{T_1}\psi_{(i)}^{(2)} + \xi^{(1)}\partial_{rT_1}\psi_{(i)}^{(1)} \\ + \partial_\vartheta\psi_{(i)}^{(1)}\partial_\vartheta\psi_{(i)}^{(2)} + \partial_r\psi_{(i)}^{(1)}\partial_r\psi_{(i)}^{(2)} + \xi^{(2)}\partial_{rT_0}\psi_{(i)}^{(1)} \\ + \xi^{(1)}(\partial_{rT_0}\psi_{(i)}^{(2)} + \partial_\vartheta\psi_{(i)}^{(1)}(\partial_{r\vartheta}\psi_{(i)}^{(1)} - \partial_\vartheta\psi_{(i)}^{(1)}) \\ + \partial_r\psi_{(i)}^{(1)}\partial_{rr}\psi_{(i)}^{(1)}) + \frac{1}{2}(\xi^{(1)})^2\partial_{rrT_0}\psi_{(i)}^{(1)} \\ - \rho_{(e)}\Big(\partial_{T_0}\psi_{(e)}^{(3)} + \partial_{T_2}\psi_{(e)}^{(1)} + \partial_{T_1}\psi_{(e)}^{(2)} + \xi^{(1)}\partial_{rT_1}\psi_{(e)}^{(1)} \\ + \partial_\vartheta\psi_{(e)}^{(1)}\partial_\vartheta\psi_{(e)}^{(2)} + \partial_r\psi_{(e)}^{(1)}\partial_r\psi_{(e)}^{(2)} + \xi^{(2)}\partial_{rT_0}\psi_{(e)}^{(1)} \\ + \xi^{(1)}(\partial_{rT_0}\psi_{(e)}^{(2)} + \partial_\vartheta\psi_{(e)}^{(1)}(\partial_{r\vartheta}\psi_{(e)}^{(1)} - \partial_\vartheta\psi_{(e)}^{(1)}) \\ + \partial_r\psi_{(e)}^{(1)}\partial_{rr}\psi_{(e)}^{(1)}) + \frac{1}{2}(\xi^{(1)})^2\partial_{rrT_0}\psi_{(e)}^{(1)}\Big) \end{gathered}$$

$$\begin{gathered} = \frac{1}{8\pi\varepsilon_d}\{2\xi^{(3)}\partial_r\phi^{(0)}\partial_{rr}\phi^{(0)} + (\xi^{(1)})^3(\partial_{rr}\phi^{(0)}\partial_{rrr}\phi^{(0)} \\ + \frac{1}{3}\partial_r\phi^{(0)}\partial_{rrrr}\phi^{(0)}\Big) + 2(\partial_\vartheta\phi^{(1)}\partial_\vartheta\phi^{(2)} \\ + \partial_r\phi^{(1)}(\xi^{(2)}\partial_{rr}\phi^{(0)} + \partial_r\phi^{(2)}) + \partial_r\phi^{(0)}\partial_r\phi^{(3)} \\ + \xi^{(2)}\partial_r\phi^{(0)}\partial_{rr}\phi^{(1)}) + 2\xi^{(1)}(\xi^{(2)}((\partial_{rr}\phi^{(0)})^2 \\ + \partial_r\phi^{(0)}\partial_{rrr}\phi^{(0)}) + \partial_{rr}\phi^{(0)}\partial_r\phi^{(2)} \\ + \partial_\vartheta\phi^{(1)}(\partial_{r\vartheta}\phi^{(1)} - \partial_\vartheta\phi^{(1)}) + \partial_r\phi^{(1)}\partial_{rr}\phi^{(1)} \\ + \partial_r\phi^{(0)}\partial_{rr}\phi^{(2)}) + (\xi^{(1)})^2(\partial_{rrr}\phi^{(0)}\partial_r\phi^{(1)} \\ + 2\partial_{rr}\phi^{(0)}\partial_{rr}\phi^{(1)} + \partial_r\phi^{(0)}\partial_{rrr}\phi^{(1)})\} \\ + (2 + \Delta_\Omega)\xi^{(3)} + 2\xi^{(1)}((\xi^{(1)})^2 - (2 + \Delta_\Omega)\xi^{(2)}) \\ - 2\xi^{(2)}\Delta_\Omega\xi^{(1)} + 3(\xi^{(1)})^2\Delta_\Omega\xi^{(1)} - (\partial_\vartheta\xi^{(1)})^2\partial_{\vartheta\vartheta}\xi^{(1)} \\ - \frac{1}{2}(\partial_\vartheta\xi^{(1)})^2\Delta_\Omega\xi^{(1)}; \end{gathered} \tag{23A}$$

$$\int_{-1}^{1}(3\xi^{(3)} + 6\xi^{(1)}\xi^{(2)} + (\xi^{(1)})^3)d(\cos\vartheta) = 0; \tag{24A}$$

$$\begin{gathered} \int_{-1}^{1}\{\partial_r\phi^{(3)} + \xi^{(3)}(\partial_{rr}\phi^{(0)} + 2\partial_r\phi^{(0)}) \\ + \xi^{(2)}(\partial_{rr}\phi^{(1)} + 2\partial_r\phi^{(1)}) \\ + (\xi^{(1)})^3\Big(\frac{1}{6}\partial_{rrrr}\phi^{(0)} + \partial_{rrr}\phi^{(0)} + \partial_{rr}\phi^{(0)}\Big) \\ + (\xi^{(1)})^2\Big(\frac{1}{2}\partial_{rrr}\phi^{(1)} + 2\partial_{rr}\phi^{(1)} + \partial_r\phi^{(1)}\Big) \\ + \xi^{(1)}(\xi^{(2)}\partial_{rrr}\phi^{(0)} + 4\partial_{rr}\phi^{(0)} + 2\partial_r\phi^{(0)}) \\ + 2\partial_r\phi^{(2)} + \partial_{rr}\phi^{(2)} - \partial_\vartheta\xi^{(1)}\partial_{r\vartheta}\phi^{(1)}) \\ - \partial_\vartheta\xi^{(2)}\partial_\vartheta\phi^{(1)} - \partial_\vartheta\xi^{(1)}\partial_\vartheta\phi^{(2)}\Big\}d(\cos\vartheta) = 0; \end{gathered} \tag{25A}$$

$$\begin{gathered} \phi^{(3)} + \xi^{(1)}\partial_r\phi^{(2)} + \xi^{(2)}\partial_r\phi^{(1)} + \xi^{(3)}\partial_r\phi^{(0)} \\ + \frac{1}{2}(\xi^{(1)})^2\partial_{rr}\phi^{(1)} + \xi^{(1)}\xi^{(2)}\partial_{rr}\phi^{(0)} \\ + \frac{1}{6}(\xi^{(1)})^3\partial_{rrr}\phi^{(0)} = \phi_S^{(3)}(t); \end{gathered} \tag{26A}$$

$$t = 0:\ \xi^{(3)} = -\sum_{k,\,m,\,l\in\Omega}\frac{h_k h_m h_l}{3(2l+1)}K_{kml}P_0(\cos\vartheta);\tag{27A}$$

$$t = 0:\ \partial_{T_0}\xi^{(3)} + \partial_{T_1}\xi^{(2)} + \partial_{T_2}\xi^{(1)} = 0,$$

where $K_{kln} = (C^{n0}_{m0l0})^2$ and C^{n0}_{m0l0} are the Clebsch–Gordan coefficients.

APPENDIX B

Expressions for the expansion coefficients:

$$H^{1(+)(-)}_{kmln} = \sum_{g=1}^{\infty}(\beta^{1(+)}_{kmgln}\lambda^{(+)}_{lmg} + \mu^{1(-)}_{kmgln}) + \sum_{g=0}^{\infty}\mu^{0(-)}_{kmgln};$$

$$H^{1(-)(+)}_{kmln} = \sum_{g=1}^{\infty}(\beta^{1(-)}_{kmgln}\lambda^{(-)}_{lmg} + \mu^{1(+)}_{kmgln}) + \sum_{g=0}^{\infty}\mu^{0(+)}_{kmgln};$$

$$H^{2(+)(+)}_{kmln} = \sum_{g=1}^{\infty}(\beta^{2(+)}_{kmgln}\lambda^{(+)}_{lmg} + \mu^{1(+)}_{kmgln}) + \sum_{g=0}^{\infty}\mu^{0(+)}_{kmgln};$$

$$H^{2(-)(-)}_{kmln} = \sum_{g=1}^{\infty}(\beta^{2(-)}_{kmgln}\lambda^{(-)}_{lmg} + \mu^{1(-)}_{kmgln}) + \sum_{g=0}^{\infty}\mu^{0(-)}_{kmgln};$$

$$H^{0(+)}_{mgn} = (\Pi^0_{mgn} - \Pi^1_{mgn}\omega_m\omega_g - \Pi^2_{mgn}\omega_g^2)(\lambda^{(+)}_{mmg} + \lambda^{(-)}_{mmg});$$

$$H^{0(-)}_{mgn} = (\Pi^0_{mgn} + \Pi^1_{mgn}\omega_m\omega_g - \Pi^2_{mgn}\omega_g^2)(\lambda^{(+)}_{mmg} + \lambda^{(-)}_{mmg});$$

$$\beta^{1(+)}_{kmgln} = \Pi^0_{kgn} - \Pi^1_{kgn}\omega_k(\omega_l + \omega_m) - \Pi^2_{kgn}(\omega_l + \omega_m)^2;$$

$$\beta^{1(-)}_{kmgln} = \Pi^0_{kgn} - \Pi^1_{kgn}\omega_k(\omega_l - \omega_m) - \Pi^2_{kgn}(\omega_l - \omega_m)^2;$$

$$\beta^{2(+)}_{kmgln} = \Pi^0_{kgn} + \Pi^1_{kgn}\omega_k(\omega_l + \omega_m) - \Pi^2_{kgn}(\omega_l + \omega_m)^2;$$

$$\beta^{2(-)}_{kmgln} = \Pi^0_{kgn} + \Pi^1_{kgn}\omega_k(\omega_l = \omega_m) - \Pi^2_{kgn}(\omega_l - \omega_m)^2;$$

$$\mu^{1(-)}_{kmgln} = \Lambda^1_{kmgln} - \Gamma^1_{kmgln}\omega_m\omega_k;$$

$$\mu^{1(+)}_{kmgln} = \Lambda^1_{kmgln} + \Gamma^1_{kmgln}\omega_m\omega_k;$$

$$\mu^{0(-)}_{kmgln} = \Lambda^0_{kmgln} - \Gamma^0_{kmgln}\omega_m\omega_k;$$

$$\mu^{0(+)}_{kmgln} = \Lambda^1_{kmgln} + \Gamma^0_{kmgln}\omega_m\omega_k;$$

$$\Lambda^0_{kmgln} = (n+1)\chi_n\omega_k^2K_{gln}(\alpha_{kmg}(k-2)/k$$
$$+ (k-1)(n-k+2)K_{kmg}/2)$$

$$+ \rho_{(e)}n\chi_n\omega_k^2(((g+1-n)K_{gln} - \alpha_{gln}/(g+1))((k+2)K_{kmg}$$
$$- \alpha_{kmg}/(k+1)) + ((k+3)\alpha_{kmg}/(k+1)$$
$$+ (k+2)(n-2-k)K_{kmg}/2)K_{gln}) + n(n+1)\chi_n$$
$$\times\Bigg(WK_{gln}\Bigg(\Bigg(\Bigg(k^3 - 2(m+1)(m+2) - k^2(n-9)$$
$$- k(2m(m+3) + 3n - 22))K_{kmg} - 2(k+2)\alpha_{kmg})/2$$
$$- ((3k(k+1) - 2)K_{kmg} - l(l+1)\alpha_{kmg}/2)K_{gln}$$
$$+ \alpha_{kmg}\Bigg(l^2K_{lgn} - \sum_{\nu=1}^{[l/2]}(2l - 4\nu + 1)K_{l-2\nu,\,g,\,n}\Bigg)\Bigg)\Bigg);$$

$$\Lambda^1_{kmgln} = n(n+1)\chi_nWkK_{kmg}$$
$$\times((g+1)(l-2-g+n)K_{lgn} + \alpha_{lgn})$$
$$+ (n+1)\chi_n((\alpha_{lgn}/g + (n+1-g)K_{lgn})$$
$$\times(\alpha_{kmg}/m + (1-m)K_{kmg}))\omega_m^2;$$

$$\Gamma^0_{kmgln} = (n+1)\chi_n((k-2)K_{gln}((k-1)K_{kmg}/2 - \alpha_{kmg}/k))$$
$$+ K_{mgn}((k-1)K_{klg}/2 - \alpha_{klg}/k))$$
$$- n(k-1)K_{gln}(\alpha_{kmg}/(mk) + K_{kmg}))$$
$$- \rho_{(e)}n\chi_n(((g+2)K_{kmg} - \alpha_{mgn}/(g+1))((k+2)K_{klg}$$
$$- \alpha_{klg}/(k+1)) + (k+3)K_{mgn}(\alpha_{klg}/(k+1)$$
$$- (k-2)K_{klg}/2) + ((g+2)K_{gln} - \alpha_{gln}/(g+1))$$
$$\times((k+2)K_{kmg} - \alpha_{kmg}/(k+1))$$
$$+ (k+3)K_{gln}(\alpha_{kmg}/(k+1) - (k+2)K_{kmg}/2)$$
$$- (n+1)((\alpha_{mgn}/((m+1)(g+1)) + K_{mgn})((k+2)K_{klg}$$
$$- \alpha_{klg}/(k+1)) + K_{gln}((k+2)K_{kmg} - \alpha_{kmg}/(k+1))$$
$$- (\alpha_{kmg}/((k+1)(m+1)) + K_{kmg})(k+2)K_{gln}));$$

$$\Gamma^1_{kmgln} = (n+1)\chi_n((\alpha_{lgn}/g + (n+1-g)K_{lgn})$$
$$\times((m-1)K_{kmg} - \alpha_{kmg}/m) + ((k+n)\alpha_{kgn}/(gk)$$
$$+ (n+1-g)K_{kgn})((m-1)K_{mlg} - \alpha_{mlg}/m));$$

$$\Pi^0_{kmn} = (n+1)\chi_n(nK_{kmn}(2((k-1)(k+2) + m(m+1))$$
$$+ W(k-1)(n-5-k)) + (\alpha_{kmn}/k + (n+1-k)K_{kmn})\omega_k^2)$$
$$- \rho_{(e)}n\chi_n\omega_k^2((n-1-k)K_{kmn} + \alpha_{kmn}/(k+1))$$
$$+ n(n+1)\chi_nW((m+1)(k+n-m-2)K_{kmn} + \alpha_{kmn});$$

$$\Pi^1_{kmn} = (n+1)\chi_n((k+m-n-2)K_{kmn}$$
$$- (n+k+m)\alpha_{kmn}/(mk))$$
$$+ n\rho_{(e)}\chi_n((n-k-m-3)K_{kmn}$$
$$+ (k+m+n+3)\alpha_{kmn}/((m+1)(k+1)));$$

$$\Pi^2_{kmn} = (n+1)\chi_n((m-n-1)K_{kmn} - \alpha_{kmn}/m)$$
$$+ n\rho_{(e)}\chi_n((n-m-1)K_{kmn} + \alpha_{kmn}/(m+1));$$

$$\Xi_n^0 = \omega_n^2 + n(n+1)\chi_n(n-1)(4+2n-5W);$$

$$\Xi_n^1 = ((n+1)(n-1) - 3n\rho_{(e)})\chi_n; \quad \Xi_n^2 = \rho_{(e)}n(n-1)\chi_n;$$

$$\psi_{kml}^{(+)(+)} = \omega_k + \omega_m + \omega_l; \quad \psi_{kml}^{(+)(-)} = \omega_k + \omega_m - \omega_l;$$

$$\psi_{kml}^{(-)(-)} = \omega_k - \omega_m - \omega_l; \quad D_{lm}^{kn} = 1 - \delta_{lm}\delta_{kn};$$

$$\lambda_{mln}^{(\pm)} = (\gamma_{mln} \pm \omega_m\omega_l\eta_{mln})/(\omega_n^2 - (\omega_m \pm \omega_l)^2);$$

$$\alpha_{mln} = -C_{m0l0}^{n0}C_{m(-1)l1}^{n0}\sqrt{m(m+1)l(l+1)};$$

$$\begin{gathered}\gamma_{mln} = (n+1)\chi_n K_{mln}(\omega_m^2(n-m+1 \\ -\rho_{(e)}n(n-m-1)/(n+1)) + 2n(l(l+1)-1) \\ +(l(m+1) - m(2m-2n+7)+3)nW/2) + (n+1)\chi_n\alpha_{mln} \\ \times((1/m - n\rho_{(e)}/((n+1)(m+1)))\omega_m^2 + nW/2);\end{gathered}$$

$$\begin{gathered}\eta_{mln} = (n+1)\chi_n K_{mln}(n/2 - m + 1 \\ +\rho_{(e)}n(2m+3-n)/(2(n+1))) \\ +(n+1)\chi_n\alpha_{mln}((1+n/(2l))/m \\ -n\rho_{(e)}(n+2l+3)/(2(m+1)(l+1)(n+1)));\end{gathered}$$

$$\chi_n = (1 + n(1+\rho_{(e)}))^{-1};$$

$$\omega_n = \sqrt{\chi_n(n-1)n(n+1)(n+2-W)}.$$

ACKNOWLEDGMENTS

This work was supported by the Russian Foundation for Basic Research, project no. 03-01-00760.

REFERENCES

1. A. I. Grigor'ev, Zh. Tekh. Fiz. **70** (5), 22 (2000) [Tech. Phys. **45**, 543 (2000)].
2. A. I. Grigor'ev and S. O. Shiryaeva, Izv. Ross. Akad. Nauk, Mekh. Zhidk. Gaza, No. 3, 3 (1994).
3. V. A. Koromyslov, S. O. Shiryaeva, and A. I. Grigor'ev, Zh. Tekh. Fiz. **73** (9), 44 (2003) [Tech. Phys. **48**, 1124 (2003)].
4. A. R. Gaibov and A. I. Grigor'ev, Zh. Tekh. Fiz. **73** (7), 13 (2003) [Tech. Phys. **48**, 813 (2003)].
5. A. N. Zharov, A. I. Grigor'ev, and S. O. Shiryaeva, Pis'ma Zh. Tekh. Fiz. **29** (9), 75 (2003) [Tech. Phys. Lett. **29**, 388 (2003)].
6. A. N. Zharov, S. O. Shiryaeva, and A. I. Grigor'ev, Zh. Tekh. Fiz. **73** (6), 36 (2003) [Tech. Phys. **48**, 697 (2003)].
7. A. N. Zharov, S. O. Shiryaeva, and A. I. Grigor'ev, Zh. Tekh. Fiz. **73** (12), 9 (2003) [Tech. Phys. **48**, 1511 (2003)].
8. S. O. Shiryaeva, A. I. Grigor'ev, V. A. Koromyslov, and A. N. Zharov, Zh. Tekh. Fiz. **73** (9), 60 (2003) [Tech. Phys. **48**, 1141 (2003)].
9. A.-H. Nayfeh, *Perturbation Methods* (Wiley, New York, 1973; Mir, Moscow, 1976).
10. R. C. Reid and T. K. Sherwood, *Properties of Gases and Liquids* (McGraw-Hill, New York, 1966; Khimiya, Moscow, 1971).

Translated by N. Mende

Technical Physics, Vol. 49, No. 7, 2004, pp. 833–838. Translated from Zhurnal Tekhnicheskoĭ Fiziki, Vol. 74, No. 7, 2004, pp. 27–32.
Original Russian Text Copyright © 2004 by Bychkov, Grachev, Esakov, Ravaev, Khodataev.

Longitudinal DC Electric Discharge in a Supersonic Air Flow

V. L. Bychkov, L. P. Grachev, I. I. Esakov, A. A. Ravaev, and K. V. Khodataev

Federal State Unitary Enterprise Moscow Radiotechnical Institute,
Russian Academy of Sciences, Moscow, 117519 Russia
e-mail: esakov@dataforce.net

Received December 10, 2003

Abstract—A longitudinal dc electric discharge in a submerged high-pressure supersonic air jet is described. Photographs of the discharge are provided. The experimental voltage across the discharge gap and the discharge current are given for two resistances of the resistor that limits the discharge current over a certain range of the discharge channel length along the air flow. The current–voltage discharge characteristic is provided at a constant discharge length. The main discharge characteristics are obtained from a comparison of the experimental and theoretical results calculated on the basis of the simplest model. *© 2004 MAIK "Nauka/Interperiodica".*

INTRODUCTION

The so-called dc discharge fed by a dc source is widely used for generating nonequilibrium plasma, especially in laboratory conditions, mostly because of the simplicity of its technical realization. The electric circuit diagram of the setup consists of only a high-voltage source; a ballast resistor R, which limits the discharge current; and the gas discharge gap connected in series. However, at a comparatively high gas pressure p (in air, at $p > 100$ Torr), problems arise with feeding the required amount of energy to the discharge plasma. Due to the instability of the plasma, which causes pinching of the discharge channel, its impedance becomes so small that most of the energy taken from the source is dissipated on the source resistance R_{in} and the ballast resistance R. Igniting the discharge in a high-velocity gas flow is one of the techniques to overcome this difficulty.

Experiments with a dc discharge in a gas flow are reported, for example, in [1] and in the literature cited therein. Most of these experiments used flows of a subsonic velocity V. Longitudinal discharges, in which the electric current J is parallel to V, and transverse discharges, in which the line connecting the electrodes is perpendicular to V, were studied.

One of the first experiments on igniting the transverse discharge in a wind tunnel with a supersonic flow are described in [2]. Studies of a similar discharge in a submerged supersonic jet are also reported in [3]. It was shown that such a discharge can be realized in its stable form only when the electrode spacing d is smaller than 0.1–0.2 cm. At a longer d, the discharge becomes essentially nonstationary. After the electrical breakdown in the gap, the discharge channel drifts away and is torn by the flow, and the cycle recurs. In this process, significant fluctuations in the voltage U across the discharge gap and in the discharge current J are observed. An experimental scheme, which makes it possible to obtain a stable combined transverse–longitudinal discharge in the paraxial region of the wind tunnel, feeding it with a power of $P_{\text{dis}} \approx 1$ kW, is described in [4, 5]. This result was obtained due to a significantly extended length of the discharge channel in the supersonic flow versus that in immobile air. The electrodes had such a shape that the discharge first occurs in the transverse field. Then the current channel is carried away by the air flow and remains stable actually along V during the entire further discharge time. In the stable stage of the discharge, the maximum transverse distance from the current channel to the downstream electrode is no longer than 0.1–0.2 cm, the total discharge length l being about a few centimeters.

Processes in this transverse–longitudinal discharge are analyzed in [6] under the assumption that the electric field E is constant over the main part of the current channel and equal to U/l. However, it is stated in [6] that this assumption leads to results that disagree with the experiment.

An experiment that demonstrates combustion of propane injected into a supersonic air flow excited by the transverse–longitudinal discharge is described in [7]. This experiment showed that the gas temperature T in the discharge region is high enough (about 800–1000 K) to ignite a propane–air mixture [8].

This paper describes the results of experiments with a longitudinal dc discharge in a supersonic high-pressure air flow. The discharge is created by the scheme developed in [4] with the difference that it occurs in a submerged jet and is longitudinal on its stable stage. Experimental and theoretical results are compared.

EXPERIMENTAL SETUP

The circuit diagram of the setup is given in Fig. 1. The electrodes of the discharge gap are in a sealed chamber placed in a submerged supersonic air jet. The

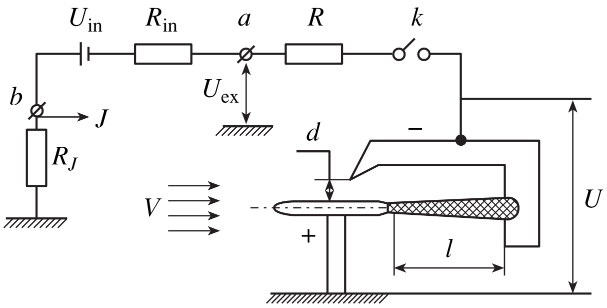

Fig. 1. Circuit diagram of the setup for a longitudinal dc discharge in a supersonic flow.

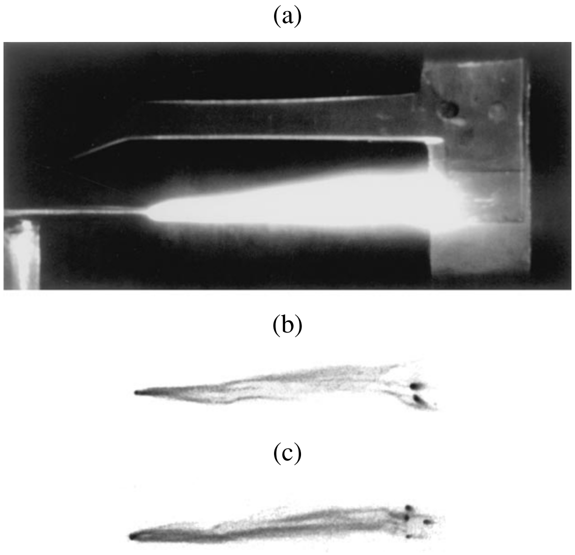

Fig. 2. Longitudinal dc discharge in a supersonic air flow.

grounded anode is made of a 5.7-cm-long aluminum bar 0.45 cm in diameter. Its ends are sharpened. The anode is installed along the jet on a streamlined support fabricated with it as a single whole. The support is 1 cm long along V and its maximum thickness is 0.2 cm. The cathode has the complex configuration shown in Fig. 1. It is made of a 0.2-cm-thick aluminum sheet. Its edges facing the flow are streamlined. The electrodes are designed so that the cathode can be moved along the flow in order to change the distance l between its vertical part and the downstream end of the anode. At a constant l, the transverse distance d between the electrodes can also be changed.

A high-voltage wire that feeds the cathode is connected to the negative terminal a of a high-voltage source through the resistor R. The output voltage of the source is U_{ex}, its equivalent voltage is U_{in}, and the internal resistance is R_{in}. The positive terminal b of the source is grounded through a 1-Ω resistor. A signal proportional to J is picked off from this resistor and applied to an oscilloscope. The voltage U_{ex} is monitored with a high-voltage voltmeter, which also uses a voltage divider to measure the signal proportional to U. The circuits used to measure J and U contain filters, which smooth ripples in the signals being monitored. The main series of experiments was carried out with two values of R: $R_1 = 7.42$ kΩ and $R_2 = 4.12$ kΩ.

The chamber with the electrodes is preliminarily evacuated to 100 Torr. When a signal is applied to the control valve, atmospheric air starts penetrating into the chamber through an axisymmetric Laval nozzle. An ultrasonic air jet with a diameter of 3 cm, a static pressure of $p_{out} = 97$ Torr, a temperature of $T_{out} = 150$ K, a molecule concentration of $n_{out} = 6 \times 10^{24}$ m^{-3}, and a Mach number of $M = 2$ at a flow velocity of $V_{out} = 507$ m/s is formed in the exit section of the nozzle. Behind the electrodes, the jet enters the confuser, which connects the chamber to the receiver. The confuser and receiver reduce the pressure in the chamber to $p = 97$ Torr at the instant the valve is opened and on. This pressure remains unchanged for about 1 s and only after that starts growing. It is during this second, as long as $p = p_{out}$, that the high voltage is applied to the electrodes with the help of the key k.

EXPERIMENTAL RESULTS

In the first experiments, the parameters of the high-voltage source (U_{in} and R_{in}) were determined. To do this, the source was disconnected from the electrodes, and resistors of known resistances were connected to its output terminals. The experiments gave $U_{in} = 7$ kV and $R_{in} = 0.54$ kΩ.

The experiment with the discharge shows that, when values of d and l are such that a stable discharge is sustained, the air breakdown initially occurs in the gap d. Subsequently, the current channel is carried away by the supersonic flow with one of its ends being fixed at the downstream end of the anode, while the other end moves along the lower edge of the horizontal part of the cathode. The discharge channel is stabilized in the horizontal position, its length becoming equal to l. Figure 2 shows typical photographs of the discharge for $R = R_2$, $d = 0.8$ cm, and $l = 6$ cm. The photograph in Fig. 2a was obtained with an exposure time of 0.1 s; photographs in Figs. 2b and 2c (in an inverted form) were obtained for a 0.1-ms exposure. It can be assumed from these photographs that the plasma pinch of diameter $2r = 0.1$–0.2 cm continuously bends following nonstationary lines of the gas flow; therefore, the integral photograph (Fig. 2a) displays a relatively wide region.

At the above values of R and d and $l > l_{max} \approx 4.5$ cm, the discharge is no longer stable. Its current channel tosses about between gap d and the vertical part of the cathode, sweeping the region between the lower edge of the horizontal part of the cathode and the anode. In this case, the intermittent transverse discharge [3] is observed. The length l_{max} follows the variation of d. At $l < l_{max}$, a stable longitudinal discharge evolves by the above scheme even when the horizontal part of the cathode is electrically insulated. In the steady discharge, U and J are almost constant when the gap length d is varied. Naturally, the maximum gap length must be such that the initial gas breakdown is possible in the gap. It was shown [4] that, at $V \leq 500$ m/s, the gas flow does not affect the intensity of the minimum critical breakdown field E_{cr}. In this case, as in immobile gas, E_{cr} is determined by the concentration n of gas molecules alone. The breakdown interelectrode voltage U_{br} in the supersonic flow also depends on the electrode shape and becomes significantly lower when the electrodes are sharpened [9].

In the process of discharge, the cathode suffers from gradual thermal sputtering (see also [4]); i.e., the temperature of the plasma that contacts it is at least higher than the aluminum melting temperature $T_{\mathrm{m\,Al}} = 932$ K [9].

Figure 3 shows the values of U measured at different l. The experimental data obtained at $R = R_1$ are shown by circles; at R_2, by crosses. It is seen that, up to a certain value of l, the experimental functions $U(l)$ at a constant R also increase with l. Their derivatives change their signs at large values of l due to the above-mentioned discharge instability at $l > l_{max}$. Figure 4 shows experimental dependences $J(l)$. As in Fig. 3, the results obtained at $R = R_1$ are shown by circles; at R_2, by squares. These functions slowly decrease with l.

It follows from Figs. 3 and 4 that, for example, at $R = R_2$ and $l = 5$ cm, the energy is supplied to the discharge with a power of $P_{dis} = UJ = 1.69$ kW, which is about 20% of the high-voltage source power $P = U_{in}J = 8.75$ kW.

Finally, Fig. 5 shows an experimental discharge current–voltage characteristic at a constant length of $l = 3$ cm with R varied from 4.12 to 12.4 kΩ. The current–voltage characteristic of the longitudinal dc discharge in the supersonic flow is seen to be a decreasing function. This fact is also corroborated by results shown in Figs. 3 and 4.

DISCUSSION

We will interpret the experimental results in the framework of the simplest model. First of all, we can write Ohm's law for the discharge circuit in Fig. 1, which relates the current J in it to the voltage U across the discharge gap:

$$U_{in} = J(R_{in} + R) + U. \quad (1)$$

This relation makes the simultaneous measurements of U and J in a certain sense redundant. In fact, if voltage U is measured, current J can be calculated from (1) and vice versa. However, a comparison of the experimental and theoretical results confirmed that the measurements were correct.

Another equation that relates U and J can be obtained from the local energy balance in the discharge channel. Let us write it under the following assumptions.

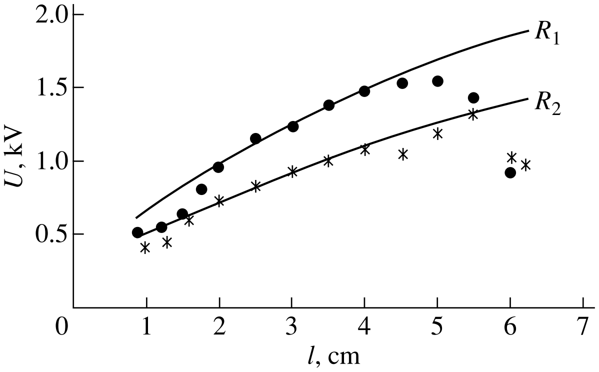

Fig. 3. Voltage U across the discharge gap versus its length l.

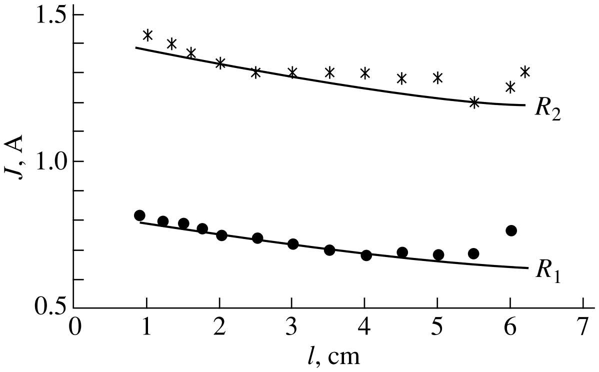

Fig. 4. Discharge current J versus length l of the discharge gap.

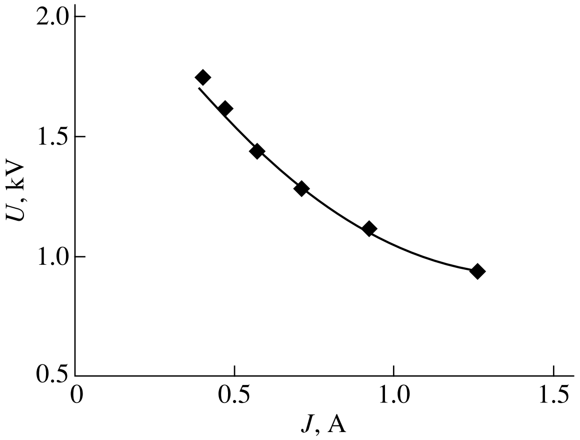

Fig. 5. Current–voltage characteristic of a longitudinal dc discharge in a supersonic air flow.

(1) The discharge is a stationary azimuthally symmetric plasma channel. Its local parameters (molecule concentration n, temperature T, electron concentration n_e, field strength E, and current density j) vary versus

the *x* coordinate along the channel, but are constant in its cross sections of radius *r* (of area *S*).

(2) The discharge evolves under isobaric conditions, i.e., at $p(x)$ = const. Therefore, in an arbitrary cross section,

$$n = n_{\mathrm{out}}(T_{\mathrm{out}}/T). \tag{2}$$

It also follows from this assumption that the longitudinal molecular velocity *V* in the discharge is constant and coincides with V_{out} [10].

In this assumption, we disregard the processes that evolve in the anode part of the discharge, where the assumption may be incorrect. The length of this region and the discharge parameters in it can only be obtained from a complete aerodynamic model, in which the airflow of a supersonic jet about the anode and the adjacent energy-release region is considered. The length of the anode region can be evaluated from Fig. 2a as 0.2–0.3 cm by the change in the rate of increase in the cross-sectional area of the discharge channel. Let us use index 0 to denote the discharge parameters in the section (that is, at this distance from the anode downstream) and use this point as an origin for the distance *x* to the section being analyzed, in which the discharge parameters will have no indices; in the section $x = l$, the parameters will be marked by index *l*.

(3) In any cross section of the discharge channel downstream from the zero section, we have

$$E_0/n_0 = E/n = \xi = \text{const}. \tag{3}$$

This assumption differs significantly from the one accepted in [6], where it is assumed that E = const along the discharge channel.

(4) The number of air molecules brought by the flow to the zero cross section of the discharge channel also remains constant over the length of the channel:

$$n_0S_0 = nS = \text{const}. \tag{4}$$

This relation together with (2) implies that, along the discharge channel, we have

$$T_0/S_0 = T/S = \text{const}. \tag{5}$$

Under the above assumptions, the equation of local energy balance has the form

$$(7/2)k\Delta Tn = \Psi jE(\Delta x/V), \tag{6}$$

where *k* is the Boltzmann constant and the coefficient Ψ shows the part of the electric energy absorbed in the discharge that is spent on increasing the gas temperature *T* in it.

Replacing *j* by *J*/*S*, with (2)–(4), we obtain

$$3.5kS_0VTdT = \Psi J\xi T_0dx.$$

Integration by parts with respect to *x* from 0 to the current position *x* and with respect to *T* from T_0 to *T* yields

$$T = T_0\sqrt{x/l_0 + 1}, \tag{7}$$

where the characteristic length is

$$l_0 = (3.5VS_0kT_0)/(2\Psi J\xi). \tag{8}$$

From this expression, with (2) and (4), we obtain

$$S = S_0\sqrt{x/l_0 + 1} \quad \text{or} \quad r = r_0\sqrt[4]{x/l_0 + 1},$$

$$n = n_0/\sqrt{x/l_0 + 1}, \tag{9}$$

$$E = \xi n_0/\sqrt{x/l_0 + 1} = E_0/\sqrt{x/l_0 + 1}.$$

These formulas give functional dependencies of the discharge parameters over the discharge length but do not give their absolute values. Theoretically, these values can only be obtained using a full-scale model of ionization and aerodynamic processes in the discharge channel, including its near-electrode regions. The absolute values of these parameters can also be estimated from the experiment. Further comparison of theoretical dependences $U(l)$, $J(l)$, and $U(J)$ with the experimental results will validate or disprove the above assumptions.

By multiplying the left- and right-hand sides of (9) by *dx* and integrating the result from 0 to *l*, we obtain

$$U = 2E_0l_0(\sqrt{l/l_0 + 1} - 1). \tag{10}$$

As follows from the experimental data in Fig. 3, at R = const, on the discharge region that is regular in *l*, values of *U* measured at two arbitrary *l* are related by

$$U_A/U_B = \sqrt{l_A/l_B}. \tag{11}$$

In particular, at $R = R_1$ and electrode spacings of l_A = 4 cm and l_B = 2 cm, the corresponding voltages are U_A = 1.5 kV and U_B = 1 kV; i.e., relation (11) is satisfied to within 6%. At $R = R_2$, this relation is valid within an even higher accuracy of 4%.

Relation (11), which follows from the experiment, can be derived from (10) if

$$\sqrt{l/l_0} \geqslant 1. \tag{12}$$

According to relation (8), parameter l_0 is inversely proportional to *J* so that, with decreasing *R*, condition (12) can be fulfilled to a higher degree of accuracy.

Under condition (12) with (8), Eqs. (10) and (7) can be simplified so that solving these equations for ξ and ψ yields

$$\xi = (UkT_l)/(2pl), \tag{13}$$

$$\psi = (7/2)(T_l/T_0)(VpS_0)/(UJ). \tag{14}$$

The values *U*, *p*, and *l* appearing in (13) are measured; only T_1 is unknown. However, it follows from our experiments that $T_l \approx T_{\mathrm{mAl}}$. Let $T_l = 10^3$ K. Then, setting $T_0 \approx T_{\mathrm{out}}$, we derive from Eq. (7) that condition

(12), which follows from the experiments, is satisfied:

$$\sqrt{l/l_0} = \sqrt{(T_l/T_0)^2 - 1} \approx 6.5.$$

To be specific, taking $l = 3$ cm and $R = R_1$ in Figs. 3 and 4, we obtain $U = 1.25$ kV and $J = 0.75$ A, which yields $\xi = 2.2 \times 10^{-20}$ V m^2 from (13).

In Eq. (14), the ratio T_l/T is to some extent uncertain and the value S_0, or the initial current channel diameter $2r_0$, is also unknown. We can obtain it from the following considerations. The calculated value of ξ is approximately five times smaller than its critical value $\xi_{cr} = 1.2 \times 10^{-19}$ V m^2 [6, 11]. Quantities ξ and ψ are related in a known manner [6, 11]. In the discharge plasma, the energy of the electric field is first taken by its electrons and, with ξ evaluated above, not more than 5% of this energy is immediately taken away by translation degrees of freedom of air molecules. The rest of the energy is initially stored in the intramolecular vibrations. The molecule transit time $\tau_l = l/V \approx 0.1$ ms is not enough for this energy to relax into heat (even at $T \approx 10^3$ K [6]). By setting $\psi = 5 \times 10^{-2}$ in formula (14) and using the quantities specified above, we obtain $2r_0 = 0.63$ mm. This value is approximately the same as the diameter of the current channel, which can be estimated from Figs. 2b and 2c.

Similar calculations based on formulas (13) and (14) at $R = R_2$ also give $\xi < \xi_{cr}$: $\xi = 1.7 \times 10^{-20}$ V m^2 and $\psi = 3.5 \times 10^{-2}$.

The conclusion that the discharge is subcritical also agrees with the following considerations. The main mechanism of electron extinction in air plasma at a high p is their dissociative adhesion to molecules O_2 [1, 6]. The characteristic time of this process is $\tau_a = 1.8 \times 10^{18}/n$ s [11]. The plasma electrons drift in a constant field with velocity $V_{dr} = \mu_e E$, where their mobility is $\mu_e = 1.1 \times 10^{24}/n$ m^2/(V s) [11]. Therefore, the adhesion length is $l_a = \tau_a V_{dr} = 1.9 \times 10^{42}\xi$ m. For the experiment at $R = R_1$ with ξ estimated above, the length is $l_a = 4.4 \times 10^{-2} m \approx l$. As follows from this result, the field does not have to sustain the ionization process over the main length of the plasma channel, maintaining the same number of electrons generated near the cathode. It can be weaker than E_{cr} and must only provide their drift velocity V_{dr} determined by the current.

Note that, in our experiments, at the estimated parameter ξ, the velocity is $V_{dr} = 1.1 \times 10^{24}\xi = 2.5 \times 10^4$ m/s $\gg V$ and the air flow in the discharge channel does not affect the electron drift in the field.

From the measured current J and estimated velocity V_{dr}, we can calculate the scale n_e in the discharge plasma. In particular, at $l = 3$ cm, the concentration is $n_{e0} = J/(V_{dr} q_e S_0) = 10^{20}$ m^{-3}, where q_e is the electron charge, or the degree of air ionization is 10^{-4}. This is a typical value for the low-temperature nonequilibrium air plasma at a relatively high p.

Under condition (12), with (1), the analytical dependence $U(l)$ has the form

$$U^3 - U_{in}U^2 + 7Vp_c^2(R_{in} + R)\xi S_0 l/(k\psi T_0) = 0. \quad (15)$$

Dependences (15) with the parameters estimated and calculated above and for $R = R_1$ and $R = R_2$ are plotted in Fig. 3. They are seen to actually coincide with the experiment in the range of l that corresponds to a steady discharge. The functions $J(l)$ and $U(J)$ calculated from Ohm's law are plotted in Figs. 4 and 5. The curves also actually pass through the experimental points.

CONCLUSIONS

Thus, a longitudinal dc discharge in a supersonic high-pressure air jet several centimeters long was realized. In the experiments, the electric energy was supplied to the discharge with a power of up to 1.7 kW, the efficiency of the high-voltage source being approximately 20%. The energy introduced into the discharge grows with its length, while the voltage across the discharge gap increases and the discharge current insignificantly decreases. The discharge current–voltage characteristic is a decreasing function.

The comparison of experimental data with calculations based on the simplest model allowed us to analyze the main properties of this type of discharge. Specifically, assumptions were proved to be true that (i) the process of heating the air along the longer side of the discharge channel is isobaric; (ii) discharge parameters vary along the channel as a result of heating by the current, but are constant in cross sections of the plasma channel; (iii) the number of air molecules that flow in the plasma channel is constant; and (iv) the ratio of electric field intensity to air molecule concentration is constant over the longer side of the discharge channel.

The analysis has shown that the electric field along the plasma discharge channel is subcritical. As a result, the energy supplied to the discharge is predominantly spent not on heating the air, but on excitation of vibrational degrees of freedom of its molecules. Nevertheless, the gas temperature in the discharge has a scale of 1000 K.

Our discharge model, although it yields correct functional dependencies, is not closed. Some of its parameters are taken from the experiment and cannot be obtained directly from the model. A full-scale model must allow for ionization and aerodynamic processes, primarily in the anode and cathode discharge regions.

Such discharges can be used in devices that require high translational, as well as high vibrational, molecular temperatures.

REFERENCES

1. E. P. Velikhov, V. S. Golubev, and S. V. Pashkin, Usp. Fiz. Nauk **137**, 117 (1982) [Sov. Phys. Usp. **25**, 340 (1982)].

2. V. I. Alferov and A. S. Bushmin, Zh. Éksp. Teor. Fiz. **44**, 1775 (1963) [Sov. Phys. JETP **17**, 1190 (1963)].
3. L. P. Grachev, N. N. Gritsov, G. I. Mishin, *et al.*, Zh. Tekh. Fiz. **61** (9), 185 (1991) [Sov. Phys. Tech. Phys. **36**, 1073 (1991)].
4. V. V. Vitkovskiĭ, L. P. Grachev, N. N. Gritsov, *et al.*, Tr. TSAGI (Zhukovsky Central Institute of Aerohydrodynamics), No. 2505, 3 (1991).
5. V. V. Vitkovskiĭ, L. P. Grachev, N. N. Gritsov, *et al.*, Teplofiz. Vys. Temp. **28**, 1156 (1990).
6. V. L. Bychkov, L. P. Grachev, I. I. Esakov, *et al.*, Preprint No. 27, IPM (Keldysh Institute of Applied Mathematics, USSR Academy of Sciences, 1977).
7. V. V. Ivanov, V. V. Skvortsov, Yu. E. Kuznetsov, *et al.*, Preprint No. 133, TSAGI (Zhukovsky Central Institute of Aerohydrodynamics, 2002).
8. S. Kumagai, *Combustion* (Khimiya, Moscow, 1979).
9. M. V. Kurlin, Ya. I. Panova, V. V. Pasynkov, and V. N. Tairov, *Electroradiomaterials* (Sudostroenie, Leningrad, 1969).
10. F. Bartl’me, *Gas Dynamics of Combustion* (Énergoizdat, Moscow, 1981).
11. Yu. P. Raĭzer, *Modern Physical Foundations of Gas Discharge* (Nauka, Moscow, 1980).

Translated by A. Khzmalyan

Technical Physics, Vol. 49, No. 7, 2004, pp. 839–842. Translated from Zhurnal Tekhnicheskoĭ Fiziki, Vol. 74, No. 7, 2004, pp. 33–37.
Original Russian Text Copyright © 2004 by Repin, Rep'ev.

GAS DISCHARGES, PLASMA

Investigation of the X-ray Radiation Produced by a Diffusive Discharge in the Rod–Plane Geometry under Atmospheric Pressure

P. B. Repin and A. G. Rep'ev
All-Russia Research Institute of Experimental Physics, Sarov, Nizhegorodskaya oblast, 607188 Russia
e-mail: ra30@yandex.ru

Received September 11, 2003; in final form, December 15, 2003

Abstract—Spatial parameters of the X-ray radiation produced by a high-voltage nanosecond discharge evolving in air under atmospheric pressure in the rod (cathode)–plane electrode system with a 10-cm electrode spacing are studied experimentally. A ~170-ns voltage pulse with an amplitude of ~200 kV and 10-ns rise time is applied to the cathode. The photoelectronic method is used to study, under the same conditions, the integrated (over the gap) characteristics of the radiation, in particular, the duration of its generation. It is found that, when the size of the X-ray source is not smaller than that of the discharge region of diffusive luminescence, radiation from the cathode region of the gap is primarily observed (i.e., from the region where the electric field distribution is sharply inhomogeneous). The X-ray generation is usually observed after the bridging of the discharge gap, the X-ray pulse having a rise time of ~3 ns, a duration of ~10 ns, and an effective radiation energy of ~6 keV. © *2004 MAIK "Nauka/Interperiodica".*

The high-voltage nanosecond discharge that occurs in a high-pressure ($\leq 10^5$ Pa) gaseous medium across long (≥10 cm) gaps with a strongly nonuniform electric field distribution is of interest due to the application of this type of discharge in a number of devices [1–3] and from the viewpoint of deepening fundamental knowledge about the nature of the gas discharge. The diffusive discharge that evolves in the classical rod–plane electrode geometry is not yet clearly understood. The discharge mechanisms are not completely clear, several questions concerning the emission of ionizing radiation that accompanies the discharge persist, and there are almost no data on the discharge radiation characteristics in the X-ray range. The change in the discharge configuration observed from pulse to pulse (from the single-channel volumetric luminescence shape to more complex multichannel shapes) is characterized by a significant variation of electric and emission discharge parameters, which stimulates experimental research.

This paper reports on volumetric parameters of X-ray radiation produced by a diffusive discharge that evolves in air under atmospheric pressure in a rod (cathode)–plane electrode system with a 10-cm-long electrode spacing. The effective discharge radiation energy in the X-ray range is estimated. Integrated time characteristics of the radiation over the gap are studied (the instant when the emission begins and its duration are determined). The amplitude of the voltage across the gap was ~200 kV at a ~10-ns pulse rise time and ~170-ns total pulse duration. The maximum discharge current was 600 A.

A circuit diagram of the setup is shown in Fig. 1. As a source *1*, a BING-6 modular pulsed nanosecond generator [4] loaded by a Lewis transformer [5] is used. The transformer consists of six 17-cm-long coaxial cables whose output ends are connected in series in the upper part of discharge chamber *2*. The body of the chamber is a metal cavity 60 cm in diameter and 60 cm high. The maximum voltage is applied to the center of the chamber where a stainless steel rod cathode 19 cm long and 1 cm in diameter is fixed on the chamber axis. On the anode side, the cathode end face has a bullet shape: it has the form of a surface of revolution of a circular arc ~30 mm in radius mated to the cylindrical surface of the rod (in a number of experiments, a cathode with a hemispherical end was used instead). The anode (aluminum current-collecting plate 18 cm in diameter) is placed symmetrically with respect to the cathode at the bottom of the chamber and geometrically is a part of its planar grounded base, which renders a highly uniform electric field distribution on the surface of this electrode.

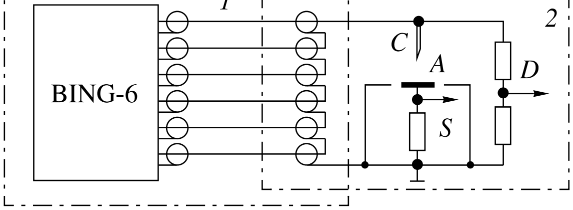

Fig. 1. Circuit diagram of the setup.

In the experiments, the voltage across the discharge gap and the discharge current were measured using low-inductance resistive divider *D* and shunt *S*. The integrated discharge radiation over the gap length in the optical (300–600 nm) and X-ray ranges were also measured with a high-speed photomultiplier. When measuring the X-ray radiation, the photomultiplier was supplied with a plastic scintillator (3% *n*-phenyl biphenyl + 0.06% POPOP in polystyrene with a de-excitation time of <1 ns); the protection against optical radiation was provided by a two-layer 20-μm-thick aluminum filter. Along with the photoelectric method, the X-ray radiation parameters were studied with the help of photoemulsions.

Electric signals were recorded by a digital oscilloscope with a pass band of 500 MHz. The oscillograms were matched with allowance for the distance between the X-ray sensor and the discharge, the length of the instrument cables, and the transit time through the photomultiplier. This time was determined in special experiments in which the pulse from a nitrogen laser (wavelength of 337 nm and duration of ~10 ns) was simultaneously recorded by the photomultiplier being calibrated and a detector with an almost zero transit time. The time resolution of electric signals was not lower than 0.5 ns for the current and voltage and ~2 ns for the X-ray pulse. In the experiments, we also visually monitored and photographed the discharge.

It was found that, at the same gap geometry, the discharge is realized in various forms of diffusive luminescence. The forms observed can be divided into three main morphological types: volumetric, multichannel, and transient. A discharge of the volumetric type (which occurs with a probability of ~0.7 with the bullet-shaped cathode) has the form of a bright central channel, which significantly differs from other channels in its size and intensity. For the gap studied, the luminescence region of this discharge visually has the form of two cones with a common base 5 cm in diameter near the middle of the gap; the vertex of one cone coincides with the cathode tip, while the vertex of the other cone is truncated by the anode plane so that the discharge diameter in this plane does not exceed 2 cm. As rule, the multichannel discharge (which occurs most frequently with a hemispherical cathode) consists of 4 to 60 channels of commensurate luminescence diameters and intensities uniformly distributed in the anode plane in a circle 6 to 16 cm in diameter. Relatively rare transient discharges include all remaining (usually asymmetric) diffusive luminescence forms. The change in the luminescence form is accompanied with a change in the electric and radiative discharge characteristics. Also, for discharges of the same luminescence form, a statistical spread in these parameters is observed. As a result, pulse-to-pulse variations in the discharge current under constant conditions are within 170 to 340 A for the volumetric discharge form (bullet-shaped cathode) and 370 to 600 A for the multichannel form (hemispherical cathode). This paper primarily focuses on the volumetric discharge form, because it exhibits a higher stability in a number of electric and spatial parameters as compared to other discharge luminescence forms. This circumstance simplifies the analysis of experimental data and helps us to reveal mechanisms of the discharge evolution that are common to all discharge types.

It was found by the photoelectron method that, for the volumetric luminescence form, X-ray radiation is observed on average in one-third of discharge pulses. The amplitude of an X-ray pulse varies within the dynamic range of our experimental technique by a factor of approximately 10. As a rule, correlation is simultaneously observed between the amplitude of the discharge current and intensity of the radiation produced by the discharge in the ultraviolet, visible, and X-ray ranges. For other forms of diffusive luminescence, a correlation is also on average observed between the discharge current and its radiation.

It was found by the photographic method that the X-ray radiation emitted by several discharge pulses is sufficient to reliably produce a uniform blackening of unmasked regions of a photographic film placed in the anode plane, as well as on the side of the discharge, and exposed through a 10- to 20-μm-thick aluminum foil. The effective energy of X-ray radiation from the discharge estimated from absorption in a nine-stage aluminum wedge with a thickness of up to ~40 mg/cm^2 [6, 7] is ~6 keV.

The spatial distribution of X-ray sources was studied by the photographic method with the help of specially designed cassettes installed in two mutually orthogonal planes. An isochromatic (with a spectral sensitivity of up to 640 nm) film was used as the X-ray sensitive material in the experiment. Cassettes of two designs were mostly used: one of the cassettes was placed at a distance of ~9 cm on the side of the discharge axis (Fig. 2), while the other was installed under the anode (Fig. 3).

Figure 2 is a diagram of the setup used to study the distribution of X-ray sources along the discharge axis. Photographic film *1* was placed with emulsion facing the discharge in lighttight cassette *2* made of 2 mm thick electrical pressboard. The electrode spacing was conventionally divided into five ~2-cm-thick layers perpendicular to the discharge axis. Due to planar collimators included in the cassette, radiation of these layers acted upon five 50 × 3-mm horizontal film regions. The outer ends of the collimators were covered with ~10-μm-thick aluminum foil strips. This design eliminated discharges sliding over the cassette surface even when it is placed at a rather small distance from the chamber axis, which allowed us to reduce the number of discharge pulses required to blacken the film so that it can be analyzed to 50–150. A typical blackening profile of the image obtained on the film is shown in Fig. 2 (on the left). It is seen that the radiation dose of the source of the X-ray radiation that accompanies the discharge is nonuniformly distributed along the gap. As the observation point approaches the cathode region, the intensity of X-ray radiation increases in a nonlinear manner, as we see from the behavior of the blackening density upon a change in the distance from the cathode.

The X-ray radiation from the discharge in the section transverse to the discharge axis was studied by the shadow technique (Fig. 3). As a rule, the experiment involved 10 to 50 discharge pulses. Under the anode, there was a lighttight metal container *1* (16 cm in diameter and ~2 cm high) covered with a 20-μm-thick aluminum foil *2* from above. The foil was used as a filter to cut off radiation in the visible and ultraviolet ranges and served as an anode, which freely passed the discharge current. Under the foil, with its emulsion facing the discharge, a photographic film *3* was pressed to the container bottom by a 0.5-mm-thick and 18-mm-high copper knife *4*, which was impenetrable for the X-rays studied. The knife vertically divided the internal cassette cavity into two halves. The X-ray shadow of the knife takes part in forming the image on the film. Near the knife, the X-ray radiation produced by one half of the discharge gap cannot reach the film exposed to the radiation produced by the other half if only the whole of the radiation source is not localized along the discharge axis at a distance comparable with the knife thickness (~1 mm).

A picture of the integral shadow image of the X-ray source obtained in one of the experiments and the respective film darkening density profile perpendicular to the knife are shown in Fig. 3 (bottom). An almost zero darkening level near the knife shows that, on average, the distribution of X-ray sources in the section perpendicular to the discharge axis is not localized near the axis. As the observation point moves away from the knife, the radiation that acts on the film does not immediately increase the darkening to a constant level, where radiation produced by both parts of the discharge are actually added together. Consequently, the knife affects the sources of radiation that are at a distance from the discharge axis determined by angle α (Fig. 3). For a 10-cm-long gap, α is typically not smaller than 34°, which corresponds to an X-ray source whose transverse size is not smaller than the visible region of the diffusive discharge luminescence and to the emitting points located, according to the above experiments, predominantly in the upper part of the discharge gap (near the cathode). The decrease in the darkening level with a further increase in the distance from the discharge axis along the profile curve is attributed mostly to the effect of the bottom of the discharge chamber. Analysis of the darkening density distribution suggests that the X-ray source may have a shape whose boundary is within curves *5* and *6* shown in Fig. 3 against the background of the boundary of the volumetric discharge shape.

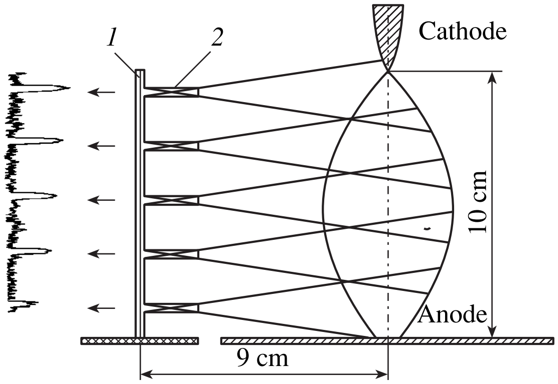

Fig. 2. Diagram of the setup used to study X-ray radiation along the discharge axis.

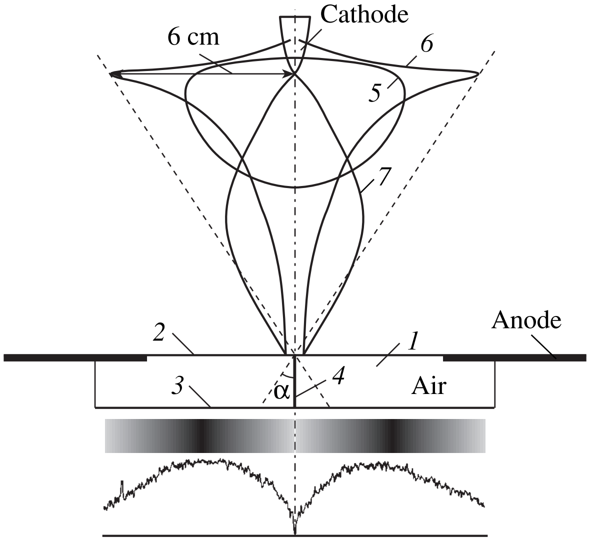

Fig. 3. Diagnostics of spatial characteristics of X-ray radiation by the shadow technique: (*1*) boundary of the volumetric discharge shape and (*2*, *3*) expected boundaries of the X-ray source.

In a special series of experiments, the spatial density distribution of the X-ray source in hardness was studied with the help of the above shadow technique complemented with a nine-step aluminum wedge, which allowed us to estimate the effective energy of radiation from the absorption in layers of a material of different thicknesses [6, 7]. The wedge was placed between knife *4* (Fig. 3) and photographic film *3* so that the steps of the wedge were perpendicular to the knife. The image obtained on the film after it was exposed to radiation produced by the discharge in this arrangement had the form of nine stripes of different darkening densities. The darkening density distribution in the direction perpendicular to the knife is formed in a manner similar to the one described above; the distribution along the knife is determined by the portion of the radiation that has passed through the corresponding step of the wedge. The thicker the aluminum layer, the higher the degree to which the image is determined by the high-energy part of the X-ray spectrum. The analysis of the experimental image darkening density profiles in the direction perpendicular to the knife for different wedge steps has shown that they are similar to the pro-

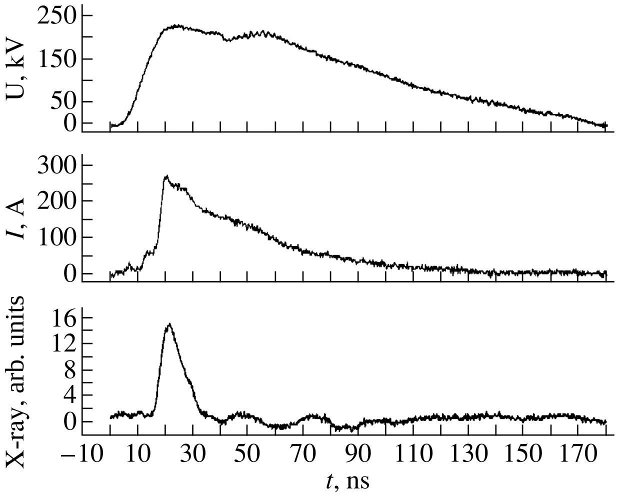

Fig. 4. Typical oscillograms of the voltage, current, and X-ray radiation pulses.

file shown in Fig. 3 and exhibit an almost identical behavior. In particular, for all wedge steps, the distance from the knife to the maximum of the darkening density is the same. This gives us a reason to assume that, on average, the hardness spatial distribution of the X-ray source is uniform. Indeed, if the radiation hardness monotonically varied from the discharge axis to its periphery, this would displace the peaks of the image darkening density along the wedge.

Oscillograms of the X-ray pulse, discharge current, and voltage across the gap typical of the volumetric discharge form are shown in Fig. 4. It should be noted that the amplitude–time parameters of X-ray radiation noticeably vary from pulse to pulse. Nevertheless, the analysis of oscillograms of several thousand discharge pulses allowed us to derive certain general regularities. As a rule, the X-ray pulse duration measured at the half-intensity points, which was 6 to 30 ns, increases with discharge current amplitude. The rise time of an X-ray pulse (between 0.1 and 0.9 points) is about 3 ns, which is close to the time resolution of our diagnostics technique. Consequently, the real rise time does not exceed this value. The beginning of an X-ray pulse as a rule coincides with the beginning of the discharge conduction current, which is detected from a sharp increase in the signal on the oscillogram of current (approximately between the 16th and 17th nanoseconds in Fig. 4). For a number of pulses, a delay (of up to 4 ns) is observed in X-ray radiation with respect to the beginning of the conduction current. There were no X-ray pulses detected ahead of the conduction current. Note that the beginning of the conduction current varies from pulse to pulse with respect to the beginning of the voltage derivative within 13 to 24 ns.

Thus, it was found that time parameters of the X-ray pulse are correlated with the discharge conduction current: the beginning of emission coincides with the end of the phase of discharge gap bridging and corresponds to the beginning of the conduction current; i.e., the X-ray radiation is close in its time parameters to the radiation observed in the multichannel diffusive discharge in the wire–plane electrode system [8]. This fact may serve as evidence that X-ray radiation in our experiments and in [8] is of a similar origin.

It was also found that the probability of generation and the intensity of X-ray radiation are related to the discharge stages that precede the conduction. In the near future, we plan to publish results of detailed statistical studies of X-ray radiation versus parameters of initial discharge stages.

Thus, we have found in our experiments that the high-voltage diffusive discharge that evolves in atmospheric air under normal pressure in the rod (cathode)–plane electrode system is accompanied by a pulse of X-ray radiation. The region where X-ray radiation is generated usually occupies almost the entire discharge gap and is characterized by a nonuniform irregular intensity distribution along the gap. The size of the region with the highest radiation intensity (near the cathode) is at least not smaller than the visible discharge luminescence size. The effective energy of the radiation is the same over the entire generation region and is about 6 keV. The X-ray pulse is observed not in the phase when streamer channels propagate in the gap, but after its bridging, which is typical of diffusive high-voltage discharges formed in gaps with sharply nonuniform electric field distributions.

REFERENCES

1. S. N. Buranov, V. V. Gorokhov, V. I. Karelin, *et al.*, Kvantovaya Élektron. (Moscow) **18**, 891 (1991).
2. S. N. Buranov, S. V. Voevodin, I. A. Voevodina, *et al.*, in *Plasma Physics Investigations*, Ed. by V. D. Selemir and A. E. Dubinov (RFYaTs-VNIIEF, Sarov, 1998), pp. 339–361.
3. S. N. Buranov, S. V. Voevodin, I. A. Voevodina, *et al.*, in *Proceedings of the 7th Session of Young Scientifics, Nizhnii Novgorod, 2002* (Inst. Prikl. Fiz. RAN, Nizhnii Novgorod, 2002), p. 130.
4. B. G. Kudasov, S. S. Pavlov, V. A. Tananakin, *et al.*, in *Proceedings of the 11th IEEE International Pulsed Power Conference, Baltimore, 1998*, Ed. by G. Cooperstein and I. Vitkovitsky, p. 1572.
5. I. A. D. Lewis and F. H. Wells, *Millimicrosecond Pulse Techniques*, 2nd ed. (Pergamon, London, 1959; Inostrannaya Literatura, Moscow, 1956).
6. *Radiation Dosimetry*, Ed. by G. J. Hine and G. L. Brownell (Academic, New York, 1956; Inostrannaya Literatura, Moscow, 1958), pp. 3–108.
7. *Physical Measurements in Gas Dynamics and Combustion*, Ed. by R. W. Ladenburg and H. S. Taylor (Princeton Univ. Press, Princeton, 1954; Inostrannaya Literatura, Moscow, 1957).
8. S. N. Buranov, V. V. Gorokhov, *et al.*, in *Plasma Physics Investigations*, Ed. by V. D. Selemir and A. E. Dubinov (RFYaTs-VNIIEF, Sarov, 1998), pp. 39–67.

Translated by A. Khzmalyan

Technical Physics, Vol. 49, No. 7, 2004, pp. 843–848. Translated from Zhurnal Tekhnicheskoĭ Fiziki, Vol. 74, No. 7, 2004, pp. 38–43.
Original Russian Text Copyright © 2004 by Oreshkin, Baksht, Labetsky, Rousskikh, Shishlov, Levashov, Khishchenko, Glazyrin.

GAS DISCHARGES, PLASMA

Study of Metal Conductivity near the Critical Point Using a Microwire Electrical Explosion in Water

V. I. Oreshkin[1]*, R. B. Baksht[1], A. Yu. Labetsky[1], A. G. Rousskikh[1], A. V. Shishlov[1],
P. R. Levashov[2], K. V. Khishchenko[2], and I. V. Glazyrin[3]*****

[1]*Institute of High Current Electronics, Siberian Division, Russian Academy of Sciences,*
Akademicheskiĭ pr. 4, Tomsk, 634055 Russia
** e-mail: oreshkin@ovpe.hcei.tsc.ru*
[2]*Institute for High Energy Densities, Russian Academy of Sciences,*
Izhorskaya ul. 13/19, Moscow, 125412 Russia
*** e-mail: konst@ihed.ras.ru*
[3]*Zababakhin Institute of Technical Physics, Snezhinsk, Chelyabinskaya oblast, 456770 Russia*
**** e-mail: i.v.glazyrin@vniitf.ru*

Received December 1, 2003

Abstract—Electrical explosion of aluminum and tungsten microwires in water was studied both experimentally and numerically. The experimental range of currents through the wire was 0.1–1 kA for explosion times of 40–300 ns and current densities up to 1.5×10^8 A/cm^2. The experimental results were interpreted on the basis of magnetohydrodynamical simulation with various metal conductivity models. A comparison of the experimental and numerical results allows the conclusion to be drawn that the metal conductivity models used in this work are adequate. *© 2004 MAIK “Nauka/Interperiodica”.*

INTRODUCTION

Wire electrical explosion (WEE) has drawn the attention of researchers for a long time [1]. On the one hand, WEE is of interest as an object of basic research, because the thermodynamic parameters in the exploding wire substance reach their extreme values. On the other hand, exploding wires are widely used in various technical applications, e.g., for sharpening electrical power in a high-voltage pulse technique [2]; for preparing nanopowders [3]; and as high-power sources of soft X-rays in multiwire liners [4, 5]. Traditionally, the WEE process is simulated using magnetohydrodynamic (MHD) approximation. Numerical calculations in this approximation require preliminary knowledge of the equations of state (EOS's) for a substance over a wide range of thermodynamic parameters, as well as knowledge of the transport coefficients, of which the electrical conductivity is the most important. Whereas the thermodynamic properties of metals can be described by a variety of semiempirical models and using various databases, the problems associated with the transport coefficients in the region of metal–insulator transition and in the vicinity of the critical point are less well understood. On the one hand, the WEE experiments and the MHD simulation of explosion provide information about the conductivity of a substance of interest and, on the other, they allow one to judge the adequacy of a particular conductivity model. From this point of view, of greatest interest is the WEE in a liquid dielectric, in particular, in water, rather than in vacuum, where WEE is accompanied by such phenomena as stratification, gas desorption from wire surface, etc., which are not directly related to the transport properties of a conductor [6].

As is known [2], at the initial (heating) WEE stage, the parameters of a metal substance move along the liquid branch of a binodal, i.e., along the boundary between the condensed and two-phase (vapor–liquid mixture) states. As for the wire explosion, it happens in the vicinity of a critical point, i.e., a point where distinction between the liquid and gas phases disappears. For this reason, knowledge of the dependence of metal conductivity near the critical point on the energy input rate into the wire substance is of prime importance in the WEE simulation. Indeed, the substance in this two-phase region of the phase diagram is a mixture of vapor and the drop fraction of liquid metal, while it is the energy input rate which determines the size of the drop fraction. Moreover, metal in this region can be in the metastable state, i.e., be a superheated liquid, whose conductivity may strongly differ from the conductivity of the vapor–drop mixture. The relaxation times in the transition of a superheated metal to the vapor–drop mixture lie in the range 1–10 ns. For this reason, we used the same conductivity models in the WEE simulation both for the microsecond current- growth regime, where the metastable metal states do not play any significant role, and for the nanosecond regime.

In this work, an electrical explosion of aluminum and tungsten wires in water was studied experimentally and numerically for different energy-input regimes and different current-growth times. The purpose of this work was to estimate the metal conductivity in the vicinity of the critical point. The experimental results were compared with the results of MHD simulation, which was carried out using different methods for the description of the thermophysical properties of the medium. Agreement between the experimental results and the results of MHD simulation of the microwire electrical explosion is taken as a criterion for the validity of the estimates obtained for metal conductivity near the critical point.

EXPERIMENTAL

Experiments were carried out with a current generator schematically illustrated in Fig. 1. It was an *LC* circuit consisting of a capacitor bank with capacity $C = 0.067$ μF assembled from IKCh-50-0.035 capacitors. The bank discharged into a load trough a controlled gas-filled gap and inductance *L*. The inductance *L* was a plug-in solenoid; in the experiments, it had either of two values 2.25 and 0.73 μH, allowing the wire explosion to be carried out in various current-growth regimes. The circuit resistances *R* in these two regimes were 0.47 and 0.35 Ω, respectively (without regard for the microwire resistance). The load unit was placed inside the generator operating chamber. Six rods with a diameter of 1 cm uniformly arranged along a circle of diameter 10 cm were used as a return wire. A rodlike return wire was chosen to minimize the stray capacitance of the load unit. The water resistivity in the experiments was no worse than 150 kΩ cm. After each shot, water was renewed, purified, and deionized.

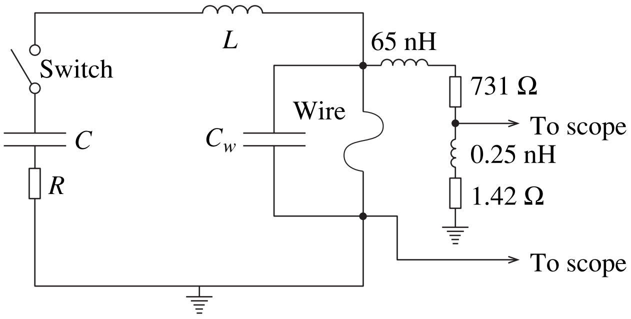

Fig. 1. Electric scheme of the experimental setup.

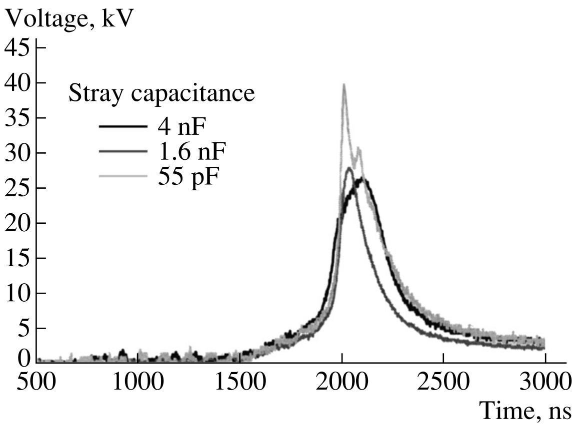

Fig. 2. Voltage oscillograms of wire explosions for different stray capacitances.

The following electrophysical diagnostics were used in the experiments: a high-ohmic divider, an inductance loop placed on the side of a high-voltage electrode (anode), and a shunt placed on the side of a grounded electrode (Fig. 1).

The load impedance is the sum of the microwire impedance consisting of the ac ohmic and inductive wire resistances and the reactance of the interelectrode-gap stray capacitance C_w. Upon an abrupt change in the bias on the gap, a portion of current goes to charging the stray capacitor. As a result, the time dependence of current measured on the side of high-voltage electrode differs from the time dependence of current measured on the grounded electrode. Since the voltage derivative at the instant of wire explosion can be very high, the presence of a stray capacitance of several picofarads can result in a considerable current loss and a decrease in the detected peak voltage. Such a measurement error may lead to an incorrect interpretation of the results obtained. We performed several test microwire explosions with different values of stray capacitance (Fig. 2). It becomes clear from the oscillograms shown in this figure that the gauge indications are related to the stray capacitance. In our experiments, the capacitance of the interelectrode gap was minimized to $C_w = 55$ pF. This value of stray capacitance was included in the scheme of the electric circuit used in our calculations.

MAGNETOHYDRODYNAMIC MODEL

The electrical explosion process was simulated within the framework of a single-temperature magnetohydrodynamic approximation. For the cylindrical geometry, the MHD equations have the form

$$\frac{d\rho}{dt} + \frac{\rho}{r}\frac{\partial v}{\partial r} = 0; \qquad (1)$$

$$\rho\frac{dv}{dt} = -\frac{\partial \rho}{\partial r} - j_z B_\varphi; \qquad (2)$$

$$\rho\frac{d\varepsilon}{dt} = -\frac{p}{r}\frac{\partial v}{\partial r} + \frac{j_z^2}{\sigma} + \frac{1}{r}\frac{\partial}{\partial r}\left(\kappa\frac{\partial T}{\partial r}\right); \qquad (3)$$

$$\frac{1}{c}\frac{\partial B_\varphi}{\partial t} = \frac{\partial E_z}{\partial r}; \quad j_z = \frac{c}{4\pi r}\frac{\partial (rB_\varphi)}{\partial r}; \qquad (4)$$

$$j_z = \sigma E_z; \qquad (5)$$

$$\varepsilon = f(\rho, T); \quad p = f(\rho, T), \tag{6}$$

where

$$\frac{d}{dt} = \frac{\partial}{\partial t} + v\frac{\partial}{\partial r}$$

is the substantial derivative; ρ and T are the substance density and temperature, respectively; v is the velocity radial component; p and ε are the pressure and the internal energy, respectively; B_φ is the azimuthal component of magnetic field; E_z is the axial component of electric field; j_z is the axial component of current density; and κ and σ are the thermal conductivity coefficient and the conductivity, respectively.

Equations (1)–(6) were solved numerically using a one-dimensional MHD code [7] written in the Lagrange coordinates. With this code, hydrodynamical Eqs. (1)–(3) were solved using the explicit difference scheme “cross” [8] with a combined pseudoviscosity (linear and quadratic) introduced for the calculation of shock waves. Maxwell Eqs. (4) complemented by Ohm’s law (5) and the heat conduction equation were solved using implicit difference schemes based on the data-flow sweep method [9]. In the numerical simulation of the WEE in water, the computational grid consisted of two regions: the conducting substance and water. It was assumed that the water conductivity is zero, so that the current flows only in metal, while the shock wave propagates in water.

The boundary condition for the Maxwell equations was written as

$$B_\varphi(R) = \frac{2I_n}{cR}, \tag{7}$$

where R is the wire outer radius and I_n is the current flowing through the wire.

The current flowing through the wire was determined from the joint solution to the Maxwell equations and the system of equations of electric circuit presented in Fig. 1. The stray capacitance in the electric circuit was also taken into account.

The system of MHD equations is closed by the EOS (6) for the substance. The wide-range EOS’s [10, 11] obtained on the basis of a semiempirical model [10] were used for metal. The EOS model [10] allows for the high-temperature melting and evaporation effects, and the special form [1] of the EOS tables can take into account the metastable states of the liquid and gas phases on the phase diagram. The EOS’s were used for water [12].

The electrical conductivity of aluminum was calculated by two methods. In the first of them, it was determined from the conductivity tables [13] compiled by M. Desjarlais at the Sandia National Laboratories (USA) on the basis of the model [14] modified with allowance for the experimental data. In the second method, the conductivity was determined by the combined computational and experimental procedure [15], in which the conductivity is considered as a certain empirical function of the density and specific energy deposited in a substance. With this method, the conductivity parametrically depends on the particular form of the EOS.

The conductivity tables in this method are constructed using the following initial data: (1) the tabulated normal-density dependence $\sigma_1(T, \delta = 1)$ and (2) the conductivity in the gas–plasma region calculated by the classical formulas [16]. In the transition region near the critical point, the conductivity is taken in the parametric form [15], which we have modified by the introduction of a new parameter γ that was set equal to unity in [15]:

$$\log\frac{\sigma(T, \delta)}{\sigma_1(T, \delta = 1)} = \Phi(T, \delta)\log\frac{\sigma_{\rm cr}}{\sigma_1}\left(\frac{\log\delta}{\log\delta_{\rm cr}}\right)^\gamma, \tag{8}$$

where $\sigma_{\rm cr}$ is the conductivity at the critical point; $\delta = \rho/\rho_0$ is the relative density of the substance; ρ_0 is its normal density; $\delta_{\rm cr}$ is the relative density at the critical point; and $\Phi(T, \delta)$ is a function, on the order of unity, depending on the position of the interface in a mixture of phases.

When constructing the conductivity tables, the value of $\sigma_{\rm cr}$ is a variable parameter, and it is assumed to be independent of temperature. The critical conductivity is chosen in such a way as to provide the best agreement between the results of MHD simulation and the totality of experimental data.

A comparison of the tables of aluminum conductivity [13] with the corresponding tables constructed using the procedure in [15] demonstrates a good agreement between them, both qualitative and quantitative. Since we lacked data on the electrical conductivity of tungsten like those for aluminum in [13], the MHD calculations were carried out using tables constructed by the computational and experimental procedure described in [15]. In this case, the value of parameter γ was chosen to be 2.2, in contrast to aluminum, for which we took $\gamma = 1$, as in [15].

COMPARISON AND DISCUSSION OF THE EXPERIMENTAL AND COMPUTATIONAL RESULTS

The experiments on electrical explosion and the MHD calculations were carried out for aluminum and tungsten microwires of different diameter. In the experiments, the current through the wire and the voltage on the wire were measured; the same quantities were calculated in the numerical simulation of electrical explosion. The current through the load unit was also calculated as the sum of the current through the wire and the displacement current flowing through the water stray capacitance. The comparison of the computational and experimental time dependences of current and voltage

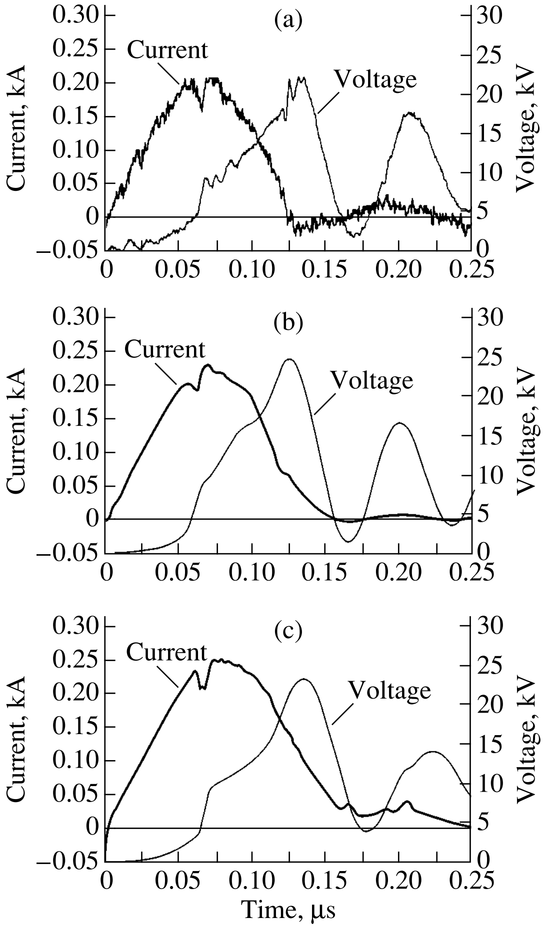

Fig. 3. (a) Experimental and (b, c) calculated time dependences of current and voltage for the explosion of aluminum wire in the regime $L = 2.25$ μH and $U_0 = 10$ kV. Calculations with the electrical conductivity from (b) [13] and (c) [15].

suggests that the conductivity models and the EOS used in the calculations were adequate.

In Fig. 3a, the experimental oscillograms of the current through the sample and the voltage on it are presented for the explosion of an aluminum wire 15 μm in diameter and 2.6 cm in length in a circuit with parameters $L = 2.25$ μH and $U_0 = 10$ kV. One can see in this figure that the current through the wire drops virtually to zero almost immediately after the voltage maximum. In other words, the discharge channel disappears. The oscillations detected by the current and voltage gauges are caused by the recharging of the stray capacitance C_w. The calculated time dependences of the current through the microwire and the voltage on the interelectrode gap are shown in Fig. 3b. For this case, the calculations were carried out using the EOS from [10] and conductivity tables from [13]. One can see in this figure that the experimental and calculated curves coincide well with each other. Both the instants of explosion and the voltage amplitudes coincide. In addition, the instant of wire melting is seen at ~60 ns in both figures. The voltage maxima after the explosion are caused by the recharging of the stray capacitance C_w.

The current and voltage time dependences calculated for the same regime using the EOS from [10] and the conductivity tables constructed by the procedure [15] are shown in Fig. 3c. One can see from a comparison of Figs. 3a and 3c that the agreement between the experimental and calculated curves is good in this case as well. As in the case with the use of the conductivity tables from [13], the instant of explosion and the voltage amplitude are described here with rather good accuracy. This is caused by the fact that both the character of the change in metal conductivity and its absolute value in models [13] and [15] approximately coincide in the time interval from the condensed state to the critical density. For example, the aluminum critical conductivity determined using the procedure [15] is $\sigma_{cr} = 2.8 \times 10^3\ \Omega^{-1}\ \text{cm}^{-1}$. The difference between this value and the values of conductivity in table [13] does not exceed 40% in the temperature range from room to ~3 eV (which is almost fivefold higher than the critical temperature). At higher temperatures, the discrepancy is greater, and, at temperatures on the order of 100 eV, the critical conductivity acquires a plasma character. However, for wire explosions in the region of near-critical densities, temperatures as high as those are not achieved.

Notice that the calculations were carried out both with and without allowance for the possible occurrence of the metastable metal states. However, the inclusion of such states had only a small effect on the current–voltage characteristics of the wire electrical explosion. The distinction between the results proved to be equal to tenths of one percent (the experimental accuracy was appreciably worse). The effect of liquid-phase superheating on the density distribution along the wire radius proved to be considerably stronger, as was already pointed out in [11].

The experimental data and their comparison with the calculations are summarized in Table 1. The five-shot-averaged values of maximal current, maximal voltage, and the explosion time measured as the time interval from zero to the voltage maximum are given in the table. The calculations were carried out with the values of conductivity obtained using the computational and experimental procedure [15]. One can see that the error of calculation comprises about 20% over a rather wide range of parameters.

When simulating the electrical explosion of tungsten wires, we used the conductivity tables constructed by procedure [15]. The tungsten critical parameters are appreciably different from those of aluminum. For instance, $\rho_{cr} = 4.85$ g/cm^3 and $T_{cr} = 1.36$ eV for tungsten and $\rho_{cr} = 0.64$ g/cm^3 and $T_{cr} = 0.67$ eV for aluminum. At the same time, the critical conductivities of these substances differ only slightly; for tungsten, $\sigma_{cr} = 2.6 \times 10^3\ \Omega^{-1}\ \text{cm}^{-1}$.

Table 1. Comparison of the experimental and calculated parameters for the explosion of aluminum wires with a diameter of 15 μm and a length of 2.6 cm

Inductance, nH	Charging voltage, kV	Explosion time, ns		Explosion voltage, kV		Maximal current, A	
		experiment	calculation	experiment	calculation	experiment	calculation
2251	10		124	20.7	24.7	200	230
2251	20	80	81	42	54.8	273	305
730	20	48	45.1	28.9	39	383	450

Table 2. Comparison of the experimental and calculated parameters for the explosion of tungsten wires with a diameter of 30 μm and a length of 2 cm

Inductance, nH	Charging voltage, kV	Explosion time, ns		Explosion voltage, kV		Maximal current, A	
		experiment	calculation	experiment	calculation	experiment	calculation
2251	10	471	434	15.5	12	417	482
2251	20	239	230	33.3	37.3	607	671
2251	30	167	175	44	60	805	853
730	10	369	389	10.8	10.1	541	646
730	20	169	160	26.5	25.6	735	832
730	30	113	105	41	51	970	1100

In Fig. 4a, the oscillograms of the current through the wire and the voltage on it in the explosion regime are shown for a tungsten wire with a diameter of 30 μm and a length of 2 cm in a circuit with $L = 0.73$ μH and $U_0 = 20$ kV. The corresponding calculated time dependences are shown in Fig. 4b. The agreement between the experimental and calculated curves in the case of tungsten wires is seen to be somewhat worse than for aluminum. In particular, the first maximum corresponding to metal melting is more pronounced in the calculated voltage curve than in the experimental curve. However, the absolute value and the time of the second maximum, which we assign to the instant of explosion, coincide rather well. At the instant of explosion, the resistance increases drastically, and the thermodynamic parameters of the wire substance are close to their values at the critical point; i.e., the temperature is 1–1.5 eV and the density is 2–6 g/cm^3.

The experimental data on the explosion of tungsten wires and the comparison with the corresponding calculations are summarized in Table 2. As before, five shots were made for each set of parameters. The calculations were carried out with the conductivities obtained by the computational and experimental procedure [15]. One can see that the error of calculation is no worse than for aluminum and does not exceed 20% over a rather wide range of parameters.

To check the applicability of the tables of tungsten conductivity for the description of wire explosions in the microsecond current-growth regime, the explosion of tungsten wire was simulated for the experimental conditions described in [17]. In those experiments, the current generator was also an LC circuit with parameters $C = 6$ μF, $L = 4.5$ μH, and $U_0 = 20$ kV. The wires were 0.35 mm in diameter and 8.7 cm in length, and they were also exploded in water. The results of the simulation are presented in Fig. 5. The solid curves are for the calculated time dependences of current and voltage, and the marks are the experimental values of these

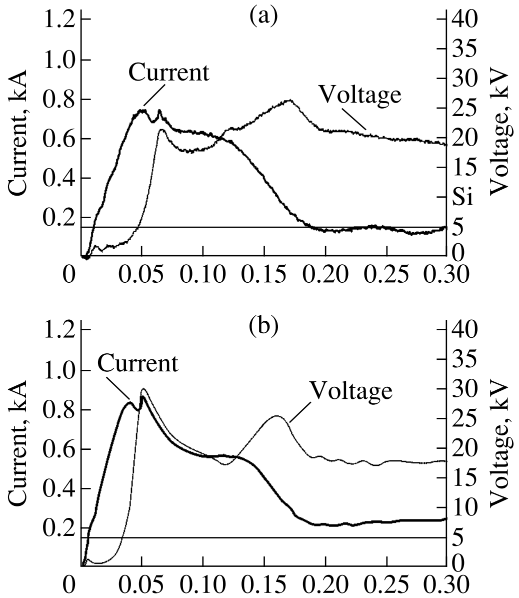

Fig. 4. (a) Experimental and (b) calculated time dependences of current and voltage for the explosion of tungsten wire in the regime $L = 0.73$ μH and $U_0 = 20$ kV.

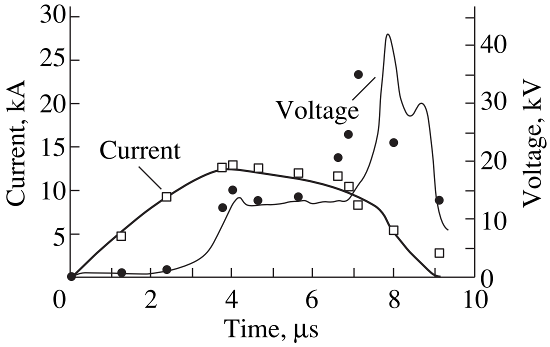

Fig. 5. Experimental (□ current, ● voltage) and calculated (solid lines) time dependences of current and voltage for the microsecond explosion of tungsten wire.

quantities. One can see that, although the tables of tungsten conductivity were constructed on the basis of the experiments on wire explosion in the nanosecond current-growth regimes, they satisfactorily describe wire electrical explosion in regimes with current-growth times longer by almost three orders of magnitude. The calculated curves coincide well with the experimental ones both in explosion time and in voltage amplitude; the discrepancy between the calculated and experimental quantities is less than 10%. This is evidence that the tungsten conductivity in the electrical explosion is independent of the rate of energy input into the substance.

CONCLUSIONS

Thus, a wire electrical explosion in water can be described rather well within the framework of magnetic hydrodynamics. The experimental data on WEE in liquid dielectrics are the source of information on the metal conductivity near the critical point. The coincidence of the experimental data with the results of MHD simulation of the WEEs with substantially different current-growth times suggests that metal conductivity near the critical point is a function of the state of the substance (temperature and density) and is independent of the energy-input rate.

ACKNOWLEDGMENTS

We are grateful to M. Desjarlais for providing the tables of aluminum conductivity and to N.A. Ratakhin and S.I. Tkachenko for discussions. This work was supported by the ISTC (grant no. 1826) and RFBR (grant no. 04-02-17292).

REFERENCES

1. *Exploding Wires*, Ed. by W. G. Chace and H. K. Moore (Plenum, New York, 1959; Mir, Moscow, 1965).
2. V. A. Burtsev, N. V. Kalinin, and A. V. Luchinskiĭ, *Electric Explosion in Conductors and Its Electrophysical Applications* (Énergoatomizdat, Moscow, 1990).
3. V. S. Sedoy, G. A. Mesyats, V. I. Oreshkin, *et al.*, IEEE Trans. Plasma Sci. **27**, 845 (1999).
4. S. A. Pikuz, T. A. Shelkovenko, J. B. Greenly, *et al.*, Phys. Rev. Lett. **83**, 4313 (1999).
5. R. B. Spielman, C. Deeney, G. A. Chandler, *et al.*, Phys. Plasmas **5**, 2105 (1998).
6. A. M. DeSilva and J. D. Katsouros, Phys. Rev. E **57**, 5945 (1998).
7. V. I. Oreshkin, V. S. Sedoĭ, and L. I. Chemezova, Prikl. Fiz., No. 3 (2001).
8. N. N. Kalitkin, *Numerical Methods* (Nauka, Moscow, 1978).
9. A. A. Samarskiĭ and Yu. P. Popov, *Difference Schemes in Gas Dynamics* (Nauka, Moscow, 1975).
10. A. V. Bushman and V. E. Fortov, Sov. Technol. Rev. B **1**, 219 (1987).
11. S. I. Tkachenko, K. V. Khishchenko, V. S. Vorob’ev, *et al.*, Teplofiz. Vys. Temp. **39**, 728 (2001) [High Temp. **39**, 674 (2001)].
12. A. T. Sapozhnikov, G. V. Kovalenko, P. D. Gershchuk, *et al.*, Vopr. At. Nauki Tekh., Ser.: Mat. Model. Fiz. Protsessov, No. 2, 15 (1991).
13. M. P. Desjarlais, Contrib. Plasma Phys. **41**, 267 (2001).
14. Y. T. Lee and R. M. More, Phys. Fluids **27**, 1273 (1984).
15. Yu. D. Bakulin, V. F. Kuropatenko, and A. V. Luchinskiĭ, Zh. Tekh. Fiz. **46**, 1963 (1976) [Sov. Phys. Tech. Phys. **21**, 1144 (1976)].
16. N. N. Kalitkin, Preprint No. 85, IPM (Institute of Applied Mathematics, Moscow, 1978).
17. N. I. Kuskova, S. I. Tkachenko, and S. V. Koval, J. Phys.: Condens. Matter **9**, 6175 (1997).

Translated by V. Sakun

Technical Physics, Vol. 49, No. 7, 2004, pp. 849–857. Translated from Zhurnal Tekhnicheskoĭ Fiziki, Vol. 74, No. 7, 2004, pp. 44–51.
Original Russian Text Copyright © 2004 by Bogdanov, Kudryavtsev, Tsendin, Arslanbekov, Kolobov.

GAS DISCHARGES, PLASMA

Nonlocal Phenomena in the Positive Column of a Medium-Pressure Glow Discharge

E. A. Bogdanov*, A. A. Kudryavtsev*, L. D. Tsendin,**
R. R. Arslanbekov*, and V. I. Kolobov*****
** St. Petersburg State University, St. Petersburg, 198504 Russia*
e-mail: akud@ak2138.spb.edu
*** St. Petersburg State Polytechnic University, St. Petersburg, 195251 Russia*
**** CFD Research Corp., 215 Wynn Drive, Huntsville, AL, USA*

Received December 25, 2003

Abstract—Commercial CFDRC software (http://www.cfdrc.com/~cfdplasma) is used to self-consistently simulate the plasma of the positive column (PC) of a medium-pressure dc discharge in argon. The software allows simulations in an arbitrary 3D geometry by using Poisson's equation for the electric potential and fluid equations for the heavy components and by solving a nonlocal kinetic equation for electrons. It is shown that, in calculating the electron distribution function, the local approximation is almost always inapplicable not only at relatively low pressures ($pR < 1$ cm Torr), but also at relatively high pressures ($pR < 10$ cm Torr), i.e., under the real conditions of a diffuse PC usually met in practice. The use of the local approximation in solving the kinetic equation for electrons leads to significant errors in determining the main parameters of the PC. A paradoxical effect has been revealed: the peaks of the profiles of the excitation rates shift from the discharge axis toward the periphery as the pressure increases from low to medium values (1 cm Torr < pR < 10 cm Torr). It is shown that the effect is related to the nonlocal character of the electron distribution function. *© 2004 MAIK "Nauka/Interperiodica".*

When simulating gas-discharge plasma with the help of, e.g., a Bolsig package [1] or the Lookup Tables technique [2], the electron distribution function (EDF) is usually calculated in the local approximation. This means that terms with both spatial gradients and a radial field are omitted in the kinetic equation and the EDF is factorized as

$$f_0(w, r) = n_e(r) f_0^0(w, E/p). \tag{1}$$

In this approximation, the electron distribution over the kinetic energy w at a fixed point r depends on the local values of the reduced longitudinal field E/p and other parameters (the gas temperature, the density of excited particles, etc.). This method is applicable if the characteristic diffusion length, which is equal to $R/2.4$ for a cylindrical discharge, exceeds the electron energy relaxation length λ_ε ($R/2/4 \gg \lambda_\varepsilon$) [3]. When terms with spatial gradients cannot be omitted in the kinetic equation, the EDF is referred to as a nonlocal EDF [3, 4], because it depends on the values of the physical parameters (primarily, the field strength) in the region defined by the inequality $\lambda_\varepsilon \gg \lambda$ (where λ is the electron mean free path) rather than on their values in a given point. In terms of the total energy

$$\varepsilon = w + e\varphi(r) = mV^2/2 + e\varphi(r) \tag{2}$$

(the kinetic energy plus the potential energy), the nonlocal EDF can be either dependent on or independent of the radius [3, 4] (cf., e.g., [5, 6], where the concept of a nonlocal EDF was considered in a narrower sense and only the functions $f_0(\varepsilon, r)$ that were independent of the radius were referred to as nonlocal EDFs).

For $\lambda_\varepsilon > R/2.4$, the use of the local model in calculating the EDF is not justified [3] and, as was demonstrated in [7, 8], leads to crude errors in determining the parameters of the positive column (PC) of a low-pressure ($pR \leq 1$ cm Torr) glow discharge. It was shown in [4] that the local approximation is almost always inapplicable up to relatively high pressures ($pR \leq 10$ cm Torr), i.e., under the real conditions of a diffuse PC usually met in practice. In this context, we recall that in calculations it is desirable to use computational elements that are known with equal accuracy, because the reliability of self-consistent models is restricted by a "bottleneck," i.e., by the most uncertain element of the model. Therefore, even if the most advanced and reliable methods are used in some computational blocks of a code, whereas its other elements are known poorly (or insufficiently), the use of these methods does not enhance the accuracy of the results obtained. In particular, this means that it is necessary to carefully verify the applicability of the local approximation when determining the parameters of a gas-discharge plasma not only at low but also at medium pressures.

In this paper, we continue the studies begun in [4]. We consider the influence of the nonlocal character of

1063-7842/04/4907-0849$26.00 © 2004 MAIK "Nauka/Interperiodica"

Table 1. The set of reactions used for the three-level scheme of terms of an argon atom

#	Reaction	ε, eV	Constant	Commentary
1	$e + \mathrm{Ar} \longrightarrow e + \mathrm{Ar}$	–	Cross section [14]	Elastic scattering (momentum transfer)
2	$e + \mathrm{Ar} \rightleftarrows e + \mathrm{Ar}_m^*$	11.55	Cross section [16]	Excitation and deexcitation of the metastable level
3	$e + \mathrm{Ar} \longrightarrow 2e + \mathrm{Ar}^+$	15.9	Cross section [14]	Direct ionization from the ground state
4	$e + \mathrm{Ar}_m^* \longrightarrow 2e + \mathrm{Ar}^+$	4.35	Cross section [16]	Step ionization from the metastable level
5	$e + \mathrm{Ar}_m^* \longrightarrow e + \mathrm{Ar}_r^*$	0.07	$k_q = 2 \times 10^{-13}$ m^3 s^{-1} [17]	Quenching of the metastable level via the transition to the resonance level (11.67 eV)
6	$e + \mathrm{Ar} \longrightarrow e + \mathrm{Ar}$	11.55	Cross section [14]	Total excitation by electron impact
7	$\mathrm{Ar}_r^* \longrightarrow \mathrm{Ar} + \hbar\nu$	–	$A_R = 10^5$ s^{-1}	Resonance emission with allowance for self-absorption (λ = 106.4 nm)
8	$2\mathrm{Ar}_m^* \longrightarrow \begin{cases} e + \mathrm{Ar}^+ + \mathrm{Ar} \\ e + \mathrm{Ar}_2^+ + \mathrm{Ar} \end{cases}$	–	$k_p = 6.2 \times 10^{-16}$ m^3 s^{-1} [17]	Penning ionization

the EDF on the parameters of the PC of a medium-pressure (1 cm Torr ≤ pR ≤ 10 cm Torr) dc discharge. It is shown that the application of the local model to solving the kinetic equation for electrons leads to significant errors in determining the main parameters of the PC. A paradoxical effect related to the nonlocal character of the EDF is revealed: the peaks of the profiles of the excitation rates shift from the discharge axis toward the periphery as the pressure increases. The object of our studies was the plasma of the PC of a dc discharge in argon.

The parameters of the PC were calculated with the help of commercial software developed in the CFD Research Corporation, Huntsville, AL, USA [2, 9]. As was shown in [4], the results obtained with the CFDRC code agree well with test calculations, and the code can be used for comprehensive self-consistent simulations. A detailed description of the self-consistent model of a discharge plasma, the iteration numerical scheme, and the methods for solving the set of equations is given in [2, 9]. The self-consistent electric field was found from Poisson's equation. Heavy particles were described in the fluid model. The nonlocal EDF was determined by solving the kinetic equation for electrons in a uniform longitudinal field and a nonuniform transverse field with allowance for the radial inhomogeneity of the plasma (we recall that the EDF in the calculation of which terms with spatial gradients in the kinetic equation play an important role is here referred to as nonlocal). For comparison, we could also solve the kinetic equation in the conventional local approximation, in which the radial electric field and the radial gradients in the kinetic equation were ignored.

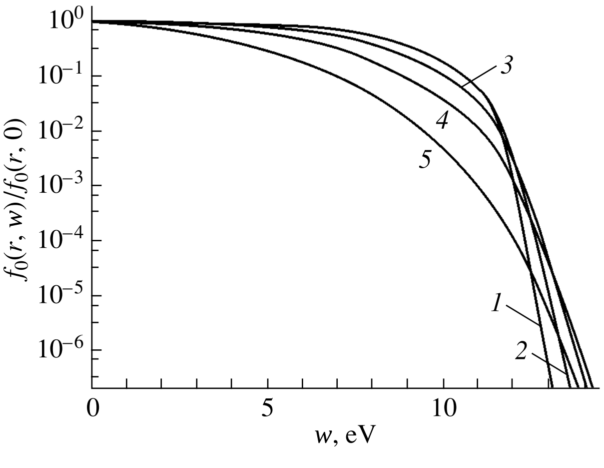

Fig. 1. Normalized EDFs $f_0(w, r)$ at different radii r as functions of the kinetic energy w: r = (*1*) 0, (*2*) 0.2R, (*3*) 0.4R, (*4*) 0.6R, and (*5*) 0.8R.

In the first stage, we performed self-consistent simulations of a PC in a tube of radius R = 1 cm at p = 6 Torr. We used a three-level model of an argon atom with one metastable state (index m), taking into account the eight main reactions listed in Table 1. The constants of the processes with the participation of electrons were calculated by convoluting the corresponding cross sections with the calculated EDF.

It can be seen from Fig. 1 that, even at a relatively high pressure, the EDF $f_0(w, r)$ is not factorized in form (1): the normalized EDF plotted as a function of the kinetic energy is different at different radii r; i.e., it is nonlocal. At the same time, the EDFs $f_0(\varepsilon, r)$ plotted as functions of total energy (2) at different radii coincide at $\varepsilon < \varepsilon^*$ (where ε^* is the threshold energy for inelastic processes), without any shift related to normalization and the spatial dependence of the potential; however, they differ in the inelastic energy range $\varepsilon > \varepsilon^*$ (Fig. 2). It is well known that, in practice, the fact that the EDF

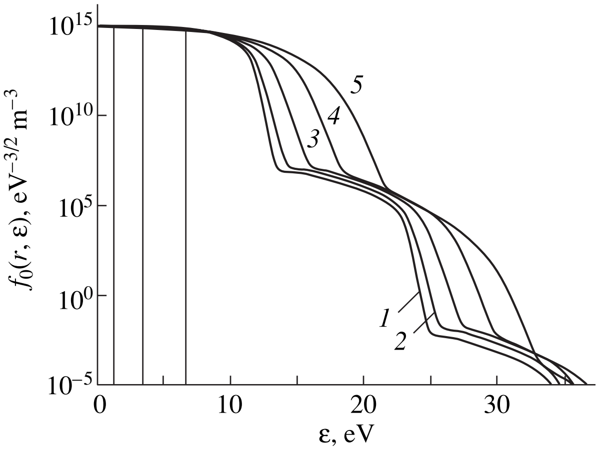

Fig. 2. EDFs $f_0(\varepsilon, r)$ at different radii r as functions of the total energy ε: r = (*1*) 0, (*2*) 0.2R, (*3*) 0.4R, (*4*) 0.6R, and (*5*) 0.8R.

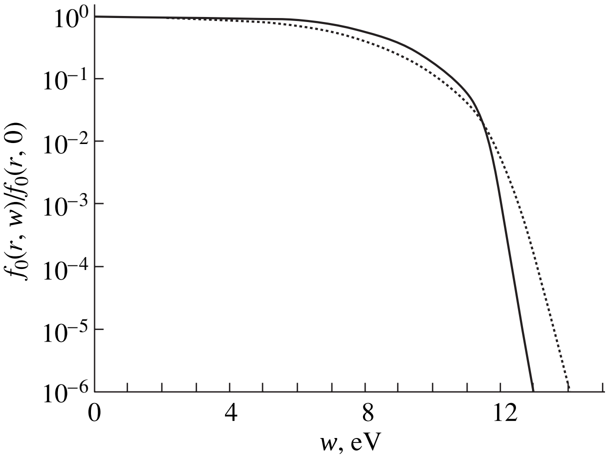

Fig. 3. Comparison of the EDF at the discharge axis ($r = 0$) with calculations in the local model (the dashed line).

$f_0(\varepsilon, r)$ of trapped electrons with $\varepsilon \le e\Phi_w$ (where Φ_w is the wall potential) does not depend on the radius clearly indicates the nonlocal character of the EDF [3] (in contrast, the EDF of transit electrons with $\varepsilon > e\Phi_w$ depends on the radius). A comparison of the calculated EDF with the results of the local model shows that the local approximation gives a significant error (Fig. 3). Note also that, the population of the fast component of the EDF is substantially enhanced due to impacts of the second kind (superelastic collisions) with metastable atoms, because a slow electron participating in the reaction $Ar^* + e \longrightarrow Ar + e$ additionally acquires the threshold excitation energy ε^* and instantaneously becomes fast. These processes substantially influence the calculated values of the constants for the excitation reactions with high threshold energies and, accordingly, the densities of highly excited states (see [4] for details). To illustrate this effect, Fig. 2 shows a wider range of f_0 and ε as compared to Figs. 1 and 3. As was shown in [4] and also can be seen from Fig. 2, the fast components of the EDF ($\varepsilon > \varepsilon^*$) can be represented as a sum $f_0 = f_{0t} + f_{0h}$. If the density n_m of metastable atoms is high enough, then the part of the EDF that corresponds to $n_m = 0$ and sharply decreases at energies above the threshold energy ($\varepsilon > \varepsilon^*$),

$$f_{0t}(\varepsilon) \simeq c_{nt}\exp(-\varepsilon/T^*), \tag{3}$$

is supplemented with a gently sloping pedestal

$$f_{0h}(\varepsilon) \simeq \frac{n_m g_a}{N_0 g_m} f_0(\varepsilon - \varepsilon^*), \tag{4}$$

replicating the shape of the slow component (the body) of the EDF (here, N_0 is the density of atoms in the ground state). Because of the low effective temperature of the fast electrons,

$$T^* = \sqrt{\nu^*/D_E}, \tag{5}$$

where $D_E = 2(eE\lambda)^2\nu/3$ is the coefficient of diffusion over energy in the electric field (see, e.g., [9, 10], for details), the EDF f_{0t} (3) falls rapidly at higher energies and, as early as at energies of a few electronvolts above the threshold ε^*, it is considerably less than the EDF f_{0h} (4) (Fig. 2). Since f_{0h} is proportional to n_m/N_0 and its energy dependence is close to that of the EDF of slow electrons ($\varepsilon < \varepsilon^*$), the spatial profiles of the frequencies and rates of the processes that are determined by these parts of the EDF can also be close to one another. This is illustrated by Fig. 4. It can be seen that the spatial profile of the direct-ionization frequency

$$\nu_{i\mathrm{dir}} = \int_{\varepsilon_i}^{\infty} \nu_{i\mathrm{dir}}(w) f_0(w)\sqrt{w}\,dw$$

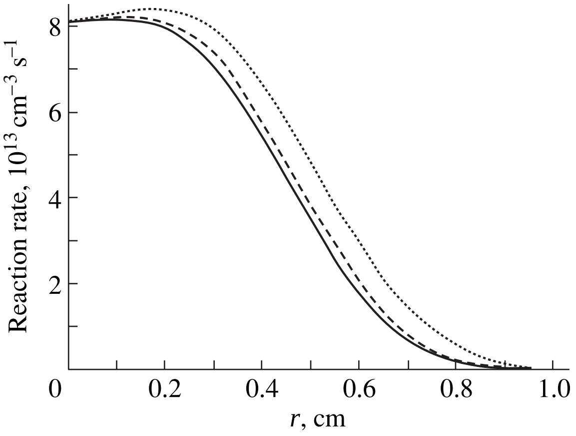

Fig. 4. Radial profiles of the direct and step ionization rates (the corresponding curves coincide). The dotted curve shows the density profile of high-energy ($w \ge 16$ eV) electrons, and the dashed line shows the $n_m(r)n_e(r)$ profile (in arbitrary units). The step ionization rate is plotted in absolute units, whereas the direct ionization rate is multiplied by 780 to bring the plots into coincidence.

almost coincides with the profile of the step-ionization rate

$$n_m\nu_{st} = n_m\int_{\varepsilon_{st}}^{\infty}\nu_{st}(w)f_0(w)\sqrt{w}dw,$$

in spite of the large difference in the thresholds ($\varepsilon_i = 15.76$ eV and $\varepsilon_{st} = 4.35$ eV, respectively). We emphasize that this result is a consequence of the self-consistent simulation of a discharge. In this case, the frequency of direct ionization ($\mathrm{Ar} + e \longrightarrow \mathrm{Ar}^+ + e + e$) is governed by EDF component (4), which is formed by impacts of the second kind. For this reason, the $\nu_{idir}(r)$ profile is similar to the $n_m(r)\nu_{st}(r)$ profile, although the step-ionization and direct-ionization processes themselves are unrelated. Accordingly, the density of the fast electrons with energies $w > \varepsilon_i$ (it is these electrons that produce direct ionization),

$$n_{ef}(\varepsilon_i) = \int_{\varepsilon_i}^{\infty}f_0(w)\sqrt{w}dw,$$

is governed by the EDF that is described by Eq. (4) and is proportional to $n_m(r)n_e(r)$ (Fig. 4).

The data presented in Figs. 1–3 show that the local approximation is inapplicable to calculating the EDF even at relatively high pressures ($pR = 6$ cm Torr); i.e., it is almost always inapplicable under the real conditions of a diffuse PC usually met in practice. We note that, the applicability of the local approximation at medium pressures has not previously been examined in detail. The consideration was usually restricted to the case of low pressures ($pR \le 1$ cm Torr) [5–8], where the electron energy balance was governed by inelastic collisions. In this case, the electron energy relaxation length is equal to several electron mean free paths, so that the inequality $\lambda_\varepsilon \gg R/2.4$ holds only for $pR \le 1$ cm Torr. It will be shown below that the applicability limit of the local approximation corresponds to pR values that are one order of magnitude higher.

To explain the results obtained and to refine the criteria for the applicability of the local model, we recall the specific features of the EDF formation in a plasma that is bounded in the direction transverse to the external current (see [3, 11, 12] for details). It is well known that, in this case, the situation depends largely on the type of collisions that govern the electron energy balance. These may be elastic (quasi-elastic) collisions, in which one collision event results in a small energy loss (in atomic gases, $\delta = 2m/M$), or inelastic collisions, in which an electron instantaneously loses almost all of its energy ($\sim\varepsilon^*$) [3]. The role these processes play in the total electron energy balance depends on the value of the longitudinal heating field E/p, supplying energy to electrons. At a given pressure and geometry, this field cannot be specified arbitrarily but should be found from the condition that a discharge is steady:

$$\nu_i\tau_a = 1, \tag{6}$$

where ν_i is the ionization frequency and τ_a is the characteristic time of ambipolar diffusion.

Since the diffusive losses of electrons and ions depend on the parameter pR, the field E/p, determining the rate of the ionization process, also depends on this parameter [3, 4]. In other words, the field in a plasma is always equal to that required to maintain this plasma. It follows from Eq. (6) that, as the pressure (the parameter pR) increases, the increase in the characteristic time of diffusive losses τ_a leads to a decrease in the ionization rate. Consequently, the value of E/p should decrease, which is confirmed by many experiments and calculations [13].

The kinetic equation for an axially uniform PC in the case of rare electron–electron collisions is a two-dimensional diffusion equation with the radial diffusion coefficient $D_r = \lambda V/3$, the coefficient of diffusion over energy $D_E = (eE)^2D_r)$, and the dynamic friction $V_{ea} = w\delta\nu$ due to quasi-elastic collisions [3]:

$$\begin{gathered}\frac{1}{r}\frac{\partial}{\partial r}\left(r\sqrt{w}D_r\frac{\partial f_0}{\partial r}\right)+\frac{\partial}{\partial\varepsilon}\left(\sqrt{w}\left(D_E\frac{\partial f_0}{\partial\varepsilon}+V_{ea.}f_0\right)\right)\\ = \nu^*(w)\sqrt{w}f_0(\varepsilon)-\sum_k\nu_k(w+\varepsilon_k)\sqrt{w+\varepsilon_k}f_0(\varepsilon+\varepsilon_k)\\ -\frac{n_mg_a\nu_{ex}(w)\sqrt{w}}{N_0g_m}f_0(\varepsilon-\varepsilon^*).\end{gathered}\tag{7}$$

The right-hand side of Eq. (7) includes sources and sinks due to inelastic processes. Here, $\nu^* = \sum\nu_k$ is the total excitation frequency to all of the electronic states with energies ε_k, and ν_{ex} is the excitation frequency of the metastable level. For a low-pressure ($pR \le 1$ cm Torr) gas-discharge plasma, the fields given by Eq. (6) are such that the electron energy balance is usually determined by inelastic collisions. This means [11] that an electron diffuses relatively rapidly through the energy range $(0, \varepsilon^*)$, corresponding to the body of the EDF. The characteristic diffusion time is

$$\tau_E = 1/\nu_E = (\varepsilon^*)^2/D_E, \tag{8}$$

and the corresponding length is

$$\lambda_E = \sqrt{D_r\tau_E} = \varepsilon^*/(eE). \tag{9}$$

Over the time τ_E given by Eq. (8), quasi-elastic energy losses are small: $\tau_E < 1/(\delta\nu) = \tau_\varepsilon$. Electrons that gain energy from the field in the range $(0, \varepsilon^*)$ merely provide the required electron energy flux to the tail of the EDF; i.e., the EDF at $\varepsilon < \varepsilon^*$ acts merely as a peculiar kind of “pipeline” from a source in the low-energy region to a sink in the tail region $\varepsilon > \varepsilon^*$. Such a pipeline

EDF, introduced in [11], depends weakly on the field and is primarily determined by the energy dependence of the cross section for elastic collisions $\sigma(w)$ [3, 11]:

$$f_0(w) \simeq \mathrm{const}\int_w^{\varepsilon^*}\frac{dw}{D_E} \simeq \mathrm{const}\int_w^{\varepsilon^*}(\sigma(w)/w)dw. \quad (10)$$

In the energy range $\varepsilon > \varepsilon^*$, which corresponds to inelastic collisions, an electron has time to cover the distance

$$\lambda_\varepsilon^* \simeq \sqrt{D_r/\nu^*} \simeq \sqrt{\lambda\lambda^*} \simeq (3-10)\lambda \quad (11)$$

over its characteristic lifetime ~$1/\nu^*$ (here, λ^* is the electron mean free path in inelastic processes).

The length λ_ε^* depends on the ratio between the cross sections for elastic and inelastic processes ($\sigma/\sigma^* \simeq 10$–$100$) and is equal to several electron mean free paths.

Thus, the pipeline EDF determined by inelastic energy losses is characterized by two very different energy scales. The average energy $\langle\varepsilon\rangle$ of distribution (10) can be taken as the energy scale of the body of the EDF ($w < \varepsilon^*$). This energy is equal to a fraction of the first excitation energy ε^* and depends on the shape of the function $\sigma(w)$. In the tail region ($w > \varepsilon^*$), the EDF falls rapidly over energy scale (5): $T^* \ll \varepsilon^*$, so that the electrons with $w > \varepsilon^* + T^*$ are almost absent. These two energy scales correspond to the frequencies τ_ε^{-1} (8) and ν^* and the lengths λ_E (9) and λ_ε^* (11).

Because of the presence of two very different energy scales, the nonlocal character of the EDF manifests itself in different ways in its different parts [12]. For $\lambda_\varepsilon^* > R/2.4$, both the body and the tail of the EDF at $\varepsilon \le e\Phi_w$ depend on the total energy ε (2). However, for $\lambda_E > R/2.4 > \lambda_\varepsilon^*$, the body of the EDF is a function of ε, whereas the tail $\varepsilon > \varepsilon^*$ depends on both ε and r.

It follows from expression (11) that the EDF depends on the total energy ε only at low pressures ($pR < 1$ cm Torr), which agrees with the results of [5–8]. So, it might seem that, in the opposite case ($pR >$ 1 cm Torr), one can use the local approximation in calculating the EDF. However, as the pressure (the parameter pR) increases, the characteristic time of diffusive losses τ_a increases, while the ionization rate decreases (see Eq. (6)). The value of E/p in this case decreases, and the contribution from elastic collisions to the electron energy balance increases. If, during the characteristic time of diffusion over energy from 0 to ε^*, an electron loses all of its energy ($\delta\nu > \nu_E$), then elastic processes are dominant in the electron energy balance. In this case, the energy and spatial scales of the tail of the EDF are also given by Eqs. (5) and (11) and the time scale is $1/\nu^*$, whereas for the body of the EDF, the time scale is $\tau_\varepsilon = (\delta\nu)^{-1}$ and the spatial scale

$$\lambda_\varepsilon = \sqrt{D_r/(\delta\nu)} \simeq \lambda/\sqrt{\delta} > 100\lambda \quad (12)$$

is more than two orders of magnitude larger than the electron mean free path. In this case, the body of the EDF is determined by the balance between the heating of electrons in the electric field and elastic energy losses and is described by the Druyvesteyn–Davydov distribution [11, 13]

$$f_0(w) \sim c_n\exp\left(-\int_0^{-w}\frac{dw}{T(w)}\right) = c_n\exp\left(-\int_0^w\frac{3m\delta v^2}{(eE)^2}dw\right). \quad (13)$$

For this EDF, the diffusive flux over the energy (Joule heating) is almost completely balanced by the drift energy flux (opposite in sign to the diffusive flux) due to elastic electron–atom collisions, so that at $\varepsilon < \varepsilon^*$, the EDF falls exponentially over the characteristic energy scale $D_E/V_{ea} \simeq eE\lambda_\varepsilon$. The energy flux outflowing into the inelastic region is equal to the difference of these two large fluxes and is much smaller than each of them. The balance between Joule heating and elastic losses takes place almost throughout the energy range $(0, \varepsilon^*)$ except for a narrow region near the threshold ε^*.

Figure 5 schematically shows how the characteristic frequencies depend on the field E/p. The solid line corresponds to the energy-relaxation frequency of the body of the EDF. The part of this line on the left of point A corresponds to the Druyvesteyn–Davydov EDF (13), whereas the part on the right of this point corresponds to the pipeline EDF (10). The fast relaxation of the tail of the EDF is described by the dashed line ν^*/p. At point B, the characteristic decay scales of the body and tail of the EDF coincide, so that the difference between them disappears. On the right of this point, the field is so large that collisions in which the energy ~ε^* is lost can be considered quasi-elastic.

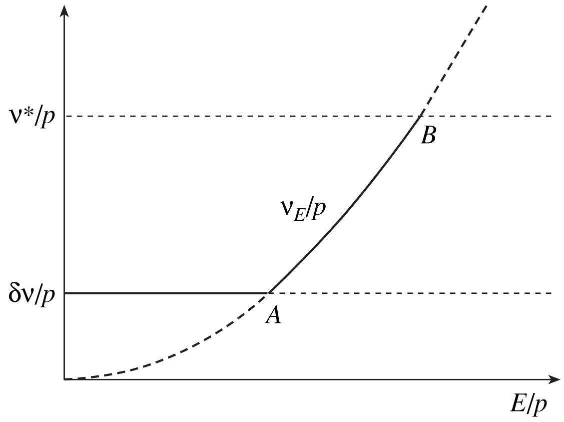

Fig. 5. Diagram illustrating the dependence of the characteristic relaxation frequencies of the EDF on the reduced field E/p.

Table 2. Comparison of the results of simulations of the plasma parameters at the discharge axis with calculations in the local model for p = 6 Torr, R = 1 cm, and I = 3 mA.

	Local approximation	Full simulation
n_e, cm^{-3}	2.9×10^{10}	1.5×10^{10}
$2\langle\varepsilon\rangle/3$, eV	3.3	3.5
Φ_w, V	68.5	18.5
n_m, cm^{-3}	1.7×10^{11}	5.4×10^{10}
ν_m, s^{-1}	4.4×10^4	1.2×10^4
ν_{ex}, s^{-1}	1.4×10^5	3.1×10^5

In atomic gases at $\lambda_E \sim R$, when the body of the EDF would become local, EDF (10) changes to EDF (13). Since in this case energy relaxation length (12) for the body of the EDF increases significantly, the range of applicability of the local approximation shifts toward higher pressures (pR > 10 cm Torr). From our calculations and the data of other authors (see, e.g., [10]), it follows that, for argon, elastic processes dominate over inelastic ones when $E/p \le 3$ V/cm. Such fields (see, e.g., [13, 15]) correspond to medium pressures such that pR > 1 cm Torr. Hence, roughly speaking, the body of the EDF at medium pressures depends only on the total energy ε, while the tail depends on both ε and r.

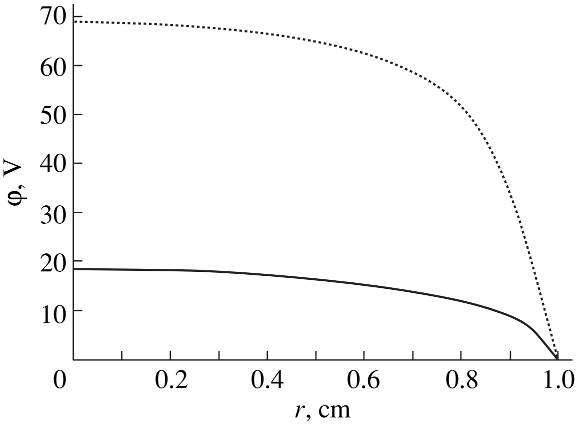

Fig. 6. Radial profile of the electric potential for p = 6 Torr and I = 3 mA. The dotted line corresponds to the local approximation.

As was shown in [7, 8], the use of the local approximation leads to significant errors in determining the parameters of the PC at low pressures. It follows from Table 2, which presents the parameter values at the discharge axis at p = 6 Torr and R = 1 cm, and from Figs. 6–14, which show the corresponding radial profiles, that the parameters calculated in the local and nonlocal models differ significantly at medium pressures. The profiles of the radial field in Fig. 7 show that this field exceeds the axial field in most of the plasma column. This fact indicates that the local approximation is inapplicable to calculating the EDF [13]. This is also confirmed by a decrease in the mean electron energy with radius (Fig. 8). We also note that the electron density profiles can be narrower or broader than the conventional (Bessel) profiles calculated in the fluid model [10]. The reason is a competition between two effects [4]. First, the ionization is nonuniform over the cross section, and the density is maximum at the tube axis (Fig. 4). Second, the average electron density decreases toward the periphery (Fig. 8), which results in a lower coefficient of ambipolar diffusion there. At low pressures, the first effect is dominant and the electron density profiles decrease almost linearly with radius [4, 7, 8]. In the case under consideration, the second mechanism turns out to be more efficient, which results in the opposite effect—the broadening of the profiles in comparison to the local model (Fig. 9).

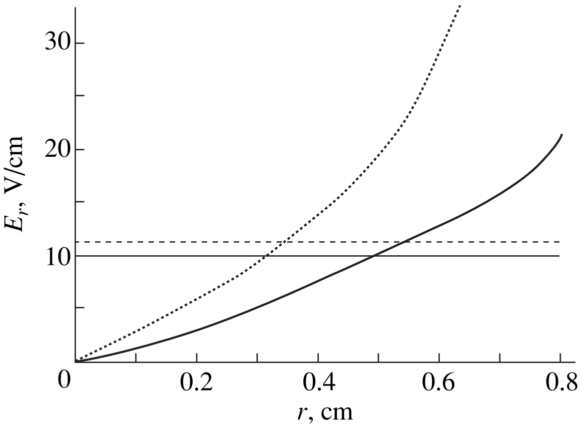

Fig. 7. Radial profile of the electric field for p = 6 Torr and I = 3 mA. The dotted lines correspond to the local approximation. The horizontal lines show the corresponding values of the longitudinal electric field E.

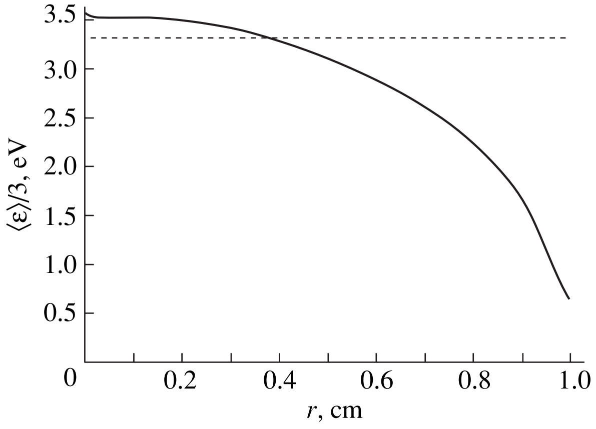

Fig. 8. Radial profile of the mean electron energy for p = 6 Torr and I = 3 mA. The dotted line corresponds to the local approximation.

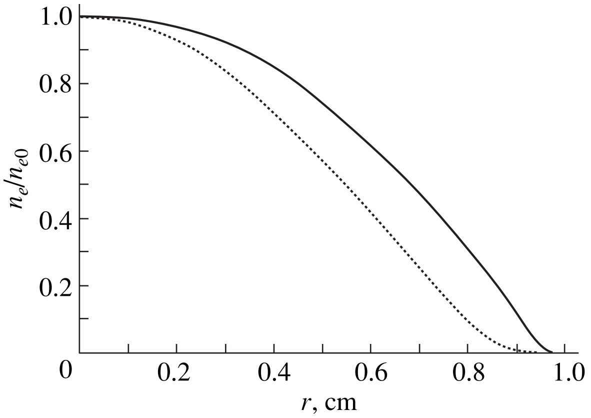

Fig. 9. Radial electron-density profile for p = 6 Torr and 3 mA. The dotted line corresponds to the local approximation.

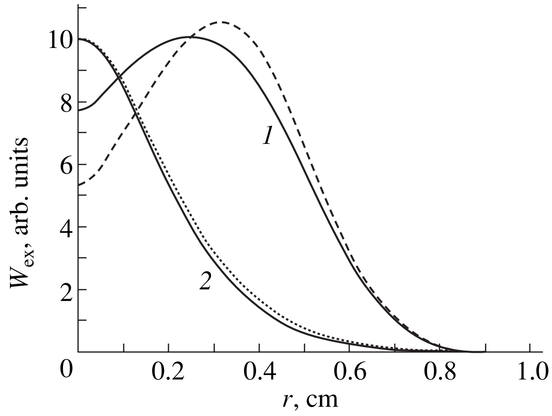

Fig. 10. Radial profiles of the excitation rate (*1*) for p = 6 Torr and I = 3 mA and (*2*) for p = 300 mTorr and I = 100 mA. The dotted lines show the density profiles of the fast electrons with kinetic energies of $w \geq 12$ eV.

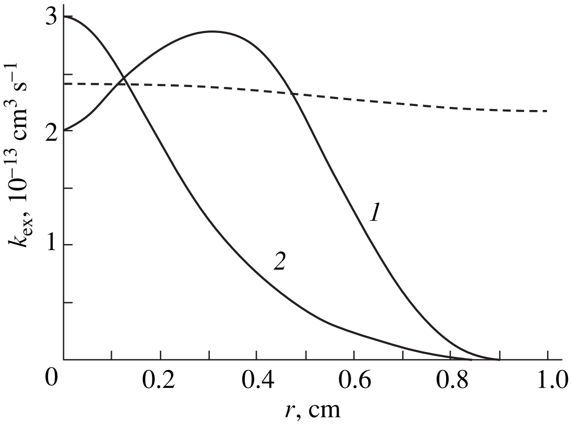

Fig. 11. Radial profiles of the excitation constant (*1*) for p = 6 Torr and 3 mA and (*2*) for p = 300 mTorr and I = 100 mA. The dashed line shows the results of calculations in the local model for p = 6 Torr and I = 3 mA. Curve *1* is plotted in absolute units. For better visualization, the results obtained in the local model (the dashed line) are multiplied by 0.2 and the simulation results shown by curve *2* are multiplied by 5×10^{-4}.

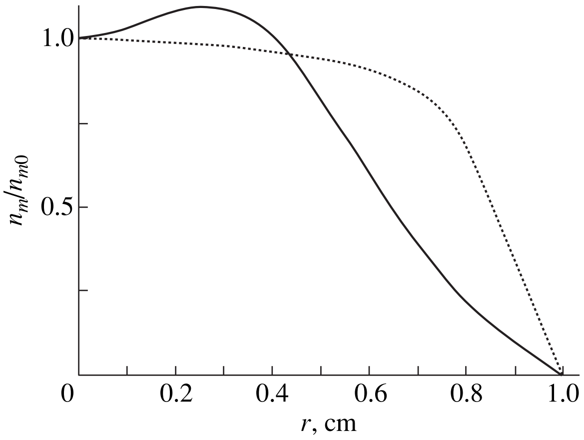

Fig. 12. Comparison of the radial profile of metastable argon atoms for p = 6 Torr and I = 3 mA with that calculated in the local model (the dotted line).

Next, we consider the radial profile of the excitation rate for the metastable level,

$$W_{ex}(r) = N_a \int_{\varepsilon^*}^{\infty} f_0(\varepsilon, w)\nu^*(w, r)\sqrt{w}dw, \qquad (14)$$

which is presented in Fig. 10. It can be seen from this figure that the peak of this profile (as well as the peak of the rate constant $k_{ex} = W_{ex}/N_a n_e$ (Fig. 11)) can be substantially displaced from the PC axis.[1]

Since the excitation rates are determined by fast electrons, there is a strong correlation (Fig. 10) between the profiles of $n_{ef}(r)$ (the dashed line in Fig. 10) and $W_{ex}(r)$. We will clarify this effect by the example of the excitation of high-lying levels with the excitation energy $\varepsilon_k > \varepsilon^* + T^*$. To the best of our knowledge, this effect has not previously been observed for a diffuse PC.

It is well known [3, 7, 8] that, if the body and tail of the EDF depend only on the total energy ε (low pressures such that $\lambda_\varepsilon^* > R/2.4$, then the excitation rates and constants are maximum at the tube axis. Our simulations for pR = 0.3 cm Torr also indicate that the excitation rates (constants) decrease toward the periphery at low pressures (Figs. 10, 11; curves *2*).

However, if the inequality $\lambda_E > R/2.4 > \lambda_\varepsilon^*$ holds, so that the body of the EDF depends only on ε, whereas its fast component depends on ε and r (Fig. 2), then the position of the peak of the excitation rate depends on both the shape of the radial profile of $\varphi(r)$ and $\nu^*(w)$ [14]. If the profile $\varphi(r)$ is rather steep (Fig. 6), then the excitation rate at the axis is low. Electrons in the axial

---

[1] We note that it is reasonable to use the rate constant k_{ex} in the local case when the EDF can be factorized in form (1) and the excitation rate is proportional to the electron density. In this case, k_{ex} is constant throughout the entire cross section (the dashed line in Fig. 11). In the nonlocal case, however, W_{ex} is not proportional to n_e and, therefore, the use of k_{ex} seems to be unreasonable.

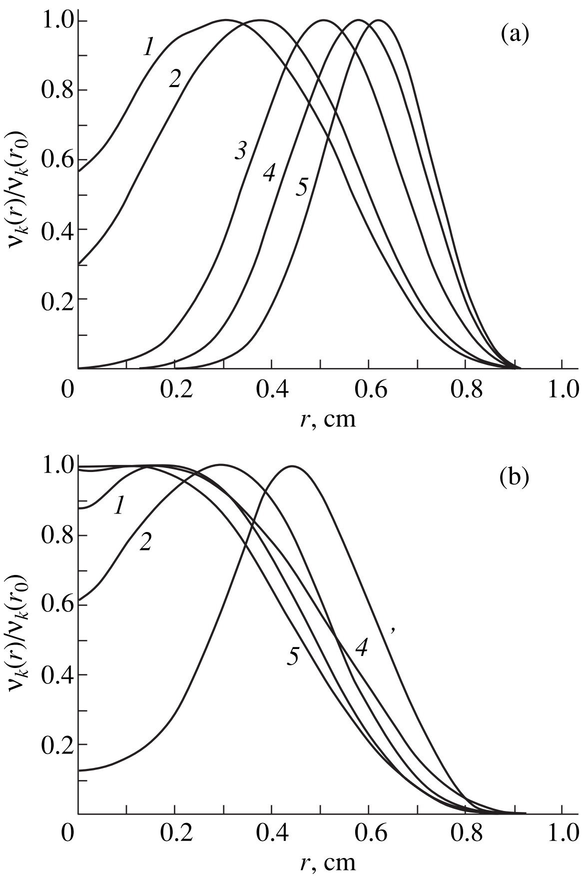

Fig. 13. Profiles of the excitation rates (normalized to their maximum values) of different levels of argon atoms k = (*1*) 1, (*2*) 3, (*3*) 5, (*4*) 17, and (*5*) 25 with energies of ε_k = 11.55, 11.72, 12.91, 14.01, and 15.2 eV, respectively, calculated (a) without and (b) with allowance for impacts of the second kind; r_0 is the coordinate of the peak of the excitation rate profile.

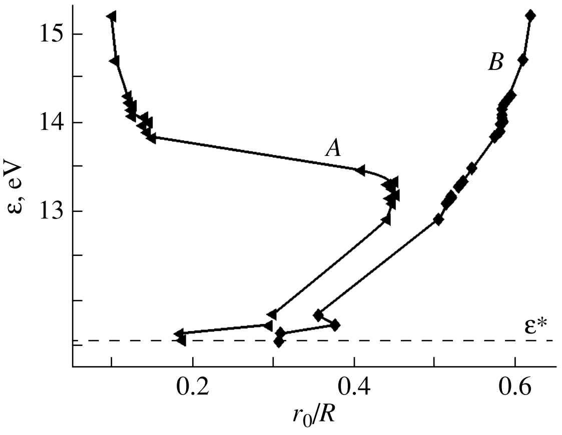

Fig. 14. Coordinate r_0 of the peak of the excitation rate profile for the kth level as a function of the energy ε_k of this level. Curves *A* and *B* show the results of calculations with and without allowance for impacts of the second kind, respectively. The dotted line corresponds to the energy of the metastable state.

region cannot gain energy $\varepsilon > \varepsilon_k$ in the electric field if they previously do not undergo inelastic collisions with lower levels because $\varepsilon_k - \varepsilon^* > T^*$. On the other hand, they cannot reach the axis due to radial diffusion because $\lambda_\varepsilon^* \ll R$. In other words, an electron with energy ε can most easily reach the region with $w > \varepsilon_k$ as follows: First, the electron diffuses over energy up to $\varepsilon > \varepsilon_k$ at the periphery of the plasma column, where the kinetic energy is low ($\varepsilon - e\varphi(r) < \varepsilon^*$) and the electron does not undergo inelastic collisions. Then, this electron diffuses in the radial direction toward the axis over a distance $\sim\lambda_\varepsilon^*$. For this reason, the maximum excitation rate (and the corresponding rate constant) of the level ε_k is shifted from the curve $r = r_k(\varepsilon)$ (where $\varepsilon - e\varphi(r_k(\varepsilon)) = \varepsilon_k$) by λ_ε^* toward the axis. It can be seen from Figs. 10 and 11 that this effect takes place for the first excited (metastable) level with energy ε*. Since the deexcitation rate of metastable atoms (which is determined by the mixing to a neighboring resonance level) is a smooth function of r, the nonmonotonic behavior of the production rate of these atoms leads to nonmonotonic $n_m(r)$ profiles (Fig. 12).

It follows from the above discussion that the higher the level, the larger the shift of the peak of the excitation rate profile toward the periphery (Fig. 13a). In a real situation, when the density n_m is fairly high, this shift is superimposed by the above effect of the replication of the slow (nonlocal) part of the EDF in its fast part (see [4] and Fig. 2). Therefore, for energies $\varepsilon > \varepsilon_h$ at which the EDF f_{0h} (4) is larger than f_{0t} (3), the effect of the shift of the peak of the excitation rate profile disappears. This is illustrated by Fig. 13b. For comparison, Fig. 14 demonstrates the position of the coordinate r_0 corresponding to the peak of the excitation rate profile for the kth level as a function of the energy ε_k of this level. The EDF was calculated with (curve *A*) and without (curve *B*) allowance for impacts of the second kind. It can be seen that curve *B* increases monotonically, while in curve *A*, this effect is absent because of the increase in the tail of the EDF due to superelastic collisions at high energies.

In summary, self-consistent simulations of the PC of a dc discharge in argon has been performed. It is shown that the local approximation is almost always inapplicable to calculating the EDF under the real conditions of a diffuse PC usually met in practice. When the pressure was increased from low (pR < 1 cm Torr) to medium (1 < pR < 10 cm Torr) values, the calculations have shown that the peak of the excitation rate profile shifts from the axis of a discharge toward the periphery due to the nonlocal character of the EDF under these conditions.

ACKNOWLEDGMENTS

This work was supported in part by the U.S. Civilian Research and Development Foundation for the Independent States of the Former Soviet Union (CRDF), grant no. RP-1-567-ST-03. L.D. Tsendin is grateful for support from the Russian Foundation for Basic Research, project no. 01-02-16874.

REFERENCES

1. http://www.siglo-kinema.com/ BOLSIG. Boltzmann solver for the SIGLO-series. CPA Tolouse&Kinema Software.
2. http://www.cfdrc.com/~cfdplasma.
3. L. D. Tsendin, Plasma Sources Sci. Technol. **4**, 200 (1995).
4. E. A. Bogdanov, A. A. Kudryavtsev, L. D. Tsendin, *et al.*, Zh. Tekh. Fiz. **73** (8), 45 (2003) [Tech. Phys. **48**, 983 (2003)].
5. C. Busch and U. Kortshagen, Phys. Rev. E **51**, 280 (1995).
6. M. Schmidt, D. Uhrland, and R. Winkler, IEEE Trans. Plasma Sci. **25**, 1271 (1999).
7. J. Behnke, Yu. Golobovsky, S. U. Nisimov, and I. A. Porokhova, Contrib. Plasma Phys. **36**, 75 (1996).
8. Yu. Golubovskii, I. A. Porokhova, J. Benke, and J. P. Benke, J. Phys. D **32**, 456 (1999).
9. CFD Research Corporation, *CFD–PLASMA: User Manual* (CFD, Huntsville, 1999–2002).
10. N. L. Aleksandrov, A. M. Konchakov, and E. E. Son, Zh. Tekh. Fiz. **50**, 481 (1980) [Sov. Phys. Tech. Phys. **25**, 291 (1980)].
11. L. D. Tsendin, Fiz. Plazmy **8**, 169 (1982) [Sov. J. Plasma Phys. **8**, 96 (1982)].
12. G. Mumken, H. Shluter, and L. D. Tsendin, Phys. Rev. E **60**, 2250 (1999).
13. Yu. P. Raizer, *Gas Discharge Physics* (Nauka, Moscow, 1987; Springer-Verlag, Berlin, 1991).
14. A. V. Phelps, JILA Inf. Cent. Rep., No. 28 (1985); ftp://jila.colorado.edu/collision_data/electronneutral/.
15. C. M. Ferreira and A. Ricard, J. Appl. Phys. **54**, 2261 (1983).
16. M. Hayashi, *Ar Cross Section Set*, ftp://jila.colorado.edu/collision_data/electronneutral/hayashi.txt.
17. A. Bogaerz and R. Gijbels, Phys. Rev. A **52**, 3743 (1995).

Translated by N. Larionova

Technical Physics, Vol. 49, No. 7, 2004, pp. 858–867. Translated from Zhurnal Tekhnicheskoĭ Fiziki, Vol. 74, No. 7, 2004, pp. 52–61.
Original Russian Text Copyright © 2004 by Yusupaliev.

Axisymmetric Pulsed Ejection of a Dense Plasma into a Gas: I. Similarity Criteria for Ejection

U. Yusupaliev
Moscow State University, Vorob'evy Gory, Moscow, 119992 Russia
e-mail: nesu@phys.msu.ru

Received October 14, 2003; in final form, December 16, 2003

Abstract—Axisymmetric pulsed ejection of a dense plasma into a gas is studied within a wide range of the parameters of the gas and the plasma jet generator. Using experimental data and the equation describing the momentum variation of the plasma jet, similarity criteria are obtained for axisymmetric pulsed ejection of a dense plasma. *© 2004 MAIK "Nauka/Interperiodica".*

INTRODUCTION

The character of plasma ejection into a gas depends on the electrodynamic processes in the plasma generator (plasma accelerator, plasma jet generator, etc.) [1−19]. From the practical point of view, two limiting regimes in which plasma ejection is completely determined by either electrodynamic or gas-dynamic processes are of interest for the acceleration of plasma flows, the creation of high-power radiation sources, and the formation of long-living currentless plasma bunches. The former regime has been thoroughly studied for different types of plasma accelerators [1–4]. The latter regime, which occurs, e.g., in plasma jet generators, has still been inadequately investigated in spite of numerous experimental studies [5–19]. The process of gas ejection into the ambient medium was considered theoretically, e.g., in [20–23]. At present, however, it is still impossible to take into account a number of important experimental factors in theoretical analysis. Experiments have shown that the gas-dynamic structure of the plasma jet is affected by the outflow currents behind the nozzle edge. The magnitude of these currents is determined by the design features of a plasma jet generator. In [3, 5–19], the pulsed ejection of a dense plasma into an atmospheric-pressure gas (air, xenon, argon, krypton, nitrogen, etc.) was studied under conditions at which the outflow currents were low (<10% of the total current). In [7, 13], the initial gas pressure in the discharge chamber of a plasma jet generator was $(5–50) \times 10^5$ Pa, whereas in [3, 5, 6, 8–12, 14–19] it did not exceed 10^5 Pa. The regimes of pulsed plasma ejection into a gas (air, nitrogen, xenon, or krypton) were studied in [18, 19], where, based on the experimental data, a similarity criterion characterizing the regime of pulsed plasma ejection was offered that included one dimensionless parameter $\theta = q/p_\infty$, where q is the specific energy deposition in a discharge and p_∞ is the gas pressure of the ambient medium. For example, the case $\theta > \theta_0$ corresponds to the regime of supersonic plasma ejection characterized by the formation of shock-wave structures (so-called "barrels"), whereas the case $\theta < \theta_0$ corresponds to the regime of subsonic ejection.

For pulsed plasma jets, the criterion parameter θ cannot account for the unsteady (pulsed) character of ejection. So far, no similarity criterion characterizing the unsteady character of plasma ejection into a gas has been found. This paper is devoted to the search for such a criterion.

1. EXPERIMENTAL SETUP

The experiments on the pulsed ejection of a dense plasma into a gas were carried out at three different facilities. The necessity of creating three facilities was related to the need for studying the dynamics of pulsed plasma ejection in a wide range of experimental parameters: the specific energy q deposited in a discharge, the initial pressure in the discharge chamber of a plasma jet generator, the diameter of the generator nozzle d, the gas pressure p_∞, the duration of pulsed plasma ejection Δt_{ej}, and the ionization potential W of the gas in the discharge chamber.

1.1. In the first facility, a modified unipolar voltage source taken from an EV-45 standard high-power radiation source was employed [9]. The modification of the source enabled variations in the output unipolar voltage from 3 to 5 kV and discrete variations in the voltage pulse duration Δt_{ej} from 75 to 150 μs. The experiments were performed for different values of the discharge chamber volume V and the diameter of the plasma generator nozzle d: $V = 0.1$, 0.56, 1.12, and 5 cm^3 and $d =$ 2, 4, and 10 mm. The ambient gas was atmospheric-pressure air. The plasma pressure in the discharge chamber of the plasma jet generator was determined by the method described in [9]. The maximum plasma pressure ($p_p = 5 \times 10^7$ Pa) was achieved for the discharge chamber volume $V = 0.1$ cm^3.

1.2. The second facility consisted of two discharge circuits with energy-storage capacitances of C_1 = 20 (30) μF and C_2 = 120 μF and working voltages of U_1 = 5–25 kV and U_2 = 8–45 kV. Two plasma generators with disc metal electrodes [18] were used as plasma jet generators. The discharge chamber (an insulating cylinder made of caprolan with a conical (or cylindrical) axial through hole) was placed tightly between these electrodes. The ends of the discharge chamber were hermetically sealed. In the top electrode, there was an axial opening (nozzle), which was hermetically covered with a metallized Mylar (or another dielectric) film (diaphragm) of thickness ~50 μm. The film withstood a static pressure of up to 0.4 MPa. The discharge chamber of the plasma jet generator was evaluated via a metal nipple in the bottom electrode down to a pressure of 0.5×10^2 Pa. The chamber volume of the plasma jet generator was varied (using dielectric inserts) in the range V_1 = 1–12 cm^3 for the discharge circuit with the capacitance C_1 and V_2 = 20–160 cm^3 for the discharge circuits with the capacitance C_2. Special measures were undertaken to significantly reduce (to 3–5% of the total discharge current) the outflow discharge currents behind the generator nozzle. The nozzle diameters were varied within the ranges d_1 = 5–12 mm and d_2 = 8–65 mm.

The pressure p_p in the discharge chamber of the plasma jet generator was measured with calibrated piezoelectric gauges [24], which were hermetically inserted through the insulator.

The ejection chamber designed to study the process of plasma ejection into a gas consisted of two sections. The first section was a metal cylinder (400 mm in diameter and 500 mm in length) with four side flanges (300 mm in diameter), to which hermetically sealed view windows were attached. One end of this cylinder was tightly attached to the top flange of the plasma jet generator, while the other end was attached to the second section of the ejection chamber. The second section was a 1.5-m-long 250-mm-diameter stainless-steel cylinder with a wall thickness of 2 mm and with a view window at its free end. The ejection chamber was pumped out and filled with a working gas through a system of nipples and valves. The chamber was filled with Xe, Kr, Ne, N_2, or air at pressures of 10^2–10^5 Pa.

The discharge voltage and current in the plasma jet generator were measured with a noninductive voltage divider and Rogowski coil, respectively [24, 25]. The energy Q deposited in a discharge was determined from the discharge current–voltage characteristic by a standard technique [18, 25]. The waveforms of the discharge current and voltage were damped sine waves with damping factors of 0.84–0.87. The maximum discharge current was $J_0 \approx 450$ kA and 50 kA for the discharge circuits with the capacitances C_2 and C_1, respectively. The quasi-period of the discharge current was varied from 65 to 110 μs by adjusting the capacitance and inserting an additional inductance in series with the plasma jet generators. Accordingly, the duration of plasma ejection varied from 120 to 540 μs, whereas the average (over time) specific energy deposition in a discharge varied in the range $q_1 \approx 10^5$–10^9 J/m^3 and $q_2 \approx 10^5$–10^8 J/m^3.

1.3. The discharge circuit of the third facility had a multisection air spark gap and a capacitor bank with a capacitance of C_3 = 1.0 μF and charging voltage of U_3 = 100 kV. The quasi-period of the discharge current was 6 μs, and the duration of plasma ejection was 28 μs. The plasma jet generators of the second facility were used as plasma generators.

The shape and characteristic size of the glowing regions of the ejected plasma were recorded using an SFR-2M high-speed streak camera [18, 25].

The gas-dynamic structure of the plasma flow was studied using the shadow technique [18, 24], which incorporated a Maksutov lens (300 mm in diameter) and a high-speed streak camera. In studying the ejection of a glowing plasma, an EV-45 high-intensity pulsed radiation source with a radiation temperature of 39 000 K [9] was used as an illumination source for shadow measurements.

The Mach number M of the supersonic plasma flow was determined from the angle of the characteristics at a thin rod with a sharp front edge [18, 26]. The velocity of the ejected plasma flow was calculated from the measured velocity of acoustic perturbations in the plasma flow (the glowing tracks on the streak images of the pulsed jet) and from the angle of the characteristics [18].

2. EXPERIMENTAL RESULTS

First of all, we note that, in all three facilities, the electron density and temperature of the ejected dense plasma at the nozzle edge of the plasma jet generator were ~$(1–8) \times 10^{18}$ cm^{-3} and $(1–4) \times 10^4$ K, respectively. Under these conditions, the optical thickness of the plasma across the jet was larger than unity, to say nothing of the optical thickness in the axial direction. Hence, this dense plasma jet emitted in the visible and near UV regions as a black body. In this case, the integral (both over the spectrum and time) radiation energy can be as high as 10–40% of the energy Q deposited in a discharge [9, 18, 19]. Note that the EV-45 standard high-intensity radiation source [9] with a radiation temperature of 39 000 K is in fact a pulsed plasma jet ejected in two opposite directions into atmospheric-pressure air from a through hole in a textolite sample, whose wall is evaporated in the course of ejection. The data presented below refer to such radiating plasma jets.

Under our experimental conditions, the flow in the boundary layer surrounding the plasma jet was highly turbulent (the Reynolds number was $\mathrm{Re} = u_\mathrm{p}d/\nu \approx 10^5$–

10^6, where u_p is the velocity of plasma flow at the nozzle edge of the plasma jet generator and ν is the kinematic viscosity of the gas). For this reason, the study of the shock-wave structures in the plasma jet by the shadow technique was rather difficult to perform. However, since the gas in the boundary layer was transparent to the jet radiation, the most preferable method for studying the ejection of a glowing plasma turned out to be measurements of the plasma glow in combination with the shadow technique.

An analysis of the experimental data showed that the character of the pulsed ejection of a dense plasma into a gas was determined by the independent parameters q, p_0, and p_∞. Variations in some of these parameters could be balanced by variations in the others, so that the gas-dynamic structure of the ejected dense plasma jet remained nearly self-similar. This allowed us to determine the similarity criterion for plasma ejection into a gas. Experiments showed that the same gas-dynamic structure of the plasma jet could be obtained by either increasing q and p_0 in the discharge chamber of the plasma jet generator or decreasing the pressure p_∞ of the ambient gas so that the ratio p_p/p_∞ was kept constant. Hence, the dimensionless parameter $\Pi = p_p/p_\infty$ is one of the similarity criteria for the ejection of a dense plasma into a gas. Since the plasma (or gas) is ejected only at $p_p > p_\infty$, we have $\Pi > 1$.

The process of plasma ejection proceeds in three characteristic stages: the initial stage, the stage of formation of the quasi-steady gas-dynamic structure of the plasma jet, and the late stage. The initial ejection stage lasts for a time period of Δt_1 (from the beginning of ejection to the instant at which the sphericity of the ejected flow breaks), whereas the late stage corresponds to the times after ejection has terminated ($t \geq \Delta t_{ej}$). The experiments show that $\Delta t_1 \approx 3d/u_p$. At $t \geq \Delta t_1$, the sphericity of the ejected plasma flow breaks and a directed plasma flow is formed.

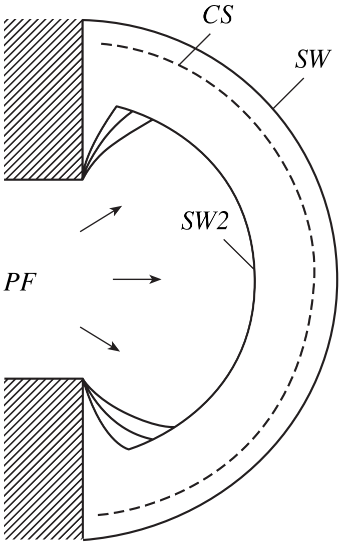

Fig. 1. Gas-dynamic structure of the ejected plasma in the initial stage of ejection for $\Pi \geq \Pi_0$: (*SW*) shock wave, (*CS*) contact surface, (*SW*2) secondary shock wave, and (*PF*) plasma flow.

Let us consider each stage separately.

2.1. Initial Stage

It was shown experimentally that the formation of the gas-dynamic structure of the ejected plasma flow depends on the value of the first criterion parameter Π. There are two characteristic regimes one of which corresponds to a finite value of the parameter Π and another corresponds to $\Pi \longrightarrow \infty$.

2.1a. Dimensionless parameter Π is finite. In this case, plasma ejection is accompanied by the formation of a contact surface separating the surrounding gas and the ejected plasma flow (Fig. 1). For any Π value, if the velocity of the contact surface u_c exceeds the sound speed in the ambient gas c_∞ ($u_c \geq c_\infty$), then the propagation of the contact surface is accompanied by the formation of a shock-compressed layer of the ambient gas. The leading edge of this layer is confined by a shock wave behind which there are the shock-compressed plasma layer and the ejected plasma flow (Fig. 1). The plasma flow, which is ejected with a relatively high velocity, is decelerated by the shock-compressed layer of the ambient gas. In the initial stage of ejection, this deceleration is mainly related to the setting into motion of the ambient gas by the plasma flow. The deceleration of the high-speed flow by the ambient gas results in the excitation of acoustic perturbations at the leading edge of the flow, in particular, those propagating upstream the flow. In the case of supersonic ejection ($\Pi > \Pi_0$), these perturbations do not reach the nozzle and, due to the increase in the temperature at the leading edge of the decelerated flow, the subsequent perturbations overtake the preceding ones. As a result, the so-called secondary shock wave propagating upstream the flow is formed. In the case of subsonic ejection ($\Pi < \Pi_0$), perturbations do reach the nozzle and no secondary shock wave is formed.

If $u_c < c_\infty$, then compressed layers and compression waves (rather than shock-compressed layers and shock waves) arise in both the plasma flow and the ambient gas. In this case, the ejected plasma flow is also decelerated and the velocity of the leading edge of the plasma jet is somewhat lower than the velocity of the ejected flow. Consequently, the deceleration efficiency is lower than for $\Pi > \Pi_0$.

2.1b. The case Π ⟶ ∞. This case corresponds to either $p_\infty \longrightarrow 0$ or $q \longrightarrow \infty$, and the ejection is similar to ejection into vacuum; i.e., the ejected plasma flow is not decelerated and, therefore, no wave structures are formed in it. Streak images of the ejected plasma flow show that the plasma glow decreases monotonically with increasing distance from the nozzle edge. The case

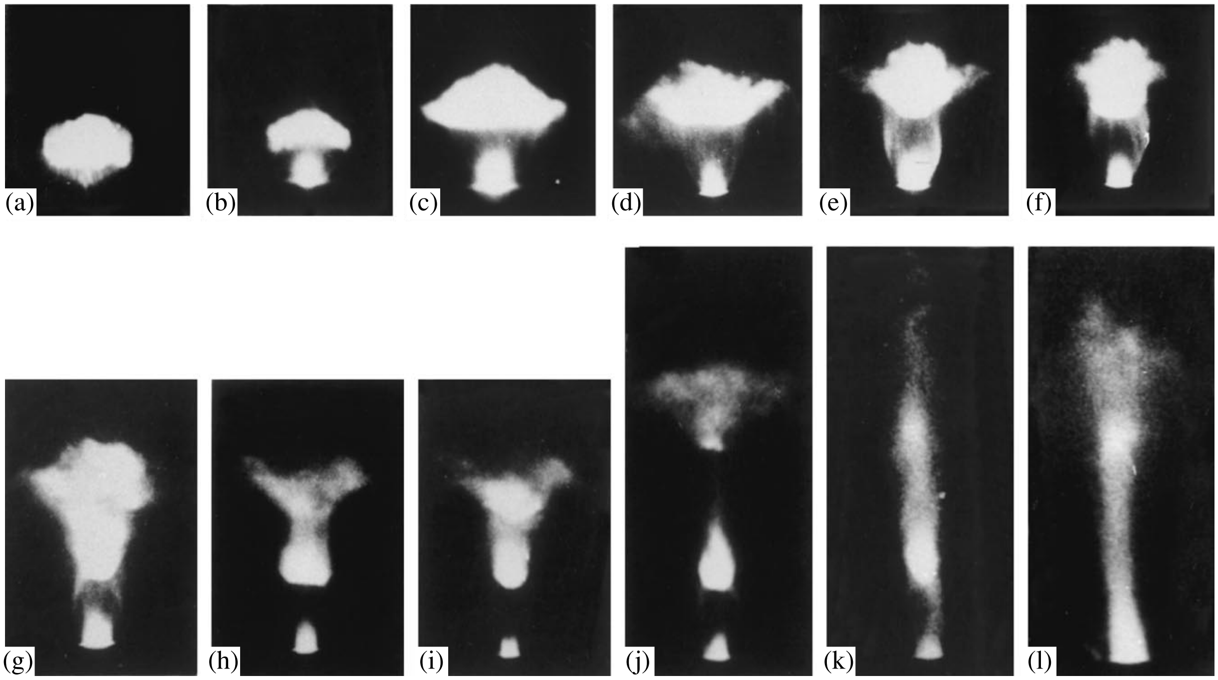

Fig. 2. Typical images of a dense supersonic plasma jet ejected into a gas for $\Pi \geq \Pi_0$ and $\tau_1 + \tau_2 + \tau_3 < \Delta t_{\mathrm{ej}} < \tau_1 + \tau_2 + \tau_3 + \tau_4$ ($\Delta t_{\mathrm{ej}} \approx 250$ μs) at times (a) 20, (b) 30, (c) 50, (d) 65, (e) 85, (f) 100, (g) 120, (h) 135, (i) 155, (j) 185, (k) 220, and (l) 250 μs.

$\Pi \longrightarrow \infty$ can be accomplished by either decreasing the pressure p_∞ of the ambient gas (by pumping out the gas from the ejection volume) or increasing the specific energy deposition q in the discharge chamber of the plasma generator. A significant increase in the plasma pressure was achieved only with a sufficiently small volume ($V = 1$ cm^3) of the discharge chamber.

2.2. The Stage of Formation of Quasi-Steady Hydrodynamic Structures

After the onset of a preferential direction of plasma motion along the axis of the pulsed jet, the leading part of the plasma jet begins to expand in the direction perpendicular to the axis due to the deceleration of the ejected flow.

The experiments showed that, at $t > \Delta t_1$, the further dynamics of plasma ejection is determined by the duration of ejection Δt_{ej} (or the energy deposited in the working chamber of the plasma generator) and the formation time τ_i of various gas-dynamic plasma structures. In other words, the quantities Δt_{ej} and τ_i are decisive independent parameters determining the dynamics of plasma ejection into a gas. Therefore, according to the theory of similarity and dimensionality [27], one can compose a single dimensionless parameter $\beta_i = \tau_i/\Delta t_{\mathrm{ej}}$ from these two decisive independent physical quantities. This parameter can be regarded as the second similarity criterion for plasma ejection.

Let us consider the effect of the β_i value on the gas-dynamic plasma structures formed in different regimes of plasma ejection.

2.2a. Supersonic ejection ($\Pi \geq \Pi_0$). In the case of supersonic ejection, shock-wave structures—the so-called “barrels” consisting of a barrel shock, a Mach disc, and a reflected shock wave—are formed [20, 21, 26]. The number of such barrels is determined by the relation between the duration of plasma ejection Δt_{ej} and the characteristic times of the barrel formation τ_i (where i is the order number of a barrel). In fact, τ_1 is the time during which strong plasma-flow perturbations excited at the nozzle edge reach the jet axis, while τ_2 is the time between the instant of reflection of these perturbations from the jet axis and their next convergence at the jet axis after their reflection from the jet boundary. Similar reflections of these strong perturbations determine the characteristic time τ_3 of the formation of the third barrel number, etc.

When $\Delta t_{\mathrm{ej}} < \tau_1$ ($\beta_1 > 1$), whatever the value of the criterion parameter Π, no barrel is formed (see Figs. 2a–2d). When $\Delta t_{\mathrm{ej}} > \tau_1$ ($\beta_1 < 1$), one should distinguish between two cases, $\Pi \gg \Pi_0$ and $\Pi \geq \Pi_0$.

For $\Pi \gg \Pi_0$, only the first barrel is formed in the vicinity of the nozzle, whereas the plasma flow in the rest of the pulsed jet remains subsonic (Fig. 3). A further increase in Δt_{ej} ($\beta_1 \ll 1$) leads to an increase in the length of the subsonic part of the pulsed plasma jet.

When $\Pi \geq \Pi_0$ and the duration of ejection satisfies the inequalities $\tau_1 < \Delta t_{\mathrm{ej}} < \tau_2 + \tau_1$ (where τ_2 is the for-

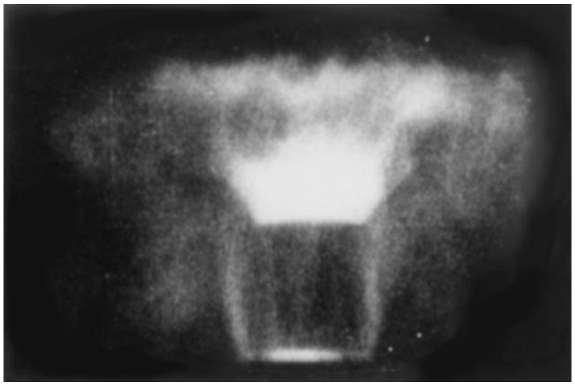

Fig. 3. Fragment of a dense supersonic plasma jet ejected into a gas for $\Pi \gg \Pi_0$ and $\Delta t_{ej} > \tau_1$.

Fig. 4. Mushroomlike plasma cloud produced at $\Pi < \Pi_0$ and $\Delta t_{ej} > \tau_v$.

mation time of the second barrel), only the first barrel is formed in the jet (Figs. 2e–2g). When $\tau_1 + \tau_2 < \Delta t_{ej} < \tau_1 + \tau_2 + \tau_3$, two barrels are formed (Figs. 2h–2j). Generally, if the duration of plasma ejection satisfies the condition $\sum_{i=1}^{j}\tau_i < \Delta t_{ej} < \sum_{i=1}^{j+1}\tau_1$, then j barrels (sections) are formed.

In the experiments, we succeeded in producing a supersonic plasma jet with a three-section shock-wave structure (Fig. 2k). Structures with one and two barrels were observed in [3, 5, 6, 14, 16–19] when ejecting supersonic pulsed plasma jets into atmospheric-pressure air. In [14], a dense plasma jet ejected into in atmospheric-pressure air was studied. The fragments of streak images presented in that paper correspond to the ejection stage shown in Fig. 2c for $\Pi \geq \Pi_0$ and $\Delta t_{ej} < \tau_1$.

Note that similar underexpanded supersonic pulsed plasma jets with a one-section shock-wave structure was obtained using a laser plasma generator [3] and by irradiating the surface of a solid target with high-power laser radiation [28]. In those experiments, the plasma was formed due to the absorption of laser radiation by either the plasma-forming substance of the plasma generator [3] or the target surface [28]. In the latter case, the plasma is ejected from a crater that is formed on the solid surface after irradiating it with laser radiation. According to the above, supersonic plasma jets with a one-section shock-wave structure are produced when $\Pi = (p_0 + q)/p_\infty \gg \Pi_0$ and $\Delta t_{ej} > \tau_1$ ($\beta_1 < 1$). Here, by q and Δt_{ej}, we mean the thermal energy density of the plasma produced under the action of high-power laser radiation and the laser pulse duration, respectively.

2.2b. Subsonic ejection ($\Pi < \Pi_0$). In this case, a mushroomlike cloud (Fig. 4) similar to that accompanying a high-power conventional or nuclear explosion is formed at $\beta = \tau_v/\Delta t_{ej} < 1$ (where τ_v is the formation time of a toroidal plasma vortex). When $\beta > 1$, a plasma cloud is formed whose shape is close to a hemisphere.

2.2c. Plasma ejection at $\Pi \longrightarrow \infty$. Let the criterion parameter Π correspond to subsonic ejection ($\Pi < \Pi_0$). Then, as Π increases, a supersonic regime first occurs ($\Pi \geq \Pi_0$), with the number of barrels depending on the value of the second similarity criterion β. As Π increases further ($\Pi \gg \Pi_0$) and $\Delta t_{ej} \longrightarrow \infty$, only one barrel is formed in the supersonic jet (Fig. 3). An increase in Π leads to an increase in the characteristic size of the barrels. At low pressures of the ambient medium ($p_\infty \longrightarrow 0$), an increase in Π leads to the blurring of the barrels and the plasma ejection becomes similar to the ejection into vacuum, when no shock-wave structures are formed (in this case, the ambient medium cannot be regarded as a continuous medium).

Thus, when $\Pi \longrightarrow \infty$, the supersonic regime with a single barrel can be regarded as a limiting regime before a transition to the regime of ejection into vacuum. In [9], the criterion parameter Π was equal to ~500; hence, no pronounced shock-wave structure was observed.

2.3. Late Stage of Pulsed Ejection ($t > \Delta t_{ej}$)

In the late stage of supersonic ejection ($\Pi \geq \Pi_0$), if $\Delta t_{ej} \leq \Delta t_1$ or $\Delta t_{ej} \leq \tau_1$, then the shock-compressed layers of both the ejected plasma and the gas of the ambient medium begin to expand. After this expansion comes to an end, a spherical cloud is formed (Fig. 5). A similar cloud is also formed in the regime of subsonic ($\Pi < \Pi_0$) ejection, provided that $\Delta t_{ej} \leq \Delta t_1$ or $\Delta t_{ej} \leq \tau_v$.

In the case of supersonic ($\Pi \geq \Pi_0$) ejection, if the duration of ejection satisfies the condition $\Delta t_{ej} > \tau_1$, then, at $t > \Delta t_{ej}$, a plasma cloud is formed whose shape is close to spherical. In this case, a circular vortex comes off from the leading part of the cloud; however, this vortex rapidly decays. In the regime of prolonged supersonic ejection, a cigarlike jet is formed after the ejection comes to an end (Fig. 2l).

In the late stage of subsonic ($\Pi < \Pi_0$) ejection, if $\Delta t_{ej} \geq \tau_v$, then a toroidal plasma vortex—a glowing plasma ring (Fig. 6)—and a plasma globe that is not involved in the vortex motion are formed from the remaining "mushroom cap." Eventually, the glowing ring detaches from the plasma cloud (Fig. 7).

The formation of a toroidal plasma vortex was observed in [8, 11, 12, 14, 15, 18, 19, 29–31]. In [29–31], a pulsed plasma jet was produced by the electric explosion of a round metal diaphragm in atmospheric-pressure air.

In [15, 18, 19], the following characteristic feature of the toroidal plasma vortex and the plasma globe was noted: the globe and the toroidal vortex emit in the visible region over time periods that are longer than the duration of energy deposition by factors of 70 and 500, respectively. A further investigation showed that the plasma vortex emit in the IR region ($\lambda = 3.2$–4.2 μm) for 1 s, whereas the duration of energy deposition in a discharge ($Q \approx 20$ kJ) is $\Delta t_{ej} \approx 200$–$250$ μs. In [31], it was shown experimentally that the afterglow duration for such a vortex is a function of the discharge current. Such an anomalously long glow of the plasma toroidal vortex in air has not yet been adequately explained.

When evaluating β_i, the characteristic formation times of gas-dynamic plasma structures, τ_i and τ_v, were determined experimentally. So far, adequate theoretical predictions of these times (especially τ_v) are still lacking.

We note two characteristic features of the plasma jet generators based on a high-current discharge supplied from a capacitor bank (the second and third experimental facilities). The first feature is the possibility of controlling the duration Δt_{ej} of energy deposition in a discharge in generators using a multisection air spark gap connected in parallel to the plasma generators. After illuminating this gap with UV radiation, the main discharge circuit gets closed through the spark gap. The jitter of such a spark gap is ~2 μs. An EV-45 high-intensity standard radiation source was used for UV illumination. This source was triggered by a GZI-6 delay generator from the control panel of the experimental facility. By varying the GZI-6 delay, one could control the time at which the discharge in the plasma generator terminated, i.e., the duration of energy deposition in the discharge. In particular, for $\Pi \geq \Pi_0$ or $\Pi \gg \Pi_0$, if the spark gap was switched on at the instant $t \approx \tau_1$, then the first barrel did not have time to form, which corresponds to the images of a pulsed jet in Figs. 2a–2d, i.e., to the case $\Delta t_{ej} \leq \tau_1$ ($\beta_1 \geq 1$). If the spark gap was switched on at $t \approx \tau_3$, then two barrels were formed, which corresponds to the case $\tau_1 + \tau_2 < \Delta t_{ej} < \tau_1 + \tau_2 + \tau_3$ (Figs. 2a–2j), where a cigarlike jet is formed in the late stage of ejection. In the case of subsonic ejection ($\Pi < \Pi_0$), the experiments with various durations of plasma ejection showed that a mushroom cloud was formed at $t \geq \tau_v$, whereas at $t < \tau_v$, such a cloud was not formed. In the late stage of plasma ejection, the same gas-dynamic plasma structures were formed as those described in Section 2.3.

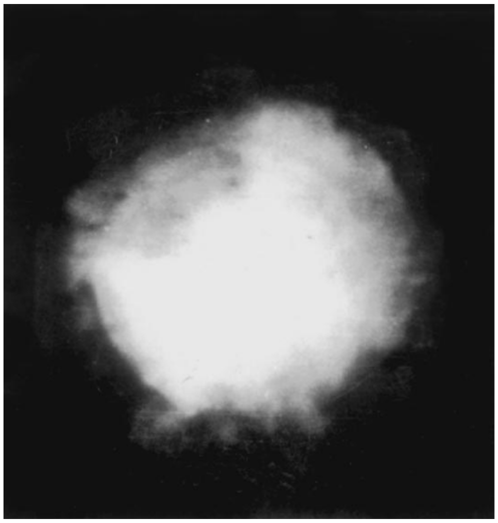

Fig. 5. Spherical plasma cloud.

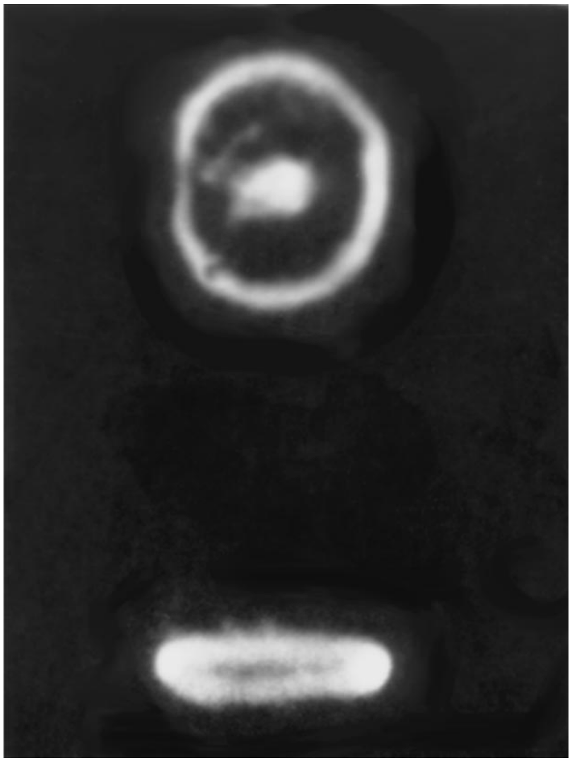

Fig. 6. Toroidal plasma vortex produced at $\Pi < \Pi_0$ and $t > \Delta t_{ej} > \tau_v$. The top and bottom photographs show the longitudinal (along the plasma jet axis) and side views of the vortex, respectively. The bright central core on the top photograph is the generator nozzle.

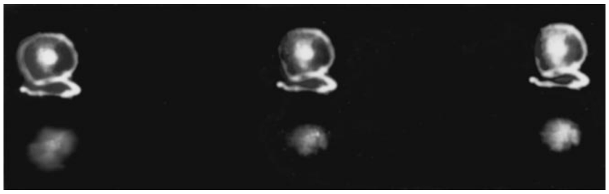

Fig. 7. Streak images of a toroidal plasma vortex and a spherical plasma cloud that is not involved in vortex motion for $\Pi < \Pi_0$ and $t > \Delta t_{\mathrm{ej}} > \tau_{\mathrm{v}}$. The frame exposure is 40 μs and the time interval between the frames is 40 μs.

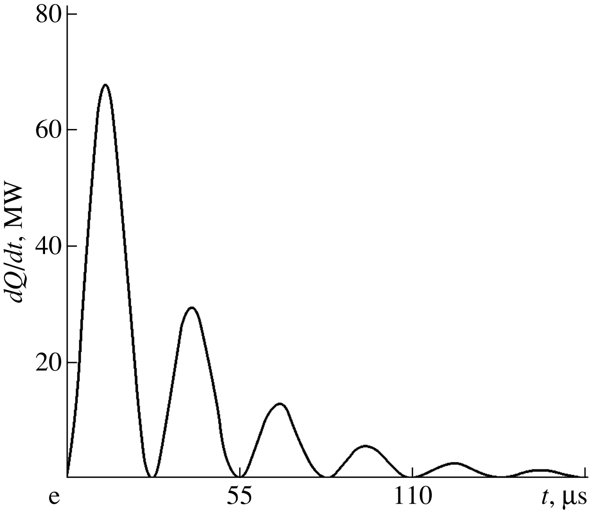

Fig. 8. Time evolution of the power deposited in a discharge in a plasma jet generator for $C_2 = 120$ μF and $U_2 = 30$ kV. The quasi-period of the discharge current is 55 μs.

The other feature is related to the way in which energy is deposited in a discharge. For a unipolar-voltage plasma jet generator (the first facility), the rate of plasma ejection remains almost constant during energy deposition. Therefore, the characteristic size of gas-dynamic plasma structures remains unchanged during a discharge. When a generator is supplied with a damped sine-wave voltage (the second and third facilities), two regimes of the plasma generator operation can be distinguished: the erosion regime and the gas filling regime. In the experiments, the rate of plasma ejection from the nozzle of the plasma generator with gas filling remained nearly constant during a discharge in spite of the oscillations in the power dQ/dt deposited in a discharge (Fig. 8).

In the erosion mode of the generator operation, the rate of plasma ejection follows the time evolution of the power deposited in a discharge (Fig. 8). Hence, at $\Pi \gg \Pi_0$ or $\Pi > \Pi_0$, the characteristic size of the gas-dynamic plasma structures varies with almost the same period as the deposited power does. At $\Pi < \Pi_0$, two (sometimes even three) toroidal plasma vortices are formed in the late stage of ejection ($t > \Delta t_{\mathrm{ej}}$). Obviously, the formation of several plasma vortexes is related to the modulation of the plasma ejection rate.

In the case of a plasma jet generator with a damped sine-wave current, the deposited power varies substantially during a discharge (Fig. 8), so that both regimes of plasma ejection can occur during one shot. First, the supersonic ejection regime occurs, which is followed by the subsonic regime. According to the above, such behavior is related to a decrease in Π, i.e., a decrease in the plasma pressure in the discharge chamber of the plasma generator at a constant p_∞. The formation of gas-dynamic plasma structures is determined by the parameters $\beta_i = \sum_{i=1}^{j} \tau_i / \Delta t_{\mathrm{ej}}$ and $\beta_{\mathrm{v}} = \tau_{\mathrm{v}} / \Delta t_{\mathrm{ej}}$.

3. DISCUSSION OF THE EXPERIMENTAL RESULTS

To determine the criteria for plasma ejection, we reduce the equation for the plasma jet momentum to a dimensionless form. Let us assume that the plasma jet is produced by a plasma generator with gas filling. A change in the jet momentum at the nozzle edge dI over the time dt in the reference frame related to the generator occurs under the action of the resultant force

$$\frac{dI}{dt} = [p_p(t)S_{\mathrm{n}} - p_\infty S_{\mathrm{n}}],$$

where

$$I = \int_0^t S_{\mathrm{n}} \rho_{\mathrm{p}}(t) u_{\mathrm{p}}^2(t)\,dt$$

is the jet momentum at the instant t, u_{p} and ρ_{p} are the velocity and density of the plasma flow at the nozzle edge, p_p is the static pressure in the plasma flow at the nozzle edge, and S_{n} is the cross-sectional area of the plasma generator nozzle.

Direct measurements of p_p in the discharge chamber showed that it was proportional to the specific energy deposition $q(t)$ in a discharge:

$$p_p \approx p_0 + bq(t) = p_0 + \frac{bQ(t)}{V} = p_0 + \frac{b\int_0^t J(t)U(t)\,dt}{V}, \quad (1)$$

where $Q(t)$ is the energy deposited in a discharge by the time t, b is the proportionality factor, and $J(t)$ and $U(t)$ are the discharge current and the voltage between the generator electrodes.

Then, the equation for the momentum of the plasma jet at the nozzle edge is

$$\frac{dI}{dt} = [p_0 + bq(t)]S_{\mathrm{n}} - p_\infty S_{\mathrm{n}}. \quad (2)$$

Dividing both sides of Eq. (2) by ($S_n p_\infty$), we obtain

$$\frac{d}{dt}\left(\frac{I}{S_n p_\infty}\right) = \frac{p_0}{p_\infty} + b\theta - 1 = \Pi - 1, \tag{3}$$

where

$$\Pi = \frac{p_0}{p_\infty} + b\theta.$$

The fact that the plasma (gas) is ejected into the surrounding gas means that

$$\frac{d}{dt}\left(\frac{I}{S_n p_\infty}\right) > 0;$$

consequently, we have $\Pi > 1$.

Next, it is easy to show [20, 21, 26] that, at a definite magnitude of the dimensionless parameter

$$\Pi_0 = \frac{p_0}{p_\infty} + b\theta_0,$$

the velocity of plasma ejection into a gas becomes equal to the speed of sound. As the distance from the nozzle edge increases, the plasma flow becomes supersonic, $M > 1$, where $M = u/c$ is the Mach number of the plasma flow (here, u and c are the plasma flow velocity and the local sound speed in a plasma, respectively). The criterion parameter θ introduced in [18, 19] is a particular case of the dimensionless criterion parameter Π.

For plasma jet generators, other parameters describing plasma can be proposed instead of the criterion parameter Π. Indeed, after substituting the expression for the pressure of an ideal plasma in the generator discharge chamber

$$p_p = n_i kT_i + n_e kT_e + n_a kT_a + \frac{B^2}{4\pi} \tag{4}$$

(where n_e, n_i, n_a, T_e, T_i, and T_a are the densities and temperatures of electrons, ions, and neutrals, respectively; B is the average magnetic field induced by the current inside the discharge chamber; and k is the Boltzmann constant) into Eq. (2) and dividing both sides of Eq. (2) by $S_n p_\infty$, we obtain

$$\frac{d}{dt}\left(\frac{I}{S_n p_\infty}\right) = \frac{n_0 kT_a}{p_\infty}\left(\alpha\frac{T_e}{T_a} + 1\right) + \frac{B^2}{4\pi p_\infty} - 1, \tag{5}$$

where $n_0 = n_e + n_a$ and $\alpha = n_e/(n_e + n_a)$ is the degree of plasma ionization.

Expression (5) is obtained with allowance for the magnetic pressure $B^2/4\pi$ in the discharge chamber of a plasma generator because the design of the discharge chamber in most generators is such that the plasma is electrodynamically accelerated (in one way or another) under the action of the magnetic pressure [3–19].

Thus, the criterion parameter Π for plasma ejection is a generalized parameter because it can be composed of the ratio of the plasma pressure to the pressure of the ambient gas $(n_0 kT_a)/p_\infty$; the degree of plasma ionization at the nozzle edge α; the parameter T_e/T_a, characterizing the degree to which the plasma is nonisothermal; and the ratio of the magnetic pressure in the discharge chamber to the pressure of the ambient gas $B^2/4\pi p_\infty$. In turn, the parameter α is a function of another dimensionless parameter—the ratio of the ionization energy W of the gas in the discharge chamber to the electron thermal energy, W/kT_e—and the degree of dissociation χ of the gas molecules in the discharge chamber: $\alpha = \varphi(W/kT_e, \chi)$.

When there is no plasma in the generator discharge chamber ($\alpha = 0$, $W = 0$, and $B = 0$) or the degree of ionization is low ($\alpha \ll 1$), the pressure is produced only by the neutral gas ($p_p \longrightarrow p_0$, where p_0 is the initial gas pressure in the discharge chamber). Then, as $\alpha \longrightarrow 0$, the dimensionless parameter Π converts into the dimensionless parameter $N = p_0/p_\infty$ (the degree of expansion for stationary gas jets [20, 21, 26]).

Even under identical initial conditions of the discharge circuits, the proportionality factor b between q and p_p can differ because of the difference in the elements of the circuit (e.g., the design features of plasma jet generators, different types of spark gaps, different methods for supplying energy to the generators, etc.). Hence, for each particular experiment on plasma ejection, one needs to evaluate the value of the threshold criterion parameter Π_0. With this in mind, we simultaneously measured the discharge current $J(t)$, the voltage between the electrodes of the plasma generator $U(t)$, the plasma flow velocity u_p, and the speed of sound c in plasma at the nozzle edge.

3.1. Initial Stage

To find other similarity criteria for plasma ejection, the momentum of the plasma flow $I(t)$ should be written with allowance for the unsteady character of plasma ejection and the plasma structures arising in the course of ejection. Pulsed plasma ejection is characterized by its duration Δt_{ej} and the characteristic time τ during which gas-dynamic structures (discontinuity surfaces, shock-wave structures, toroidal plasma vortices, etc.) form. In what follows, time is normalized as $t' = t/\Delta t_{ej}$.

The processes in the initial stage of ejection will be described in spherical coordinates whose origin resides at the center of the nozzle edge. Then, taking into account that the momentum of the ejected flow is conserved, the left-hand side of Eq. (2) takes the form (Fig. 1)

$$\frac{d}{dt}\left(\frac{I}{S_n p_\infty}\right) = \left(\frac{1}{S_n p_\infty}\right)\frac{d}{dt} \times\left[(m_1 + m_2)\frac{dr_c}{dt} + 4\pi\int_0^{r_2}\rho u r^2 dr\right], \tag{6}$$

where m_1 and m_2 are the masses of the shock-compressed layers of the ambient gas and plasma at the time t, respectively; r_c is the coordinate of the contact surface; r_2 is the coordinate of the secondary shock wave; and u is the velocity of the plasma flow behind the nozzle edge.

The masses m_1 and m_2 can be found from the mass conservation law [32]:

$$m_1 = \frac{2\pi}{3}\rho_\infty r_c^3, \quad m_2 = \rho_p S_n u_p t - 2\pi\int_0^{r_2}\rho r^2 dr. \tag{7}$$

In the initial stage, assuming $\rho \approx \rho_p$ and taking into account that $r_2 = u_c\tau_s$, Eq. (3) reduces to the form

$$\begin{aligned}&\frac{d}{dt}\left[\left(\frac{\rho_p u_p^2}{p_\infty}\right)\right]\left[\left(\frac{u_c}{u_p}\right)\left(\frac{t}{\Delta t_{ej}}\right) - \frac{2\pi}{3}\left(\frac{u_c^2}{u_p^2}\right)\left(\frac{u_c^2\tau_c^2}{S_n}\right)\left(\frac{\tau_s}{\Delta t_{ej}}\right)\right.\\ &\left.+ \frac{2\pi}{3}\left(\frac{u_c}{u_p}\right)\left(\frac{u_c^2\tau_s^2}{S_n}\right)\left(\frac{\tau_s}{\Delta t_{ej}}\right) + \left(\frac{2\pi\rho_\infty u_c r_c^3}{3S_n\rho_p u_p^2\Delta t_{ej}}\right)\right] = \Pi - 1,\end{aligned} \tag{8}$$

where τ_s is the formation time of the secondary shock wave.

It follows from Eq. (8) that the ejection dynamics depends, besides the criterion parameter Π, on the ratio between the formation time of the secondary shock wave and the duration of plasma ejection, $\tau_s/\Delta t_{ej}$; the Euler number $(\rho_p u_p^2)/p_\infty$; the ratio of the velocity of the contact surface to the velocity of the plasma flow at the nozzle edge, u_c/u_p; and the ratio between the momentum of the shock-compressed layer of the ambient gas and the impulse of force produced by the plasma flow, $(2\pi\rho_\infty u_c r_c^3)/(3S_n\rho_p u_p^2\Delta t_{ej})$.

3.2. *Supersonic Ejection* ($\Pi \ge \Pi_0$)

The experiments showed that, in this case, the mass of the shock-compressed layer of the ambient gas in the leading part of the jet is small compared to that in the initial stage of ejection because of the existence of a preferential direction of the plasma flow. Hence, the momentum of a supersonic plasma flow in cylindrical coordinates whose origin resides at the center of the nozzle edge (Fig. 1) is

$$\begin{aligned}I &= \sum_{i=0}^{j}\int_0^{m_i} u(r, z, t)dm\\ &= \sum_{i=0}^{j}\int_{Z_i}^{Z_{i+1}}\rho(r, z, t)u(r, z, t)S(z, t)dz,\end{aligned} \tag{9}$$

where j is the number of barrels in the plasma jet, Z_i and Z_{i+1} are the coordinates of the ith and $(i + 1)$th Mach discs in the jet, m_i is the plasma mass in the ith barrel, and $S(z, t)$ is the jet cross-sectional area.

For $i = 0$, we have $Z_0 = 0$. Using the expression $Z_{i+1} - Z_i = \bar{u}\tau_i$ and the theorem of the mean over the r and z coordinates, we calculate the total momentum of the jet,

$$I(t) = \bar{\rho}(t)\bar{u}^2(t)\bar{S}(t)\sum_{i=1}^{j}\tau_i(t), \tag{10}$$

where τ_i is the formation time of the ith barrel; $\bar{\rho}$ and $\bar{u}$ are the spatially averaged density and velocity of the plasma flow, respectively; and $\bar{S}$ is the jet cross-sectional area averaged over z.

Substituting Eq. (10) into Eq. (2) and taking into account that $t = t'\Delta t_{ej}$, we obtain the dimensionless equation

$$\frac{d}{dt}\left[\left(\frac{\bar{S}(t)}{S_n}\right)\left(\frac{\bar{\rho}(t)\bar{u}^2(t)}{p_\infty}\right)\left(\frac{\sum_{i=1}^{j}\tau_i(t)}{\Delta t_{ej}}\right)\right] = \Pi - 1. \tag{11}$$

It follows from Eq. (11) that, for $\Pi > \Pi_0$, the dynamics of plasma ejection into a gas depends, besides the criterion parameter Π, on the ratio between the sum of characteristic times and the duration of plasma ejection, $(\sum_{i=1}^{j}\tau_i)/\Delta t_{ej}$; the geometrical factor $\bar{S}(t)/S_n$; and the ratio of the average dynamic pressure of the plasma flow to the static pressure of the ambient gas, $[\bar{\rho}(t)\overline{u^2}(t)]/p_\infty$.

3.3. *Subsonic Ejection* ($\Pi < \Pi_0$)

In this case, as in the case $\Pi > \Pi_0$, the mass of the compressed layer of the ambient gas is relatively small and the total momentum of the plasma jet $I(t)$ is equal to the sum of the momenta of the toroidal plasma vortex and the jet particles that are not involved in vortex motion:

$$I(t) = \rho_p(t)u_p(t)S_n u_v\tau_v + \rho_p(t)u_p^2(t)S_n(\Delta t_{ej} - \tau_v), \tag{12}$$

where u_v is the velocity of the toroidal plasma vortex as a whole and τ_v is the characteristic time of vortex formation.

After substituting Eq. (12) into Eq. (3), we obtain the equation

$$\begin{aligned}&\frac{d}{dt}\left[\left(\frac{\rho_p(t)u_p^2(t)}{p_\infty}\right)\right]\\ &\times\left[\left(1 - \frac{\tau_v}{\Delta t_{ej}}\right) + \left(\frac{u_v(t)}{u_p}\right)\left(\frac{\tau_v}{\Delta t_{ej}}\right)\right] = \Pi - 1.\end{aligned} \tag{13}$$

It follows from Eq. (13) that, for $\Pi < \Pi_0$, the dynamics of plasma ejection into a gas depends, besides the criterion parameter Π, on the ratio between the average dynamic pressure and the static pressure of the ambient gas, $\rho_p(t)u_p^2(t)/p_\infty$; the ratio between the characteristic time of vortex formation and the duration of plasma ejection, $\tau_v/\Delta t_{ej}$; and the ratio u_v/u_p, which characterizes the relative velocity of the toroidal plasma vortex.

Thus, the formation of various gas-dynamic plasma structures in a dense pulsed plasma flow ejected into a gas is determined by the criterion parameters Π and β_i, characterizing the regimes of plasma ejection.

ACKNOWLEDGMENTS

I am grateful to A.F. Aleksandrov, A.A. Rukhadze, L.S. Kuz'menkov, I.B. Timofeev, V.A. Chernikov, and M.A. Prusakov for their help and useful discussions.

REFERENCES

1. *Plasma Accelerators*, Ed. by L. A. Artsimovich (Mashinostroenie, Moscow, 1973).
2. A. I. Morozov, *Physical Foundations of Space Electrojet Engines* (Atomizdat, Moscow, 1978).
3. *Physics and Application of Plasma Accelerators*, Ed. by A. I. Morozov (Nauka i Tekhnika, Minsk, 1974).
4. *Radiation Plasma Dynamics: Proceedings of the 1st All-Union Symposium on Radiation Plasmodynamics*, Ed. by Yu. S. Protasov (Énergoatomizdat, Moscow, 1991), Vol. 1.
5. L. Ya. Min'ko, *Formation and Analysis of Pulsed Plasma Flows* (Nauka i Tekhnika, Minsk, 1970).
6. M. A. El'yashevich, L. Ya. Min'ko, and B. B. Davydov, *Heat Properties of Low-Temperature Plasmas* (Nauka, Moscow, 1970), pp. 106–112.
7. B. P. Levchenko and F. G. Rutberg, *Plasma Jet Generators and High-Current Arcs* (Nauka, Leningrad, 1973), pp. 9–20.
8. A. M. Andrianov and V. N. Sinitsyn, Zh. Tekh. Fiz. **47**, 1318 (1977) [Sov. Phys. Tech. Phys. **22**, 1342 (1977)].
9. N. N. Ogurtsov and I. V. Podmoshenskiĭ, Opt. Spektrosk. **15**, 741 (1963).
10. V. S. Komel'kov, Zh. Tekh. Fiz. **42**, 203 (1972) [Sov. Phys. Tech. Phys. **17**, 163 (1972)].
11. A. I. Klimov and F. V. Shugaev, Vestn. Mosk. Univ., Ser. 3: Fiz., Astron., No. 3, 24 (1978).
12. A. A. Luchnikov, A. M. Gozhakov, P. D. Sereda, *et al.*, Prib. Tekh. Éksp., No. 2, 237 (1981).
13. I. A. Glebov and F. G. Rutberg, *High-Power Plasma Generators* (Énergoatomizdat, Moscow, 1985).
14. A. F. Aleksandrov, I. B. Timofeev, B. A. Chernikov, and U. Yusupaliev, Zh. Tekh. Fiz. **56**, 2392 (1986) [Sov. Phys. Tech. Phys. **31**, 1431 (1986)].
15. A. Aleksandrov, I. Timofeev, B. A. Chernikov, and U. Yusupaliev, in *Proceedings of the 17th International Conference on Ionized Gas Plasmas, Suansu, 1987*, Part 2, p. 426.
16. A. Anders, Contrib. Plasma Phys. **27**, 203 (1987).
17. A. F. Aleksandrov, I. B. Timofeev, B. A. Chernikov, and U. Yusupaliev, High Temp. **26**, 475 (1988).
18. U. Yusupaliev, Candidate's Dissertation (Mosk. Gos. Univ., Moscow, 1988).
19. A. F. Aleksandrov, I. B. Timofeev, and U. Yusupaliev, Teplofiz. Vys. Temp. **29**, 108 (1991).
20. G. A. Luk'yanov, *Supersonic Plasma Jets* (Mashinostroenie, Leningrad, 1985).
21. V. G. Dulov and G. A. Luk'yanov, *Gas Dynamics of Outflow* (Nauka, Novosibirsk, 1984).
22. I. M. Naboko, *Nonstationary Gas Flows with Shock Waves* (Akad. Nauk SSSR, Leningrad, 1990), p. 393.
23. *Proceedings of the 18th International Seminar on Gas and Plasma Flows in Nozzles, Jets, and Wakes, St. Petersburg, 2000.*
24. W. Lochte-Holtgreven, *Plasma Diagnostics* (North-Holland, Amsterdam, 1968; Mir, Moscow, 1971).
25. A. F. Aleksandrov and A. A. Rukhadze, *Physics of High-Current Electric-Discharge Sources of Light* (Atomizdat, Moscow, 1976).
26. G. N. Abramovich, *Applied Gas Dynamics* (Nauka, Moscow, 1991).
27. L. I. Sedov, *Similarity and Dimensional Methods in Mechanics* (Nauka, Moscow, 1981; Academic, New York, 1959).
28. V. D. Zvorykin, Proc. SPIE **4065**, 128 (2000).
29. V. N. Kunin and L. V. Furov, Izv. Vyssh. Uchebn. Zaved. Fiz., No. 6, 119 (1990).
30. V. N. Kunin and L. V. Furov, in *Proceedings of the European Interdisciplinary Congress on Ball Lightning "Vizotum'93," Salzburg, 1993*, p. 50.
31. V. N. Kunin, V. S. Pleshivtsev, and L. V. Furov, Teplofiz. Vys. Temp., No. 6, 866 (1997).
32. S. F. Chekmarev, Prikl. Mekh. Tekh. Fiz., No. 2, 70 (1975).

Translated by N. Ustinovskiĭ

Technical Physics, Vol. 49, No. 7, 2004, pp. 868–871. Translated from Zhurnal Tekhnicheskoĭ Fiziki, Vol. 74, No. 7, 2004, pp. 62–65.
Original Russian Text Copyright © 2004 by Svalov, Kurlyandskaya, Hammer, Savin, Tutynina.

SOLIDS

Modification of the “Transcritical” State in $Ni_{75}Fe_{16}Cu_5Mo_4$ Films Produced by RF Sputtering

A. V. Svalov[1], G. V. Kurlyandskaya[1,2], H. Hammer[3], P. A. Savin[1], and O. I. Tutynina[4]
[1] *Ural State University, pr. Lenina 51, Yekaterinburg, 620083 Russia*
e-mail: andrey.svalov@usu.ru
[2] *Universidad de Oviedo, Oviedo, Spain*
[3] *Institut für Angewandte Physik, Heinrich Heine Universität, Düsseldorf, Germany*
[4] *Ural Technical Institute of Communication and Informatics, Yekaterinburg, Russia*

Received December 9, 2003

Abstract—The saturation magnetization, the perpendicular and rotational anisotropy constants, and the coercitivity of $Ni_{75}Fe_{16}Cu_5Mo_4$ thin magnetic films produced by rf sputtering are measured in the initial state and after annealing. A relation between the presence of perpendicular anisotropy and the “transcritical” state in the films is established. It is shown that, after additional thermal treatment, the magnetic softness of the films can be improved. *© 2004 MAIK “Nauka/Interperiodica”.*

INTRODUCTION

In recent years, the soft magnetic alloy $Ni_{75}Fe_{16}Cu_5Mo_4$ (so-called μ-metal) has once again attracted attention of researchers in connection with the possibility of using it in electronic devices based on the effect of giant magnetic impedance (GMI). The essence of the GMI effect lies in the variation of impedance Z obtained from ac (at a frequency of ω) measurements (i.e., the impedance of a conductor made of a soft magnetic ferromagnet and subjected to an external magnetic field): $Z(\omega) = R(\omega) - iX(\omega)$ [1, 2]. For such devices, the conductors are fabricated, as a rule, in the form of wires, tapes, foils, or film structures [3–5]. Today, the results of investigations of μ-metal samples in the form of foil [6] and films produced by magnetron sputtering [7] are available. These results show that these materials are suitable for GMI sensors. However, it should be noted that certain corrections accounting for the film state must be introduced and the properties of films can differ from those of a bulk sample made of the same material. The features of magnetic film production by sputtering can give rise to an induced perpendicular magnetic anisotropy in the samples. The emergence of such an anisotropy may be related to the columnar structure in the films, stresses existing in the films, the anisotropic distribution of atom pairs, etc. In each particular case, this anisotropy seems to be determined by the film material, as well as by the method and conditions under which the film is produced [8, 9]. The presence of the perpendicular anisotropy in a film, in its turn, can give rise to a “transcritical” state in it. This state is characterized by a specific hysteresis loop, enhanced coercitivity H_c, rotational magnetic in-plane anisotropy in the sample, and a fine strip domain structure when spontaneous magnetization in domains is oriented at an angle to the film surface [10, 11]. In this study, we investigate the “transcritical” state in $Ni_{75}Fe_{16}Cu_5Mo_4$ films produced by rf ion-plasma deposition.

EXPERIMENTAL

The films were deposited on water-cooled glass substrates in an argon atmosphere at a pressure of 1×10^{-3} Torr. The fore vacuum was 5×10^{-7} Torr. As a target, we used a plate 10 cm in diameter and made of $Ni_{75}Fe_{16}Cu_5Mo_4$ alloy. The composition of the deposited films was assumed to be the same as that of the target. The films were deposited in an external magnetic field parallel to the substrate surface to form anisotropy with an easy magnetization axis (EMA) in the plane of the sample. The magnitude of the field was about 100 Oe. The film thickness was measured by the Tolansky interference method. The hysteresis loops were measured by using the magnetooptical Kerr effect in a field range of ±100 Oe (the frequency of field variation was 50Hz) and by a vibrating-coil magnetometer in a field range of ±500 Oe. Saturation magnetization M_s and the perpendicular anisotropy constant K_p were determined by using a torquemeter according to the method described in [12]. The rotational anisotropy constant K_{rot} was found from the torque curves (TC) measured in various fields from 10 to 500 Oe, with the field direction varying in the film plane. The domain structure was observed with the help of the powder figure method. The samples were annealed *in vacuo* under a pressure of 1×10^{-6} Torr.

RESULTS AND DISCUSSION

In this study, we present the results of investigation of two kinds of samples: 0.1 μm thick (sample 1) and 0.31 μm thick (sample 2). Figures 1a and 1b show the hysteresis loops measured by using a vibrating-coil magnetometer for samples 1 and 2 in the initial state, respectively. The field was applied parallel to the film surface. For the first (thin) film, a low-coercitivity rectangular loop typical of in-plane magnetized films is observed. The thicker sample has a loop typical of the films in the “transcritical” states. Such a state appears when the film thickness L exceeds a certain critical value $L_c = 2\pi(A/K_p)^{1/2}$ and the Q factor is $Q = K_p/2\pi M_s^2 < 1$, where A is the exchange interaction parameter. Assuming that, for this alloy, $A = 2 \times 10^{-6}$ erg/cm [11] and using the values of the quantities M_s and K_p obtained for this sample (see table), we find that $L_c = 0.1$ μm. For the thin sample, a similar estimate gives $L_c = 0.1$ μm. Note that the values of L_c are given within an accuracy of 0.1 μm and with allowance for the approximate nature of the used value of the exchange interaction parameter. Nevertheless, a comparison of the results of these estimates with the sample thickness makes it possible to assume that the probability of the second sample being in the transcritical state is higher than for the first sample.

One more argument in favor of this assumption is the observation of a microstripe domain structure in this sample (Fig. 2), which we failed to detect in the first film. It is the rearrangement of this domain structure during the magnetization reversal in the film that is responsible for the higher coercitivity and saturation field as compared to those for the first sample (see Fig. 1).

The third indication of the transcritical state in the thick sample is the presence of the rotational magnetic in-plane anisotropy in the film whose easy magnetization axis (EMA) is determined by the applied strong magnetic field. This field is capable of changing the strip domain orientation, which defines the position of the EMA. During the rotation of a weak magnetic field parallel to the film surface, the orientation of the strip domains remains unchanged, while the direction of magnetization in the domains is changed [10, 11]. Manifestations of the rotational anisotropy can be seen on the magnetooptical hysteresis loops and TCs.

Figure 3 shows schematically the magnetooptic hysteresis loops measured in the plane of sample 1 along (Fig. 3a) and perpendicularly to (Fig. 3b) the EMA. These loops are typical of the films characterized by in-plane anisotropy and in-plane magnetization. The same figure shows the magnetooptical hysteresis loop measured in the plane of sample 2 in any direction after a strong magnetic field (≥100 Oe) was applied in this direction. The field oriented in this direction the strip domains that determined the EMA position. However, if we rotate the sample (after the action of a strong field)

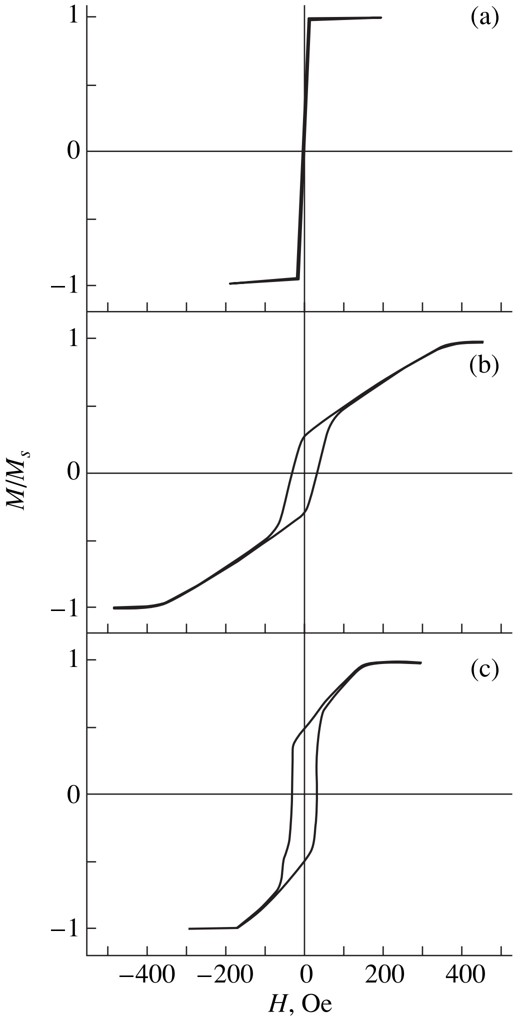

Fig. 1. Hysteresis loops measured with the vibrating-coil magnetometer for samples 1 (a) and 2 (b, c) in the initial state (a, b) and after annealing for 1 h at $T = 420$°C.

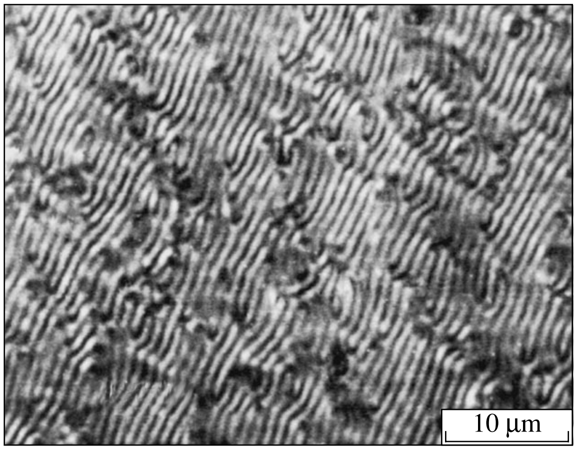

Fig. 2. Microstrip domain structure observed in sample 2 in the initial state.

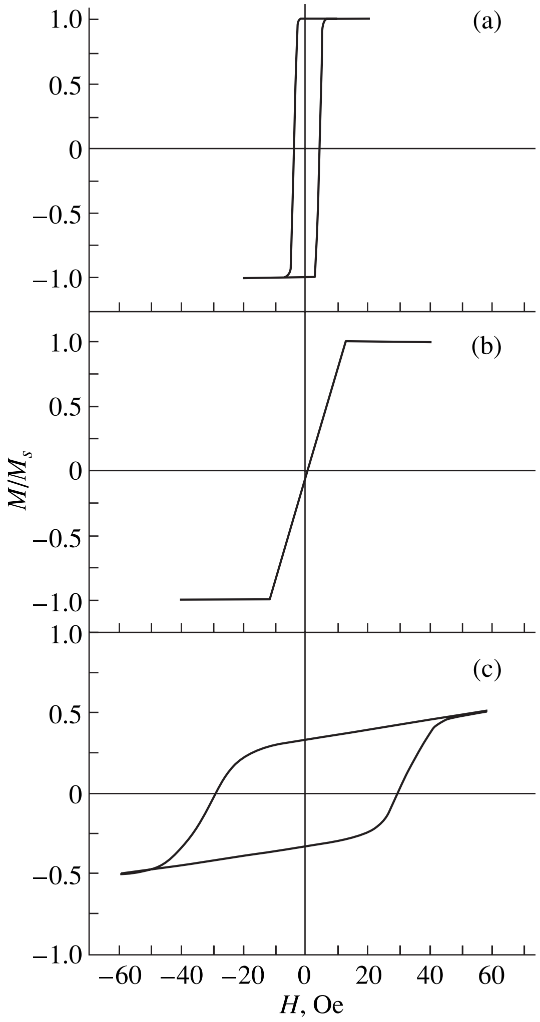

Fig. 3. Scheme of the magnetooptical hysteresis loops measured for samples 1 (a, b) and 2 (c) in the initial state along the EMA (a), perpendicularly to the EMA (b), and in any direction in the film plane after applying a high magnetic field (c).

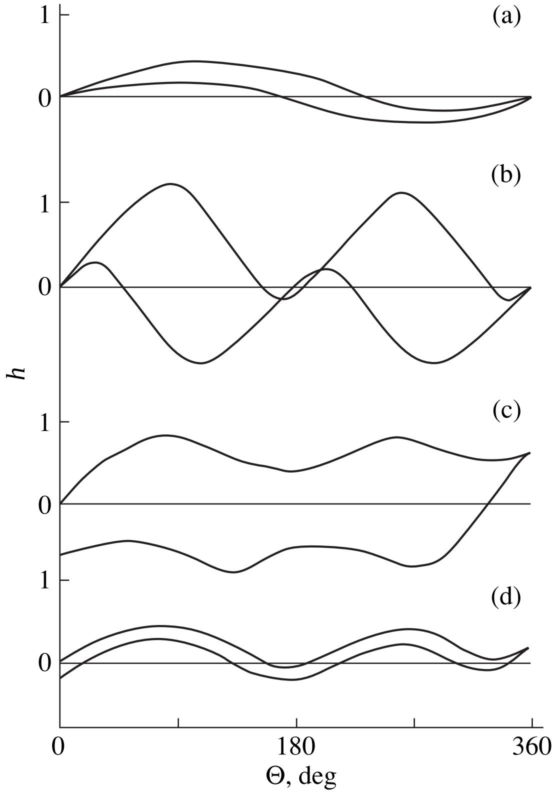

Fig. 4. Scheme of the TCs measured in the film plane (sample 2). Magnitudes of the measurement field: 10 (a), 50 (b), 100 (c), and 500 Oe (d); L is measured in arbitrary units.

in its plane through 90° and measure the hysteresis loop, gradually increasing the field, we find that, in low fields, we have a zero-coercivity loop characteristic of measurements perpendicularly to the EMA. After exceeding a certain value of the field, the loop acquires a width and becomes a typical loop measured along the EMA (Fig. 3c). Such a procedure can be repeated for any direction of the initial application of a high magnetic field to the sample. Such a character of magnetooptical hysteresis loops indicates that, in this sample, the value of rotational anisotropy exceeds that of the induced anisotropy.

Figure 4 shows the scheme of the TCs measured for sample 2 by using a torquemeter (the field direction varied in the film plane). Prior to measurements, the sample was in-plane magnetized in a field of 1 kOe. In low fields, the film still does not experience magnetization reversal and the TC obeys the law $L \sim \sin\theta$ (Fig. 4a). In higher fields, the curve is described by the law $L \sim \sin 2\theta$ that is typical of uniaxial anisotropy (Fig. 4b). With increasing field, the shape of the TC indicates that the EMA rotation follows the external field (Fig. 4c). With a further increase in the field, the TC transforms into a curve described by the law $L \sim \sin 2\theta$ with a small amplitude independent of the field magnitude (Fig. 4d). If we apply a constant field of 1 kOe in the direction perpendicular to the initial direction, the phase of curve in Fig. 1b changes by 90°, while the phase of curve in Fig. 1d remains unchanged. This indicates that curve in Fig. 1d describes induced uniaxial anisotropy existing in the film and curve in Fig. 1b, rotational magnetic anisotropy.

The samples under investigation were subjected to successive stepped annealing at temperatures of 320 and 420°C. The duration of the thermal treatment at each temperature was 1 h. At higher temperatures, the annealing was not performed due to the limited thermal stability of the glass substrate.

The thermal treatment affected slightly the properties of the thin film: the character of the hysteresis loops remained unchanged, while the coercitivity H_c and K_p insignificantly decreased (see table). For the thicker sample, more noticeable changes were observed. After annealing, the hysteresis loops measured with the

Table

	L, µm	M_s, G	H_c, Oe	K_p, erg/cm^3	K_{rot}, erg/cm^3	L_c, µm
Sample 1	0.1					
Initial state		600	4	4×10^5	–	0.1
After annealing at 320°C for 1 h		600	3	3×10^5	–	0.2
After annealing at 420°C for 1h		600	3	1×10^5	–	0.3
Sample 2	0.31					
Initial state		600	20	5×10^5	1.8×10^4	0.1
After annealing at 320°C for 1 h		600	14	2×10^5	1.2×10^4	0.2
After annealing at 420°C for 1h		600	10	8×10^4	–	0.3

vibrating-coil magnetometer retained their transcritical shape, but the coercitivity and the saturation field decreased (Fig. 1c). For the TCs measured with the help of the torquemeter in the plane of sample 2 after annealing at 420°C, the character of transformation of the TCs was modified as the measurement field was increased. It was observed that the curve of the type shown in Fig. 4a transforms at once into a curve of the type in Fig. 4d omitting stages depicted in Figs. 4b and 4c. This is associated with the fact that a decrease in K_p due to annealing leads to a decrease in the angle of emergence of the magnetization in strip domains [11]. This, in turn, makes the domain walls and the EMA given by the walls follow a field lower than in the initial state. In this case, the determination of K_{rot} becomes impossible. The estimates of L_c indicate that, after annealing at 420°C, sample 2 is on the verge of transition into the transcritical state. Analysis of the available data leads to the conclusion that a decrease in the level of transcriticality as a result of the annealing of the $Ni_{75}Fe_{16}Cu_5Mo_4$ film is associated with a decrease in the value of perpendicular anisotropy, which, in its turn, can be caused by either the destruction of the columnar structure or relaxation of internal stresses in the film.

CONCLUSIONS

In this study, we have shown for the first time that a realization of the so-called transcritical state in $Ni_{75}Fe_{16}Cu_5Mo_4$ films is possible for a certain combination of the values of perpendicular anisotropy and size parameters of the films. Annealing decreases the value of perpendicular anisotropy that results in a decrease in the degree of transcriticality of the films and enhances their magnetic softness. Since the magnetic properties of thin films in the transcritical state, which are intended for applications in the regime of high-frequency magnetization reversal, are noticeably worse than those in the films with in-plane anisotropy, understanding the mechanism and conditions under which the transcritical state is formed is important from the standpoint of their possible use in electronic devices.

ACKNOWLEDGMENTS

This work was supported by the Ministry of Education of the Russian Federation (grant no. T02-05:1-3153), grant REC-005 (EK-005-X1), and the program “Ramon y Cajál” of the Ministry of Science and Technology of Spain.

REFERENCES

1. R. S. Beach and A. E. Berkowitz, Appl. Phys. Lett. **64**, 3652 (1994).
2. A. S. Antonov, S. N. Gadetskiĭ, A. B. Granovskiĭ, *et al.*, Fiz. Met. Metalloved. **83** (6), 60 (1997).
3. L. V. Panina and K. Mohri, Appl. Phys. Lett. **65**, 1189 (1994).
4. M. L. Sánchez, V. M. Prida, B. Hernando, *et al.*, Chin. Phys. Lett. **19**, 1870 (2002).
5. N. A. Buznikov, A. S. Antonov, and A. L. Rakhmanov, Pis’ma Zh. Tekh. Fiz. **29** (21), 88 (2003) [Tech. Phys. Lett. **29**, 920 (2003)].
6. H. B. Nie, A. B. Pakhomov, X. Yan, *et al.*, Solid State Commun. **112**, 285 (1999).
7. W.-S. Cho, H. Lee, and C.-O. Kim, Thin Solid Films **375**, 51 (2000).
8. Y. Sugita, H. Fujiwara, and T. Sato, Appl. Phys. Lett. **10**, 229 (1967).
9. W. H. Meiklejohn, F. E. Luborsky, and P. G. Frischmann, IEEE Trans. Magn. **23**, 2272 (1987).
10. H. Fujiwara, Y. Sugita, and N. Saito, Appl. Phys. Lett. **4**, 199 (1964).
11. A. A. Glazer, I. Yu. Konstantinova, A. P. Potapov, *et al.*, Fiz. Met. Metalloved. **33**, 946 (1972).
12. H. Miyajima, K. Sato, and T. Mizoguchi, J. Appl. Phys. **47**, 4669 (1976).

Translated by Yu. Vishnyakov

Technical Physics, Vol. 49, No. 7, 2004, pp. 872–875. Translated from Zhurnal Tekhnicheskoĭ Fiziki, Vol. 74, No. 7, 2004, pp. 66–69.
Original Russian Text Copyright © 2004 by Golyshev, Zhukov, Samartsev, Slepov.

OPTICS, QUANTUM ELECTRONICS

The Effect of Self-Phase-Modulation on the Stimulated Mandelstam–Brillouin Scattering in Fiber-Optic Communication Lines

V. Yu. Golyshev, E. A. Zhukov, I. É. Samartsev, and D. G. Slepov
Scientific–Technical Association IRE–Polyus, Fryazino, Moscow oblast, 141120 Russia
e-mail: mail@ntoire-polus.ru

Received August 27, 2003; in final form, December 9, 2003

Abstract—Stimulated Mandelstam–Brillouin scattering (SMBS) is experimentally studied in a fiber-optic communication line at a high power of the transmitted signal. The SMBS threshold is not observed at a power of up to 400 mW, which is due to an alternative nonlinear effect (self-phase-modulation (SPM)). An analytical model of SMBS in a single-mode fiber is developed with allowance for SPM. The theoretically estimated power of spontaneous scattering is substantially lower than the power obtained in the absence of SPM. The SMBS efficiency is plotted versus the spectral width of the signal at the input of the communication line. It is demonstrated that the SMBS effect is negligibly weak when the initial spectral width of the signal exceeds a certain threshold level. *© 2004 MAIK “Nauka/Interperiodica”.*

INTRODUCTION

In modern optical fiber communication lines (OFCLs), an increase in the transmission range is achieved by using erbium amplifiers working at wavelengths of about 1.5 μm. However, the increase in the power of the transmitted signal gives rise to various nonlinear effects (stimulated Raman scattering, self-phase modulation, cross-phase modulation, stimulated Mandelstam–Brillouin scattering (SMBS), and four-wave mixing) [1, 2]. In this work, we study the limitations imposed by SMBS on the transmission range of optical fibers.

SMBS is light scattering by acoustic vibrations of the medium. SMBS exhibits a very narrow gain spectrum ($\Gamma \approx 20$ MHz). At a certain critical level of the input signal power, an intense backward scattering can be induced. This scattering leads to a deterioration in the transmission quality. Therefore, the power of the transmitted signal must always be lower than the threshold level.

Smith [3] defines the SMBS critical power P_{crit} (SMBS radiation serves as the pumping for the backward Stokes radiation) in the approximation disregarding the signal depletion. This power is defined as the input pump power, at which the SMBS power at the beginning of the fiber equals the input pump power. For typical parameters of a single-mode fiber, the critical power is given by

$$P_{\text{crit}} \approx 21\frac{\alpha A}{g_0}. \qquad (1)$$

Quantities entering formula (1) and their values for a conventional single-mode coupled fiber and a wavelength of about 1.5 μm are presented in the table.

The SMBS threshold depends on both the parameters of the fiber and the signal linewidth [4–6]. If the gain $g(\nu)$ and pump spectra can be approximated using Lorentzian curves, the threshold power is still given by formula (1), but the peak gain is represented as

$$g_0^{\text{eff}} \approx \frac{\Gamma}{\Gamma + \Gamma_{\text{p}}} g_0, \qquad (2)$$

where Γ_{p} is the pump linewidth and Γ is presented in table.

Values of parameters

Parameter	Value
Fiber loss coefficient, α	5×10^{-5} m^{-1}
Nonlinear coefficient, γ	1.621×10^{-3} W^{-1} m^{-1}
Number of the fiber transverse modes, M	2
Temperature, T	300 K
Total SMBS spectral width	2×10^{7} Hz
Gain at half-maximum, Γ	
Peak SMBS gain, g_0	4×10^{-11} W^{-1} m
Effective area of the fiber transverse cross section, A	5×10^{-11} m^2
Acoustic phonon frequency, ν_{B}	1.11×10^{10} Hz
Pump radiation frequency, ν_{p}	1.93×10^{14} Hz

1063-7842/04/4907-0872$26.00 © 2004 MAIK “Nauka/Interperiodica”

Thus, if $\Gamma_p \gg \Gamma$, the SMBS gain decreases by a factor of Γ_p/Γ.

In the general case, the SMBS gain and, hence, the threshold power depend on a convolution of the SMBS spectrum and the pump radiation spectrum [4, 5]. In this connection, the type of modulation (amplitude, phase, or frequency) also plays an important role. Cotter [7] analyzes in details various types of modulation of the transmitted signal. The dependences of the gain on the data rate in the optical fiber are obtained in [5, 8] for the amplitude, phase, and frequency modulation. The threshold powers of the input signals with the amplitude modulation calculated using these dependences for various data rates (622, 1000, 1250, and 2500 Mbit/s) are about 15 dBm.

EXPERIMENT

We measured the SMBS threshold in a single-mode fiber with a length of 200 km. An unmodulated laser diode with a distributed feedback, a wavelength of 1550 nm, and a spectral width of 50 MHz served as a source of radiation. The solid curve in Fig. 1 shows the dependence of the signal power at the fiber exit on the input power. The experimental data are in good agreement with the calculated values of the threshold. For a cw signal, the calculated threshold power is about 9.7 dBm.

The dashed line in Fig. 1 shows a similar dependence corresponding to the transmission of a bit chain at a rate of 2500 Mbit/s. In the presence of a direct modulation of the laser diode, the SMBS threshold is not reached when the input power ranges from 1 to 400 mW. This fact contradicts the theoretical estimates (18–19 dBm). In our opinion, the reason for this is the spectral broadening of the transmitted signal that is related to the self-phase modulation (SPM).

SPM emerges owing to the dependence of the refractive index of the nonlinear medium on the radiation intensity. SPM leads to the spectral broadening of optical pulses [6]. Figure 2 shows the spectral profiles of the signals having passed through the 200-km-long fiber. The results were obtained using an optical analyzer. The curves correspond to the input power ranging from 3 to 25.5 dBm. It is seen that the increase in the input power results in a substantial broadening of the base of the central peak. The broadening of the central peak is within the analyzer resolution (0.1 nm).

The existing calculations of the SMBS threshold do not take into account the SPM effect. We propose an analytical model of SMBS evolution that takes into account the SPM effect and is used to theoretically calculate the critical power in long ($L \gg \alpha^{-1}$) communication lines.

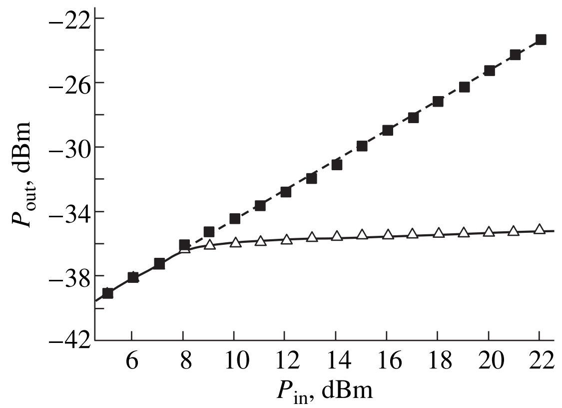

Fig. 1. Plot of the output optical power P_{out} vs. the input optical power P_{in} for the optical fiber with a length of 200 km.

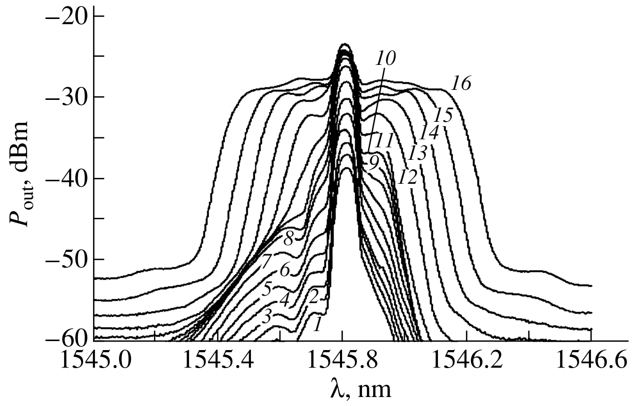

Fig. 2. Spectra of the output signal for the single-mode fiber with a length of 200 km transmitting a bit chain at a rate of 2500 Mbit/s and input optical powers of (*1*) 3, (*2*) 4.5, etc. (with an increment of 1.5 dB), (*16*) 25.5 dBm.

ANALYTICAL MODEL

We assume that the pump and Stokes waves propagate along the positive and negative directions of the z axis, respectively, in a fiber with the length L. In accordance with the results from [3, 8], the differential equation for the spectral density of the number N_S of the Stokes photons is written as

$$\left(\frac{d}{dz} - \alpha\right) N_S(z, \nu_S) = -\frac{1}{A}[g(\nu) \otimes P_p(z, \nu)]_{\nu_S} \times (N_S(z, \nu_S) + 1), \tag{3}$$

where $P_p(z, \nu)$ is the spectral power density of the pump radiation, $g(\nu)$ is the SMBS gain spectrum, and the symbol $\otimes$ denotes the convolution of the spectral functions.

In the absence of the signal at the fiber exit, the solution of Eq. (3) is represented as

$$N_S(0, \nu_S) = \frac{1}{A}\int_0^L d\xi [g(\nu) \otimes P_p(\xi, \nu)]_{\nu_S} \times \exp\left\{\frac{1}{A}\int_0^{\xi} d\eta [g(\nu) \otimes P_p(\eta, \nu)]_{\nu_S} - \alpha\xi\right\}. \tag{4}$$

Then, the total power of the Stokes radiation at the beginning of the fiber is represented as

$$P_S(0) = M\left(1 + \frac{k_B T}{h\nu_B}\right)\int_{-\infty}^{+\infty} d\nu_S h\nu_S N_S(0, \nu_S), \tag{5}$$

where k_B is the Boltzmann constant.

It is demonstrated in [9, 10] that, at a high pump power, the SMBS spectrum can be approximated using a linear combination of the Lorentzian and Gaussian curves. To simplify the calculations, we assume that the SMBS gain spectrum is approximated with the Gaussian function

$$g(\nu) = g_0 \exp\left\{-4\ln 2\frac{(\nu - \nu_B)^2}{\Gamma^2}\right\}. \tag{6}$$

We also assume that the pumping is a series of Gaussian pulses with the peak power $P_p(\xi)$ and the repetition period τ. It can easily be demonstrated that the pump power spectrum is given by

$$P_p(\xi, \nu) = \frac{P_p(\xi)}{4\pi\tau\langle\nu^2\rangle_{\xi}}\exp\left\{-\frac{(\nu - \nu_p)^2}{2\langle\nu^2\rangle_{\xi}}\right\}, \tag{7}$$

where $\langle\nu^2\rangle_{\xi}$ is the mean-square spectral width of a single pulse.

It is demonstrated in the Appendix that the main contribution to the integral in expression (5) is related to the values that $P_p(z, \nu)$ and $g(\nu)$ take in the vicinity of the corresponding maxima. Therefore, the specific types of spectral functions are not important. For simplicity, we choose the Gaussian profiles.

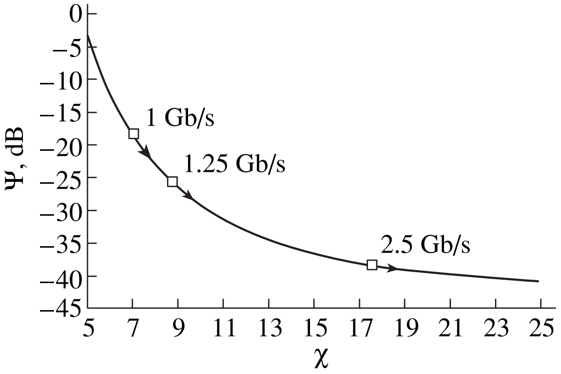

Fig. 3. Plot of pump-to-SMBS transformation efficiency vs. the normalized mean-square width of the pump spectrum at the beginning of the fiber.

In the absence of the pump depletion related to SMBS, the pump power is given by $P_p(z) = P_p(0)\exp\{-\alpha z\}$. The pump spectral width increases with fiber length owing to SPM [6]:

$$\langle\nu^2\rangle_z = \langle\nu^2\rangle_0\left(1 + \frac{4}{3^{3/2}}\left(\frac{\gamma}{\alpha}P_p(0)\right)^2(1 - \exp\{-\alpha z\}^2)\right). \tag{8}$$

Here, $\langle\nu^2\rangle_0$ is the mean-square spectral width of the pump radiation at the beginning of the fiber.

In the Appendix, we perform a calculation using formula (5) with allowance for expressions (4) and (6)–(8). The final result is

$$P_S(0) = \Psi(\xi)P_p(0), \tag{9}$$

where the pump-to-Stokes transformation efficiency is given by

$$\Psi(\chi) = Mk_B T\frac{2\pi^{3/2}}{3^{3/4}}\frac{\nu_p}{\nu_B}\sqrt{\frac{\Gamma\chi}{\tau}}\frac{\gamma}{\alpha}G(\chi)^{-3/2}\exp G(\chi). \tag{10}$$

Here, $\chi = \langle\nu^2\rangle_0\tau/\Gamma$ is the normalized mean-square width of the pump spectrum and

$$G(\chi) = \frac{3^{3/4}}{32}\sqrt{\frac{\pi}{\ln 2}}\frac{g_0}{\gamma A}\frac{1}{\chi}.$$

Figure 3 shows the dependence $\Psi(\chi)$. In calculations, we employ the parameters presented in the table.

Let us use the definition of the critical SMBS power from [3]: $P_{crit} = P_p(0) = P_S(0)$. Taking into account the power balance, we can use this definition only for the solution derived disregarding the pump depletion related to the backscattering. At $\Psi = 1$, the mean-square width of the pump spectrum corresponding to the threshold is $\chi_{cr} = 4.8$ and the bit rate is $B_{cr} = 680$ Mbit/s. The increase in the data rate leads to a sharp decrease in the pump transformation efficiency, so that the SMBS threshold cannot be reached at an arbitrary high power. In this case, the nonlinear broadening of the pump spectrum dominates over the SMBS process. Thus, at a data rate of greater than 1 Gbit/s and a relatively high power of the signal (expression (10) is obtained at $P_p(0) \gg 35$ mW), we can neglect the Mandelstam–Brillouin scattering in OFCS.

Squares in Fig. 3 show the values of Ψ calculated for various bit rates of the data transmission in OFCS. To estimate the mean-square spectral width of the Gaussian pulsed pump radiation, we used the following formula from [6]: $\langle\nu^2\rangle_0 \approx 2\left(\frac{B}{\pi}\right)^2\ln 2$. Note that we overestimated the SMBS efficiencies owing to the following reasons. First, the leading edges of the transmitted pulses are steeper than the leading edge of the Gaussian pulse especially at low data transmission rates. Second, in the case of a direct modulation of the laser diode (source of the signal), its emission line exhibits a chirped structure resulting in additional spectral broadening. Therefore, even at a data transmission rate of about 622 Mbit/s, the SMBS effect is relatively weak.

CONCLUSIONS

We propose an analytical model of SMBS in OFCS, which takes into account the SPM effect, and present the results of theoretical calculations. We demonstrate that the power of the Stokes scattering substantially decreases owing to the SPM-induced spectral broadening of the signal. Consequently, the pump transformation efficiency decreases with increasing width of the radiation spectrum at the fiber entrance. We estimate the upper limit of the efficiency for a conventional single-mode fiber and a wavelength of about 1.5 μm for various bit rates of data transfer. If the mean-square spectral width $\chi = \tau\langle\nu^2\rangle_0/\Gamma$ is greater than 6 and the bit rate is higher than 622 Mbit/s, SMBS is negligibly low (the efficiency is less than 6.6%). In this case, the SPM-induced nonlinear broadening dominates over the SMBS process. The results obtained can be helpful in developing modern fiber-optic systems for long-range communications.

APPENDIX

Substituting expressions (4) and (6)–(8) into formula (5) and changing variables ($x = 1 - \exp\{-\alpha\xi\}$, $y = 1 - \exp\{-\alpha\eta\}$, and $f = \nu/\sqrt{2\langle\nu^2\rangle_0}$) with allowance for $h(\nu_p - \nu_B)\left(1 + \frac{k_B T}{h\nu_B}\right) \approx \frac{\nu_p}{\nu_B}k_B T$, $1 - \exp\{-\alpha L\} \approx 1$, and $\sqrt{\langle\nu^2\rangle_0} \gg \Gamma/\sqrt{8\ln 2} \approx 8.5$ MHz, we find that

$$P_S(0) = Mk_B T\frac{\nu_p}{\nu_B}\frac{g_0 P_p(0)}{\alpha A}\frac{\Gamma}{4\tau\sqrt{2\pi\langle\nu^2\rangle_0\ln 2}}$$

$$\times\int_{-\infty}^{+\infty}df\int_0^1 dx\frac{1-x}{1+\frac{4}{3^{3/2}}\left(\frac{\gamma}{\alpha}P_p(0)x\right)^2}$$

$$\times\exp\left\{-\frac{f^2}{1+\frac{4}{3^{3/2}}\left(\frac{\gamma}{\alpha}P_p(0)x\right)^2}\right\}\exp\left\{\frac{g_0 P_p(0)}{\alpha A}\frac{\Gamma}{8\tau\langle\nu^2\rangle_0\sqrt{\pi\ln 2}}\right. \tag{11}$$

$$\left.\times\int_0^x dy\frac{1}{1+\frac{4}{3^{3/2}}\left(\frac{\gamma}{\alpha}P_p(0)y\right)^2}\exp\left\{-\frac{f^2}{1+\frac{4}{3^{3/2}}\left(\frac{\gamma}{\alpha}P_p(0)y\right)^2}\right\}\right\}.$$

We assume that the peak value of the exponent of the second exponential function is much greater than unity:

$$G = \frac{3^{3/4}}{32}\sqrt{\frac{\pi}{\ln 2}}\frac{g_0}{\gamma A}\frac{1}{\chi} \gg 1.$$

This condition is satisfied for the parameters presented in the table at $\chi = \tau\langle\nu^2\rangle_0/\Gamma \ll 75$. In this case, we can use the Laplace method to estimate the integrals with respect to variables f and x. At $G \gg 1$, the main contribution to the integral

$$\int_{-\infty}^{+\infty}df\int_0^1 dx\,u(f, x)\exp\{Gh(f, x)\}$$

corresponds to the points where the positive function $h(f, x)$ reaches maximum (i.e., in the vicinity of $f = 0$ and $x = 1$). We expand function $h(f, x)$ into a Taylor series in the vicinity of the maximum points and retain the terms f^2 and $x - 1$. Then, we integrate with respect to f and x. The final result (expression (9)) is written for the case

$$P_p(0) \gg \frac{3^{3/4}}{2}\frac{\alpha}{\gamma} \approx 35 \text{ mW}.$$

REFERENCES

1. R. H. Stolen, Proc. IEEE **68**, 1232 (1980).
2. A. R. Chraplyvy, J. Lightwave Technol. **8**, 1548 (1990).
3. R. G. Smith, Appl. Opt. **11**, 2489 (1972).
4. E. Lichtman and A. A. Friesem, Opt. Commun. **64**, 544 (1987).
5. Ya. Aoki, K. Tajima, and I. Mito, J. Lightwave Technol. **6**, 710 (1988).
6. G. P. Agrawal, *Nonlinear Fiber Optics* (Academic, London, 1995).
7. D. Cotter, Electron. Lett. **18**, 504 (1982).
8. E. Lichtman, R. G. Waarts, and A. A. Friesem, J. Lightwave Technol. **7**, 171 (1989).
9. A. Gaeta and R. W. Boyd, Phys. Rev. A **44**, 3205 (1991).
10. X. Bao *et al.*, Opt. Lett. **24**, 510 (1999).

Translated by A. Chikishev

Technical Physics, Vol. 49, No. 7, 2004, pp. 876–883. Translated from Zhurnal Tekhnicheskoĭ Fiziki, Vol. 74, No. 7, 2004, pp. 70–77.
Original Russian Text Copyright © 2004 by Kucherov.

OPTICS, QUANTUM ELECTRONICS

Bleaching Channel in a Fluid Layer under Laser Pulse Propagation

A. N. Kucherov
Zhukovsky Central Institute of Aerohydrodynamics, Zhukovskiĭ, Moscow oblast, 140180 Russia
e-mail: ank@aerocentr.msk.su

Received September 15, 2003; in final form, December 29, 2003

Abstract—The bleaching effect induced by a short microsecond laser pulse in a fluid layer is studied. In the first approximation, the refractive and absorption indices are assumed to be linearly dependent on the fluid density. The similarity parameters are derived, the characteristics of the bleaching channel are studied as functions of the heat-release parameter and Euler number, and the results are interpreted in terms of physical variables. *© 2004 MAIK “Nauka/Interperiodica”.*

INTRODUCTION

The increase in the transparency of strongly absorbing fluids (including water) under the action of a short laser pulse was first observed in [1] and studied experimentally in [2–7]. Giant pulses with duration $\tau = 1.2$–1.3 µs, pulse trains (with total duration $\Delta t \sim 1$ µs), and single short pulses with duration $\tau \sim 10^{-10}$ s, wavelengths $\lambda = 2.94$ [3] and 2.79 µm [4], and an energy up to 20 mJ have been studied. The transparency increased by a factor of 20 in the experiments with a giant pulse, by a factor of 40 for a single short pulse, and by a factor of 540 for a pulse train [6]. It was shown in [8] that, for $\tau \sim 1$ µs (giant pulse) and $\lambda = 2.94$ µm, the hydrodynamic mechanism (expansion of a strongly heated substance from the center of a laser spot and a decrease in the absorption coefficient because of a decrease in the density of irradiated substance) explains the experimental data on water bleaching. This work is devoted to the study of the characteristics of the bleaching channel and ambient fluid (extreme velocities, densities, temperatures, and pressures and width of the bleaching channel) as functions of the parameters of the laser pulse (its energy, transverse size, and duration) and medium.

STATEMENT OF THE PROBLEM

A thin layer of a strongly absorbing fluid with thickness $L \leq \alpha^{-1} \sim 1$ µm $\ll r_0$ (α is the absorption coefficient and r_0 is the pulse transverse size) is placed between two ~1-mm-thick quartz plates [1, 6]. A radiation pulse with the transverse intensity distribution $g(r)$, the time shape $f(t)$, wavelength $\lambda \sim 3$ µm, and energy E_{in} on the order of 1–10 mJ is incident perpendicularly on one of the plates. A photodetector behind another plate measures the radiation intensity I and energy E_{out} transmitted through the layer. The bleaching effect consists in an increase in the medium transparency (transmittance) $T_{\text{tr}} = E_{\text{out}}/E_{\text{in}}$ by one or more orders of magnitude with an increase in the pulse energy. We assume that the quantum-mechanical properties of water molecules remain unchanged. It follows from the Lorentz–Lorenz relation [9; 10, p. 67] that, in the leading approximation, the absorption coefficient and refractive index depend linearly on the medium density; i.e., $\alpha \approx \alpha_0\rho/\rho_0$ (Fig. 1).

Using the Maxwell equation for a nonlinear strongly absorbing medium [11–14] and taking into account that the pulse transverse size r_0 far exceeds the layer thickness L, one can obtain ordinary differential equations for the radiation intensity $I = EE^*$, and phase Φ ($E = \sqrt{I}\exp(ik\Phi)$ is the perpendicular component of a

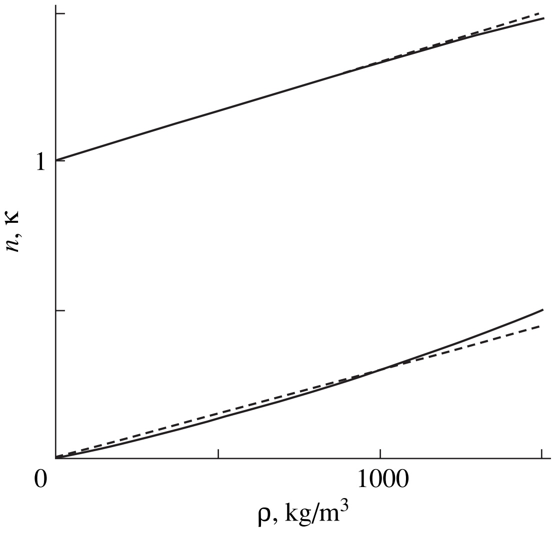

Fig. 1. Refractive n and absorption κ indices (lower curves, absorption coefficient $\alpha = 4\pi\kappa/\lambda$) as functions of medium density ρ. The dashed lines are linear approximations $n = n_0\rho/\rho_0$ and $\kappa = \kappa_0\rho/\rho_0$.

slowly varying electric-vector component [13] and $k = 2\pi/\lambda$ is the wave number)

$$\begin{cases} \dfrac{\partial^2 I}{\partial z^2} - \dfrac{1}{2I}\left(\dfrac{\partial I}{\partial z}\right)^2 - 2k^2 I\left(\dfrac{\partial \Phi}{\partial z}\right)^2 + 2k^2 I(n^2 - \kappa^2) = 0 \\ \dfrac{\partial^2 \Phi}{\partial z^2} + \dfrac{1}{I}\dfrac{\partial \Phi}{\partial z}\dfrac{\partial I}{\partial z} + 2kn\kappa = 0. \end{cases} \tag{1}$$

The initial conditions are

$$I(z=0) = I_0, \quad \Phi(z=0) = 0,$$
$$\frac{\partial I(0)}{\partial z} = \alpha_0, \quad \frac{\partial \Phi(0)}{\partial z} = n_0, \tag{2}$$

where I_0, $\alpha_0 = 2k\kappa_0$, and n_0 are, respectively, the intensity, absorption coefficient, and refractive index at the medium input $z = 0$.

We have found that, when obtaining the numerical solution, the radiation intensity decay in the absorbing medium obeys the exponential law at each z step; i.e., $I(z + \Delta z, r, t) = I(z, r, t)\exp(-\alpha(\rho)\Delta z)$. The resonance phenomena are disregarded in this work. The density perturbation can be found from the hydrodynamical equations [15]. In our case, these are the complete Navier–Stokes equations in the cylindrical coordinates. An important role belongs to the equation of state for water [16, 17], which was chosen here as a relationship between the pressure p, density ρ, and internal energy ε using the Helmholtz free energy $F(\rho, T)$, where T is temperature [18],

$$p(\rho, T) = \rho^2\left(\frac{\partial F}{\partial \rho}\right)_T, \quad \varepsilon(\rho, T) = F - T\left(\frac{\partial F}{\partial T}\right)_\rho. \tag{3}$$

The equations for the medium were solved numerically by the large-particle method [19], which allowed continuous computation without considering the discontinuity surfaces and lines for the required functions (shock waves). The initial and boundary conditions for the hydrodynamic parameters are

$$u = 0, \quad w = 0, \quad \rho = \rho_0,$$
$$\varepsilon = \varepsilon_0, \quad p = p_0, \quad T = T_0 \quad \text{for} \quad t = 0; \tag{4}$$

$$u = 0 = \frac{\partial \rho}{\partial r} = \frac{\partial w}{\partial r} = \frac{\partial \varepsilon}{\partial r} = \frac{\partial p}{\partial r} \quad \text{for} \quad r = 0; \tag{5}$$

$$L \quad w = 0 \quad \text{for} \quad z = 0. \tag{6}$$

It follows from the law of conservation of the longitudinal momentum component that, if $L \ll r_0$, the pressure is constant along the longitudinal coordinate z and, in the main approximation, the longitudinal velocity component is identically equal to zero ($w \equiv 0$). Next we consider a one-dimensional nonstationary problem with two independent variables: coordinate r and time t.

Let us introduce the dimensionless parameters through normalizing the time t to the pulse duration τ; the coordinate r to the exponential radius r_0; the coordinate z to the path length (layer thickness) L; the intensity I to its characteristic value $I_{00} = E_{\text{in}}/(\pi r_0^2 \tau)$; the density ρ, pressure p, and temperature T to their critical values $\rho_* = 317.763$ kg/m^3, $p_* = 221.15 \times 10^5$ Pa, and $T_* = 647.27$ K (water), respectively; the internal energy ε to $\varepsilon_* = 2.026$ MJ/kg; the velocity u to its characteristic value $u_0 = r_0/\tau$; and the dynamic viscosity μ to its value $\mu_0 = 6.44 \times 10^{-5}$ kg/(m s) at the near-critical temperature $T = 644$ K. On the pulse time scale $\tau \sim 10^{-6}$ s, the fluid undergoes acoustic turbulization (in a time on the order of the time $\tau_a \sim L/a \sim 10^{-9}$ s of perturbation passage across the layer, where $a \sim 1.5 \times 10^3$ m/s is the sound velocity in fluid), and its transport parameters, such as viscosity, diffusivity, and heat conductivity, increase substantially. A comparison of the theoretical and experimental dependences of transparency showed that the coefficients of turbulent viscosity and heat conductivity are several orders greater than the corresponding molecular transport parameters. The dimensionless equations include the following similarity parameters (in addition to the initial ρ_0/ρ_*, p_0/p_*, and $\varepsilon_0/\varepsilon_*$):

$$\text{Re} = \frac{\rho_* u_0 r_0}{\mu_0}, \quad \text{Eu} = \frac{p_*}{\rho_* u_0^2}, \quad \text{Pe} = \text{RePr},$$

$$Q = \frac{\alpha I_{00} \tau}{\rho_0 \varepsilon_*} = \frac{\alpha E_{\text{in}}}{\rho_0 \pi r_0^2 \varepsilon_*}.$$

Here, Eu is the Euler number; Q is the heat-release parameter; $I_{00} = E_{\text{in}}/(\pi r_0^2 \tau)$ is the characteristic radiation intensity; Re and Pe are the Reynolds and Peclet numbers, respectively; $\text{Pr} = \nu/\chi$ is the Prandtl number; ν is the kinematic viscosity coefficient; and χ is the temperature conductivity coefficient of the medium (we take $\text{Pr} \approx 1$ for a turbulent medium). In the dimensionless variables, the rate of heat release in the layer can be written as

$$q(r, t) = Q\rho I(r, t),$$
$$I(r, t) = f(t)g(r)\exp[-N_\alpha \Delta z \rho(r, t)], \tag{7}$$
$$N_\alpha = \alpha L \rho_*/\rho_0,$$

where N_α is the absorption parameter or optical thickness of the layer, $f(t)$ is a Gaussian pulse time shape [1] (Fig. 2, curve II) or a linear shape up to τ/n ($n = 2$–5) followed by a Gaussian decrease (Fig. 2, curve I), Δz is the layer effective thickness (introduced to take into account the radiation absorption in an optically thick medium).

Consider the initial Gaussian radiation transverse distribution $g(r) = \exp(-r^2)$. A numerical solution was constructed using a step Δr of $0.05r_0$ and the time step $\Delta t = 0.002$–0.000125τ. The grid points covered the region $-0 \le r/r_0 \le 400\Delta r/r_0 = 20$ and $0 \le t/\tau \le 3$.

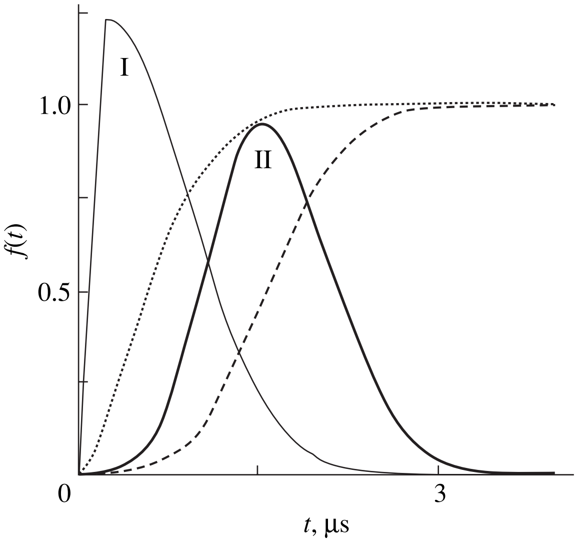

Fig. 2. Pulse time shape $f(t)$ (dots and dashes are for the time integrals $\int f(t)dt$: (I) $f(t) = C_1t/\tau$ at $0 \le t \le t_1 = \tau/n$ (n = 2–5, $C_1 = 2n/[1/n + \sqrt{(\pi/C_2)}]$, $C_2 = \ln 2/[1 - 1/2n]^2$ and $f(t) = 0.5C_1\exp[-C_2((t - t_1)/\tau)^2]$ at $t > t_1$; (II) $f(t) = C\exp[-C_i((t_i - t_1)/\tau)^2]$, where $C = 2/[\sqrt{\pi}(1/\sqrt{C_2} + 1/\sqrt{C_3})]$, $C_i = \ln 2/((t - t_1)/\tau)^2$, $i = 2$ and $t_2 = 0.848\tau$ for $0 \le t \le t_1 = 1.273\tau$, and i = 3 and $t_3 = 1.848\tau$ for $t > t_1$ [1, 6].

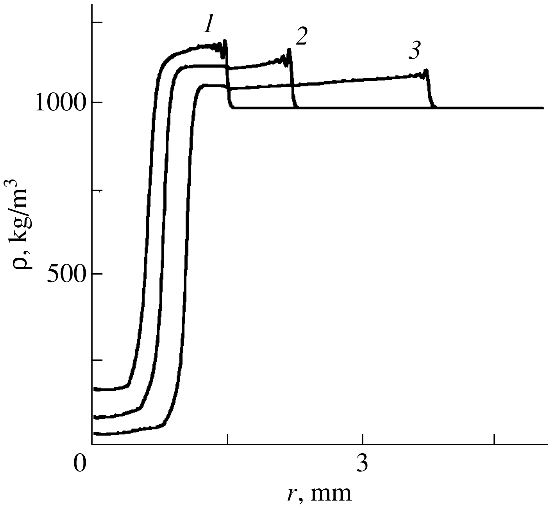

Fig. 3. Water density $\rho(r, t)$ at different instants of time: t = (*1*) 0.72, (*2*) 1.08, and (*3*) 1.9 μs. The similarity parameters are: Q = 47.47 (E_{in} = 15 mJ), Euler number Eu = 1.578, absorption parameter N_α = 0.0334 ($T_{tr,0}$ = 0.9), Reynolds number Re = 5.222, Prandtl number Pr = 1, and pulse shape $f(t)$ I.

SOLUTIONS FOR A GIANT PULSE: OPTICALLY THIN LAYER

We first consider an optically thin layer with the initial transparency $T_{tr,0}$ = 0.9, thickness $L = (1/\alpha_0)\ln[1/T_{tr,0}]$ = 0.0823 μm, and absorption parameter N_α = 0.0334 (absorption coefficient $\alpha_0 = 1.28 \times 10^6$ m^{-1} for λ = 2.94 μm). Let the area of laser spot be $s = \pi r_0^2 = 2 \times 10^{-7}$ m^2 (r_0 = 0.252 mm) and the pulse duration τ = 1.2 μs. We are interested in the medium and bleaching-channel parameters as functions of the heat-release parameter in the range Q = 0–47.47 (E_{in} = 0–15 mJ) with fixed remaining parameters. The heating process is characterized by a rapid rise in temperature T and internal energy ε in the irradiated region and a sharp maximum at the center. The fluid density in this strongly heated region decreases monotonically (by more than two orders of magnitude) up to $t \sim 10\tau \sim 10^{-5}$ s. The pressure at the initial stage increases rapidly to ~1 GPa (Table 1) to initiate fluid motion from the center with a velocity on the order of u_0 = 219 m/s. After the velocity at the front of the perturbed fluid region increases to ~$10r_0$ in a time ~τ and exceeds the sound velocity, a bow shock wave arises. A low-density region formed by the pulse leading edge, where the absorption coefficient decreases by more than an order of magnitude, is a bleaching channel through which the tail of the pulse energy passes [8]. The bleaching channel (transverse distributions $\rho(r, t)$) is shown in Fig. 3 for different instants of time in the interval 0–1.9 μs. In Table 1, the transparency T_{tr} and the maximal values of temperature T_m, pressure p_m (at the center r = 0), velocity $u_m = \max[u(r, t)]$, and sound velocity a_m (r = 0) are given as functions of pulse energy E_{in} or heat-release parameter Q. The minimal values of density (at the center at t = 1.9 μs) and the channel width on a level of $0.5\alpha_0$ toward the pulse end Δ_1 (t = 1.9 μs), and at the middle of the pulse Δ_2 (at t = 0.78 μs, when the energy $E(t)$ of emitted radiation is equal to one-half of the total energy $E = 0.5E_{in}$) are also given in the table.

The densities $\rho(r, t)$ at the pulse end (t = 1.9 μs) are shown in Fig. 4 for the heat-release parameters Q = 3.17, 9.495, 28.48, and 47.47 (curves *1*–*4*, respectively). The bleaching channel expands and deepens with an increase in Q. The interval ΔQ = 1.58–3.165 is the threshold of the effect relative to the parameter Q (absorbed laser energy αE_{in}). The transparency T_{tr} increases almost threefold (from 0.01 to 0.028), whereas it changes by only a factor of 2.3 in the main range of heat-release parameter Q from 3.165 to 47.47. In the heat-release range considered, the channel width increases severalfold, and the growth rate decreases from ~100% (Q = 1.58) to almost zero (at Q = 47.47).

Note that the results presented in Table 1 can be considered, in physical variables, as functions obtained at a fixed pulse energy E_{in} = 15 mJ for different absorption coefficients in the range $\alpha_0 = 4.267 \times 10^4$ m^{-1}–1.28×10^6 m^{-1}, λ = 2.94 μm (E_{in} = 37.2 mJ, $\alpha_0 = 1.720 \times 10^4$ m^{-1}–0.516×10^6 m^{-1}, λ = 2.79 μm), and different layer thicknesses $L = [\ln(1/T_{tr,0})]/\alpha_0$ = 2.47–0.0823 μm (L = 6.125–0.204 μm for λ = 2.79 μm). Another possible interpretation of the results in Table 1 is the follow-

Table 1. Transparency T_{tr}; maximal temperature T_m, pressure p_m, sound velocity a_m (at the center $r = 0$), and velocity $u_m = \max[u(r, t)]$; minimal density (at $t = 1.9$ µs and $r = 0$); the transverse size (radius) of the bleaching channel at the end Δ_1 ($t = 1.9$ µs) and middle Δ_2 ($t = 0.785$ µs) of the pulse. Similarity parameters: heat-release parameter $Q = 1.58$–47.47 ($E_{in} = 0.5$–15 mJ); Euler number Eu = 1.578; absorption parameter $N_\alpha = 0.0334$ ($T_{tr,\,0} = 0.9$); Reynolds number Re = 5.222; Prandtl number Pr = 1; and pulse shape $f(t)$ I (absorption coefficient $\alpha_0 = 1.28 \times 10^6$ m^{-1}, wavelength $\lambda = 2.94$ µm, $L = 0.0823$ µm, $r_0 = 252$ µm)

E_{in}, mJ	0.5	1	3	5	9	13	15
Q	1.58	3.165	9.495	15.82	28.48	41.14	47.47
T_{tr}	0.91	0.928	0.949	0.956	0.961	0.9637	0.9645
T_m, K	750	1345	3604	4370	4475	4552	4580
t, µs	1.427	1.536	1.438	1.267	1.382	1.421	1.751
p_m, GPa	0.078	0.1953	0.5799	0.8233	1.142	1.362	1.468
t, µs	0.3714	0.3696	0.3024	0.2808	0.2554	0.2406	0.2400
a_m, m/s	1667	1748	1882	1943	2008	2044	2154
t, µs	0.311	0.247	0.178	0.149	0.122	0.118	0.264
u_m, m/s	99.5	187	338	418	520	591	624
t, µs	1.739	1.082	0.648	0.523	0.444	0.406	0.408
ρ_{min}, kg/m^3	208.2	90.66	42.79	39.31	39.24	37.39	34.56
Δ_1, mm	0.246	0.442	0.706	0.824	0.943	1.00	1.003
Δ_2, mm	0	0.134	0.362	0.451	0.542	0.599	0.619

ing: at a fixed absorption coefficient $\alpha_0 = 0.516 \times 10^6$ m^{-1} ($\lambda = 2.79$ µm) and water layer thickness $L = 0.204$ µm, pulse energy varies in the range $E_{in} = 1.24$–37.2 mJ.

Let us fix the heat-release parameter $Q = 47.47$ and absorption parameter $N_\alpha = 0.0334$ and vary the Euler number Eu in the range 0.1–10. In physical variables, this test series can be interpreted as a variation of the pulse transverse size $r_0 = 1.001$–0.1001 mm with a simultaneous change in the pulse energy E_{in} from 2.361 to 236.1 mJ or as a change in the pulse duration $\tau = 0.302$–3.02 µs ($r_0 = 0.252$ mm, $E_{in} = 15$ mJ). In Table 2, the medium and bleaching-channel parameters are given for various Euler numbers Eu = 0.1–10 and fixed heat-release ($Q = 47.47$) and absorption ($N_\alpha = 0.0334$) parameters.

The channel relative radius at the middle Δ_2 of the pulse and at its end Δ_1 are shown in Fig. 5 as functions of the Euler number (curves *1*, *2*; parameters $Q = 47.47$, $N_\alpha = 0.0334$, Re = 5.222). A bleaching channel produced by a pulse with Gaussian transverse intensity distribution is wider than the initial pulse size by a factor of two to three even at the middle of the pulse duration (for Eu = 0.5–10). If a second (even wider) pulse is emitted at the subsequent time interval, its transmittance can be close to unity. The particular value of the transparency function for the second pulse clearly depends on its transverse size, duration, and on the medium absorption coefficient (radiation wavelength). As the Euler number decreases from 0.5 to 0.1, the bleaching effect weakens drastically and disappears as Eu $\longrightarrow$ 0.

OPTICALLY THICK LAYER

We next consider the situation where the initial transparency is low, $T_{tr,\,0} = 0.02$ (Fig. 3 in [6]), $\tau = 1.2$ µs, $r_0 = 0.252$ mm, $\alpha_0 = 1.28 \times 10^6$ m^{-1} ($\lambda = 2.94$ µm), $L = 3.056$ µm, and the pulse time shape has the form II. In [8], a satisfactory agreement (~10%) with the experimental data was attained for this variant in a model of a one-dimensional (thin) layer with $Q =$

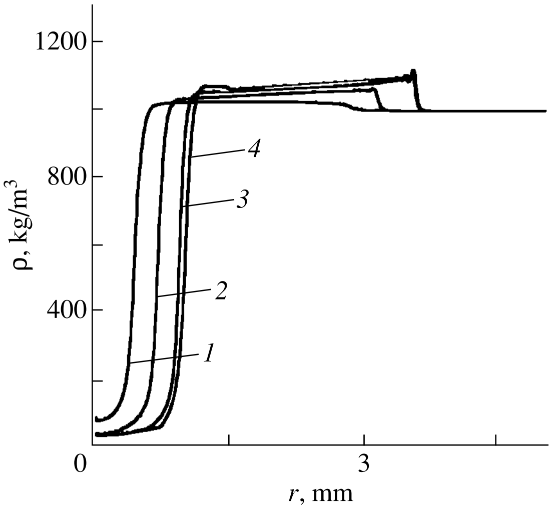

Fig. 4. Water density $\rho(r, t)$ for different values of similarity parameters: Q = (*1*) 3.17, (*2*) 9.5, (*3*) 28.5, and (*4*) 47.5 (E_{in} = 1, 3, 9, and 15 mJ, respectively) for time $t = 1.9$ µs. Euler number Eu = 1.578, absorption parameter N_α = 0.0334 ($T_{tr,\,0} = 0.9$), Reynolds number Re = 5.222, Prandtl number Pr = 1, and pulse shape $f(t)$ I.

Table 2. The extreme values of the medium parameters: maximal temperature T_m, pressure p_m, density ρ_m, sound velocity a_m (at $r = 0$), and fluid velocity $u_m = \max[u(r, t)]$ at the corresponding instants of time t; the transverse size of the bleaching channel at the end Δ_1 ($t = 1.5$ μs) and middle Δ_2 ($t = 0.785$ μs) of the pulse; the integrated layer transparency $T_{tr} = E_{out}/E_{in}$; and the minimal density ρ_{min} ($t = 1.5$ μs) as functions of the Euler number $\mathrm{Eu} = p_*/\rho_* u_0 = 0.1$–10 for the heat-release parameter $Q = \alpha E_{in}/(\rho_0 \varepsilon_* \pi r_0^2) = 47.47$ ($I_{00} = 6.25 \times 10^{11}$ W/m^2) and absorption parameter $N_\alpha = 0.0334$ ($T_{tr,0} = 0.9$); pulse shape $f(t)$ I

Eu	0.1	0.5	1.578	3	5	10
r_0, μm	1001	447.7	252	182.8	141.6	100.1
E_{in}, mJ	236.1	47.2	15	7.87	4.72	2.36
T_{tr}	0.9326	0.9536	0.9645	0.9720	0.9760	0.9795
T_m, K	4600	4571	4563	4511	4487	4458
t, μs	1.627	1.378	1.103	1.090	0.9672	0.8484
p_m, GPa	3.860	2.483	1.468	1.071	0.8388	0.5956
t, μs	0.288	0.2856	0.2400	0.2160	0.192	0.180
ρ_m, kg/m^3	1315	1252	1182	1176	1151	1121
t, μs	0.9120	0.8736	0.7176	0.4776	0.3120	0.2760
a_m, m/s	2630	2466	2154	2036	1987	1820
t, μs	0.288	0.262	0.264	0.276	0.288	0.288
u_m, m/s	975.4	720	624	534	481	410
t, μs	0.624	0.454	0.408	0.371	0.336	0.300
ρ_{min}, kg/m^3	230.1	126.4	52.02	31.45	17.75	13.33
Δ_1, mm	2.11	1.33	0.90	0.735	0.615	0.525
Δ_1/r_0	2.108	2.970	3.571	4.020	4.343	5.25
Δ_2, mm	0	0.851	0.619	0.501	0.421	0.330
Δ_2/r_0	0	1.90	2.456	2.740	2.973	3.30

0–18.96 (E_{in} = 0–6 mJ, Eu = 1.578, $N_\alpha = 0.318$). The heat source was taken to be $q = Qg(r)f(t)$. The agreement can be improved by the introduction of an effective absorption layer Δz, $q = Qg(r)f(t)\exp[-N_\alpha \rho(r, t)\Delta z]$, to take into account the variation of heat-release intensity with absorption-layer depth. In Fig. 6, the experimental (+ signs in [6]) and theoretical (curve *1*) results are presented for the effective thicknesses of absorbing layer $\Delta z = \Delta z_{phys}/L$ = 0, 0.13, 0.28, 0.30, and 0.35 (Q = 1.6, 3.17, 9.5, 15.8, and 22.2, respectively; E_{in} = 0.5–7 mJ). The discrepancy with the experimental data is ~1%. In the range $Q \approx 16$–48, the heat-source function $q(r, t) = Qg(r)f(t)\{1 - \exp[-N_\alpha \rho(r, t)]\}/N_\alpha \rho(r, t)$ (Fig. 6, curve *2*) provides a good agreement (~1%) with the experimental data. The expression for $q(r, t)$ was obtained by integrating the heat-source function over the whole layer thickness under the assumption that the density was constant. Therefore, the density in this case is a certain effective quantity averaged over the width of the strongly absorbing layer. Note that the pulse time shape has little effect on the transparency (Fig. 6, curve *3*). The difference between the functions $f(t)$ I and II, whose maxima are separated by τ, i.e., by the characteristic pulse duration, is less than 10% in the range Q = 9.5–50. The extreme parameters of the medium, maximal temperature T_m and pressure p_m, minimal density ρ_{min} at the corresponding instants of time t (μs); integrated layer transparency $T_{tr} = E_{out}/E_{in}$; and the bleaching-channel width are given in Table 3 for differ-

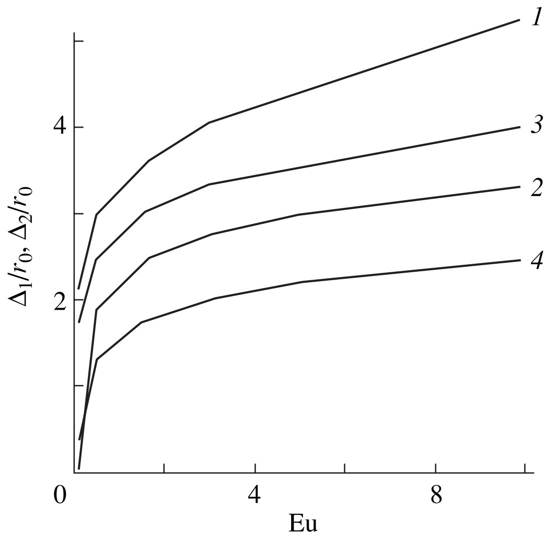

Fig. 5. Relative (on a level of $0.5\alpha_0$) radius of the bleaching channel at the (*1*, *3*) end (Δ_1/r_0) and (*2*, *4*) middle (Δ_2/r_0) of the pulse: (*1*, *2*) optically thin water layer with $T_{tr,0} = 0.9$ ($N_\alpha = 0.0334$) and (*3*, *4*) optically thick layer with $T_{tr,0} = 0.02$ (absorption parameter $N_\alpha = 0.318$).

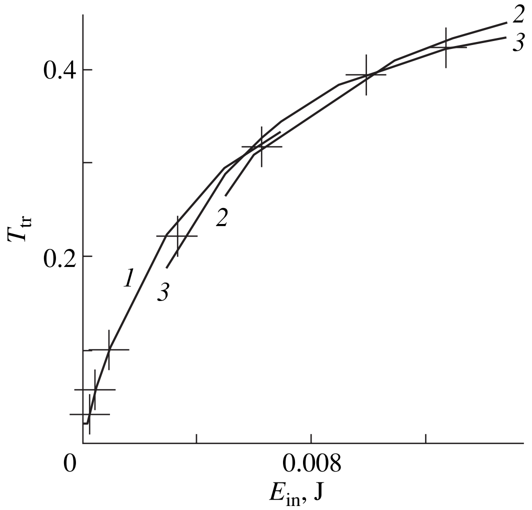

Fig. 6. Transparency T_{tr} of a water layer vs. heat-release parameter Q (i.e., pulse energy E_{in}). The initial transparency $T_{tr,\,0}$ = 0.02 (absorption parameter N_α = 0.318), Euler number Eu = 1.578, Reynolds number Re = 5.222, and the Prandtl number Pr = 1. Notation: (+) experimental data, (*1*) heat-source function $q = Q\exp[-r^2]f(t)\exp[-N_\alpha\rho(r, t)\Delta z]$ with the pulse shape $f(t)$ II; (*2*) $q = Q\exp[-r^2]f(t)\{1 - \exp[-N_\alpha\rho(r, t)\}/N_\alpha\rho(r, t)$ with $f(t)$ II; and (*3*) the same with $f(t)$ I.

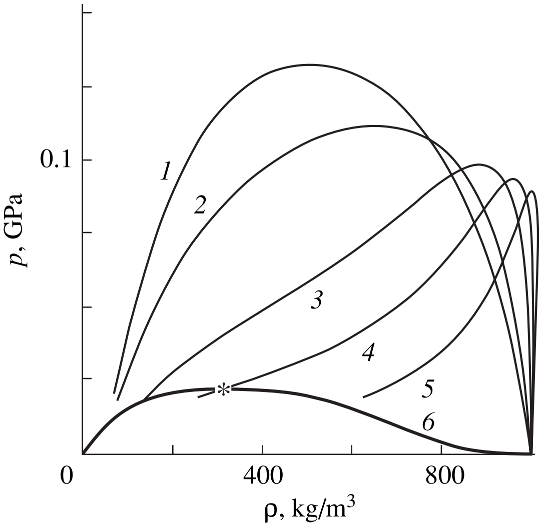

Fig. 7. The p–ρ trajectories of different points in fluid during the process of heating: r = (*1*) 0, (*2*) 63, (*3*) 252 (r_0), (*4*) 315, and (*5*) 378 μm; (*6*) binodal and (*) critical point. Parameter Q = 3.17 (E_{in} = 1 mJ, τ = 1.2 μs), time t = 3.2 μs, Euler number Eu = 1.578, pulse shape $f(t)$ II, and initial transparency $T_{tr,\,0}$ = 0.02 (absorption parameter N_α = 0.318).

ent values of heat-release parameter Q = 1.6–50 (Eu = 1.6; N_α = 0.318; $T_{tr,\,0}$ = 0.02). The medium and channel parameters as functions of the Euler number Eu = 0.1–10 are given in Table 4 for a fixed Q = 47.47 (N_α = 0.318; $T_{tr,\,0}$ = 0.02). The transverse sizes of the bleaching channel at the end and middle of the pulse are given as functions of the Euler number in Fig. 5 (curves *3*, *4*). At the second half of the pulse, the transverse size of the channel exceeds the transverse size of the bleaching pulse by a factor of 1.3–2.5 (in the range Eu = 0.5–10). The transverse size of the bleaching channel increases

Table 3. The maximal temperature T_m, pressure p_m, and the minimal density ρ_{min} at the corresponding instants of time t (μs); the transparency $T_{tr} = E_{out}/E_{in}$; the width of bleaching channel at the end Δ_1 (t = 2.5 μs) and middle Δ_2 (t = 1.62 μs) of the pulse for the heat-release parameters Q = 1.58–47.47. The Euler number Eu = 1.578; the absorption parameter N_α = 0.318 (initial transparency $T_{tr,\,0}$ = 0.02); the heat-release function $q(r, t) = Q\exp[-r^2]f(t)\exp[-N_\alpha\rho(r, t)\Delta z]$ for E_{in} = 0.5–7 mJ; $q(r, t) = \exp[-r^2]f(t)[1 - \exp(-N_\alpha\rho(r, t))]/N_\alpha\rho(r, t)$ for E_{in} = 9–15 mJ; $f(t)$ has the form II

E_{in}, mJ	0.5	1	3	7	9	13	15
Q	1.58	3.165	9.495	22.15	28.48	41.14	47.47
T_{tr}	0.063	0.102	0.218	0.333	0.369	0.431	0.449
T_m, K	797	1100	2273	4251	4329	4435	4469
t, μs	2.203	2.347	2.352	2.119	2.143	2.107	2.131
p_m, GPa	0.0862	0.1326	0.260	0.3985	0.4198	0.489	0.515
t, μs	1.675	1.723	1.536	1.387	1.363	1.291	1.246
ρ_{min}, kg/m^3 t = 2.5 μs	213	140.1	68.4	53.96	55.38	54.02	56.2
Δ_1, mm	0.260	0.315	0.475	0.610	0.655	0.760	0.765
Δ_2, mm	0	0	0.181	0.310	0.345	0.415	0.441
u_m, m/s	117.9	164.4	261	329.6	344.2	383.7	397.7
t, μs	2.419	2.203	1.872	1.651	1.627	1.531	1.529
a_m, m/s	1600	1604	1616	1711	1711	1712	1858
t, μs	1.056	1.008	0.912	1.723	1.627	1.435	1.361

Table 4. The maximal temperature T_{m}, pressure p_{m}, and the minimal density $\rho_{\min}$ (t = 2.5 μs) at the corresponding instants of time t; the integrated layer transparency $T_{\mathrm{tr}} = E_{\mathrm{out}}/E_{\mathrm{in}}$; the width of bleaching channel at the end Δ_1 (t = 2.5 μs) and middle Δ_2 (t = 1.62 μs) of the pulse for the Euler numbers Eu = 0.1–10. The heat-release parameter Q = 47.47; the absorption parameter N_α = 0.318 (initial transparency $T_{\mathrm{tr},\,0}$ = 0.02); the heat-release function $q(r, t) = \exp[-r^2]f(t)[1 - \exp(-N_\alpha\rho(r, t))]/N_\alpha\rho(r, t)$; $f(t)$ has the form II

Eu	0.1	0.5	1.6	3	5	10
E_{in}, mJ	236.1	47.2	15	7.87	4.72	2.36
T_{tr}	0.118	0.2864	0.449	0.5316	0.608	0.6866
T_{m}, K	4442	4473	4469	4465	4491	4462
t, μs	2.419	2.314	2.131	2.269	2.119	1.976
p_{m}, GPa	1.881	0.8842	0.515	0.381	0.2954	0.2158
t, μs	1.507	1.344	1.246	1.219	1.152	1.104
$\rho_{\min}$, kg/m^3	279.5	119.8	56.2	32.68	20.08	9.922
r_0, μm	1001	447.7	252	182.8	141.6	100.1
Δ_1, mm (2.5 μs)	1.725	1.10	0.765	0.610	0.50	0.40
Δ_1/r_0	1.723	2.457	3.036	3.336	3.531	4.00
Δ_2, mm (1.62 μs)	0.365	0.582	0.441	0.364	0.310	0.2455
Δ_2/r_0	0.3646	1.30	1.75	1.991	2.189	2.450

as the Euler number increases for the optically thin and thick layers. At Eu ⟶ 0, the bleaching effect vanishes.

After the pulse (or at its end stage with a relatively low energy), the fluid curve in the p–ρ–ε phase diagrams intersects a binodal (fluid–vapor equilibrium curve) and a spinodal (absolute-instability curve, after which the state of a superheated fluid or supercooled vapor is impossible). The situations corresponding to the onset of vapor–fluid bubble formation are shown in the p–ρ diagram in Fig. 7: (*1*–*3*) droplets start to condense in a supercooled vapor, and the density increases; (*4*) fluid completely transforms into vapor after reaching the critical point, and the density decreases; and (*5*) vapor bubbles appear in a superheated fluid, and the density decreases. The temperature corresponding to curves *1*–*3* may slightly increase (more precisely, the decrease in temperature is decelerated) after intersecting the binodal (or spinodal), while, for curves *4* and *5*, it is accelerated. Subsequently, the pressure and temperature in the perturbed vapor–fluid region continue to decrease, and the density increases. Fluid returns to the state that is close to its initial state.

Analysis showed that, for a single short pulse ($\tau \sim 10^{-10}$ s), the hydrodynamic bleaching mechanism is of little importance; the density variations are small, although the variations of pressure and internal energy (temperature) are significant. As in the case of a giant pulse ($\tau \sim 10^{-6}$ s), the evaporative mechanism is inoperative. The bleaching mechanisms based on the absorption saturation, band broadening, and line shift are also discussed in the literature ([6, 7]). Future studies will reveal which of these effects is dominant for single pulses.

CONCLUSIONS

The bleaching channel expands and deepens (as regards the transverse distribution of density or absorption coefficient) as the value of heat-release parameter Q increases when the remaining similarity parameters are fixed. The increase in the channel width slows down with increasing Q.

The transverse size of the bleaching channel increases with increasing Euler number Eu (at fixed values of the heat-release parameter Q and other parameters) for both the optically thin (small absorption parameter, $N_\alpha \ll 1$, and initial transparency $T_{\mathrm{tr},\,0} \sim 1$) and thick ($N_\alpha \sim 1$, $T_{\mathrm{tr},\,0} \ll 1$) layers. In the second half of the pulse, the bleaching channel is several times wider than the transverse size of the laser pulse. As the Euler number Eu decreases from 0.5 to 0.1, the bleaching effect rapidly vanishes.

For single short pulses ($\tau \sim 10^{-10}$ s, Eu $\ll 1$), the density perturbations are much smaller than for a giant pulse ($\tau \sim 10^{-6}$ s, Eu ~ 1). The hydrodynamic bleaching mechanism is inoperative in this case.

REFERENCES

1. K. L. Vodop’yanov, L. A. Kulevskiĭ, P. P. Pashinin, and A. M. Prokhorov, Zh. Éksp. Teor. Fiz. **82**, 1820 (1982) [Sov. Phys. JETP **55**, 1049 (1982)].
2. K. L. Vodop’yanov, L. A. Kulevskiĭ, V. G. Mikhalevich, and A. M. Rodin, Zh. Éksp. Teor. Fiz. **91** (7), 114 (1986) [Sov. Phys. JETP **64**, 67 (1986)].
3. L. I. Andreeva, K. L. Vodop’yanov, S. A. Kaĭdalov, *et al.*, Kvantovaya Élektron. (Moscow) **13**, 499 (1986).
4. K. L. Vodop’yanov, L. A. Kulevskiĭ, P. P. Pashinin, *et al.*, Kvantovaya Élektron. (Moscow) **14**, 1219 (1987).

5. K. L. Vodop'yanov, M. E. Karasev, and L. A. Kulevskiĭ, Pis'ma Zh. Tekh. Fiz. **14**, 324 (1988) [Sov. Tech. Phys. Lett. **14**, 143 (1988)].
6. K. L. Vodop'yanov, Zh. Éksp. Teor. Fiz. **97**, 205 (1990) [Sov. Phys. JETP **70**, 114 (1990)].
7. K. L. Vodop'yanov, L. A. Kulevskiĭ, A. V. Lukashev, and P. P. Pashinin, Kvantovaya Élektron. (Moscow) **30**, 975 (2000).
8. A. N. Kucherov, Dokl. Akad. Nauk **388**, 616 (2003) [Dokl. Phys. **48**, 90 (2003)].
9. M. Born and E. Wolf, *Principles of Optics*, 4th ed. (Pergamon, Oxford, 1969; Nauka, Moscow, 1973).
10. M. B. Vinogradova, O. V. Rudenko, and A. P. Sukhorukov, *Theory of Waves* (Nauka, Moscow, 1979).
11. V. L. Ginzburg, *The Propagation of Electromagnetic Waves in Plasmas* (Nauka, Moscow, 1967; Pergamon, Oxford, 1970).
12. S. A. Akhmanov, A. P. Sukhorukov, and R. V. Khokhlov, Usp. Fiz. Nauk **93** (6), 19 (1967).
13. V. N. Lugovoĭ and A. M. Prokhorov, Usp. Fiz. Nauk **111**, 203 (1973).
14. D. Marcuse, *Light Transmission Optics* (Van Nostrand, New York, 1972; Mir, Moscow, 1974).
15. L. G. Loĭtsyanskiĭ, *Mechanics of Liquids and Gases* (Nauka, Moscow, 1973; Pergamon, Oxford, 1966).
16. M. P. Vukalovich, S. L. Rivkin, and A. A. Aleksandrov, *Tables of Thermal Properties of Water and Water Vapor* (Izd. Standartov, Moscow, 1969).
17. *State Standard No. 98-86: Water* (Izd. Standartov, Moscow, 1986).
18. L. D. Landau and E. M. Lifshitz, *Course of Theoretical Physics*, Vol. 5: *Statistical Physics* (Nauka, Moscow, 1976; Pergamon, Oxford, 1980).
19. O. M. Belotserkovskiĭ and Yu. M. Davydov, *Large Particle Method in Gas Dynamics* (Nauka, Moscow, 1982).

Translated by V. Sakun

Technical Physics, Vol. 49, No. 7, 2004, pp. 884–886. Translated from Zhurnal Tekhnicheskoĭ Fiziki, Vol. 74, No. 7, 2004, pp. 78–80.
Original Russian Text Copyright © 2004 by Mishkin, Filatov, Nekorkin, Kutergina.

OPTICS, QUANTUM ELECTRONICS

The Effect of Selective Chemical Etching on the Directivity Pattern for Radiation of a Semiconductor Laser

V. P. Mishkin[1], D. O. Filatov[1], S. M. Nekorkin[2], and J. V. Kutergina[2]

[1] *Research and Educational Center for Physics of Solid-State Nanostructures,*
University of Nizhni Novgorod, Nizhni Novgorod, 603950 Russia
e-mail: spm@phys.unn.ru
[2] *Physicotechnical Research Institute, University of Nizhni Novgorod, Nizhni Novgorod, 603950 Russia*

Received October 15, 2003

Abstract—The effect of the selective wet chemical etching of the emitting surface on the directivity pattern of radiation in the plane normal to the *p–n* junction is studied for InGaP/GaAs lasers with InGaAs quantum wells. It is found by atomic-force microscopy that the cylindrical lens (converging or diverging, depending on the type of etchant) is self-formed on the emitting surface due to the different etching rate of wide-gap layers (InGaP) and active layers (GaAs, InGaAs) of the lasers. By adjusting the corresponding etching time, the aperture angle of the laser radiation pattern in the plane normal to the *p–n* junction can be changed in the range of 57°–82° at the initial aperture angle at the half maximum level of 6°. *© 2004 MAIK "Nauka/Interperiodica".*

INTRODUCTION

Semiconductor laser diodes (LDs) are now widely used in different electronic and optoelectronic applications [1]. Since the size of the emitting surface of LDs in the direction normal to the *p–n* junction is comparable with the emission wavelength, the divergence of LD radiation in this plane is quite large. The reduction of beam divergence is a vital problem because it determines the efficiency of coupling of a LD with various optical devices. To date there are different ways for changing the aperture angle of the radiation pattern. Usually, different collimator units based on cylindrical lenses are employed to focus LD radiation, as well as for its injection into optical fibers, which complicates the design of optoelectronic devices and makes their adjustment difficult.

In general, the divergence of LD radiation in the plane normal to the *p–n* junction is determined by a diffraction limit and, hence, by the thickness of the optical waveguide. In the methods of directivity-pattern modification described in [2–6], the aperture angle decrease is attained by increasing the total thickness of the waveguide layer. There are also methods for the modification of the directional radiation pattern in the plane normal to the *p–n* junction without increasing the laser-structure thickness. In these methods, the radiation injected into the substrate through the bottom thin confining layer is used as the output laser radiation [7, 8].

In this paper, we suggest a simple and practically feasible way to modify the directivity pattern of LDs using the selective etching of the LD emitting surface in the solution, which etches the materials of confining waveguide layers and active layers of the lasers at different rates, which results in self-formation of the cylindrical lens (converging or diverging, depending on the type of etchant) on the emitting surface. We have studied experimentally the effect of selective chemical etching on the morphology of the emitting surface of InGaP/GaAs LDs with InGaAs quantum wells (QWs) and the LD directivity pattern in the plane normal to the *p–n* junction by adjusting the corresponding time of etching.

EXPERIMENTAL

We studied GaAs LDs with two $In_{0.49}Ga_{0.51}P$ waveguide-confining layers and two $In_{0.2}Ga_{0.8}As$ QWs. The schematic representation of the heterostructure is shown in Fig. 1. The structures were grown using atmospheric pressure metal–organic chemical vapor deposition (AP-MOCVD) [9]. These structures were used for fabrication of multimode LDs with a stripe width of 100 μm. In order to make possible the modification of the emitting area by wet chemical etching, no antireflection coating was deposited onto the LD faces. The radiation wavelength of laser diodes was 0.987 μm at 300 K, and the aperture angle of the directivity radiation pattern at the half-maximum level was 66°. The LDs under study have the following characteristics: power 0.38 W at a pumping current of 1 A, a threshold current of 0.24 A, and a quantum efficiency of 41%.

In order to form the cylindrical converging lens on the front face of the LD, the selective etchant HCl + $KMnO_4$ (1000 : 3) (*A*) was used.

The etching rate of InGaP with this etchant was 0.4 μm/min. Etching rate calibration was carried out by a standard method using etching of the step in a uniform InGaP/GaAs epitaxial layer 0.6 μm thick. Part of the structure was covered by chemically stable varnish, and the sample was immersed in the etchant for a certain specified time so that the height of the etched step was about 100 nm according to preliminary estimations. After that, the varnish was removed by boiling in acetone, and the height of the etched step was measured by atomic-force microscopy (AFM). It was found that this etchant does not affect GaAs; in particular, after sample exposure in the solution for 0.25 min, no step on the sample surface was found by AFM.

LDs were completely immersed in the solution for a preset time and then were rinsed with distilled water. It should be noted here that LDs continued to lase after etching and their parameters specified above were practically unchanged if the etching time did not exceed a certain limit, whereupon LDs degraded (their lasing was not observed any longer).

In order to form a cylindrical diverging lens on the front laser face, the selective etchant (*B*) H_3PO_4 + H_2O_2 + H_2O (1 : 8 : 1) was used. In this solution the etching rate for GaAs was 4 μm/min, while for InGaP it was an order of magnitude lower.

The morphology of the etched surface of LDs was studied with an atomic-force microscope TopoMetrix TMX-2100 Accurex in a contact mode. V-shaped Si_3N_4 cantilevers with pyramidal probes were used with a radius of the tip curvature of about 50 nm and a ratio of probe height to the base width (aspect ratio) of 1 : 1.

The aperture angle of the directivity radiation pattern of LDs in the plane normal to the *p–n* junction was measured using a motorized goniometric setup. An LD was installed on a goniometric head, which was rotated using a stepping motor. The aperture angle of the detector was 0.5°. The intensity of LD radiation was measured by a Si photodiode using the lock-in technique with lock-on detection. Modulation of LD radiation intensity was accomplished by modulating the pumping current with rectangular pulses.

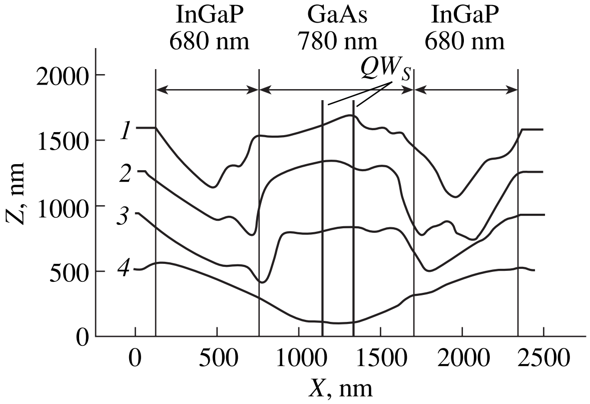

Fig. 1. Surface profiles of the emitting area of the laser diodes in the direction normal to the *p–n* junction after selective etching (*1–3*) in etchant (*A*) and (*4*) in etchant (*B*). Etching time t_e = (*1*) 7.5, (*2*) 15, (*3*) 30, and (*4*) 3 s.

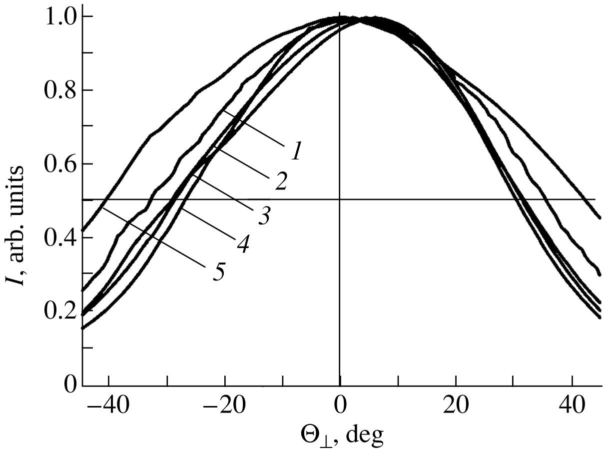

Fig. 2. Distribution of the intensity of the far-field radiation over the plane normal to the *p–n* junction at different times of etching of the laser diode (*1–4*) in etchant (*A*) and (*5*) in etchant (*B*). Etching time t_e = (*1*) 0, (*2*) 7.5, (*3*) 15, (*4*) 30, and (*5*) 3 s.

RESULTS AND DISCUSSION

The profiles of the emitting surface of LDs after selective etching are shown in Fig. 1. Etched waveguide cladding layers and the active region of LDs are clearly seen in these profiles. Selective chemical etching was previously used to determine the layer thickness of the laser structure by AFM [10]. It is evident from Fig. 1 that the thickness of the cladding waveguide and active layers of LDs are in a good agreement with the values specified before growth of the heterostructure.

On the emitting surface, the profile in the shape of either a converging or a diverging lens is formed depending on the type of etchant used. Imperfections observed in the surface profiles are related to etching nonuniformities and irregularities, because the etchants used possess no polishing effect. The etchant (*A*) is more selective than (*B*), as follows from data of measurement of the etching rates for different materials presented in the previous section. It is confirmed by the AFM data shown in Fig. 1: the steps corresponding to InGaP/GaAs heterojunctions in the profiles *1–3* are more steep than in the structure treated with etchant (*B*) (curve *4*). In this case, the less selective etchant is preferable since the smoother profile *4* is closer to the desired result, i.e., formation of the cylindrical surface.

As is evident from Fig. 1, after etching for 7.5 s, the height difference at the InGaP/GaAs interface is equal to 600 nm. Further etching results in an insignificant change in the height difference, which is due to the hindering of mass transport in the groove at the site of the etched InGaP layer that causes equalization of the etching rates of GaAs and InGaP.

The angular dependencies of the intensity of LD radiation are shown in Fig. 2 for different times of etch-

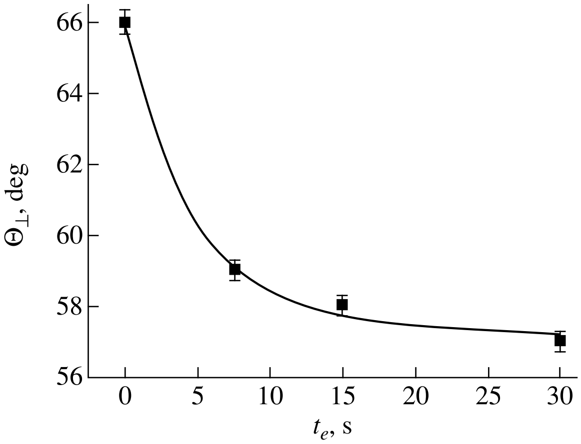

Fig. 3. Dependence of the aperture angle of the directivity radiation pattern on the time of etching.

ing. After etching for 7.5 s, the aperture of the directivity pattern at the half-maximum level decreased by 7° (Fig. 3). Further etching causes only a negligible change in the aperture angle. As follows from Fig. 1, the greatest change in the emitting area configuration is observed after the first etching; further etching negligibly affects the configuration of the active area and, correspondingly, the directivity pattern. After etching for 30 s, the aperture angle of the directivity pattern was reduced by approximately 10°. After etching for 45 s, no lasing was observed in LDs, which is probably related to degradation of the laser structure.

After the treatment of the laser structure in the etchant (*B*), a broadening of the directional radiation pattern to 82° was observed (Fig. 2). Thus, selecting the appropriate etchant, the aperture of the directivity pattern can be both broadened and narrowed. The narrowing of the directivity pattern is of the most practical interest. Further optimization of the etchant composition and etching procedure can probably result in more substantial narrowing of the directivity radiation pattern of LDs in the plane normal to the *p–n* junction.

The special feature of the approach described here for modification of the directivity pattern of LDs is that the required shape of the emitting surface is obtained as a result of self-formation. If the external cylindrical lens is used for LD radiation focusing, the axis of the lens should be aligned with the emitting surface of the LD, and the planes of the lens axis and the *p–n* junction should be parallel, which requires fine adjustment. If selective etching is used, the specified alignment is provided automatically, which is undoubtedly an advantage of this method.

CONCLUSION

Thus, in this paper we showed that it is possible to control the aperture of the directional radiation pattern of the semiconductor laser by formation of the cylindrical lens on their emitting surface using selective wet etching.

ACKNOWLEDGMENTS

This study was supported by the joint Russian–American program “Basic Research and High Education” sponsored jointly by the Ministry of Education of the Russian Federation, and the Civilian Research and Development Foundation (CRDF) (grant no. REC-NN-001-1).

REFERENCES

1. Zh. I. Alferov, Fiz. Tekh. Poluprovodn. (St. Petersburg) **32**, 3 (1998) [Semiconductors **32**, 1 (1998)].
2. H. Asonen, A. Ovtchinnikov, G. Zhang, *et al.*, IEEE J. Quantum Electron. **30**, 415 (1994).
3. M. Ohcudo, T. Ijichi, A. Iketani, *et al.*, IEEE J. Quantum Electron. **30**, 408 (1994).
4. M. C. Wu, Y. K. Cchen, M. Hong, *et al.*, Appl. Phys. Lett. **59**, 1046 (1991).
5. I. A. Avrutskiĭ, E. M. Dianov, B. N. Zvonkov, *et al.*, Kvantovaya Élektron. (Moscow) **24**, 123 (1997).
6. N. B. Zvonkov, S. A. Akhlestina, A. V. Ershov, *et al.*, Kvantovaya Élektron. (Moscow) **26**, 217 (1999).
7. D. R. Scifres, W. Streifer, and D. R. Burnham, Appl. Phys. Lett. **29**, 23 (1976).
8. N. B. Zvonkov, B. N. Zvonkov, A. V. Ershov, *et al.*, Kvantovaya Élektron. (Moscow) **25**, 622 (1998).
9. I. A. Avrutskiĭ, L. M. Batukova, E. M. Dianov, *et al.*, Kvantovaya Élektron. (Moscow) **21**, 921 (1994).
10. V. V. Levichev, G. A. Maximov, V. P. Mishkin, *et al.*, Phys. Low-Dimens. Semicond. Struct. **3/4**, 277 (2003).

Translated by M. Lebedev

Technical Physics, Vol. 49, No. 7, 2004, pp. 887–894. Translated from Zhurnal Tekhnicheskoĭ Fiziki, Vol. 74, No. 7, 2004, pp. 81–89.
Original Russian Text Copyright © 2004 by Gandel, Zaginaylov, Steshenko.

RADIOPHYSICS

Rigorous Electrodynamic Analysis of Resonator Systems of Coaxial Gyrotrons

Y. V. Gandel*, G. I. Zaginaylov*, and S. A. Steshenko**
** Karazin Kharkiv National University, Kharkiv, 61077 Ukraine*
e-mail: zaginaylov@postmaster.co.uk
*** Usikov Institute of Radiophysics and Electronics, National Academy of Sciences of Ukraine, Kharkiv, 61085 Ukraine*

Received August 21, 2003; in final form, December 3, 2003

Abstract—An efficient and rigorous numerical method is developed for numerical analysis of resonators of coaxial gyrotrons used for plasma heating, drag current generation, and for other purposes in controlled thermonuclear fusion facilities with magnetic confinement. Results obtained may be used to simulate operation of coaxial gyrotrons, to optimize their resonators, and to develop efficient software intended for studying the physics of coaxial gyrotrons and for their design. *© 2004 MAIK “Nauka/Interperiodica”.*

INTRODUCTION

Current progress in controlled thermonuclear fusion (CTF) largely depends on advances in modern technical physics and technology. In particular, the development of high-power millimeter-wave sources is very important for the improvement of systems of electron cyclotron resonance heating (ECRH) of plasma in magnetic plasma confinement installations. Millimeter-wave radiation can be used not only for additional heating of the plasma, but also for generating drag currents, for igniting the thermonuclear reaction and controlling its stability, and so on [1–3]. Millimeter-wave radiation will be widely used for many purposes in the most significant project today in the CTF field—the International Thermonuclear Experimental Reactor (ITER).

ECRH systems employ gyrotrons as sources of millimeter-wave radiation. To make them simpler and to reduce their cost to an admissible level, it is necessary for one gyrotron to produce about 2 MW of continuous-wave (cw) power (pulses longer than 10 s) at a frequency in the range from 140 to 200 GHz, frequency tuning being very desirable [4].

Gyrotrons with traditional resonators in the form of a cylindrical waveguide that are being developed under the ITER project have attained levels of 1 MW at 170 GHz in the cw mode [5, 6]. However, increasing the power in this type of gyrotrons faces significant engineering problems mostly due to overheating of resonator walls, too high competition between modes, and the effect associated with the space charge of the electron beam. These difficulties can successfully be overcome in new-generation gyrotrons, which use coaxial resonators with a corrugated inner conductor [7–9].

Presently, the most extensive experimental and theoretical research into gyrotrons with coaxial resonators is being conducted at the Karlsruhe Research Center (Germany) [8, 9], Institute of Applied Physics (Nizhni Novgorod, Russia) [10], and Massachusetts Institute of Technology (United States) [11]. A record-high output power of about 2.2 MW attained in gyrotrons of this type with an efficiency of 28% has been reported in [12]. The pulse length was 0.8 ms at a pulse repetition rate of 1 Hz. The coaxial gyrotron operated in the $\mathrm{TE}_{31,17}$ mode at a frequency of about 165 GHz. High-frequency and low-frequency spurious oscillations were also found. The main tasks in the development of coaxial gyrotrons for CTF installations are to increase the pulse length, decrease the heat load on the inner conductor, and improve the mode purity. To efficiently cope with these challenges, the designer needs new reliable information about the mode competition scenarios and about the loss in the inner conductor.

Until recently, the parameters of coaxial gyrotron resonators were calculated in terms of a simplified impedance model of the corrugated inner conductor [13–15]. This model replaces the corrugated inner conductor of the coaxial resonator (Fig. 1) with an equivalent circular impedance smooth conductor. The equivalent surface impedance depends on the corrugation parameters, which accounts for the effect of corrugation. The methods for defining the equivalent impedance and the corresponding expressions can be found in [13–15]. The impedance model is simple and convenient for calculations. It was used to assess and optimize a number of experimental versions of coaxial gyrotrons. However, it is difficult to outline the applicability limits of this model. A commonly used validity criterion for the impedance approximation in the theory of coaxial gyrotrons is the condition $s < \pi R_\mathrm{i}/m$, where $s = 2\pi R_\mathrm{i}/N$, N is the number of corrugations on the inner conductor, m is the azimuthal index of the fundamental space harmonic, and R_i is the radius of the inner con-

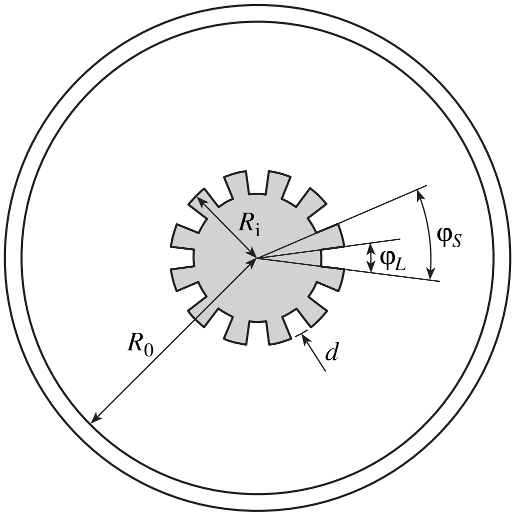

Fig. 1. Cross section of a coaxial gyrotron resonator.

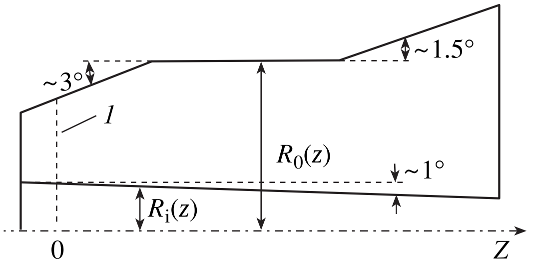

Fig. 2. Typical geometry of a coaxial gyrotron resonator (*1* is the critical cross section).

ductor [13–15]. This condition requires that the corrugation period be smaller than the azimuthal period of the fundamental space harmonic. Approximate calculations were compared with the rigorous electrodynamic analysis for a rectangular waveguide structure with a periodic array on one side [16, 17]. It was shown that, under the above condition, the impedance model yields a propagation constant with a good relative accuracy (~1%), although it is far from providing small amplitudes of higher-order spatial harmonics, which are disregarded in the framework of the impedance approximation. As a result, the field near the corrugated surface, calculated within the impedance approximation, may significantly differ from the true one. Another serious drawback of the impedance model is that it is inapplicable for describing degenerate modes and resonance conditions. For example, for a mode with azimuthal index $m = N/2$, the impedance approximation may predict incorrect field values not only near the corrugated surface, but also far from it, because radial field distributions of the fundamental and first spatial harmonics in this case are identical.

The above drawbacks of the impedance model may cause serious mistakes in optimizing the resonators of coaxial gyrotrons. Selective properties of the coaxial resonator rely on the difference in behavior of the eigenvalues χ of different modes versus the resonator external-to-internal conductor radius ratio $C = R_0/R_i$. If C varies along the resonator (Fig. 2), the values of $d\chi/dC$ are different for different modes, which is used for their selection. Because the operating modes of high-power gyrotrons are characterized by high azimuthal and radial indices, the total relative longitudinal eigenvalue variations $\Delta\chi/\chi$ that provide the mode selection are very small (about 0.1 to 0.3%). Thus, the error (~1%) of the impedance approximation does not guarantee that the value of $d\chi/dC$ calculated for competing modes is sufficiently accurate to keep the relative error in the estimated eigenvalue much smaller than the total relative eigenvalue variation $\Delta\chi/\chi$ along the resonator. Such an accuracy (<0.01%) can only be attained in the framework of a rigorous electrodynamic approach.

A rigorous method for analyzing coaxial azimuth-periodic structures was developed in [18] for designing magnetron resonators. Later, it was further developed and applied to coaxial gyrotrons [19]. This method provides a significantly higher accuracy, especially for modes with moderately high azimuthal and radial indices. However, its error increases with the radial and azimuthal indices. The idea to develop and apply stable direct numerical methods for solving a system of integral equations (SIE) of the first kind to microwave radiophysics problems was proposed and mathematically substantiated in [20–24]. A rigorous electrodynamic analysis of a coaxial resonator with a corrugated inner conductor, which is proposed in this paper, relies on direct numerical methods for solving the SIE of the first kind, to which the corresponding boundary value problem is equivalently reduced [25]. In our opinion, this approach provides a reasonable trade-off between the complexity of analytical transformations on the one hand and the convergence and stability of numerical solutions on the other. A similar rigorous electrodynamic approach was earlier applied to analyze a rectangular waveguide array [16, 17], finite-length open oversize arrays [26–28], and microstrip lines [29, 30]. In all these cases, the numerical results exhibited good convergence and stability for a sufficiently short machine time.

The paper is arranged as follows. Section 1 formulates the initial boundary value problem for the Helmholtz equation and equivalently reduces it to an integral equation of the first kind with a logarithmic singularity. Section 2 equivalently reduces the integral equation of the first kind with the logarithmic singularity to a SIE of the first kind under an additional condition and develops direct numerical methods for the SIE. Section 3 provides examples of practical calculations. The results are compared with those obtained within the impedance approximation. It is shown that the error in the estimated $d\chi/dC$ or $\Delta\chi/\chi$ along the resonators of coaxial gyrotrons that are being designed for heating plasma in the ITER and other magnetic confinement facilities may be as high as 50% or above, which may cause serious errors in predicting the mode competition scenario and in optimizing parameters of resonators of coaxial gyrotrons (also see [31]). The conclusion summarizes results of the study.

1. FORMULATION OF THE PROBLEM AND DERIVATION OF THE BASIC INTEGRAL EQUATION

The resonator of a coaxial gyrotron has the form of a segment of a tapered waveguide. Its cross section is illustrated in Fig. 1. Simulations usually represent the field in each cross section as a superposition of several modes whose characteristics locally depend on the parameters of the cross section, thus disregarding the interaction between different modes due to the longitudinal nonuniformity. Therefore, the field structure in each cross section of the resonator is calculated independently under the assumption that it is the same as in an infinite waveguide of the same cross section. This is a traditional and rather efficient approach for tapered waveguides [32]. Simulation of one resonator usually requires from 300 to 400 cross sections. These results are further used in solving the problem of excitation of the resonator by an electron beam.

Thus, the key problem in simulating resonators of coaxial gyrotrons is the calculation of the propagation constants and the field structure of natural waves of an infinite waveguide whose cross section is the same as that of the coaxial resonator.

As is known, natural waves of a regular hollow waveguide of an arbitrary cross section can be represented as a superposition of TE and TM modes. We will further consider the TE modes, because they are either the operating modes or the most dangerous spurious modes in the coaxial gyrotron.

All components of an arbitrary TE mode can be expressed in terms of one function $\Psi(r, \varphi)$ (membrane function) [32], which is proportional to H_z:

$$E_r = (ikR_0^2/r)\partial\Psi/\partial\varphi, \quad E_\varphi = -ikR_0^2\partial\Psi/\partial\varphi,$$
$$E_z = 0,$$

$$H_r = ik_zR_0^2\partial\Psi/\partial r, \quad H_\varphi = (ik_zR_0^2/r)\partial\Psi/\partial\varphi,$$
$$H_z = \chi^2\Psi,$$

where r and φ are the cylindrical coordinates; R_0 is the radius of the outer conductor; $k = 2\pi/\lambda$ is the wave number; λ is the wavelength; k_z is the transverse wave number; and $\chi = R_0\sqrt{k^2 - k_z^2}$ is the normalized transverse wave number, which depends on the cross section geometry alone (we will further call it the eigenvalue in keeping with the common terminology of coaxial gyrotrons); phase factor $\exp[i(k_zz - \omega t)]$ factor is omitted.

The membrane function for TE modes satisfies the equation

$$[\Delta_\perp + (\chi/R_0)^2]\Psi = 0, \tag{1}$$

where $\Delta_\perp = (1/r)(\partial/\partial r)(r\partial/\partial r) + (1/r^2)\partial^2/\partial\varphi^2$, under the Dirichlet boundary condition

$$\partial\Psi/\partial n = 0 \tag{2}$$

on the cross section boundary.

Let us introduce the notation $C = R_0/R_\mathrm{i}$ and $C' = R_0/(R_\mathrm{i} - d)$. Here, R_i is the radius of the corrugated inner insert and d is the corrugation depth. In the region above the corrugations ($R_\mathrm{i} < r < R_0$), the membrane function can be represented as a superposition of space harmonics

$$\Psi \equiv \Psi^+ = \sum_{n=-\infty}^{\infty} A_nG_{k_n}(\chi, \chi/C, \chi r/R_0)\exp(ik_n\varphi), \tag{3}$$

where $G_n = (a, b, c) = (J'_\nu(a)Y_\nu(c) - Y'_\nu(a)J_n(c))/(J'_\nu(a)Y'_\nu(b) - Y'_\nu(a)J'_\nu(b))$; $k_n = m + nk_S$; $k_S = 2\pi/\varphi_S = N$; $\varphi_S = 2\pi/N$ is the angular corrugation period; m is the azimuthal index of the mode; $J_\nu(x)$ and $Y_\nu(x)$ are the Bessel and Neumann functions, respectively; and the angle φ is measured from the center of the groove.

Representation (3) automatically satisfies boundary condition (2) on the surface of the outer conductor.

Since representation (3) is quasi-periodic, it is convenient to restrict the analysis to one period in φ: $-\varphi_S/2 < \varphi < \varphi_S/2$. Let us represent the membrane function in a groove ($R_\mathrm{i} - d < r < R_\mathrm{i}$, $-\varphi_L/2 < \varphi < \varphi_L/2$) as a truncated Fourier series

$$\Psi \equiv \Psi^- = \sum_{n=-\infty}^{\infty} X_nG_{\xi_n}\left(\frac{\chi}{C'}, \frac{\chi}{C}, \frac{\chi r}{R_0}\right)\cos(\xi_n(\varphi + \varphi_L/2)), \tag{4}$$

where $\xi_n = \pi n/\varphi_L$.

We introduce a new unknown function $F(\varphi) = (R_0/\chi)\partial\Psi^+/\partial r|_{r = R_i}$, for which the following representation follows from (3):

$$F(\varphi) = \sum_{n=-\infty}^{\infty} A_n\exp(ik_n\varphi). \tag{5}$$

Due to boundary condition (2), we have

$$F(\varphi) = 0, \quad \varphi \in [-\varphi_S/2, -\varphi_L/2] \cup [\varphi_L/2, \varphi_S/2]. \tag{6}$$

Using relations (5) and (6), we can represent coefficients A_n in terms of $F(\varphi)$ as

$$A_n = \frac{1}{\varphi_S}\int_{-\varphi_L/2}^{\varphi_L/2} F(\theta)\exp(-ik_n\theta)d\theta. \tag{7}$$

The field must comply with the continuity conditions at $r = R_i$, $-\varphi_L/2 < \varphi < \varphi_L/2$:

$$\Psi^+(R_i, \varphi) = \Psi^-(R_i, \varphi), \tag{8}$$

$$\frac{R_0}{\chi}\frac{\partial\Psi^-}{\partial r}(R_i, \varphi) = F(\varphi). \tag{9}$$

Using formulas (4) and (9), we represent coefficients X_n in terms of $F(\varphi)$:

$$X_n = \frac{2\varepsilon_n}{\varphi_L}\int_{-\varphi_L/2}^{\varphi_L/2} F(\theta)\cos(\xi_n(\theta + \varphi_L/2))d\theta, \tag{10}$$

where

$$\varepsilon_n = \begin{cases} 1/2, & n = 0 \\ 1, & n \neq 0. \end{cases}$$

With (3) and (4), the first continuity condition (8) yields the relation

$$\sum_{n=-\infty}^{\infty} A_n W_{k_n}(\chi, \chi/C)\exp(ik_n\varphi) = \sum_{n=0}^{\infty} X_n W_{\xi_n}(\chi/C', \chi/C)\cos(\xi_n(\varphi + \varphi_L/2)), \quad -\varphi_L/2 < \varphi < \varphi_L/2, \tag{11}$$

where $W_\nu(a, b) = (1/b)G_\nu(a, b, b)$.

Substituting relations (7) and (10) into (11) and interchanging the order of summation and integration, we arrive at the initial integral equation of the first kind on an interval:

$$\int_{-\varphi_L/2}^{\varphi_L/2} H(\varphi, \theta)F(\theta)d\theta = 0, \quad -\varphi_L/2 < \varphi < \varphi_L/2, \tag{12}$$

where

$$H(\varphi, \theta) = G_1(\varphi - \theta) + G_2(\varphi - \theta) + G_2(\varphi + \theta + \varphi_L),$$

$$G_1(x) = (1/\varphi_S)\sum_{n=-\infty}^{\infty} W_{k_n}(\chi, \chi/C)\exp(ik_nx),$$

$$G_2 = -(1/\varphi_L)\sum_{n=0}^{\infty}\varepsilon_n W_{\xi_n}(\chi/C', \chi/C)\cos(\xi_nx).$$

Integral equation (12) is equivalent to the two-dimensional boundary value problem (1), (2). It allows for the contribution of all spatial and Fourier harmonics of the field. The kernel of integral equation (12) can easily be shown to contain a logarithmic singularity at $\varphi = 0$: $H(\varphi, \theta) = (2/\pi)\ln|\varphi - \theta| + H_r(\varphi, \theta)$, where $H_r(\varphi, \theta)$ is a smooth function in the interval $(-\varphi_L/2, \varphi_L/2)$ in both variables. Many problems of microwave radiophysics can be reduced to an equation of the form (12) [20–30, 33]. Therefore, knowledge of certain issues of the theory of these equations is useful and may significantly help in the development of efficient numerical methods. It is known that integral equations with a logarithmic singularity are very similar in their properties to the Fredholm equations and are often referred to as quasi-Fredholm equations. Direct solution of these equations may not be stable enough. This observation is corroborated by numerous results of solving such problems by using the mode matching method or the moment method. The integral equations are often not written explicitly; instead, equations like (11) are used to obtain infinite systems of linear algebraic equations (SLAE) with respect to unknown coefficients A_n or X_n (see, e.g., [18, 19]). If these SLAE are truncated directly, the numerical solution may exhibit poor stability and be dependent on the scheme used to truncate coefficients A_n and X_n, because the truncated SLAE is equivalent to a Fredholm equation of the first kind. The truncation procedure eliminates the singular part of the kernel of Eq. (12), which appears due to the contribution of an infinite number of spatial harmonics.

The next section proposes certain rigorous numerical methods for finding the unknown function $F(\varphi)$ and eigenvalue χ from Eq. (12), which accurately allow for the kernel singularity.

2. RIGOROUS NUMERICAL ANALYSIS METHODS FOR THE INITIAL INTEGRAL EQUATION

Differentiating Eq. (12) with respect to φ, we obtain a SIE of the first kind:

$$\int_{-\varphi_L/2}^{\varphi_L/2} F(\theta)d\theta/(\theta - \varphi) + \int_{-\varphi_L/2}^{\varphi_L/2} K(\varphi, \theta)F(\theta)d\theta = 0, \quad \varphi \in (-\varphi_L/2, \varphi_L/2), \tag{13}$$

where the first integral should be understood as the principal value in the sense of Cauchy and $K(\varphi, \theta) = -(\pi/2)\partial H(\varphi, \theta)/\partial\varphi - 1(\theta - \varphi)$ is a smooth function of both variables.

For the solution to Eq. (12) to be unique, an additional condition is necessary, which can be obtained by integrating (12) with respect to φ:

$$\int_{-\varphi_L/2}^{\varphi_L/2} L(\theta)F(\theta)d\theta = 0, \tag{14}$$

where $L(\theta) = \int_{-\varphi_L/2}^{\varphi_L/2} H(\varphi, \theta)d\varphi$ is a smooth function. For convenience, let us introduce the dimensionless variables $t = 2\varphi/\varphi_L$ and $\tau = 2\theta/\varphi_L$. In terms of the new vari-

Table 1. Comparison of diffraction Q factors of competing modes calculated within the impedance approximation and by using the rigorous approach for the $TE_{31,\,17}$ coaxial gyrotron [12]

Mode	Q_{IMP}	Q_{SIE}	ΔQ, %
$TE_{31,\,17}$	1866	1892	1.39
$TE_{28,\,18}$	1275	1419	11.29
$TE_{29,\,18}$	1518	1647	8.5
$TE_{29,\,17}$	1602	1671	4.31
$TE_{30,\,17}$	1752	1797	2.5
$TE_{30,\,18}$	1731	1831	5.78
$TE_{32,\,17}$	1951	1965	0.07

Table 2. Calculations by quadrature formulas based on Chebyshev polynomials

n	χ
2	94.646576961
3	94.645294198
4	94.645102862
5	94.645022786
10	94.644937760
20	94.644923566
30	94.644921730
40	94.644921225

ables, (13) and (14) take the form

$$\int_{-1}^{1} \nu(\tau) f\tau/(\tau - t) + \int_{-1}^{1} K_1(t, \tau)\nu(\tau)d\tau = 0, \quad t \in (-1, 1), \tag{15}$$

$$\int_{-1}^{1} L_1(\tau)\nu(\tau)d\tau = 0, \tag{16}$$

where $\nu(\tau) = F(\varphi_L\tau/2)$, $K_1(t, \tau) = (\varphi_L/2)K(\varphi_L t/2, \varphi_L\tau/2)$, and $L_1(\tau) = L(\varphi_L\tau/2)$.

Equations of type (15) under additional condition (16) are often met in aerodynamics [34], elasticity theory, electrostatics, etc. A number of direct numerical methods, called the discrete singularity method [20, 22, 34], have been developed and mathematically substantiated for these equations. The key feature of these approaches is that they replace singular integrals with quadrature formulas. The accuracy of these quadrature formulas can be estimated analytically. As a result, SIE (11) under additional condition (12) is reduced to a SLAE. The unknown eigenvalues are obtained by equating the determinant of this SLAE to zero. Two discretization methods for Eqs. (11) and (12) are provided in the Appendix.

It should also be noted that significant difficulties associated with the calculation of Bessel functions of high orders and large arguments are met when the kernels of the SIE are calculated for parameters of real coaxial gyrotrons. Direct calculation of Bessel functions with the help of standard embedded programs is only possible for a few first terms of the series in Eq. (10). Because these series converge slowly ($W_\nu(a, b) \sim (|b - a|/(b - a))/|\nu| + O(|\nu|^{-3})$, $\nu \longrightarrow \pm\infty$), one has to apply dedicated convergence acceleration techniques when calculating functions $G_1(x)$, $G_2(x)$, and the Bessel functions, which do not lead to error accumulation. Otherwise, it is impossible to provide the required accuracy (<0.01%) of calculating the eigenvalues. One of such convergence-acceleration techniques is described in [25].

3. NUMERICAL EXAMPLES

Particular numerical calculations were performed for resonators of two coaxial gyrotrons. One of them is the coaxial gyrotron operating in the $TE_{31,17}$ mode, which has been experimentally realized in Karlsruhe, Germany [12]. The geometry of the $TE_{31,17}$ resonator of the coaxial gyrotron is qualitatively the same as that illustrated in Fig. 2. The inner conductor carries 72 rectangular grooves. The grooves are 0.35 mm wide and 0.45 mm deep. In this gyrotron, the most dangerous spurious modes are $TE_{28,18}$, $TE_{29,18}$, $TE_{29,17}$, $TE_{30,17}$, $TE_{32,17}$, and $TE_{30,18}$. The Q factors of these modes calculated using the rigorous approach (Q_{SIE}) and the impedance approximation (Q_{IMP}) summarized in Table 1.

As we see from the table, more rigorous calculations yield higher Q factors for all modes without exception. However, the excess is different for different modes. For modes with a lower Q factor, the excess is higher as a rule. An insignificant exception is the $TE_{30,18}$ mode alone. As an illustration, Fig. 3 shows the eigenvalue of the $TE_{29,18}$ mode versus the longitudinal coordinate for the $TE_{31,17}$ resonator of a coaxial gyrotron, $\chi_{29,\,18}(z)$, calculated (thick curve) by rigorous electrodynamic

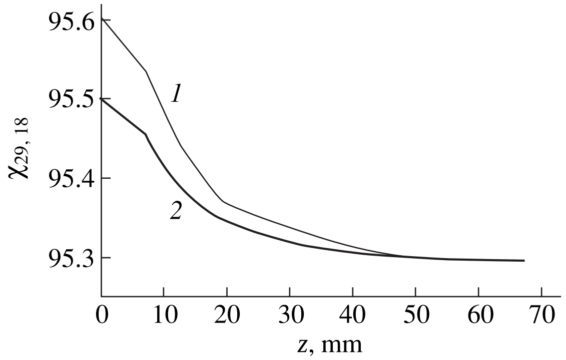

Fig. 3. Comparison of eigenvalues of the $TE_{29,18}$ mode of the $TE_{31,17}$ resonator of a coaxial gyrotron calculated versus longitudinal coordinate (*1*) within the impedance approximation and (*2*) by using the rigorous approach.

Table 3. Calculations by quadrature formulas based on Jacobi polynomials

n	χ
2	94.645055902
3	94.644915529
4	94.644907864
5	94.644912573
6	94.644917864
7	94.644918747
8	94.644919839
9	94.644920050

analysis and (thin curve) within the impedance approximation. As is seen from the plots, the true value of χ is smaller than the one given by the impedance approximation. The relative error of the impedance approximation is not very high (~0.01%). However, it amounts to as high as 50% of the total variation of $\chi_{29,\,18}(z)$ along the resonator, which may significantly corrupt the predictions of selective properties of coaxial resonators derived from the impedance approximation. Similar plots for the eigenvalues of other modes of this resonator are qualitatively the same as those given in Fig. 3. It should be noted that the error of the impedance approximation is more significant for modes with lower Q factors.

The results obtained for another resonator (operating in the $TE_{34,19}$ mode [35]) of the coaxial gyrotron, which is presently in the design stage and is intended to be used in the ITER project, have shown very similar differences [31]. The $TE_{34,19}$ resonator of the coaxial gyrotron is qualitatively the same as that illustrated in Fig. 2; it is described in greater detail in [35]. In addition to Q factors and eigenvalues, the mode competition scenario was predicted for both resonators [31]. It was shown that, for the $TE_{34,19}$ gyrotron, more accurate calculation of eigenvalues based on the rigorous electrodynamic approach predicts more significant changes in the mode competition scenario than that based on the impedance approximation. For the $TE_{31,17}$ gyrotron, the mode competition scenario proved to be less sensitive to errors produced by the impedance model. A detailed comparative analysis of the mode competition can be found in [31].

In conclusion, note that the calculations were performed independently on the basis of two algorithms that use different discretization schemes and different formulas for the matrix elements. The results agreed to a high accuracy, which removes any doubts concerning their authenticity. The convergence of the eigenvalues is illustrated in the Appendix. The results allow us to conclude that the eigenvalues are calculated with an absolute error not higher than 5×10^{-7}, which is quite sufficient for adequately predicting the mode competition scenario in spite of its high sensitivity to the error in the calculated eigenvalues.

CONCLUSIONS

Calculations performed for coaxial gyrotrons based on the rigorous electrodynamic approach revealed significant differences from the results obtained within the approximate impedance model, which gives overestimated eigenvalues of coaxial resonator modes, especially near the entrance to the resonator. The excess is on the order of the total variation of the eigenvalue along the length of the resonator and depends on the radial and azimuthal mode indices. The analysis of Q factors of competing modes for two gyrotrons operating in the $TE_{31,17}$ and $TE_{34,19}$ modes allows us to conclude that the results calculated using the impedance model are in the most part underestimated. The error increases with the radial index and decreases with increasing azimuthal index. At the same time, its effect on the mode competition scenario increases with both radial and azimuthal indices. For the $TE_{31,17}$ gyrotron, the average error in the Q factor is significantly higher than that for the $TE_{34,19}$ gyrotron; however, the mode competition scenario qualitatively differs little from that predicted within the impedance approximation. At the same time, for the $TE_{34,19}$ gyrotron, the mode competition scenario predicted on the bases of the rigorous approach significantly differs from that predicted within the impedance approximation [31]. Taking into consideration the fact that resonators of coaxial gyrotrons evolve towards higher azimuthal and radial indices of the operating and competing modes, the use of the impedance model for predicting selective properties of coaxial resonators with a corrugated inner conductor seems to be more and more doubtful. The rigorous electrodynamic approach proposed in this paper based on SIE is an efficient alternative to the impedance approximation. The relatively low machine time due to its improved algorithm makes it possible to use this approach for optimizing parameters of coaxial gyrotrons and for perfecting the geometry of their resonators.

APPENDIX

Using interpolation-type quadrature formulas with nodes at zeros of the Chebyshev polynomials, Eqs. (15) and (16) can be reduced to a SLAE without any additional analytical transformations. This approach was proposed and elaborated in [22, 36]. It represents the unknown function $\nu(\tau)$ in the form

$$\nu(\tau) = \frac{\vartheta_0(\tau)}{\sqrt{1-\tau^2}}, \qquad (17)$$

where $\vartheta_0(\tau)$ is a bounded function.

Let us seek an approximation $\vartheta_0^{(n)}(\tau)$ to the new unknown function $\vartheta(\tau)$ in the form of a polynomial of degree $(n-1)$ from the approximate SIE

$$\int_{-1}^{1}\frac{\vartheta_0^{(n)}(\tau)}{\tau-t}\frac{d\tau}{\sqrt{1-\tau^2}}+\int_{-1}^{1}K_1^{(n)}(t,\tau)\vartheta_0^{(n)}(\tau)\frac{d\tau}{\sqrt{1-\tau^2}} = 0, \tag{18}$$

$$t\in(-1,1)$$

under the approximate additional condition

$$\int_{-1}^{1}L_1^{(n)}(\tau)\vartheta_0^{(n)}(\tau)\frac{d\tau}{\sqrt{1-\tau^2}} = 0. \tag{19}$$

Here, the kernels are replaced with the Lagrange interpolation polynomials:

$$K_1^{(n)}(t,\tau) = \sum_{k=1}^{n}\sum_{j=1}^{n-1}K_1(t_j^{(2,n)},t_k^{(1,n)})$$

$$\times\frac{T_n(\tau)}{(\tau-t_k^{(1,n)})T'_n(t_k^{(1,n)})}\frac{U_{n-1}(t)}{(t-t_j^{(2,n)})U'_{n-1}(t_j^{(2,n)})},$$

$$L_1^{(n)}(\tau) = \sum_{k=1}^{n}L_1(t_k^{(1,n)})\frac{T_n(\tau)}{(\tau-t_k^{(1,n)})T'_n(t_k^{(1,n)})}.$$

Here, interpolation nodes are at zeros of the Chebyshev polynomial of the first kind, $T_n(\tau)$,

$$t_k^{(1,n)} = \cos\frac{(2k-1)\pi}{2n};\quad k = 1,2,\ldots,n,$$

in variable τ and at zeros of the Chebyshev polynomial of the second kind, $U_{n-1}(t)$, in the variable t,

$$t_j^{(2,n)} = \cos\frac{j\pi}{n};\quad j = 1,2,\ldots,n-1.$$

As follows from the properties of an integral operator with the Cauchy kernel, the left-hand side of Eq. (18) contains a polynomial of degree $n-2$. Therefore, for Eq. (18) to be satisfied, it is sufficient that it is satisfied at the points $t = t_j^{(2,n)}$; $j = 1, 2, \ldots, n-1$. By calculating the integrals that enter into Eqs. (18) and (19) with the help of Gauss quadrature formulas, we obtain an SLAE for $\vartheta_0^{(n)}(t_k^{1,n})$:

$$\frac{\pi}{n}\sum_{k=1}^{n}\vartheta_0^{(n)}(t_k^{1,n})\left[\frac{1}{t_k^{(1,n)}-t_j^{(2,n)}}+K_1(t_j^{(2,n)}-t_k^{(1,n)})\right] = 0;$$

$$j = 1,2,\ldots,n-1, \tag{20}$$

$$\frac{\pi}{n}\sum_{k=1}^{n}\vartheta_0^{(n)}(t_k^{1,n})L_1(t_k^{(1,n)}) = 0.$$

SLAE (20) is completely equivalent to problem (18), (19).

The convergence can be accelerated if we use another representation of the unknown function, which is more adequate for the physics of the problem:

$$\nu(\tau) = \frac{\vartheta_0(\tau)}{\sqrt[3]{1-\tau^2}}. \tag{21}$$

Let us describe the discretization method used in this case. Let $\{P_n(t)\}$ be a system of Jacobi polynomials, which is orthogonal on the interval $[-1, 1]$ with the weight $(1-t^2)^{-1/3}$, and $\{Q_n(t)\}$ be the system of adjoint Jacobi functions

$$Q_n(t) = \int_{-1}^{1}\frac{P_n(\tau)}{\tau-t}\frac{d\tau}{\sqrt[3]{1-\tau^2}}.$$

Let us seek the approximation $\vartheta_r^{(n)}(\tau)$ to function $\vartheta_r(\tau)$ in the form of a polynomial of degree $n-1$ from the approximate SIEs and an additional condition in which the kernels are replaced with interpolation polynomials. Let the interpolation nodes be at zeros of the polynomial $P_n(t)$ ($x_k^{(1,n)}$; $k = 1, 2, \ldots, n$) in variable τ and at the points that lie between them ($x_j^{(2,n)} = (x_j^{(1,n)}+x_{j+1}^{(1,n)})/2$; $j = 1, 2, \ldots, n-1$) in variable t.

Taking Eq. (15) at the points $x_j^{(2,n)}$; $j = 1, 2, \ldots, n-1$ and using the interpolation-type quadrature formula to calculate the singular integral [37] and the Gaussian formula to calculate the remaining integrals, we obtain a system of linear algebraic equations for $\vartheta_r^{(n)}(x_k^{(1,n)})$; $k = 1, 2, \ldots, n$:

$$\sum_{k=1}^{n}\vartheta_r^{(n)}(x_k^{(1,n)})\left[\frac{Q_n(x_k^{(1,n)})-Q_n(x_j^{(2,n)})}{P'_n(x_k^{(1,n)})(x_k^{(1,n)}-x_j^{(2,n)})}\right.$$

$$\left.+\lambda_k^{(n)}K_1(x_j^{(2,n)},x_k^{(1,n)})\right] = 0;\quad j = 1,2,\ldots,n-1,$$

$$\sum_{k=1}^{n}\vartheta_r^{(n)}(x_k^{(1,n)})L_1(x_k^{(1,n)}) = 0.$$

Here,

$$\lambda_k^{(n)} = \int_{-1}^{1}\left[\frac{P_n(\tau)}{P'_n(x_k^{(1,n)})(\tau-x_k^{(1,n)})}\right]^2\frac{d\tau}{\sqrt[3]{1-\tau_2}}$$

are the Christoffel coefficients [38]. Due to the Meixner edge condition for the rectangular wedge, function $\vartheta_0(\tau)$ in Eq. (17) behaves as $(1-\tau^2)^{1/6}$ near the ends of the integration interval. Therefore, its derivative tends to infinity as $\tau \longrightarrow \pm 1$. The function $\vartheta_r(\tau)$ defined in (21) is smoother ($\vartheta'_r(\tau)$ is a bounded function); therefore, it can be interpolated by polynomials more successfully. However, to apply this approach, it is necessary to calculate $x_j^{(2,n)}$, $x_j^{(1,n)}$, $P'(x_k^{(1,n)})$, $Q_n(x_k^{(1,n)})$, and $Q_n(x_j^{(2,n)})$; $k = 1, 2, \ldots, n$ and $j = 1, 2, \ldots, n-1$.

Tables 2 and 3 illustrate the accuracy and convergence rate of the eigenvalue χ of the operating $TE_{31,17}$ mode of the gyrotron resonator at the section $z = 0$ ($R_0 = 26.38425$, $R_i = 7.71946$), where the error of the impedance approximation, as well as the sensitivity of the results to errors, are the highest.

ACKNOWLEDGMENTS

We are grateful to Professor O. Dumbrajs (Helsinki University of Technology); Professor K. Schünemann (Technical University Hamburg–Harburg); Director of Institut für Hochleistungsimpuls- und Mikrowellentechnik Professor M. Thumm (Forschungszentrum Karlsruhe); and members of this institute Dr. B. Piosczyk and Dr. G. Dammertz for their interest in this work and valuable criticism.

This work was supported in part by the Academy of Sciences of Finland.

REFERENCES

1. M. Thumm, Int. J. Infrared Millim. Waves **22**, 377 (2001).
2. K. L. Felch *et al.*, Proc. IEEE **87**, 752 (1999).
3. M. Makovski, IEEE Trans. Plasma Sci. **24**, 1023 (1996).
4. O. Dumbrajs, J. A. Heikkenen, and H. Zohm, Nucl. Fusion **41**, 927 (2001).
5. V. E. Myasnikov *et al.*, in *Proceedings of the 23rd International Conference on Infrared and Millimeter Waves, Colchester, 1998*, pp. 24–25.
6. K. Sakomoto *et al.*, J. Phys. Soc. Jpn. **65**, 1888 (1996).
7. B. Piosczyk *et al.*, IEEE Trans. Plasma Sci. **26**, 393 (1998).
8. B. Piosczyk *et al.*, Frequenz **55**, 242 (2001).
9. M. Kuntze *et al.*, Fusion Eng. Des. **56–57**, 645 (2001).
10. V. A. Flyagin *et al.*, in *Proceedings of the 22nd International Conference on Infrared and Millimeter Waves, Wintergreen, 1997*, pp. 112–113.
11. R. Advani *et al.*, IEEE Trans. Plasma Sci. **29**, 943 (2001).
12. B. Piosczyk *et al.*, in *Proceedings of the 25th International Conference on Infrared and Millimeter Waves, Beijing, 2000*, pp. 19–20.
13. C. T. Iatrou, IEEE Trans. Plasma Sci. **24**, 596 (1996).
14. C. T. Iatrou, S. Kern, and A. B. Pavelyev, IEEE Trans. Microwave Theory Tech. **44**, 596 (1996).
15. J. J. Barosso, R. A. Correa, and P. J. de Castro, IEEE Trans. Microwave Theory Tech. **46**, 1221 (1998).
16. G. I. Zaginaylov, A. Hirata, T. Ueda, *et al.*, IEEE Trans. Plasma Sci. **28**, 614 (2000).
17. G. I. Zaginaylov, Y. V. Gandel, O. P. Kamyshan, *et al.*, IEEE Trans. Plasma Sci. **30**, 1151 (2002).
18. A. S. Omar, A. Jostingmeier, C. Rieckmann, *et al.*, IEEE Trans. Microwave Theory Tech. **42**, 2139 (1994).
19. J.-Y. Raguin and K. Schuenemann, in *Proceedings of the International Conference “Electronics and Radiophysics of Ultra-High Frequencies,” St. Petersburg, 1999*, pp. 403–409.
20. Y. V. Gandel, *Problems of Cybernetics* (Izd. Akad. Nauk SSSR, Moscow, 1986), Issue 124, pp. 166–183.
21. Yu. V. Gandel and T. S. Polyanskaya, J. Soviet Math. **48** (2), 144 (1990).
22. Y. V. Gandel, S. V. Eremenko, and T. S. Polyanskaya, *Mathematical Aspects of Discrete Currents Method. Substantiation of the Numerical Method of Discrete Singularities in Two-Dimensional Problems of Electromagnetic Wave Diffraction: Student’s Manual* (Kharkov. Gos. Univ., Kharkov, 1992), Part 2.
23. Y. V. Gandel, *Nonlinear Boundary-Value Problems of Mathematical Physics and Their Applications* (Inst. Matematiki NAN Ukrainy, Kiev, 1995), pp. 65–66.
24. Y. V. Gandel, Élektromagnitnye Yavleniya **1**, 220 (1998).
25. Y. V. Gandel, G. I. Zaginaylov, and S. A. Steshenko, *Radiophysics and Electronics* (Inst. Radiofiz. Élektron. NAN Ukrainy, Khar’kov, 2002), Vol. 7, Special Issue, pp. 196–203.
26. G. I. Zaginaylov, Y. V. Gandel, and P. V. Turbin, Microwave Opt. Technol. Lett. **16**, 50 (1997).
27. Y. V. Gandel and G. I. Zaginaylov, Dokl. Akad. Nauk **359**, 475 (1998) [Dokl. Phys. **43**, 214 (1998)].
28. G. I. Zaginaylov, Dokl. Akad. Nauk **367**, 40 (1999) [Dokl. Phys. **44**, 432 (1999)].
29. Y. V. Gandel and V. V. Khoroshun, in *Proceedings of the 46th All-Union Scientific Session of Popov Society, Devotion to the Day of Radio* (Radio i Svyaz’, Moscow, 1991), p. 33.
30. J. L. Tsalamengas, IEEE Trans. Microwave Theory Tech. **49**, 555 (2001).
31. O. Dumbrajs, Y. V. Gandel, and G. I. Zaginaylov, in *Proceedings of the 27th International Conference on Infrared and Millimeter Waves, San-Diego, 2002*, pp. 185–186.
32. B. Z. Katsenelenbaum, *Theory of Irregular Waveguides with Slowly Varying Parameters* (Izd. Akad. Nauk SSSR, Moscow, 1961).
33. A. I. Nosich, IEEE Antennas Propag. Mag. **41** (3), 34 (1999).
34. I. K. Lifanov, *Method of Singular Integral Equations and Numerical Experiment* (Yanus, Moscow, 1995).
35. B. Piosczyk *et al.*, in *Proceedings of the 26th International Conference on Infrared and Millimeter Waves, Toulouse, 2001*, pp. 5-15–5-16.
36. Y. V. Gandel, *Introduction to Methods for Evaluating Singular and Hypersingular Integrals* (Kharkiv, 2001).
37. A. A. Korneĭchuk, in *Numerical Methods for Solving Differential and Integral Equations and Quadrature Formulas*, Ed. by A. A. Abramov (Nauka, Moscow, 1964), pp. 64–74.
38. G. Szegö, *Orthogonal Polynomials* (American Mathematical Society, New York, 1959; Fizmatgiz, Moscow, 1962).

Translated by A. Khzmalyan

Technical Physics, Vol. 49, No. 7, 2004, pp. 895–904. Translated from Zhurnal Tekhnicheskoĭ Fiziki, Vol. 74, No. 7, 2004, pp. 90–98.
Original Russian Text Copyright © 2004 by Furman.

ELECTRON AND ION BEAMS, ACCELERATORS

Leakage-Flux Betatron

É. G. Furman
Research Institute of High-Voltage Equipment,
Tomsk Polytechnic University, Tomsk, 634050 Russia
e-mail: furman@hvd.tpu.ru

Received September 29, 2003

Abstract—A betatron on the leakage flux from two windings connected oppositely and laid around a closed magnetic circuit is considered. The governing magnetic field in the interpole gap is created by a leakage magnetic flux between the windings, while the accelerating magnetic flux is generated by the difference of the ampere-turns of the windings in a closed magnetic circuit. Results are presented that were obtained by examining the proposed scheme and by comparing it with the classical betatron scheme. It is shown that the use of a closed magnetic circuit, with the demagnetization of steel, makes it possible to implement, in the most economical way, the potential of the induction method of acceleration. *© 2004 MAIK “Nauka/Interperiodica”.*

INTRODUCTION

In a classical scheme, fulfillment of the 2 : 1 betatron relation is realized owing to magnetic gaps in the interpole space and in the central part (disk-coil unit), which ensure the required relationship between the magnetic-field inductions at the radius of the equilibrium orbit and within the circle of the orbit that are created by the magnetization coil [1, 2]. With increasing radius, the magnetic-field energy grows according to a quadratic law, while the kinetic energy of electrons is proportional to the radius; that is,

$$E_k = \langle\beta\rangle cBR_0, \quad \langle\beta\rangle = \int_1^{\gamma}\sqrt{1-\frac{1}{\gamma^2}}d\gamma, \qquad (1)$$

where $\langle\beta\rangle$ is a mean relative velocity, $\gamma = 1 + E_k/E_0$ is a relativistic factor, c is the speed of light, and B is the magnetic-field induction at the equilibrium radius R_0.

With respect to the energy of an oscillatory circuit, the electromagnet weight, and the kinetic energy, the most elaborate constructions of betatrons—a small-size betatron with $R_0 = 6$ cm and a high-current betatron with $R_0 = 30$ cm [2], which are characterized by the same ratio of the chamber height to the radius, $H/R_0 = 0.7$, and by identical values of the magnetic-field induction in steel—are in the ratios $6^2/30^2$–120 J/3 × 10^3 J – 90 kg/2.7 × 10^3 kg–6 MeV/30 MeV.

There are many approaches aimed at reducing the electromagnet weight owing to the demagnetization of steel and an increase in the magnetic-field-induction variations in it. However, a practical implementation of these approaches in [5] for a model of a 300-MeV betatron revealed that acceleration is unstable from one cycle to another and that the resulting intensity proves to be much lower than its calculated counterpart. A simpler scheme of the demagnetization of an electromagnet was proposed in [6]. This scheme ensured the calculated acceleration of a charge, but it required a considerable interval between pulses in order to demagnetize the electromagnet core. In the classical scheme featuring air gaps, the nonlinearity of the hysteresis loop has virtually no effect on the behavior of the radius of the equilibrium orbit at the beginning of the acceleration cycle, but, in the case of a closed magnetic circuit, it requires the application of dedicated correction circuits. For this, use was made of a saturable-core choke coil (weight about 20% of the magnet weight) in [5] and of an additional circuit with an independent power-supply unit in [6, 7]. The connection of windings in parallel and, as a consequence, the appearance of equating currents in response to a change in the Q factor of the windings because of heating, as well as the requirement of a high precision in synchronizing the operation of high-voltage power supply units, reduced the effect of harnessing the demagnetization of steel and hindered its application in practice.

1. ENERGY RELATIONS IN A LEAKAGE-FLUX BETATRON

The leakage flux in a transformer is determined by the loading current and is localized in the air gap between the primary and the secondary winding. The strength of the leakage-flux magnetic field is governed by the magnetization current in the primary winding. Together with the electric-field strength, this magnetic-field strength forms the Poynting vector [8] responsible for energy transfer from the primary to the secondary circuit.

An electron beam in the orbit in the electromagnetic field of a betatron plays the role of a winding and a load simultaneously and interacts with the energy flux coming from the capacitance storage device in a magnetic

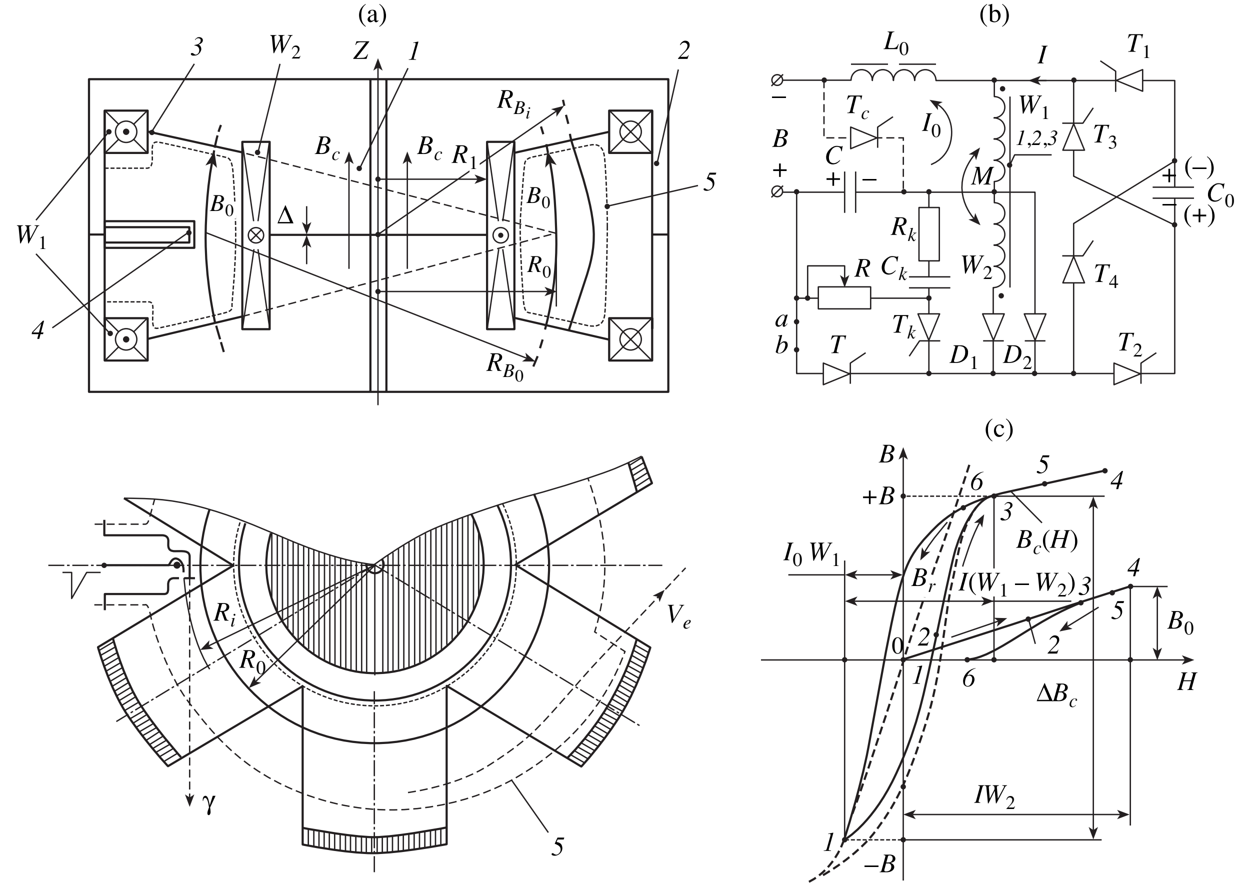

Fig. 1. (a) Electromagnet of a leakage-flux betatron: (W_1, W_2) magnetization and compensation windings, (*1*) central core, (*2*) backward magnetic circuit, (*3*) poles, (*4*) injector, and (*5*) contour of the vacuum chamber; (b) circuit of the betatron power-supply unit: (*B*) rectifier, (C_0) capacitance storage device, (T_1–T_4, D_1, D_2) thyristors and diodes of the high-voltage circuit, (T_k) thyristor of the *R*, C_k, R_k circuit of equilibrium-radius correction, (*T*) discharge thyristor, (*C*, L_0) capacitor and inductance choke of the filter, and (T_c) thyristor of the stabilization and control of energy; and (c) magnetic characteristics of the electromagnet and the air gap: [$B_c(H)$, $B_0(H)$] dependence of the magnetic-field induction in steel and in the air gap on the magnetic-field strength and (*1*–*6*) characteristic points on the magnetic curves matched in time with the values of the current in the windings (Fig. 2).

field. The electric-field strength is determined by the derivative of the magnetic flux and is therefore independent of its absolute value; it follows that part of the increment of the magnetic flux in the central region of the orbit can be changed from negative to positive values of the magnetic induction, and this circumstance is used in a leakage-flux betatron [9, 10] (see Fig. 1).

In the initial state, the thyristors *T*, T_3, and T_4 are switched on and the capacitance storage device C_0 and the capacitor *C* are preliminarily charged through the choke coil from the rectifier *B*. In the steady-state regime (see Fig. 2), the magnetic state of the magnetic circuit is determined by the magnetic flux of the winding W_1 carrying the current I_0 and is given by

$$-B = B_r - L_1 I_0 / W_1 S_c, \tag{2}$$

where L_1 is the inductance of the winding on a closed magnetic circuit, B_r is the residual magnetic-field induction in the steel of the magnetic circuit with allowance for the technological gap Δ, and S_c is the cross-sectional area of steel in the segment being considered.

In Fig. 1c, the initial magnetic state of the core is characterized by point *1* and the magnetic-field induction *B*. The thyristors T_1, T_2, and T_k are switched on at the instant t_1. The current discharging the capacitance storage device C_0 flows in the windings W_1 and W_2 connected in series and oppositely, and the formation of the magnetic fields $B_c(t)$ and $B_0(t)$ occurs there (see Fig. 2). As to the magnetic field in the interpole gap (leakage flux), it is determined by the ampere-turns of the winding W_2 and is dependent on the height *H* of the interpole space, so that

$$B_0(t) = \frac{\mu_0 i_2(t) W_2 K}{H}, \tag{3}$$

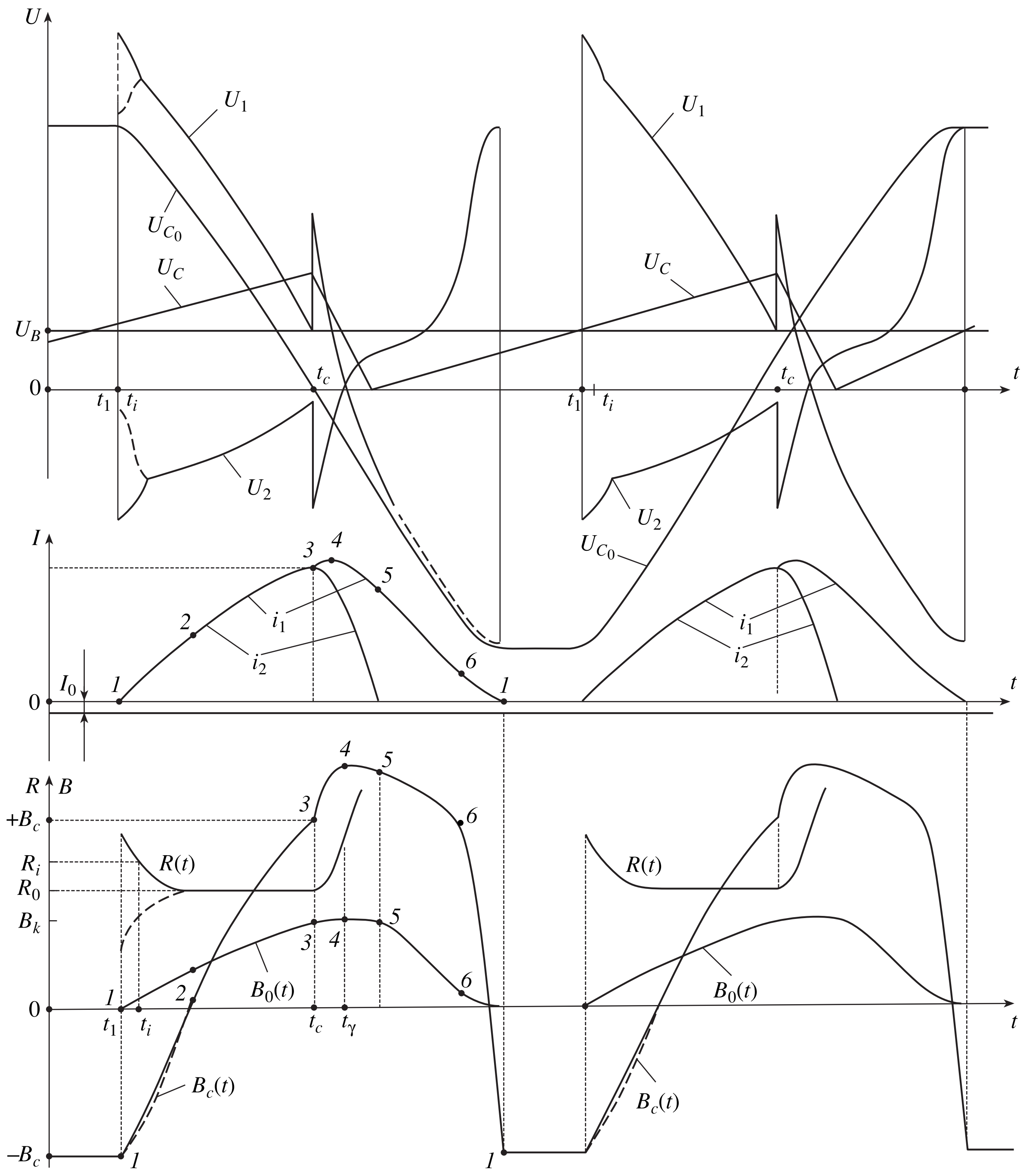

Fig. 2. Time profiles of the voltages across the capacitance storage device (U_{C_0}), the magnetization winding (U_1), the compensation winding (U_2), the capacitor of the filter (U_C), and the rectifier (U_B); time profiles of the currents in the windings W_1 (i_1) and W_2 (i_2) and the inductance coil L_0 (I_0); time profiles of the magnetic-field induction in central-core steel [$B_c(t)$] and in the interpole gap [$B_0(t)$]; and time profile of the equilibrium-orbit radius [$R(t)$], R_i being the radius of injection.

where μ_0 is a magnetic permeability, H is the gap height, and K is a coefficient that takes into account the curvature of lines of force.

The central core undergoes magnetic reversal under the effect of the ampere-turn difference $I(t)(W_1 - W_2)$. For the 2 : 1 betatron relation to be satisfied, it is necessary that

$$\frac{\langle \Delta B_c \rangle (t)}{B_0(t)} = 2 \approx \frac{U_2(t)(R_0^2 - R_1^2)}{U_{C_0}(t) R_1^2}. \tag{4}$$

Since $U_{C_0}(t) = U_1(t) - U_2(t)$ (see Fig. 2), the ratio of the voltages across the windings serves for monitoring the behavior of the equilibrium-orbit radius. If the thyristor T_k is not switched on, the voltages U_1 and U_2 will exhibit dips at the beginning of the accelerator cycle, with the result that the equilibrium radius $R(t)$ will begin to change from values less than R_0. In Fig. 2, these dependences are represented by dotted lines; they are determined by the nonlinearity of the hysteresis loop. Specifying the required initial voltage across the capacitor C_k, one can control the behavior of the radius $R(t)$. At the instant t_i, an injection of electrons and acceleration of the beam occur. At the instant t_c (point *3* on magnetic cycles), the thyristor T is switched on, with the result that the charged capacitor is connected to the winding W_2, which begins to be de-energized. Concurrently, the central core undergoes magnetic reversal faster and is saturated, which is accompanied by an additional acceleration of the beam and by a sharp increase in the equilibrium-orbit radius; touching the target mounted within the injector, the beam generates gamma radiation (at the instant t_γ). The capacitor C is completely discharged, its energy being transferred to the oscillatory circuit; the diode D_2 is switched on, while the thyristor T and the diode D_1 are switched off. The capacitor C is charged anew by the current I_0, while the magnetic circuit recovers its initial magnetic state (point *1* in Figs. 1 and 2). The next acceleration cycle begins from the switching on of the thyristors T_3, T_4, and T_k.

In the central part of the orbit, the magnetic flux traverses the closed core, and the magnetic-field energy per unit volume, which is proportional to $B^2/2\mu\mu_0$, decreases by the relative magnetic permeability μ of steel. Therefore, an increase in the acceleration radius R_0 and in the central-core radius R_1 leads to a reduction of the oscillatory-circuit energy. At a given value of the final electron energy (1) and a given value of the cross-sectional area S of the interpole gap (vacuum chamber), the energy stored in the circuit (energy of the capacitance storage device C_0) is given by

$$Q = K\frac{\pi E^2 S}{\mu_0(\langle\beta\rangle c)^2}\frac{1}{R_0} + Q_c, \tag{5}$$

where Q_c is the energy in the volume of the magnetic circuit; this energy, which decreases at the beginning of the acceleration cycle, is accumulated again by its end.

In contrast to what occurs in the classical scheme, the oscillatory-circuit energy in a leakage-flux betatron decreases in inverse proportion to the radius of the facility, while a nearly twofold change in the magnetic-field induction in steel leads to a considerable reduction of the electromagnet weight.

2. SOME SPECIAL FEATURES OF ELECTRON MOTION IN THE ELECTROMAGNETIC FIELD OF A BETATRON

In the region of acceleration, the magnetic field of a betatron is characterized by a damping index [4]

$$n = \frac{dB_Z}{dr}\frac{R}{B_Z}, \quad 0 > n > -1, \tag{6}$$

which determines the ratio of the radius R of the orbit of electron motion about the Z axis to the radius R_B of curvature of the magnetic line of force at the point of measurement. Figure 1a shows the profile of the interpole space for $n = -0.5$. In the region R_i where the injector is installed, $n \le -1$ because of the curvature of the lines of force, but we arrive, along the field lines of force, at $n = -0.5$ in the vicinity of the poles. This configuration of a magnetic field is characteristic of open-type magnetic traps [3], which have a loss-cone opening angle α given by

$$\sin\alpha = \sqrt{\frac{B_0}{B_Z}} = \frac{V_\perp}{V}, \quad |\bar{V}| = \sqrt{V_\perp^2 + V_\parallel^2}, \tag{7}$$

where B_0 is the magnetic-field induction in the symmetry plane (median plane); B_Z is the magnetic-field induction in the vicinity of the poles along the line of force; and $V_\perp$ and $V_\parallel$ are the components of the total electron velocity that are, respectively, orthogonal and parallel to the lines of force of the magnetic field in the median plane.

The motion of an electron in the electromagnetic field of a betatron is based on the equality of the Lorentz force and the force of the centripetal acceleration [4],

$$\frac{(m\mathbf{V})\cdot\mathbf{V}_\perp}{\mathbf{R}_0} = -e(\mathbf{E} + \mathbf{V}_\perp \times \mathbf{B}_0), \tag{8}$$

under the conditions

$$\frac{d(m\mathbf{V})}{dt} = -e\cdot\mathbf{E}, \quad \mathbf{E} = \frac{\mathbf{R}_0}{2}\frac{d\mathbf{B}_c}{dt}, \quad 2\frac{dB_0}{dt} = \frac{dB_c}{dt}, \tag{9}$$

where e and m are the electron charge and the relativistic electron mass, respectively; $m\mathbf{V}$ is the total particle momentum; E is the electric-field strength; and B_c is the mean value of the magnetic-field induction within a circle of radius R_0.

Since $\mathbf{V} \times \mathbf{B}/\mathbf{E} > 10^4$ even at the stage of injection, then, in the relativistic notation, we find from (1) and (8) at $V = V_\perp$ that the magnetic potential—that is, the

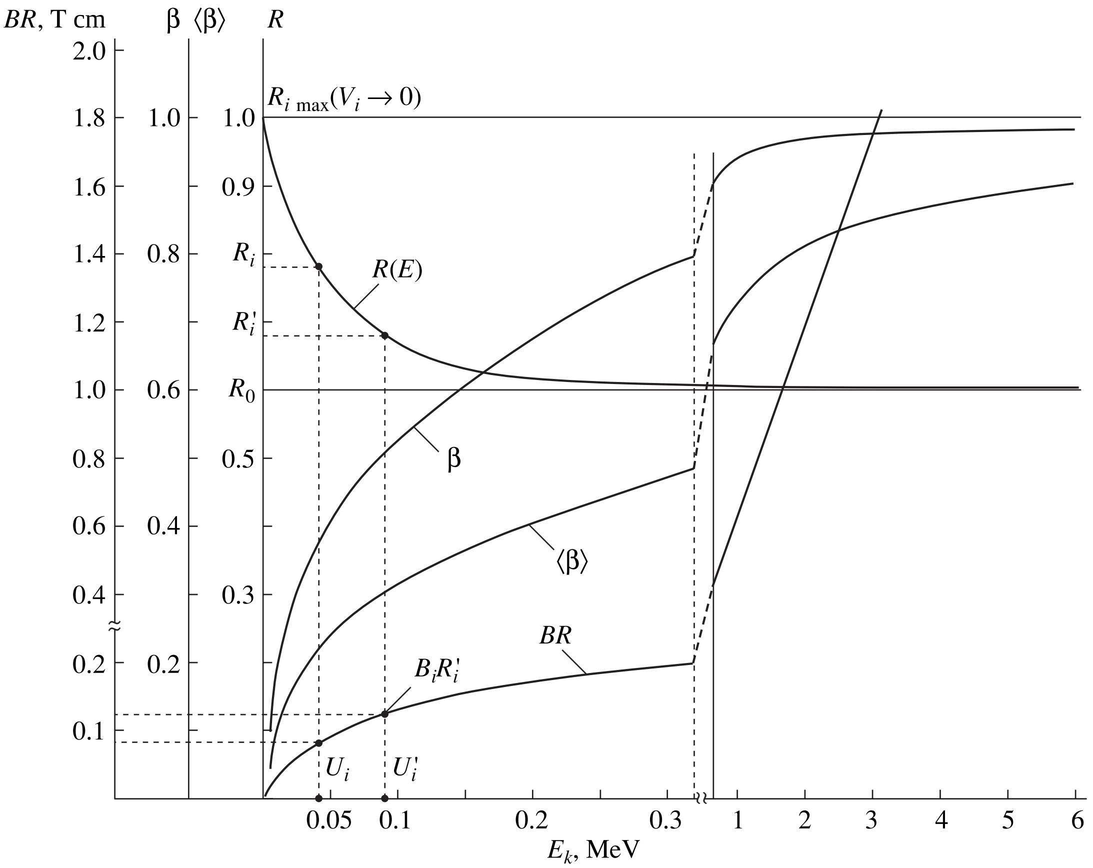

Fig. 3. Equilibrium-orbit radius $R(E)$, relative velocity β, mean relative velocity ⟨β⟩, and magnetic potential BR versus the electron kinetic energy.

product of the magnetic-field induction and the radius of revolution—is given by

$$BR = \frac{\sqrt{2E_kE_0 + E_k^2}}{e} = \frac{m_0c}{e}\sqrt{\gamma^2 - 1}, \qquad (10)$$

where E_k is the electron kinetic energy.

For the case where the governing magnetic field $B_0(t)$ grows linearly (see Fig. 2), which is valid at the beginning of the acceleration cycle, Fig. 3 shows the magnetic potential BR, the relative velocity β, the mean relative velocity ⟨β⟩, and the radius of revolution versus kinetic energy. In the regime of low-voltage ($U_i \le$ 80 kV) injection (see Fig. 3), contractors efficiently operate in classical betatrons [1], and the lower the voltage U_i, the higher the efficiency of their operation. In high-current betatrons [2], the application of a contractor does not lead to a positive effect since $U_i > 200$ kV there. In a leakage-flux betatron, an appropriate choice of the time constant for the C_k, R_k correction circuit and of the initial voltage across the capacitor C_k makes it possible to ensure the behavior of the radius $R(t)$ (see Fig. 2) according to Eq. (10) and to achieve the maximum possible capture of charge into the accelerated beam [10].

The kinetic energy of a rectilinearly propagating laminar beam of electrons is

$$J_k = E_kIt_0 = NeE_k = Nm_0c^2(\gamma - 1), \qquad (11)$$

where t_0 is the time it takes for N particles to travel a given distance (length of the orbit in a betatron) and $I = Ne/t_0$ is the beam current.

The kinetic energy of an electron beam in the form of a torus with radii R_0 and r in a magnetic field,

$$J_k = \frac{N(R^2 + r^2)(eB)^2}{\gamma m_0}, \qquad (12)$$

is given by (11), while the period of electron motion along the orbit is $t_0 = 2\pi/\omega_c$, where $\omega_c = eB/\gamma m_0$.

According to the Ampère law, a force proportional to grad$B$ associated with the magnetic potential BR acts on a ring current, with the result that, for an electron traveling along the orbit of equilibrium radius, the orbit plane acquires the moment of momentum

$$M = -\frac{\mathrm{grad}B_r}{F} = \frac{eE_k\mathrm{grad}B_r}{B}. \qquad (13)$$

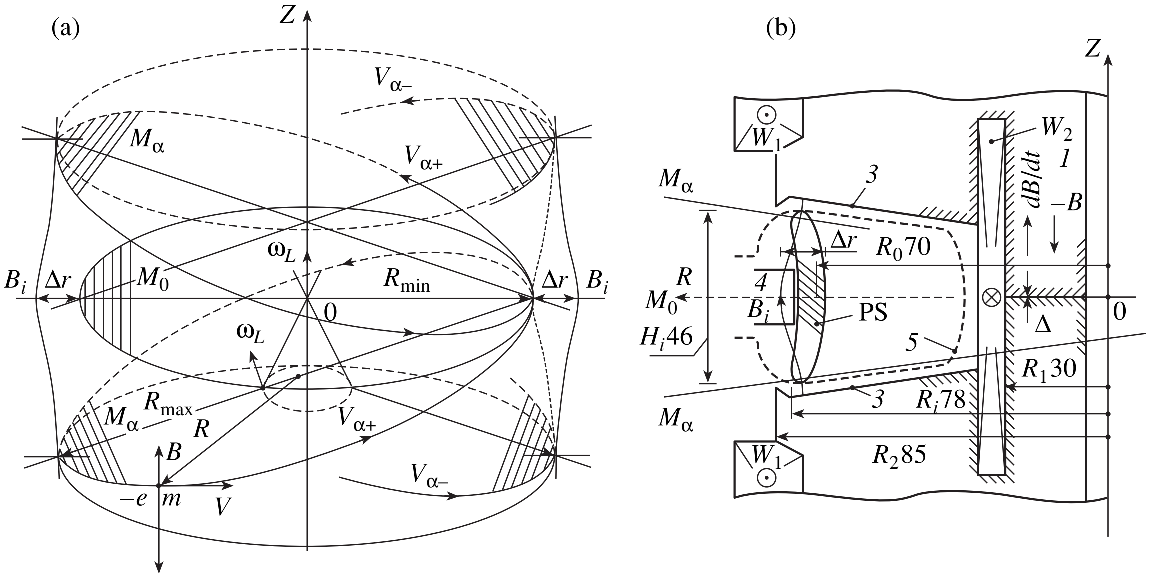

Fig. 4. (a) Electron trajectories in a magnetic trap upon the completion of injection and (b) interpole space of a leakage-flux-betatron model.

The gradient associated with BR must be of alternating sign and must be an integral multiple of the frequency of revolution, and its integral over the time of motion must be equal to zero. Concurrently, it should be borne in mind that the law of electromagnetic induction for an electron moving in a constant magnetic field is the following: the magnetic flux swept out along the trajectory of motion with time and divided by the period of revolution at the Larmor frequency is equal to kinetic energy. By way of example, we indicate that, in the model considered below for a leakage-flux betatron, it follows from (1), (11), and (12) that the kinetic energy of an electron at $R = 6 \times 10^{-2}$ m, $B = (0.361 \pm 5 \times 10^{-4})$ T, $\gamma = 12.74$, $\beta = 0.9969$, $\langle\beta\rangle = 0.9243$, $\omega_c = eB/\gamma m_0 = \beta c/R = 4.985 \times 10^9$ rad/s, and $t_0 = 1.264 \times 10^{-9}$ s is

$$E_k = \frac{m_0 c^2}{e}(\gamma - 1) = \langle\beta\rangle cRB = \frac{\langle\beta\rangle e R^2 B^2}{\gamma m_0}$$

$$= \frac{2\langle\beta\rangle \pi R^2 B}{t_0} = 6 \times 10^6 \text{ eV}.$$

The law of electromagnetic induction is satisfied at $\omega = \omega_c/2\langle\beta\rangle$—that is, for $\gamma \longrightarrow \infty$ and $\langle\beta\rangle \longrightarrow \beta \longrightarrow 1$—and we have the Larmor circular frequency $\omega = \omega_L = \omega_c/2$. In the process of acceleration, an additional magnetic flux traverses the electron orbit (2 : 1 condition), and the conversion from electric to kinetic energy occurs at the cyclotron frequency.

In the injection of electrons, flat beams of small angular divergence are used in betatrons. The injection voltage U_i and the magnetic-field induction at the injection radius are related by the equation

$$U_i = (B_i R_i)^2 \sqrt{\frac{e}{2\gamma_i m_0}}. \qquad (14)$$

Upon closing a circle, electrons that have the velocity $V_i = V_\perp = eB_iR_i/\gamma_i m_0$ hit the back side of the injector (zero electrons). Electrons for which the angle at which they escape from the injector with respect to the tangent to the circle of radius R_i is nonzero will execute betatron oscillations. If there are deviations only from the median plane, an electron does not have a chance to miss the injector. Electrons having an angle $+\alpha$ and going to radii larger than R_i and electrons having an angle $-\alpha$ and going to radii smaller than R_i are deflected from the median plane in opposite directions. In the course of their motion, they sweep out different magnetic fluxes since the magnetic field as a function of radius exhibits the power-law behavior given by $B(r) = B_0(r/R_0)^n$, and the vector of the injected-electron velocity acquires the component $V_\parallel$, the velocity component $V_\perp$ decreasing concurrently without any change in $V_i = \sqrt{V_\perp^2 + V_\parallel^2}$. The change in the kinetic energy of electrons in the capture process can be disregarded. The decrease in $V_\perp$ for electrons injected at the initial angle $+\alpha$ will lead to a decrease in the radius of revolution; for electrons having the initial angle $-\alpha$, this will lead to an increase in the radius of revolution, and they will traverse the projection of the orbit of radius R_i prior to making half of a full turn. The velocity component $V_\parallel$ will begin to decrease, while the component $V_\perp$ will increase; it follows that, in their subsequent turns, electrons will tend to traverse the median plane, having a maximum value of $V_{\parallel}$, a minimum value of $V_{\perp}$, and a minimum radius $R_{\min}$ of the orbit. In the steady-state regime, the trajectories of electrons that escaped from the injector at angles $\pm\alpha$ are displayed in Fig. 4a, while the phase space (PS) occupied by the beam upon the completion of capture is shown Fig. 4b. Such a trajectory makes it possible to ensure the equality of three frequencies: the mechanical frequency V/R, the cyclotron frequency ω_c, and the Larmor frequency ω_L. The beginning of the radius vector associated with an individual electron precesses by Δr with respect to the symmetry axis Z,

$$\Delta r = R_i\left[1-\left(\frac{V_{\perp}}{V_i}\right)^{-n}\right], \tag{15}$$

the loss-cone opening angle being at $V_{\perp} = V_{\parallel}$. From (7), we have $\sin\alpha = (V_{\perp} = V_{\parallel})/V_i = 1/\sqrt{2} = (B_i/B_Z)^{-1/2}$ fm and the value of $B_i/B_Z = 0.8409$ at the injection radius along a line of force. This value is obtained from magnetic measurements in the median plane M_0 and at the pole surface M_{α} (see Fig. 4a) in the interpole space of betatrons involving a maximum charge in the acceleration process. For the condition $V_{\perp} = V_{\parallel}$ to be satisfied, the height of the chamber under the injector and the injection radius must be related here by the equation

$$H_i = \frac{\pi}{4}R_i \quad \text{at} \quad n_{\alpha} = -0.5. \tag{16}$$

The critical angle of divergence of the injected beam, 2α ($\pm\alpha$), can be estimated on the basis of the condition $\sin\alpha \le \Delta r/R_i$. Because of matching with the lines of force of the magnetic field in the radial direction, the electron moves along the surface that is the mirror reflection of the pattern of lines of force in space with respect to the surface of a cylinder of radius R_i, and its orbit precesses with respect to the Z axis with the circular frequency

$$\omega = \omega_c P\langle\beta\rangle^{-1}, \tag{17}$$

where P is the periodicity of the weakly focusing magnetic field of a betatron (equal to two).

The application of an azimuthal variation, which is an element of strong focusing, increases the periodicity and decreases the amplitudes of radial and vertical oscillations, the cross-sectional area of the phase space, and (as a consequence) the number of particles involved in the acceleration process. Under the condition $H_i = 0.25\pi R_i$, fulfillment of the relation $V_{\perp} = V_{\parallel} = V_i/\sqrt{2}$ is ensured, and the maximum values of the amplitudes of radial and vertical oscillations are in the ratio 1 : 4 ($0.5\Delta r : 0.5H_i$) at $n = -0.5$. Considering that the electric-field strength at the phase-space surface is $\mathbf{E} = \mathbf{V}_i \times \mathbf{B}_i$ and taking into account the charge-density distribution over the cross section (the charge density in the median plane is twice as high as that at the edges, since an electron intersects M_0 two times over the period of revolution), we can estimate the number of particles captured into the magnetic trap of the betatron as

$$N \le \frac{\varepsilon_0 BVR_i^3}{1.5e\sqrt{1-\beta^2}} = \frac{\varepsilon_0\gamma\beta m_0c^2R_i^2}{1.5e^2\sqrt{1-\beta^2}} = \frac{\beta}{1-\beta^2}\times 1.88\times 10^{13}R_i^2 \ \text{(particles)}, \tag{18}$$

where the values of V, γ, and β correspond to the injected beam; the magnetic-field induction at the injection radius is $B_i = \beta\gamma m_0c/eR_i$; and the coefficient $1/\sqrt{1-\beta^2}$ takes into account the redistribution of the electric field of a moving electron with respect to that which is generated by an electron at rest.

The current circulating in the magnetic flux

$$I = \frac{eN\omega}{2\pi} = \frac{e^2B_iN}{2\pi\gamma m_0} \tag{19}$$

is distributed over the phase space and, in the acceleration process, is contracted into the M_0 plane (see Fig. 4a).

If the beam has a round cross section, which determines the vertical size of the focused spot, we have

$$r = 0.4H_i\sqrt{\frac{B_i\beta_i}{\pi B_k\beta_k}}, \tag{20}$$

where B_k and β_k are, respectively, the magnetic-field induction and the relative velocity at the end of the acceleration cycle.

The number of particles involved in the acceleration process must be related in some specific way to the number of injected particles. The repulsive electric field of zero electrons, which complete their revolution within the first turns, efficiently distributes electrons over the phase-space cross section, with the result that the orbit plane acquires a moment of momentum for $n \le -1$ (a spherical surface of the lines of force of the field B), which is transformed into $n = -0.5$ at the poles. Consequently, there exists an optimum injection-current value [1, 2] above which the number of particles involved in the acceleration process does not increase. The application of inflector systems removes the current of zero electrons to the injector in high-current betatrons [2], improving the efficiency of capture. In an iron-free betatron for obtaining electron rings [11], the efficiency of capture is quite high, about 0.8 of the number of injected electrons at an injection-pulse duration of 15×10^{-9} s. At $E_i \sim 1.5$ MeV, $I_m = 800$ A (the mean value is about 400 A), and $R_i = 0.3$ m, about 2.6×10^{13} particles are captured [$\beta/(1-\beta^2) = 15.5$], which corresponds to (18). In a high-current betatron [2] at $E_i = 300$ kV, $R_i = 0.28$ cm (which is the radius at which an electrostatic inflector is installed), and $H_i/R_i = 0.7$, the cycle of acceleration was completed for 2×10^{12} particles, and the result obtained by measuring, upon the passage of an injection pulse, the charge involved in the acceleration process was about 3×10^{12} [$\beta/(1 - \beta^2) = 1.92$], which is also in accord with (18). In an industrial small-size betatron (ISSB-6) [12], the vertical size of the focused gamma-radiation spot at $B_i = 0.88 \times 10^{-2}$ T, $R_i = 7.8$ cm, $H_i = 4.6$ cm, $U_i = 40$ kV, and $B_k = 0.36$ T is about 2.2 mm, while the spot radius at the end of the acceleration cycle is 1.1×10^{-3} m according to (20). The horizontal size of the focused spot is determined by the geometry of the target. In the ISSB-6 chamber, the phase-space volume is $0.5\pi H_i^2 R_i = 2.6 \times 10^{-4}$ m^3, and about 1.2×10^{10} particles are involved in the acceleration process at a current of 0.55 A circulating along the orbit, the optimum phase-space volume being about $R_i^3 = 4.75 \times 10^{-4}$ m^3.

The results of experiments in which the cross section of the betatron acceleration chamber was covered by 30 MeV in the vertical and the radial direction at $H_i/R_i = 7/30$ were given in [1, p. 168]. In the first case, the intensity of radiation disappeared when the vertical chamber size became equal to the injector height of about 1 cm. As the vertical size was increased, the intensity of radiation grew approximately in proportion to the cube of the chamber height. A multiplier-phototube signal that appeared at an energy of 1.5 MeV (U_i = 24 kV) when the wire intersected the equilibrium radius of $R_0 = 27$ cm and when there remained a distance of about 2.5 cm to the injector, $\Delta r/R_i = 2.5/30$ and $2(\pm\alpha) < 5°$, was monitored in the second case. An experiment devoted to determining the charge captured into the acceleration process within a short time after the passage of the injection pulse (2, 10, 20, 50, …, 300) $\times 10^{-6}$ s was performed in [13] for an acceleration cycle of duration 5×10^{-1} s discharged onto a segmented vertical collector. After 2×10^{-6} s, the charge distribution over the chamber height was greater at the center than at the edges by a factor of 2 and corresponded to the model represented in Fig. 4. The number of particles according to (18) was 1.3 times greater than that which was measured after 2×10^{-6} s ($R_i = 29$ cm, $H_i = 4.5$ cm, $U_i = 24$ kV, and $N_0 = 1.25 \times 10^9$), but, with allowance for the dynamics of losses ($N_1 = 10^9$ at 2×10^{-6} s, $N_2 = 0.3 \times 10^9$ at 10×10^6 s, $N_3 = 0.2 \times 10^9$ at 20×10^{-6} s, and $N_4 \approx 10^8$ at 300×10^{-6} s), the experimental result is in agreement with that calculated on the basis of (18). The dynamics of the adiabatic compression of the phase space by the increasing magnetic field was satisfied ($B_i = 0.15 \times 10^{-2}$ T, $\beta_i = 0.296$]; at 300×10^{-6} s (B_k = 0.045 T, $\beta_k = 0.98$]), and the entire accelerated charge arrived at the central collector in the median plane of height 5 mm; according to (20), the beam radius decreased to 1.8 mm at this instant. These direct and reliable experiments confirm the validity of the proposed model of electron capture by the betatron electromagnetic field (open magnetic trap).

3. EXPERIMENTAL INVESTIGATIONS OF A LEAKAGE-FLUX BETATRON

A model of a leakage-flux betatron was manufactured on the basis of an ISSB-6 device [12] by using a sealed-off vacuum chamber of internal diameter 74 mm. The central disk-coil unit with a total air gap of 11 mm was replaced by a continuous ferromagnet core of diameter 60 mm with a winding W_2 formed by 56 turns of a wire having a cross-sectional area of 6 mm^2. The magnetization winding W_1 contained 60 turns, 30 turns in each half, the technological gap being $\Delta = 0.1$ mm. The power-supply circuit is displayed in Fig. 1b, while the interpole space of the leakage-flux betatron is shown in Fig. 4b. In the ISSB-6 device, an oscillatory-circuit energy of 120 J was required to obtain an electron kinetic energy of 6 MeV. In our leakage-flux betatron, an identical electron energy was achieved at an energy of 87 J in the capacitance storage device C_0, and this value was reduced by an energy of 33 J stored in the disk-coil unit, this corresponding to the energy calculated by formula (5). Concurrently, the power consumed from the power-supply system was reduced by a factor of 2 owing to a reduction of losses in the circuit and to the elimination of discharge circuits and a contractor. The maximum intensity of radiation was obtained in the case where the circuit intended for correcting the equilibrium-orbit radius ensured the behavior of the radius according to (10) (see Fig. 3) at $U_i = 40$ kV. The resulting intensity was not less than in well-elaborated betatrons employing a contractor (0.1 mGy/s at a distance of 1 m from the target at 100 pulse/s). Upon an increase in the oscillatory-circuit energy to 120 J, the electron kinetic energy reached 6.9 MeV, while at 150 J, it amounted to about 8 MeV. As to the range of the magnetic-field-induction variation, it was $\Delta B_c = 2.75$ T in steel and 2.15 T in the backward magnetic circuit (see Fig. 1c).

Unfortunately, available vacuum chambers gave no way to increase the diameter of the central core to 75 mm, which would permit taking full advantage of employing the backward magnetic circuit of the ISSB-6 electromagnet of weight about 80 kg, whereby one could reach an electron energy of about 11 MeV.

In order to test mirror ratio (7) for the magnetic trap of the betatron and to study the behavior of the beam at the instant of capture at the pole radius of $R = 8.2$ cm at $R_i = 7.8$ cm, one turn was laid in each winding, these two being similarly connected. The windings were connected in parallel to the diode D_2 through the circuit formed by a 0.1-μF capacitor and a variable resistor. When the direction of the current pulse in the winding was identical to that which is associated with the ampere-turns W_1I, the field exponent at the poles in the plane M_α (see Fig. 4a) changed from –0.5 to –1. In the vicinity of the poles, the lines of force that traversed the injector formed the spherical surface $R_B = R_i$. In the case where the direction of the current in the windings was opposite to that which is associated with W_1I, the field exponent at the poles approached zero, so that the field became uniform in the region above the injector, $R_B \longrightarrow \infty$.

In the first case and at a current of $I(t_i) \sim 0.5$ A in the windings (at the instant of injection, $W_1I(t_i) \sim 350$ A × turn), the intensity of radiation increased by 15%, whereupon it began to decrease monotonically with increasing current in the windings. At a current of 6 A in the windings, it was about 60% of the initial value, while at a current of 10 A, it fell short of 20%. In this case, the field exponent was close to –1, and the electrons were lost at the upper and lower walls of the chamber because of the moment of momentum of the orbit plane M_α. In the second case, where the direction of the current in the windings was opposite to that which is associated with the ampere-turns W_1I_i, the intensity of radiation began to decrease with increasing current, by 10, 50, and more than 90% at a current of 0.2, 0.5, and 6 A, respectively, in the windings. In this case, the electron-orbit planes developed translational motion in a uniform field with respect to the median plane M_0, with the result that electrons settled on the upper and lower parts of the chamber, as in the preceding case. Our experiment clearly demonstrates that, at the instant of capture, the electromagnetic field of a betatron can be treated as an open magnetic trap and that the theory of adiabatic invariant processes [3], which takes into account the energy of rotational motion, the moment of inertia of electrons in an orbit [see Eq. (12)], and gyroscopic effects associated with this, can be used in this case.

With allowance for all of the aforesaid, the extraction of an electron beam from the acceleration chamber through an inlet window in it was implemented in a leakage-flux betatron. The height H_i above the injector was about 30 mm. The gamma-radiation intensity obtained with this chamber was one-half as high as that for the $H_i = 46$ mm chamber, all other conditions being the same, and this corresponded to (18). In order to create a magnetic-field gradient in the plane M_0, use was made of two sector windings laid along the lateral surface of the chamber, each having an azimuthal length of about 30°. The common axis of these windings was orthogonal to the radius of the injector. The windings were connected in series and oppositely in the circuit of the thyristor T (Fig. 1b, points a, b). In response to a displacement of the beam in a leakage-flux betatron of the design being considered, the expansion of the orbit radius proceeds at a rate $V_r = \Delta r/\Delta t \sim 10^4$ m/s. During the expansion of an orbit, the current increased in the windings, creating an additional magnetic field that enhanced the field in the region where the beam approached the injector and reduced it upon passing this region. The magnetic-field gradient caused a drift of the center of the expanding orbit at the velocity

$$V_d = K\frac{(\beta c)^2\gamma m_0}{eB_0R_i}, \tag{21}$$

where $K \simeq 10^{-2}B_+/B_0$, B_+ being the additional field generated by the windings in the region of the injection radius.

At $V_+ \approx 10^{-3}B_0$, the equality of the velocities V_r and V_d was ensured, the loss of electrons at the injector was negligible, and the segment within which electrons traversed the release orbit was in front of the injector. The last circumstance made it possible to match the axis of the extracted beam in controlling energy. At a distance of 0.3 m from the Z axis of the betatron, the intensity of electron-beam emission was 1.6 Gy/s at $E_k \sim 5$ MeV and $N = 50$ pulse/s. At this distance, the cross section of the beam had the shape of an ellipse contracted along the Z axis to a size of 4×1.5 cm^2, the density being approximately uniform over the cross section. It should be noted that, if a filter (iron 4 mm thick) was arranged on the trajectory of the beam, the gamma-radiation-flux density determined by recording gamma radiation with a dosimeter at a distance of 1 m was approximately identical to that in the case of a target at a distance of 1 m. It is worthy of note that, by merely shorting out points at which the windings are connected (leads a and b in Fig. 1b), the leakage-flux betatron could be switched to the gamma-radiation mode.

At energies above 6 MeV, the orbit was found to be contracted at the end of the acceleration cycle for $N \leq 50$ pulses/s because of a decrease in the demagnetization current. In this regime, use was made of an additional circuit formed by an inductance coil and a thyristor and connected in parallel to the thyristor T, which was switched on at the end of the acceleration cycle, ensuring a slow transfer of energy to the oscillatory circuit. Here, the radius of the equilibrium orbit did not decrease. It was maintained at a level of about 7 cm to the beginning of the dumping of electrons on the target. By applying, instead of the inductance coil in the additional circuit, a parallel LC circuit whose natural frequency was much higher than the frequency of the betatron high-voltage circuit, an oscillatory character of the motion of the equilibrium-orbit radius was ensured; as a result, the beam could repeatedly touch the target, generating pulses of gamma radiation with a frequency equal to that of the LC circuit.

CONCLUSIONS

The main flaw in the classical scheme of the betatron—a quadratic dependence of the magnetic-field energy and of the electromagnet weight on the radius of injection—is removed in a leakage-flux betatron [see Eq. (5)]. An increase in the radius of injection in a betatron is advantageous in all respects: this increases the beam energy (1) and the number of beam particles (18) and reduces problems associated with synchrotron radiation at energies above 300 MeV. In a leakage-flux betatron, the control of the equilibrium-orbit radius in the process of capture, acceleration, and dump is implemented by varying the derivative of the magnetic flux in steel without introducing additional windings in the interpole space (this would distort the structure of the magnetic field of a magnetic trap) or additional power-supply units. The power-supply system developed for the betatron is multipurpose; the commuting equipment does not have limiting values of di/dt and dU/dt, and the frequency potential of the circuit is very high, which makes it possible, by means of an appropriate choice of materials, to improve the Q factor of the betatron oscillatory circuit and to reduce the energy loss per acceleration cycle, pushing it down to that which is described by Eqs. (11) and (12).

We will now present a derivation of formula (1) for the kinetic energy of electrons in a betatron. The mean voltage across the turn of the radius of revolution (increment of the magnetic-field induction per unit time interval) is $\langle U\rangle = \pi R^2\Delta B_c/\Delta t$; the time of one revolution is $t_0 = 2\pi R_0/V = 2\pi R_0/\beta c$, where $V = c\sqrt{1-1/\gamma^2}$. Within the time over which the magnetic-field induction changes in the circle of radius R (the acceleration time is t_0), an electron acquires the potential $E_k = \langle U\rangle\Delta t/t_0$ with respect to the walls of the vacuum chamber; in the acceleration process, the relativistic factor changes from γ_i to γ. Taking into account the relations in (9), we then have

$$E_k = c\int_{\gamma_i}^{\gamma}\sqrt{1-1/\gamma^2}\,d\gamma\Delta B_c R_0/2 = \langle\beta\rangle cBR_0.$$

In the case of low-voltage injection, γ_i tends to unity, and we arrive at Eq. (1).

ACKNOWLEDGMENTS

I am grateful to V.A. Kasyanov (Research Institute of Introscopy, Tomsk Polytechnic University) for providing the possibility of experimentally investigating the statements formulated in [9] and to M.M. Rychkov and A.A. Chertov for assistance in the work.

REFERENCES

1. L. M. Anan’ev, A. A. Vorob’ev, and V. I. Gorbunov, *Betatron: An Induction Electron Accelerator* (Gosatomizdat, Moscow, 1961).
2. V. A. Moskalev, *Betatrons* (Énergoizdat, Moscow, 1981).
3. L. A. Artsimovich and R. Z. Sagdeev, *Plasma Physics* (Atomizdat, Moscow, 1979).
4. J. D. Lawson, *The Physics of Charged-Particle Beams* (Clarendon, Oxford, 1977; Mir, Moscow, 1980).
5. P. W. Kerst, J. P. Adams, and H. W. Koch, Rev. Sci. Instrum. **21**, 462 (1950).
6. V. V. Vasil’ev, V. A. Moskalev, and É. G. Furman, Prib. Tekh. Éksp., No. 4, 27 (1979).
7. V. V. Vasil’ev, G. V. Milyutin, and É. G. Furman, Izv. Vyssh. Uchebn. Zaved. Fiz., No. 12, 89 (1979).
8. L. V. Leĭtes, Élektrichestvo, No. 7, 45 (1978).
9. É. G. Furman, RF Patent No. 2173035 (2000).
10. V. A. Kas’yanov, É. G. Furman, and A. V. Chertov, Prib. Tekh. Éksp., No. 1, 6 (2002).
11. V. P. Sarantsev and É. A. Perel’shteĭn, *Collective Acceleration of Ions by Electron Rings* (Atomizdat, Moscow, 1979).
12. L. M. Anan’ev, Defektoskopiya, No. 6, 43 (1968).
13. O. V. Sokolov, in *Proceedings of the 3rd Interinstitute Conference, Tomsk, 1961*, pp. 75–78.

Translated by A. Isaakyan

Technical Physics, Vol. 49, No. 7, 2004, pp. 905–908. Translated from Zhurnal Tekhnicheskoĭ Fiziki, Vol. 74, No. 7, 2004, pp. 99–101.

Thermally Stimulated Desorption of Ionized Particles from the Oxygen-Activated Na/Au Surface

M. V. Knat'ko, M. N. Lapushkin, and V. I. Paleev

Ioffe Physicotechnical Institute, Russian Academy of Sciences,
Politekhnicheskaya ul. 26, St. Petersburg, 194021 Russia
e-mail: Lapushkin@ms.ioffe.rssi.ru

Received December 8, 2003

Abstract—A heated Na/Au surface alloy film grown on gold substrate is found to be an efficient thermal desorber of polyatomic positive ions produced from organic molecules and oxygen falling on its surface. The ionization of diethylamine molecules at this thermal emitter is studied by mass-spectrometry means. Special features of the heterogeneous formation of polyatomic complexes and the thermal desorption of cluster ions are revealed. A model explaining the efficient thermal desorption of ions from the surface of an alloy which is a wide-gap semiconductor is proposed. © *2004 MAIK "Nauka/Interperiodica".*

For a long time, surface alloys that result from the adsorption of alkali metals (Cs, Rb, K, Na) on gold have been the objects of numerous comprehensive studies. It is shown that these alloys greatly differ in their properties from other intermetallic compounds. For example, the alloy CsAu is an electron semiconductor with a band gap of $\cong$2.6 eV, its crystal structure being similar to that of CsCl [1].

We investigate the vacuum interaction between alkali metals and metal gold in the conditions when the atomic flows with $\nu = 10^{11}$–10^{13} cm^{-2} s^{-1} are directed to the Au substrate heated to T = 700–1250 K. It is known that, at $T \leq 300$ K, the initiation of the reconstruction of the metallic gold surface and the formation of the surface alloy Alk/Au (where Alk is the atom of an alkali metal) requires an initial accumulation of adsorbate with surface concentration Θ within several tenths of the monolayer thickness [2]. At elevated substrate temperatures T, the lifetime of Alk adatoms at the Au surface is short and the reverse flow of thermal desorption of particles from the surface into vacuum leads to a substantial reduction of the equilibrium value of Θ. However, we observed the formation of $\mathrm{Alk}_x\mathrm{Au}_y$ alloys on the Au surface and a number of special effects that are determined by the electronic properties and the structure of these alloys. For example, the presence of the $\mathrm{Alk}_x\mathrm{Au}_y$ alloy on the Au surface considerably decreases the rate of Au sublimation and increases the diffusion coefficient of Alk atoms in the alloy compared to these values for the pure metal [3, 4]. Photostimulation of the diffusion of Alk atoms in the alloy was observed in [5–7]. In systems of $\mathrm{Na}_x\mathrm{Au}_y$ [4] and $\mathrm{K}_x\mathrm{Au}_y$ [8], the formation and destruction of surface alloys were studied by means of surface ionization mass spectrometry. It is shown that $\mathrm{Na}_x\mathrm{Au}_y$ and $\mathrm{K}_x\mathrm{Au}_y$ feature the properties of wide-gap semiconductors with the band gap between 2.6 and 2.8 eV [7], which is close to that of CsAu.

In this study, we present experimental data indicating that the interaction between the amine molecules and the oxygen-activated heated surface of Na/Au alloy results in the thermal ionization of the formed polyatomic particles and the desorption of positive ions. In this case, the efficiency of ion formation approaches the value obtained by mass spectrometry of alkylamines ionized on the surface of thermal emitters from oxidized refractory metals.

We used the experimental setup previously described in [4]. After the substrate surface (a gold tape 99.99%) was cleaned of the initial impurities and reconstructed by the method presented in [5], we obtained a homogeneous structure with a work function $\varphi_{\mathrm{Au}} = 4.7 \pm 0.1$ eV. The technique for the formation of surface alloy $\mathrm{Na}_x\mathrm{Au}_y$ on gold is described in [4, 5]. As a test organic compound, we chose diethylamine $[(C_2H_5)_2NH]$. The purity of the initial substance was confirmed by comparing the experimental electron ionization mass-spectra to the reference mass-spectra of diethylamine (DEA) [9]. The surface ionization of DEA, as well as of other alkylamines, on emitters from pure and oxidized refractory metals has been thoroughly studied [10, 11]. The main components in the surface ionization mass spectrum of DEA are the ionized products of the heterogeneous thermal decomposition of molecules (M) with a detachment of hydrogen $(\mathrm{M{-}H})^+$ or of the methyl radical $(\mathrm{M{-}CH_3})^+$. With a decrease in temperature, protonated ions $(\mathrm{M + H})^+$ are observed.

In our case, the alkali metal atoms were ionized on the surface of pure gold, which was heated to T = 1000–1250 K; the temperature dependences of the positive-ion currents coincided with those predicted by the surface ionization theory [12] in the form of the relation $(eU - \varphi)/kT$, where eU is the ionization energy per particle. The inflow of oxygen to a pressure of $P_{O_2} \leq 5 \times 10^{-6}$ Torr had little or no effect on the magnitude or the temperature dependence of currents; i.e., the Au emitter retained its thermoemission properties in O_2. In the temperature range considered, the incidence of DEA molecules ($P \sim 1\text{–}2 \times 10^{-7}$ Torr) on the emitter did not lead to the emergence of new lines in the ionization mass spectrum within the achieved experimental accuracy; i.e., no thermal ionization of DEA was observed. The products of DEA heterogeneous dissociation on metals are characterized by high ionization energies ($eU > 7$ eV) [10] compared to the values of φ in metals; therefore, to obtain measurable ion currents, an increase in the emitter temperature far above the Au melting point is required.

We judged the dynamics of the multilayer surface alloy formation by detecting the change in the resistivity R of the tape upon the deposition of Na atoms at T = const. Estimating the resulting NaAu film thickness, we concluded that the deposition provides for surface coatings with a thickness of ~2–3 μm.

Upon heating the Au tape coated with the NaAu film to temperatures $1000 \leq T \leq 1250$ K, we detected the thermally stimulated desorption of Na^+ ions related to the thermal destruction of the alloy. At $T \leq 1100$ K, the intrinsic thermal emission current of Na^+ is small. When Na atoms from an external source were directed onto the alloy-coated emitter surface, the increase in the Na^+ current was considerably smaller than that in the current obtained under same conditions (emitter temperature, alkali atom flow density ν) from a pure gold surface. This fact might suggest that $\varphi_{NaAu} \ll \varphi_{Au}$ under the assumption that the surface ionization is the only process resulting in the ion production. However, this statement contradicts the results of our measurements [3] of the change in the work function of Au during the formation NaAu alloy. According to the measurements of φ carried out by the contact potential difference method [12] in the course of the aforementioned experiments, the formation of the alloy is accompanied by a gradual increase in the minimal work function φ_{min} by $\Delta\varphi_{min} \approx 0.4$ eV to the instant when a stable alloy coating of the metal is attained.

No new mass lines appeared in the spectrum of thermionic emission from the NaAu surface after an inflow of DEA molecules into the working chamber.

A considerable change in the thermoemission and catalytic properties of the alloy was observed for the inflow of oxygen with $P_{O_2} \sim 2\text{–}3 \times 10^{-6}$ Torr to its surface. At the initial stages of the alloy formation, the combined inflow of Na and O_2 to the substrate led, first, to a complete cessation of the thermal emission of Na^+ and, then, to a gradual increase in the ionic current to values much higher (by up to 300 times at $T = 1100$ K) than those obtained before the emitter exposure to oxygen. With the assumption that the thermal desorption of Na^+ is governed by surface ionization, the observed increase in the ion emission points to an increase in φ_{max} by $\Delta\varphi_{max} \approx 0.5\text{–}0.6$ eV. Such an increase in φ should provide for the thermal desorption of sodium in the form of Na^+ ions with an almost 100% probability. However, this current was smaller than that initially obtained as a result of ion emission from pure gold. In the case of the formation of a multilayer coating of NaAu, the presence of oxygen on the surface decreased the thermoemission current of Na^+ ions. Apparently, a considerable change in the emitter composition and properties under the exposure to O_2 affects both the emitter surface and the near-surface layers (an oxygen-induced destruction of the AlkAu alloy surface is well known [13]).

As a consequence of the oxygen-induced change in the properties of the alloy surface, the heated tape became an efficient thermal ionizer of organic compounds that come to the surface from an external source. Thus, a part of the products of DEA heterogeneous thermal catalysis was desorbed on the emitter surface in the form of ions. Similar to the case of surface ionization of DEA on oxidized tungsten [14], the mass spectrum of its thermal ionization on the alloy included the lines of ionized radicals that resulted from the initial molecule (M = 73 u) after the loss of a H atom (m = 72 u) and the CH_3 radical (m = 58 u). However, unlike the emitters from oxidized refractory metals [15], the emitter studied here efficiently ionized numerous products of the association reactions that take place on its surface. These reactions include the decay products of the initial DEA molecule, the oxygen atoms that are present in the emitter surface layer, and sodium either ionized or neutral. First, we detected the current of ions with mass m = 86 u, which were formed in the process of substitution $H \longrightarrow CH_3$ in the radical (M–H). In addition, we detected the products of the association $[(C_2H_5)_2N(CH_2)_nNa]^+$, as well as the series of ions $[C_2H_5(CH_2)_nNHONa]^+$ and $[C_2H_5(CH_2)_nNHNa]^+ \cdot H_2O$, where factor n varies in the range $1 \leq n \leq 8$. The associative ionic currents decrease with increasing n. The thermal desorption of ionized complexes from the alloy surface takes place at high temperatures $T > 1100$ K as well. In the case of surface ionization on oxidized refractory metals, associative ions, which are the products of heterogeneous reactions of protonation, are observed only at low emitter temperatures $550 \text{ K} < T < 900$ K.

The relative intensities of ionic currents and their temperature behavior strongly depend on the experimental conditions (the presence or absence of the O_2 and Na inflows to the surface). Table lists the main lines in the mass spectrum of the thermal desorption of ions related to the DEA adsorption on the oxygen-activated surface of NaAu alloy heated to $T = 1100$ K in various experimental conditions. A change in the values of mass lines can be traced upon variation of experimental conditions: (*1*) the oxygen-activated alloy surface was exposed to DEA molecules ($P \sim 1 \times 10^{-7}$ Torr), and the mass spectra were obtained after two-hour-long inflow of organic molecules; (*2*) the same in O_2 ($P_{O_2} \sim 2 \times 10^{-6}$ Torr); and (*3*) the surface is exposed to Na atomic flow ($\nu \sim 10^{11}$ cm^{-2} s^{-1}).

It is seen that the oxygen flow to the surface increases the intensities of all mass lines. It seems possible that the presence of O_2 promotes surface cleaning from carbon coating, which lowers work function φ of the emitter and reduces its catalytic activity. According to the theory [12], if the surface ionization were the only process leading to the emission of ions, the growth of current would correspond to an increase in the value of φ of the alloy surface by ~0.2 eV. However, the thermal desorption of ionized clusters at high temperature points to the radical difference of the emitter studied here from the surface-ionization emitters mentioned above. The participation of Na atoms, as well as H_2O molecules, in the formation of the associative products substantiates the conclusion that the clusterization and ionization processes are connected with the presence of active centers on the emitter surface, which are responsible for both the formation and the emission of polyatomic ions. Note that, at $T < 1050$ K, the emission of Na^+ ions is almost undetectable, though sodium atoms appear in the composition of the surface layer and are present in cluster ions, whose current is detected at $T < 800$ K. The inflow of Na atoms to the surface has only a slight influence on the ionized cluster yield in comparison to that of oxygen. Apparently, at a considered density, the Na flow results in only a slight change in the concentration of the alkali metal in the surface layer of the alloy. Moreover, one should note that the alloy film features the properties of a wide-gap semiconductor and permits the thermal ionization of alkali metal ions at the alloy–metal gold interface with the subsequent emergence of ions at the surface [8]. It is not improbable that the ions emerging at the surface from the bulk of the layer are active charged centers and participate in the electron exchange with the particles occurring within the range of their action. The results of electron transitions manifest themselves in the formation of radicals and clusters, as well as in their ionization.

Note that the ionization efficiency of M–H and M–CH_3 radicals in the system considered above is close to that obtained for the same products of DEA decomposition on the efficient surface-ionization emitters from oxidized tungsten [10, 11]. However, these two types of emitters differ in the temperatures corresponding to the maximal efficiency of ion formation; specifically, the efficiency of Alk/Au emitter peaks at $T > 1000$ K, while the efficiency of oxidized refractory metals is maximal in the range $650 < T < 750$ K.

Table

Mass, u	Presumed ion composition	Flows to the surface		
		DEA	DEA + O_2	DEA + O_2 Na
58	$CH_2{=}N^+H{-}C_2H_5$	0.02	0.25	0.25
72	$CH_3{-}CH{=}N^+H{-}C_2H_5$	1.0	11.0	10.5
86	$CH_3{-}CH{=}N^+CH_3{-}C_2H_5$	0.1	1.1	1.10
97	$[C_2H_5NHCH_2ONa]^+$	0.07	0.9	0.95
99	$[C_2H_5NHCH_2Na]^+ \cdot H_2O$	0.06	0.8	0.65
109	$[(C_2H_5)_2NCH_2Na]^+$	0.01	0.15	0.20
113	$[C_2H_5NH(CH_2)_2Na]^+ \cdot H_2O$	0.03	0.50	0.50
123	$[(C_2H_5)_2N(CH_2)_2Na]^+$	0.01	0.07	0.07
127	$[C_2H_5NH(CH_2)_3Na]^+ \cdot H_2O$	0.01	0.50	0.05
141	$[(C_2H_5)_2N(CH_2)_3Na]^+$	0.005	0.25	0.04

Thus, a highly efficient thermal emitter of organic ions is realized on the basis of a wide-gap semiconductor alloy Alk/Au. The emitter is capable of cluster formation from the initial molecule decay products with the participation of alkali atoms; the clusterization process occurs at high temperatures.

Heterogeneous processes resulting in cluster formation and ion thermal emission call for further investigation since these processes are responsible for the selectivity of the ionization of individual organic compounds.

ACKNOWLEDGMENTS

This study was supported by Russian Program "Surface Atomic Structures," project SC (State Contract) no. 1152.

REFERENCES

1. W. E. Spicer, A. H. Sommer, and J. G. White, Phys. Rev. **115**, 57 (1959).
2. M. S. Skottke-Klein, A. Boettcher, and R. Imbeek, Thin Solid Films **203**, 131 (1991).
3. M. V. Knat'ko, V. I. Paleev, and E. Ya. Zandberg, Phys. Low-Dimens. Semicond. Struct., No. 7/8, 27 (1996).
4. M. V. Knat'ko, V. I. Paleev, and M. N. Lapushkin, Phys. Low-Dimens. Semicond. Struct., No. 5/6, 85 (1998).
5. É. Ya. Zandberg, I. D. Pelekhatyĭ, and M. M. Sushchikh, Pis'ma Zh. Tekh. Fiz. **21** (19), 15 (1995) [Tech. Phys. Lett. **21**, 774 (1995)].
6. M. V. Knat'ko, V. I. Paleev, and M. N. Lapushkin, Zh. Tekh. Fiz. **68** (10), 104 (1998) [Tech. Phys. **43**, 1231 (1998)].

7. M. V. Knat’ko, M. N. Lapushkin, and V. I. Paleev, Zh. Tekh. Fiz. **68** (10), 108 (1998) [Tech. Phys. **43**, 1235 (1998)].
8. M. V. Knat’ko, M. N. Lapushkin, and V. I. Paleev, Phys. Low-Dimens. Semicond. Struct., No. 9/10, 85 (1999).
9. *Short Mass Spectra Catalog* (Nauka, Novosibirsk, 1981).
10. É. Ya. Zandberg and U. Kh. Rasulev, Usp. Khim. **51**, 1425 (1982).
11. U. Kh. Rasulev and E. Ya. Zandberg, Prog. Surf. Sci. **28**, 181 (1988).
12. É. Ya. Zandberg and N. I. Ionov, *Surface Ionization* (Nauka, Moscow, 1969).
13. S. Chaturvedi and J. A. Rodriguez, Surf. Sci. **401**, 282 (1988).
14. É. Ya. Zandberg, U. Kh. Rasulev, and M. R. Sharapudinov, Teor. Éksp. Khim. **7**, 363 (1971).
15. É. Ya. Zandberg, U. Kh. Rasulev, and Sh. M. Khalikov, Zh. Tekh. Fiz. **46**, 832 (1976) [Sov. Phys. Tech. Phys. **21**, 483 (1976)].

Translated by A. Sidorova

Technical Physics, Vol. 49, No. 7, 2004, pp. 909–915. Translated from Zhurnal Tekhnicheskoĭ Fiziki, Vol. 74, No. 7, 2004, pp. 102–109.
Original Russian Text Copyright © 2004 by Frolov.

SURFACES, ELECTRON AND ION EMISSION

Magnetic Properties of 3*d*-Metal Nanocrystalline Films

G. I. Frolov

Kirenskiĭ Institute of Physics, Siberian Division, Russian Academy of Sciences,
Akademgorodok, Krasnoyarsk, 660036 Russia
e-mail: SVA@iph.krasn.ru

Received December 16, 2003

Abstract—The problem of designing high-resistivity soft magnetic materials based on 3*d*-metal nanocrystalline films is discussed. To increase the electrical resistivity, nanogranular composites are proposed; they consist of superparamagnetic particles embedded into a dielectric matrix. To obtain the required soft magnetic properties in such composites, it is necessary to realize magnetic ordering due to the effects of magnetic interaction between nanoparticles. As an example, magnetic films that exhibit good high-frequency properties in a range up to several hundreds of megahertz are presented. *© 2004 MAIK “Nauka/Interperiodica”.*

INTRODUCTION

The nanocrystalline state of materials is a topical cross-disciplinary scientific problem involving materials science, solid-state physics, and solid-state chemistry [1–4]. During the last 15 years, the interest in this problem has been substantially increased due to the fact that a decrease in the grain size (primarily, in metals) to $D < 10$ nm results in significant changes in the properties of nanoparticles. To study the parameters of nanocrystalline materials, it is necessary to take into account not only the properties of nanoparticles but also the interaction between them.

Nanocrystalline composites are applied in various fields of modern engineering for creating soft and hard magnetic materials [1, 5] and data media for magnetic-memory devices [6]. We already discussed the problem of data media in [7], and, in this work, we study the problems dealing with the development of soft magnetic nanocrystalline materials.

One may question the expediency of designing new materials if amorphous alloys have excellent soft magnetic properties. The point is that 3*d* metal-based amorphous alloys have high electrical conductivity and cannot be used at frequencies above the kilohertz range. Nanoparticles consist of a core and a shell—phases having different physical properties, which should naturally increase the resistivity of such nanocomposites. Therefore, soft magnetic nanocrystalline materials open opportunities for their application in high-frequency devices.

STRUCTURE–COERCIVITY CORRELATION IN NANOCRYSTALLINE MAGNETIC MATERIALS

In the mid-1960s, the soft magnetic properties of nanocrystalline materials were described in a number of reviews [5, 8]. It was noted in [5] that the authors of [9, 10] were the first to study the effect of annealing on the magnetic properties of amorphous tapes. The annealed samples consisted of magnetic grains separated by an amorphous phase, whose volume fraction in the composite was ~20%. To decrease the sizes of the magnetic particles, Cu and Nb were added to the alloy; an interesting dependence of the coercive force on the diameter of the magnetic particles was discovered.

However, to be more exact, it was shown in the mid-1970s that a decrease in the crystallite size in permalloy films caused a sharp decrease in the coercive force [11]. The magnetic properties of FeNi(SiO) films were studied depending on the dielectric concentration (Figs. 1, 2).

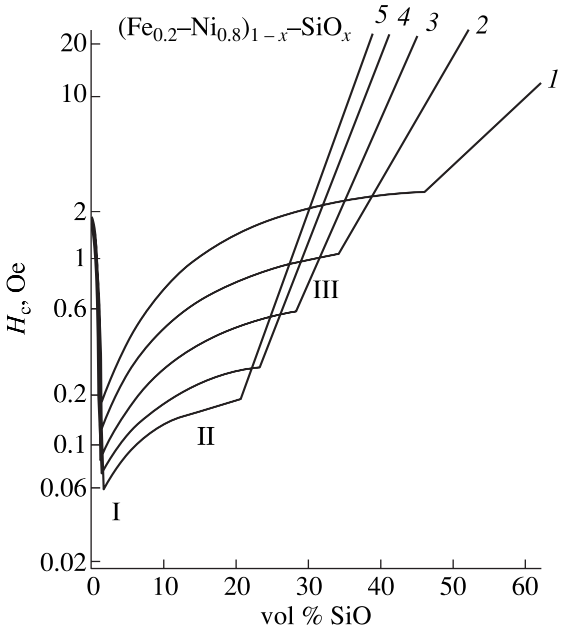

Fig. 1. Dependence of the coercive force in (Fe–Ni)–SiO films on the volume fraction of silicon monoxide. The film thickness is (*1*) 100, (*2*) 200, (*3*) 300, (*4*) 400, and (*5*) 500 nm.

1063-7842/04/4907-0909$26.00 © 2004 MAIK “Nauka/Interperiodica”

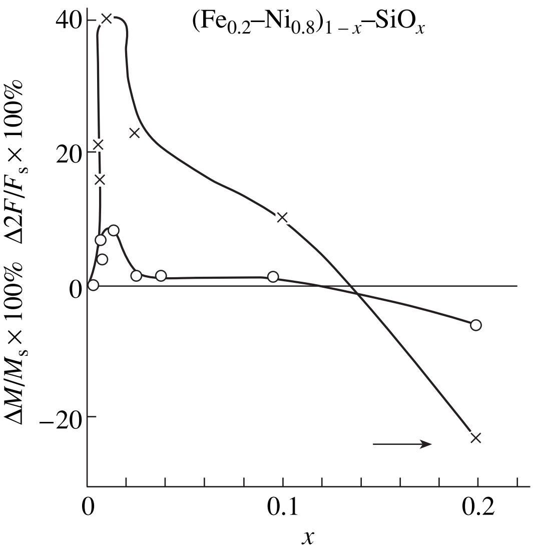

Fig. 2. Dependences of the relative changes in the saturation magnetization M_s and the Faraday rotation $2F$ in permalloy films on the volume fraction of silicon monoxide. ○, M_s; ×, $2F$.

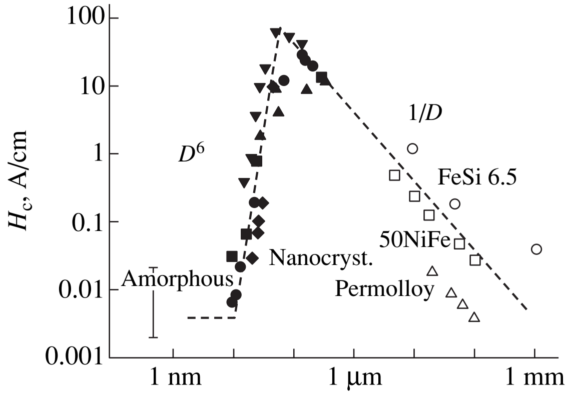

Fig. 3. Dependence of the coercive force on the grain size D in Fe-based nanocrystalline films. $T = 300$ K [8].

In this case, dielectric serves as a source of impurity states in the band structure of a metal and, on the other hand, increases the number of nucleation centers during condensation. In the former case, the introduction of a dielectric impurity modifies the electron spectra and, hence, changes the fundamental properties of the magnet [12]. In the latter case, it favors the formation of a nanocrystalline structure.

Experiments show that the composition range of permalloys for which relative changes in the magnetization and Faraday rotation are positive coincides with the range where these alloys have the properties of a strong ferromagnet. The concentration dependences of the saturation magnetization and the Curie temperature were simulated in [13]. An impurity (Si–O complexes) was assumed to penetrate into the permalloy lattice and to create a Coulomb potential that is caused by unsaturated valence bonds and is different from the potential of the unperturbed matrix. The screening of this charge by electrons of the d band, which has a higher density of states at the Fermi level, leads to changes in the fundamental magnetic parameters. However, the significant decrease in the coercive force H_c at ~2 vol % impurity (Fig. 1) was not explained. Electron-microscopic analysis shows that the crystallite size decreases to the values when a single-domain state is formed in crystallites. In this case, the main magnetization-reversal mechanism is rotation of the magnetic moment, which should increase the threshold magnetization-reversal fields [14].

These results, along with the data obtained in [9, 10], were explained in 1990 [15]. In the model proposed, the key factor of the dependence of the coercive force on the microstructure of a magnet is magnetic anisotropy and the possibility of controlling its value. The value of magnetic anisotropy mainly depends on the crystalline magnetic anisotropy K_1, which is determined by lattice symmetry. For $3d$ metals, K_1 is too high to reach low values of H_c. However, the effective contribution of K_1 can substantially be decreased by decreasing the grain size and taking into account the exchange interaction between grains.

According to the model of random anisotropy proposed to describe the properties of amorphous ferromagnets [16], the effective anisotropy K_{eff} in an ensemble of disoriented magnetic particles is determined by the ratio of the grain size D to the exchange-interaction radius

$$L_0 = \left(\frac{A}{K_1}\right)^{1/2},$$

where A is the interparticle exchange parameter.

At $D > L_0$, we have $K_{\text{eff}} = K_1 N^{1/2}$, where $N = (L_0/D)^3$. At $D < L_0$, $K_{\text{eff}} = K_1 N^{-1/2}$. Therefore, the dependence of H_c on the grain size has the form shown in Fig. 3 [8]. Three regions can be distinguished in this curve: in region I, where $D > L_0$, $H_c \sim 1/D$; that is, H_c increases with decreasing grain size; in region II, where $D = L_0$, $H_c = 2K_1/M_s$, where M_s is the saturation magnetization; and, in region III, where $D < L_0$, $H_c \sim D^6$. Figure 3 also shows the experimental data for Fe-based nanocrystalline materials, which confirm the calculation results.

Thus, we can assume that the model proposed correctly describes the experimental dependence of the coercive force on the particle size in nanocrystalline materials produced by annealing of amorphous samples. A specific feature of these materials is a particle size as small as ~10 nm. These materials can be applied at frequencies as high as several hundred kilohertz [5]. To use these materials at higher frequencies, their resistivity ρ must be increased.

One of the methods for solving this problem is the use of nanogranular condensates in which magnetic nanoparticles are embedded into a dielectric matrix.

However, the fraction of a dielectric layer should be low enough to retain good soft magnetic properties (high M_s). Therefore, the potential of this approach is limited by the probability of conduction-electron tunneling through a grain boundary [17]. To further increase ρ, one can use the dependence of the carrier density on the particle size. The authors of [18] showed that, when the particle size was smaller than the electron mean free path, some carriers were localized. The localization was found to affect the electrical conductivity more strongly than an increase in the scattering by boundaries, defects, and impurities. This effect was detected for 3*d*-metal nanoparticles with a size $D <$ 7 nm.

Thus, to create high-resistivity nanocrystalline materials, one has to apply composites with a particle size <10 nm. Based on the model described above [8], the coercivity of such composites should be $H_c \approx 10^{-3}$ Oe. However, other values of H_c were detected experimentally. For example, in nanocrystalline Fe films with a particle size $D < 10$ nm, researchers found that $H_c = 30$ Oe in the films with $D = 6$ nm [19] and $H_c =$ 3–5 Oe in the films with $D < 4$ nm [20].

Such a significant deviation from the calculated data can be due to the fact that the model assumed the independence of the main magnetic parameters of nanoparticles of their sizes. However, experiments show that the situation is different. As the value of D decreases, changes in the structure of nanoparticles increase the anisotropy constant and decrease M_s and A. For example, in the Fe films with $D = 6$ nm, $K = 2.5 \times 10^6$ erg/cm^3, $M_s = 850$ G, and $A = 10^{-7}$ erg/cm [19]. Thus, the exchange-interaction radius in these samples decreases as compared to the films with a particle size $D > 10$ nm and is equal to $L_0 = 5$ nm; i.e., $L_0 \approx D$. Then, to calculate H_c, we have to use the formula $H_c = 2K/M_s$; in this case, we obtain $H_c > 10^3$ Oe. This value is also inconsistent with the experimental data. This discrepancy indicates that a specific magnetic order is formed in 3*d*-metal films having a particle size <10 nm.

MAGNETIC HYSTERESIS IN NANOGRANULAR SYSTEMS WITH SUPERPARAMAGNETIC PARTICLES

To analyze the magnetic state of 3*d*-metal nanocrystalline films, let us turn to the results of [21], where the effects of thermal magnetization relaxation were studied in an ensemble of noninteracting single-domain particles having a uniaxial anisotropy. If this system is magnetized in a field H and the field is then removed, the remanent magnetization obeys the law

$$M_r = M_s \exp(-t/\tau), \tag{1}$$

where t is the time after the field removal and τ is the relaxation time to the state of thermodynamic equilibrium.

The relaxation time is described by the expression

$$\tau = f_0 \exp(-KV/k_B T), \tag{2}$$

where K is the uniaxial anisotropy constant; V is the particle volume; f_0 is the frequency factor, which is equal to the precession frequency of the magnetic moment of a particle ($f_0 = 10^9$ s^{-1}) in a first approximation; k_B is the Boltzmann constant; and T is the temperature. This exponential dependence results from the fact that the uniaxial-anisotropy energy of a particle depends on the angle between its magnetization and the easy axis. At $\tau/t \le 1$, the system changes to a superparamagnetic state ($M_r = 0$, $H_c = 0$).

Equation (2) can be used to determine the critical size V_{cr} of a particle at which it becomes superparamagnetic at $T =$ const or the temperature T_B of transformation of a particle into a superparamagnetic state at $V_{cr} =$ const.

At $\tau = 100$ s, which is the relaxation time characteristic of induction methods of measuring M_r, we find

$$V_{cr} = \frac{25 k_B T}{K}, \quad T_B = \frac{KV}{25 k_B}. \tag{3), (4}$$

At $H = 0$, the threshold for the transformation of the system to a superparamagnetic state is $E = KV$. At $H \neq 0$, the threshold decreases and is given by

$$\Delta E(H) = KV\left[1 - \frac{HM_s}{2K}\right]^2. \tag{5}$$

The coercive force of a particle at $T \neq 0$ is equal to the field at which the magnetization-reversal threshold $E(H)$ decreases to a value at which magnetization reversal occurs due to thermal effects in the experimental time t. Using Eqs. (3)–(5), we obtain [22]

$$H_c = H_{c_0}\left[1 - \left(\frac{V_{cr}}{V}\right)^{1/2}\right] = H_{c_0}\left[1 - \left(\frac{D_{cr}}{D}\right)^{3/2}\right], \tag{6}$$

$$H_c = H_{c_0}\left[1 - \left(\frac{T}{T_B}\right)^{1/2}\right], \tag{7}$$

where H_{c_0} is the coercive force of the particle at $T = 0$.

As follows from Eq. (6), the value of H_c decreases significantly as the nanoparticle size approaches D_{cr}. This dependence can be applied to produce nanocrystalline materials with a low coercive force. To this end, it is necessary to determine D_{cr} for 3*d*-metal nanoparticles.

Using the parameters of bulk materials, the authors of [21] obtained $D_{cr} \approx 20$ nm for α-Fe particles at $T =$ 300 K. However, more recent studies showed that, as the particle size decreases, the particle structure changes to yield a core–shell system. As a result of restructuring, the uniaxial-anisotropy energy increases and D_{cr} decreases correspondingly. The experimental dependence of H_c on the core diameter of α-Fe nano-

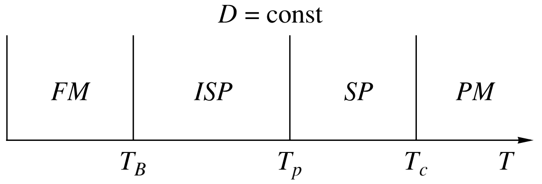

Fig. 4. Temperature dependence of the diagram for the magnetic state of an ensemble of nanoparticles (D = const).

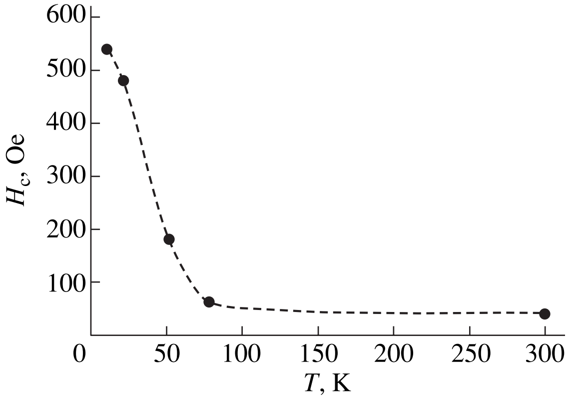

Fig. 5. Temperature dependence of the coercive force of Fe nanocrystalline films [19].

particles is given in [23]; at T = 300 K, particles with a core diameter of ~4 nm were found to transform into a superparamagnetic state (H_c = 0). An oxide shell around the core is ~2 nm thick. Therefore, for α-Fe nanoparticles, the critical diameter of the transformation to a superparamagnetic state at room temperature decreases to $D_{cr} \approx 6$ nm.

Thus, the data given above indicate that thermal effects cause a strong dependence of the coercive force on the magnetic-particle size. It should be noted that numerous experimental results obtained upon studying the properties of nanogranular magnetic materials formed by superparamagnetic particles have not been completely understood. For example, the appearance of magnetic hysteresis and magnetic ordering in an ensemble of superparamagnetic particles in the high-temperature limit ($T > T_B$) has not been interpreted [24]. Such effects are explained using several factors, such as a large scatter of particle sizes, the presence of a set of structurally or magnetically different phases, local anisotropy, and magnetic interaction between particles [25].

Therefore, one has to determine a factor that is predominant in the magnetic behavior of a nanogranular system in a certain particular case. In this respect, the experiments [26] on studying the effect of the interparticle distance on the magnetic properties of an ensemble of 3d-metal clusters placed in a nonmagnetic matrix are of interest. The authors provided constant nanoparticles sizes and structures and showed that, as the content of a magnetic phase decreased, the system is transformed from a magnetically ordered to a superparamagnetic state. This experiment indicates that the interparticle interaction substantially affects the magnetic state of the system.

Allia *et al.* [27] studied the effects of interparticle interaction and proposed a diagram of the magnetic state of an ensemble of nanoparticles depending on the particle size and temperature. The temperature dependence of this diagram is shown in Fig. 4.

At $T < T_B$, the system is in the ferromagnetic state. At $T > T_B$, the particles become superparamagnetic and the magnetic order remains unchanged (ISP region). According to [27], the magnetic energy of the ith particle that interacts with its neighbors can be written as

$$E = KV\sin^2\alpha + \sum K_m^{ij} M_i(T)M_j(T), \qquad (8)$$

where the first term on the right-hand side characterizes the uniaxial-anisotropy energy of the particle; the second term describes the energy of interaction between the particle and the nearest neighbors; M_i and M_j are the magnetization vectors of the ith and jth particles, respectively, and summation is carried out over all neighboring jth particles; and K_m^{ij} is the interparticle magnetic coupling constant.

Using the mean field theory, we can write

$$E = KV + K_m M^2(T)V. \qquad (9)$$

The temperature of transition from region FM to region ISP is $T_B = KV/25k_B$ (Fig. 5). At $T > T_B$, magnetic ordering in the system is formed due to the effects of magnetic interparticle interaction. In this case, the temperature of transition to the region of a superparamagnetic (SP) state is

$$T_p = \frac{K_m M^2(T)}{3k_B}. \qquad (10)$$

Region II on the diagram ($T_B < T < T_p$) has various names: the region of interacting superparamagnetic particles (ISP) [27] or the region of superferromagnetic ordering [28]. Since the contributions from the dipole–dipole and exchange interactions have not been exactly estimated, we prefer the name ISP. At $T > T_p$, the system transforms to the superparamagnetic state, and, at $T > T_C$, to the paramagnetic state (T_C is the Curie temperature). We now consider the behavior of the coercive force for the transitions described above. Figure 5 shows the experimental dependence $H_c = f(T)$ for α-Fe nanocrystalline films with a particle size of D = 6 nm [19]. Recall that, at T = 300 K, nanoparticles of this diameter should be paramagnetic. As is seen from Fig. 5, H_c = const in a wide temperature range (T = 70–300 K), and, at T < 70 K, this dependence obeys Eq. (7); that is, T_B = 70 K for these films. Similar results were obtained for Fe–SiO_2 films with a mean particle size of $D = 6$ nm [29].

To explain the unusual behavior of the $H_c = f(T)$ dependence in the ISP region (at $T > T_B$), we assume that magnetization only weakly depends on temperature here; hence, the interparticle magnetic interaction energy is constant. Therefore, H_c = const.

Thus, a magnetic order can be created in a system of interacting superparamagnetic particles; this order is characterized by a low coercive force and a weak temperature dependence of the coercive force. Since the 3*d*-particle size in this system is $D < 7$ nm, this system can have a high electrical resistivity.

MAGNETIC PROPERTIES OF HIGH-RESISTIVITY NANOGRANULAR FILMS

The idea of increasing resistivity in nanocrystalline materials by creating a dielectric layer between magnetic nanoparticles was realized in [30]; the authors studied the structure and magnetic properties of Fe–Sm–O films. The films were produced by reactive rf sputtering of an Fe target with Sm_2O_3 pellets on its surface in an Ar + O_2 atmosphere. The oxygen pressure was varied in the range 0–10% to produce films of various compositions. The structure, phase composition, and magnetic and electric properties of these films were studied (see table).

The film thickness was $d = 1$ μm. Electron-microscopic analysis showed that the films consisted of two phases: α-Fe nanocrystallites ($D = 10$ nm) and samarium oxide particles ($D = 3$ nm). The most interesting results were obtained for the $Fe_{83.5}Sm_{3.5}O_{13}$ film. The study of the frequency dependence of the quality factor ($Q = \mu_1/\mu_2$ is the ratio of the real to the imaginary component of magnetic permeability) showed that Q remained high up to $f = 40$ MHz.

The high-frequency magnetic properties of granular Co–Al–O films were studied in [31]. The films were produced by the same methods as in [30]; they consist of fcc Co particles with $D = 5$ nm surrounded by a dielectric Al–O layer. The properties of these films are the following: $d = 1.7$ μm, $M_s = 800$ G, $H_c = 5$ Oe, and $\rho = 1100$ μΩ cm. The frequency dependence of the magnetic permeability of the films was studied. The real part μ_1 of the magnetic permeability remains virtually constant up to $f = 500$ MHz and coincides with the calculated data. The high resistivity in these films is caused by a decrease in the size of magnetic nanoparticles to $D < 7$ nm and by the presence of a dielectric layer between them. The films produced represent a new class of high-frequency magnetic materials, which have a high value of μ_1 and a low value of μ_2 in a frequency range up to 200 MHz. A higher resistivity was realized in nanogranular Co–Sm–O films produced by the pulse-plasma evaporation of a Co_5Sm target in a vacuum of 10^{-6} Torr. This method of film deposition was described in [7].

Table

PO_2, %	Composition	Saturation magnetization, G	Coercivity, Oe	Magnetic permeability ($f = 100$ MHz)	Electrical resistivity, μΩ cm
0	$Fe_{93}Sm_{3.5}O_{3.5}$	1570	13.7	153	40
2	$Fe_{87}Sm_4O_9$	1520	9	285	70
5	$Fe_{83.5}Sm_{3.5}O_{13}$	1430	0.8	2600	130
8	$Fe_{81}Sm_{3.5}O_{15.5}$	1330	8.5	550	170
10	$Fe_{56}Sm_3O_{41}$	310	24	44	240

In the initial state, the films are superparamagnetic ($T_B \approx 80$ K) and consist of Co particles ~2 nm in size surrounded by Sm_2O_3 layers. Annealing in a vacuum of 10^{-6} Torr changes the structure and properties of the films. Figure 6 shows the dependences of the resistivity, coercive force, and saturation magnetization on the annealing temperature. In the initial state, resistivity ρ of the films is equal to 5×10^{-2} Ω cm, which is about four orders of magnitude higher than the values characteristic of the corresponding metallic samples having a polycrystalline structure. The sharp decrease in ρ at $T_{ann} > 600$°C is caused by the destruction of the separating Sm_2O_3 interlayers and the formation of a galvanic contact between the metallic particles.

The variation of the coercive force with the annealing temperature is complex (Fig. 6b). Three regions with different values of H_c can be distinguished on this curve. Hysteresis loops that are typical of these regions are shown in Fig. 7. In region I, the loop becomes open only at $T < 80$ K, which indicates a superparamagnetic state of the samples. In region II (T_{ann} = 200–350°C), the loop becomes open at room temperature and has small values of H_c (H_c = 0.1–2 Oe, Fig. 7b). At $T_{ann} >$ 400°C, H_c exhibits two specific features: it first increases jumpwise to 250 Oe and then increases to 450 Oe as a result of the second jump. Electron-microscopic analysis shows that, at these annealing temperatures, a polycrystalline structure is formed in the films and the sizes of Co particles increase by an order of magnitude. Note that, over the whole range of annealing temperatures, the saturation magnetization increases virtually threefold (Fig. 6c). Apparently, this effect is caused by not only structural factors but also phase transformations [32].

Figure 8 shows the temperature dependence of the coercive force for two films annealed at T_{ann} = 250 and 350°C in a constant magnetic field. Two segments can be distinguished on these curves: at low temperatures,

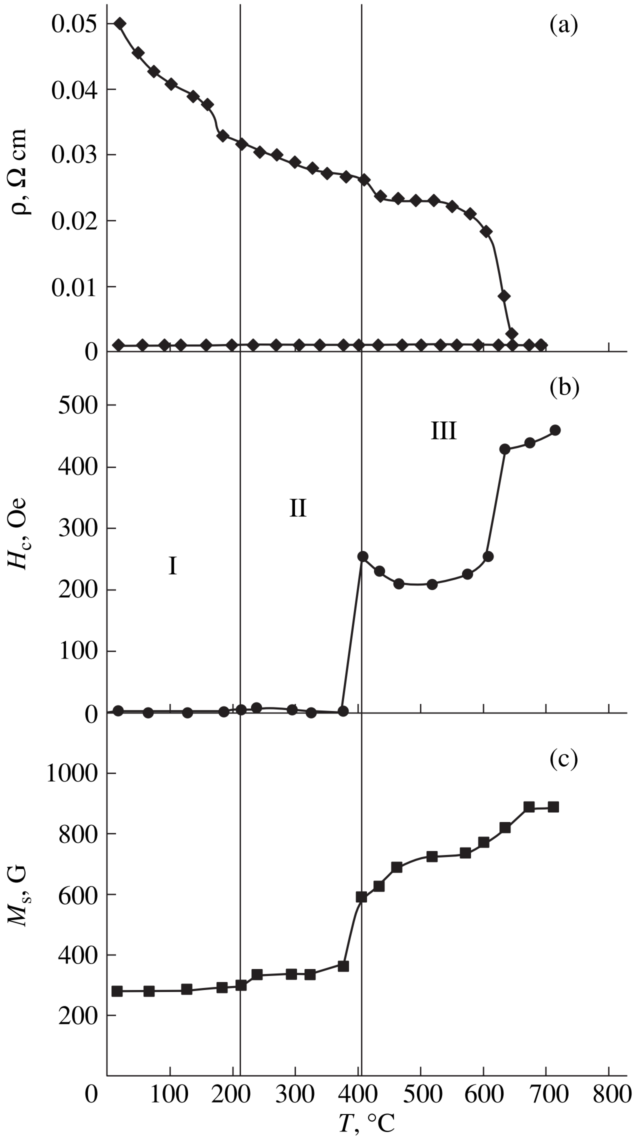

Fig. 6. Dependences of the (a) resistivity, (b) coercive force, and (c) saturation magnetization on the annealing temperature T_{ann} for Co–Sm–O films.

H_c exhibits a strong dependence, while at high temperatures, H_c is virtually unchanged. Performing $dM/dH = f(T)$ measurements, Zhao *et al.* [33] determined the blocking temperature. The transition between the first and second segments on the $H_c = f(T)$ dependence in Fig. 8 coincides with the T_B temperature. This result repeats the data given in Fig. 5. This finding allows the conclusion that the films annealed at T_{ann} = 250–350°C undergo the transition from the superparamagnetic state to the state of magnetic ordering of superparamagnetic particles (ISP region).

These results indicate that, indeed, an ensemble of interacting superparamagnetic particles can provide good magnetic properties at a high electrical resistivity.

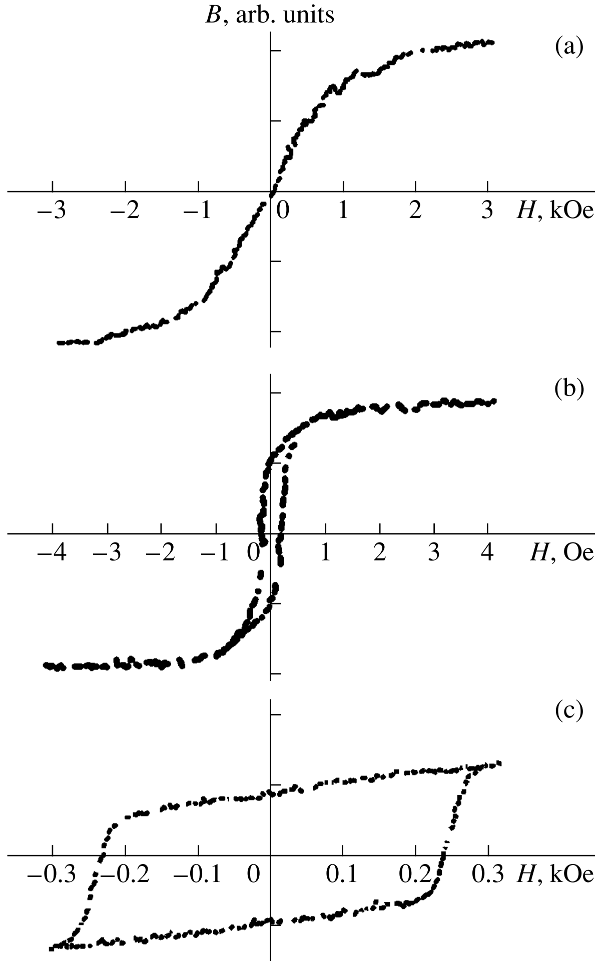

Fig. 7. Characteristic hysteresis loops for Co–Sm–O films (T = 300 K) (a) in the initial state and after annealing at T_{ann} = (b) 300 and (c) 480°C.

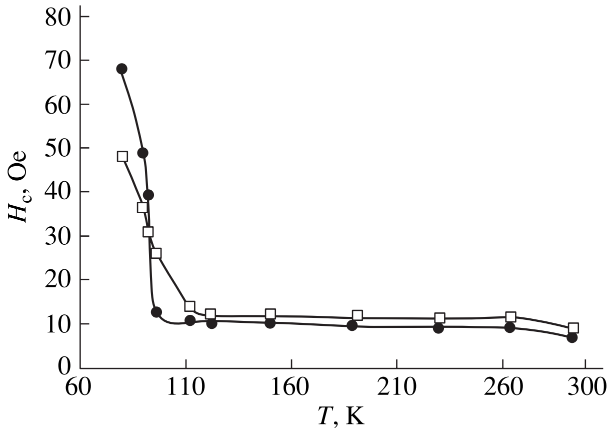

Fig. 8. Temperature dependence of the coercive force of Co–Sm–O films annealed at T_{ann} = 250 (●) and 350°C (□).

CONCLUSIONS

Analysis of the correlation between the microstructure and physical properties of nanocrystalline materials shows that 3*d*-metal granular films with a grain size <10 nm can provide a high resistivity, which offers the prospect of their application in microwave devices. The required soft magnetic properties in these materials can be ensured by the magnetic interaction between nanoparticles. The most interesting technological approach consists in the deposition of a film having a high content of a superparamagnetic phase at $T = 300$ K. Upon further annealing, the initial composite transforms into a specific state where magnetic ordering is realized but the particles remain superparamagnetic. The variation of the annealing temperature and the residual-gas pressure and the application of a constant magnetic field allow one to control the physical properties of such nanocrystalline films over a wide range.

REFERENCES

1. M. E. McHenry and D. E. Laughlin, Acta Mater. **48**, 223 (2000).
2. A. D. Pomogaĭlo, A. S. Rozenberg, and I. E. Uflyand, *Nanoparticles of Metals in Polymers* (Khimiya, Moscow, 2000).
3. A. I. Gusev and A. A. Rempel’, *Nanocrystalline Materials* (Fizmatlit, Moscow, 2001).
4. S. P. Gubin and Yu. A. Koksharov, Neorg. Mater. **38**, 1287 (2002).
5. J. H. Vincent and S. P. S. Sangha, GEC J. Res. **13**, 2 (1996).
6. M. H. Kryder, W. Messner, and L. K. Garley, J. Appl. Phys. **79**, 4485 (1996).
7. G. I. Frolov, Zh. Tekh. Fiz. **71** (12), 50 (2001) [Tech. Phys. **46**, 1537 (2001)].
8. G. Herzer, Scr. Metall. Mater. **33**, 1741 (1995).
9. S. Y. Yoshizawa, S. Oguma, and K. Yamauchi, J. Appl. Phys. **64**, 6044 (1988).
10. S. Y. Yoshizawa, K. Yamauchi, T. Yamane, and H. Sugihara, J. Appl. Phys. **64**, 6047 (1988).
11. G. I. Frolov and V. S. Zhigalov, Fiz. Met. Metalloved. **40**, 518 (1975).
12. V. S. Zhigalov, Yu. M. Fedorov, and G. I. Frolov, Fiz. Met. Metalloved. **44**, 1303 (1977).
13. M. Sh. Erukhimov, V. S. Zhigalov, and G. I. Frolov, Fiz. Met. Metalloved. **49**, 1210 (1980).
14. E. C. Stoner and E. P. Wohlfarth, Philos. Trans. R. Soc. London, Ser. A **240**, 559 (1948).
15. G. Herzer, IEEE Trans. Magn. **26**, 1397 (1990).
16. R. Alben, J. J. Becker, and M. C. Chi, J. Appl. Phys. **49**, 1653 (1978).
17. G. Reiss, J. Vancea, and H. Hoffmann, Phys. Rev. Lett. **56**, 2100 (1986).
18. J. Vancea and H. Hoffmann, Thin Solid Films **92**, 219 (1982).
19. J. P. Perez, V. Dupuis, J. Tuaillon, *et al.*, J. Magn. Magn. Mater. **145**, 709 (1995).
20. G. I. Frolov, V. S. Zhigalov, L. I. Kveglis, *et al.*, Fiz. Met. Metalloved. **88** (2), 85 (1999).
21. C. P. Bean and J. D. Livingston, J. Appl. Phys. **30** (4), 120s (1959).
22. E. F. Kneller and F. E. Luborsky, J. Appl. Phys. **34**, 656 (1963).
23. S. Gandopadhyay, G. C. Hadjipanayis, B. Dale, *et al.*, Phys. Rev. B **45**, 9778 (1992).
24. P. Allia, M. Coisson, M. Knobel, *et al.*, Phys. Rev. B **60**, 12207 (1999).
25. *Proceedings of NMP Conference, Spain 1998*; J. Magn. Magn. Mater. **203** (1999).
26. V. Dupuis, J. Tuaillon, B. Prevel, *et al.*, J. Magn. Magn. Mater. **165**, 42 (1997).
27. P. Allia, M. Coisson, P. Tiberto, *et al.*, Phys. Rev. B **64**, 144420 (2001).
28. S. Morup, Europhys. Lett. **28**, 671 (1994).
29. B. J. Jonsson, T. Turrki, V. Strom, *et al.*, J. Appl. Phys. **79**, 5063 (1996).
30. T.-S. Yoon, Y. Li, W.-S. Cho, and C.-O. Kim, J. Magn. Magn. Mater. **237**, 288 (2001).
31. H. Fujimori, S. Mitani, and T. Matsumoto, J. Appl. Phys. **79**, 5130 (1996).
32. G. I. Frolov, V. S. Zhigalov, S. M. Zharkov, *et al.*, Fiz. Tverd. Tela (St. Petersburg) **45**, 2198 (2003) [Phys. Solid State **45**, 2303 (2003)].
33. B. Zhao, J. Y. Chow, and X. Yan, J. Appl. Phys. **79**, 6022 (1996).

Translated by K. Shakhlevich

Technical Physics, Vol. 49, No. 7, 2004, pp. 916–919. Translated from Zhurnal Tekhnicheskoĭ Fiziki, Vol. 74, No. 7, 2004, pp. 110–113.

SURFACES, ELECTRON AND ION EMISSION

Potassium-Induced Activation of Field Emitters with Fullerene Coating

T. A. Tumareva, G. G. Sominskiĭ, and A. A. Veselov
St. Petersburg State Technical University, ul. Politekhnicheskaya 29, St. Petersburg, 195251 Russia
e-mail: tumareva@rphf.spbstu.ru; sominski@rphf.spbstu.ru

Received December 29, 2003

Abstract—The influence of potassium deposition on the emission characteristics of field tip emitters with fullerene coatings is studied. It is shown that a three- to fourfold reduction of the typical voltage U_1 required for the given emission current can be attained by rapid deposition of potassium layer with a thickness exceeding a monolayer. The deactivation of emitters at room temperature in the absence of electric field is observed and studied. Presumably, the deactivation is caused by potassium redistribution within the coating and/or the formation of bonds between potassium atoms and fullerene molecules. Deactivation of this type actually comes to an end in one or two days. The deposition of potassium on fullerene coating results in an appreciable (up to 50%) decrease in U_1 of the field emitters even after their long-term (about five days) deactivation. *© 2004 MAIK “Nauka/Interperiodica”.*

INTRODUCTION

Field emitters are attractive electron sources for vacuum electron devices. The advantages of these emitters include fast response, compactness, the absence of heating, and the possibility of attaining high current densities. Their disadvantages are also well known: one can readily obtain current densities of up to 10^3–10^4 A/cm^2 from a micrometer or submicrometer tip, but it is extremely difficult to obtain high current values even with the use of much larger emitting areas. The problem is that the field value of $\geq 10^7$ V/cm, which is necessary for autoemission, is practically unattainable near smooth surfaces. At moderate voltages, only the emission from field-enhancing surface irregularities occurs. However, it is extremely difficult to form a large number of small protrusions that are required for the emission to be uniform over the surface. Another problem is the short durability of field emitters because of the instability of protrusions to ion bombardment in the conditions of technical vacuum, as well as to the effect of high electric fields.

It is considered that coatings from carbon-containing materials are highly resistant to ion bombardment and to operation in the conditions of technical vacuum (see, e.g., [1]). Efforts are made to search for the carbon materials and to elaborate the technologies of the production of special coatings for field emitters on their basis. Several lines of the search can be identified. For example, attempts are being made to fabricate ordered structures from graphite, diamond films, and nanotubes. In recent years, we concentrated on the investigation of potential of fullerene coatings from C_{60} molecules [2–7]. These spherical molecules seem to be a convenient structural material for the formation of field-enhancing microstructures on the surface of tip field emitters. Previous experiments showed that individual microprotrusions produced on a tungsten emitter surface ensured fairly high current densities of up to approximately 10^7 A/cm^2 from an area with a diameter of 10–15 nm. Such “point” high-intensity sources are of considerable interest for analytical instrument-making applications. Along with this, we developed the technology of the formation of so-called “distributed fullerene structures,” which consist of a number (several tens) of nearly similar microprotrusions on the surface of the tip. Such distributed structures showed stable operation in the static regime up to a current of about 100 μA from a single tip with the characteristic top tip radius ranging from 0.3 to 0.5 μm. The corresponding limiting currents, which initiated the destruction of the tip, were $I_{\max} \sim 120$–150 μA. Hence, the results of studying fullerene coatings favored our choice of C_{60} molecules as material for the formation of microstructures with required parameters on the emitter surface. Also, the main mechanism of growth of the system of microprotrusions was established. This mechanism is related to the polarization and transport of large fullerene molecules in highly nonuniform electric fields in the surface region.

An obvious disadvantage of field emitters with carbon-containing coatings, including fullerene ones, is associated with the fact that the work function of these coatings is about 5 eV, which is even greater than that of tungsten. Because of this circumstance, the collection of large currents from such emitters requires the application of high potential differences between the emitter and the anode. The work function of carbon-containing coatings and of carbon emitters can be lowered using special activating additives. For example, the implantation of cesium ions into the bulk planar graphite samples and samples from carbon fiber resulted in the reduction of their work function [1] by a factor of 1.5–2. However, in this case, the emission current was unstable and rapidly decreased during the operation. According to [1], the situation can be improved by an optimal choice of the energy of cesium ions during the implantation.

A decrease in the work function of the fullerene coatings studied by us can be attained by a combined or subsequent deposition of fullerene and the molecules of the activating substance. Principally, the deposition procedure admits gaining a predetermined distribution of the activating additive over the coating thickness. We investigated the addition of potassium atoms for the feasibility of activating the fullerene coating. The first studies on the matter were described in [2]. Here, we continued the studies and report the latest results. We studied the coatings obtained by the deposition of fullerene molecules and potassium atoms on a tungsten tip and on a tungsten tip with a ribbed crystal (RC) [2–5] of tungsten carbide on its surface [8].

EXPERIMENTAL

The measurements were carried out in a multipurpose vacuum chamber with an autoemission microscope with up to 10^6 magnification. From patterns appearing on the screen under the exposure to the electron flux from cathode, we determined the distribution of the emission-current density and revealed flow inhomogeneities with characteristic sizes of ≥2 nm on the cathode surface. Due to continuous pumping, the pressure in the chamber was no higher than 10^{-9} Torr.

A cross-section view of the chamber is shown in Fig. 1. The scheme includes the tip cathode (tungsten emitter) mounted on a movable support, phosphor-covered screen, fullerene and potassium sources, and the screen viewing window. Characteristics of tip emitters with top tip radii 0.3 μm ≤ R_t ≤ 1 μm were measured. The emitter can be rotated on its mounting and face subsequently either of the sources and the screen. The possibility of moving the sources, first, facilitates their degassing far away from the cathode and, second, makes it possible to choose the optimal for deposition distance from a source to cathode (~1–2 cm).

The deposition rate of coating layers was varied in a wide range by changing the source temperature. The emitter can be heated to approximately 2800 K by passing a current through the tungsten mounting bow. A ribbed crystal was formed on the tungsten surface as a result of the decomposition at $T \geq 1000$ K of preliminary deposited fullerene coating.

In various experiments, the distance between the screen and the emitter ranged from 3 to 5 cm. With the power-supply systems available, negative voltages of up to 30 kV relative the grounded screen and the metal case of the chamber were applied to the emitter.

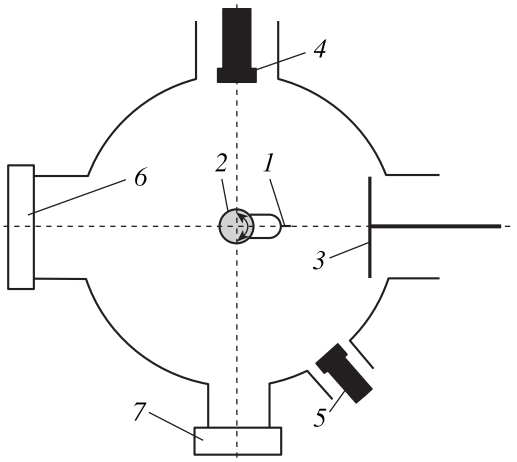

Fig. 1. Cross section of the experimental chamber: (*1*) tip emitter on a movable support (*2*), (*3*) screen, (*4*) potassium source, (*5*) fullerene source, (*6*) screen viewing window, and (*7*) additional window for viewing the microscope components.

We characterize the cathode emissivity by voltage U_I that is required for obtaining a given current *I*. In order to minimize the influence of strong fields on the coating structure, the values of U_I were measured at currents that were substantially lower than the limiting values for the cathode considered. Usually, we chose $I = 0.002$ μA in such measurements; i.e., the values $U_{0.002}$ were detected. For the sake of control over the potassium and fullerene deposition rates, as well as over the deposited layer thickness θ, we measured the "deposition parameters" (the dependences of U_I versus the deposition time t_d) [3, 5]. Typical curves $U_{0.002}(t_d)$ obtained during the deposition of potassium and fullerene on the tungsten tip *C*1 with a top tip radius $R_t \approx 0.3$ μm are shown in Figs. 2a and 2b. The time instants when monolayer thickness is attained are indicated.

Note that the coatings were deposited in the absence of electric field. In this case, the resulting coatings were almost homogeneous and remained without structural rearrangement after the measurements at $U_{0.002}$. The field-enhancing microstructures were formed on the fullerene surfaces with the use of the thermal and the field processing methods elaborated previously [2–7].

RESULTS AND DISCUSSION

The expected result of activation was obtained when a small amount of potassium was deposited on the field emitters. Figure 3 shows the typical deposition curves $U_{0.002}(t_d)$. The deposition of coating with a thickness from two to six monolayers resulted in a threefold or fourfold reduction of $U_{0.002}$. The activation degree

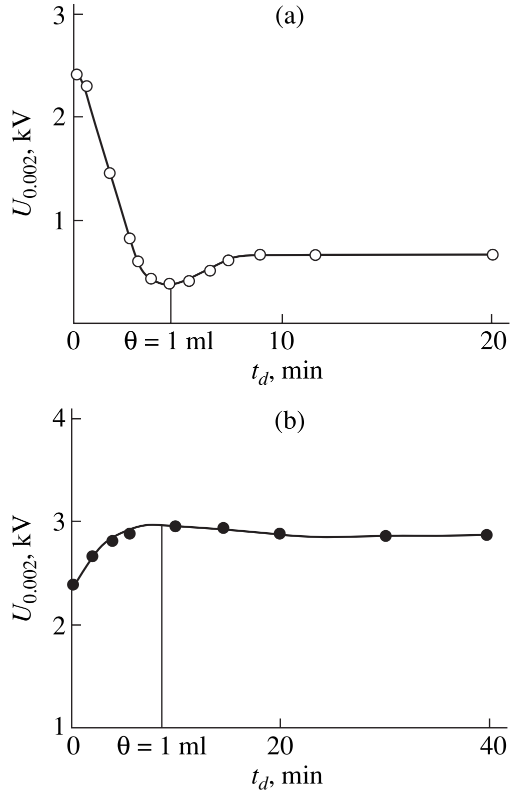

Fig. 2. The curves $U_{0.002}(t_d)$ of (a) potassium and (b) fullerene deposition on the tungsten tip *C*1 with top tip radius $R_t \approx 0.3$ μm.

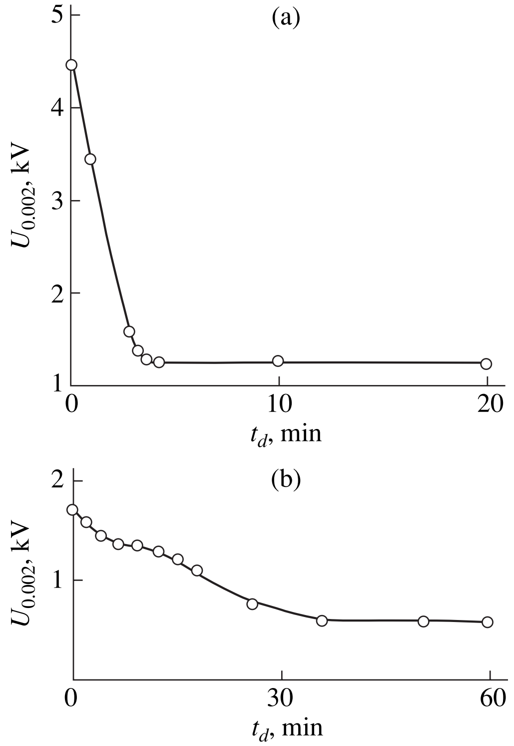

Fig. 3. The curve of potassium deposition on the surface of different emitting systems: (a) cathode *C*2 with top tip radius $R_t \approx 0.7$ μm and the initial coating W–K–C_{60} and (b) cathode *C*1 with top tip radius $R_t \approx 0.3$ μm and the distributed fullerene structure of microprotrusions on the surface of the initial W–RC–C_{60} coating.

depended on the composition and structure of the preliminary coating. This is clearly seen from the comparison of the dependences $U_{0.002}(t_d)$ plotted in Figs. 3a and 3b. The curve in Fig. 3a was obtained in the case when potassium was deposited on the tungsten tip *C*2 after the preliminary deposition of five monolayers of potassium and subsequent deposition of ten-monolayer-thick fullerene coating. For such coatings, which were not subjected to the field treatment, the voltage $U_{0.002}$ measured before the subsequent deposition of potassium exceeded 4 kV. Minimal values of $U_{0.002}$ were attained when potassium was deposited on an optimized distributed fullerene structure, which appeared on the emitter with a ribbed crystal formed on its top (Fig. 3b). In our opinion, the predictability of the results in the case of rapid deposition of comparably thin potassium layers can be attributed to the fact that, in this case, the surface profile and, consequently, an electric field enhancement are controlled by the initial structure of fullerene coating. It seems that the deposition of thin potassium layer affects this structure only slightly and results in the lowering of the surface work function.

The results of measurements indicate that the properties of a potassium-activated surface appreciably change in time when it is held at room temperature in the absence of electric field. The time dependence of $U_{0.002}$ is sensitive to both the surface characteristics of the initial coating and the amount of potassium deposited. Figure 4 shows the typical dependences of $U_{0.002}$ on the exposition time *t* for the cathode *C*2 with two coatings that differ greatly in characteristics. Curve *1* (Fig. 4) was measured after ten monolayers of potassium were deposited on the preliminarily formed multilayer coating W–K–C_{60} with ten monolayers of fullerene molecules on the surface. Curve *2* was obtained after 30 monolayers of potassium were sputtered on the fullerene coating with a thickness of four monolayers deposited on top of the ribbed crystal.

For the cathodes studied, time dependences $U_{0.002}(t)$ turned out to be similar. A characteristic increase in voltage $U_{0.002}$ corresponding to the rapid initial deactivation of emitter during the first hours is observed. Then, after the exposition for one to two days, the dependences $U_{0.002}(t)$ level off and the further deactivation nearly cease. The initial rapid increase in $U_{0.002}(t)$ might be associated with the gas adsorption at the emitter surface. However, the subsequent emitter heating to 350–450 K, which should lead to the gas desorption, resulted in only an insignificant (by 10–15%) lowering of $U_{0.002}$. Apparently, the considered increase in $U_{0.002}$

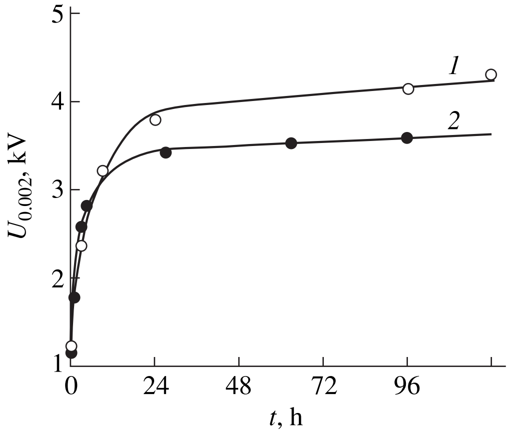

Fig. 4. Evolution of the characteristic voltage $U_{0.002}$ for cathode $C2$ with top tip radius $R_t \approx 0.7$ μm and with (*1*) W–K–C_{60}–K and (*2*) W–RC–C_{60}–K coatings.

has a different origin. In our opinion, the cathode deactivation is related to a greater extent to the redistribution of potassium in the tip coating, for example, to the potassium migration from the field-enhancing microstructures into the valleys between them. Along with this redistribution over the surface, potassium can also migrate into the bulk of the fullerene layer or form bonds with fullerene molecules (for example, of exohedral type).

So far, the complete understanding of mechanisms behind the evolution of the emitting characteristics of cathodes with multilayer coatings is still a challenge and requires further investigation. However, even the available data bear evidence of the activation effect resulting from the introduction of potassium into the fullerene coatings. An important practical point is that the voltages established after a long-term exposition are lower than those typical of the emitters before the potassium deposition. For some types of emitters, this lowering amounted to at least 50%.

CONCLUSIONS

The most important results of this study are listed below. Up to a threefold or fourfold reduction of characteristic voltages U_I required for the given currents is obtained after the rapid deposition of potassium atoms in an amount exceeding a monolayer.

The phenomenon of the emitter deactivation at room temperature in the absence of electric field is observed and studied. Possible causes of the deactivation are the potassium redistribution within the coating and/or formation of bonds between potassium atoms and fullerene molecules.

It is also established that the potassium deposition on fullerene coating allows a noticeable (to 50%) reduction of U_I in the field emitters considered, even after their long-term (five days) deactivation.

ACKNOWLEDGMENTS

This study was supported by the Russian Foundation for Basic Research, project no. 02-02-16211.

REFERENCES

1. A. F. Bobkov, E. V. Davydov, S. V. Zaĭtsev, *et al.*, Zh. Tekh. Fiz. **71** (6), 95 (2001) [Tech. Phys. **46**, 736 (2001)].
2. G. G. Sominski, T. A. Tumareva, A. S. Polyakov, and K. K. Zabello, in *Proceedings of the International Conference on Microwave Electronics and Radiophysics, St. Petersburg, 1999*, pp. 327–330.
3. T. A. Tumareva and G. G. Sominski, J. Commun. Technol. Electron. **45** (Suppl. 1), 110 (2000).
4. T. A. Tumareva, G. G. Sominski, and A. S. Polyakov, in *Proceedings of the 9th Triennial ITG-Conference on Displays and Vacuum Electronics, Garmisch-Partenkirchen, 2001* (Verlag, Berlin, 2001), No. 165, pp. 269–274.
5. T. A. Tumareva, G. G. Sominskiĭ, A. A. Efremov, and A. S. Polyakov, Zh. Tekh. Fiz. **72** (2), 105 (2002) [Tech. Phys. **47**, 244 (2002)].
6. T. A. Tumareva, G. G. Sominskiĭ, and A. S. Polyakov, Zh. Tekh. Fiz. **72** (2), 111 (2002) [Tech. Phys. **47**, 250 (2002)].
7. G. G. Sominskiĭ, T. A. Tumareva, A. A. Veselov, and A. A. Efremov, in *Proceedings of the 12th Winter School on Microwave Electronics and Radiophysics, Saratov, 2003* (Gos. UNTs “Kolledzh,” Saratov, 2003), pp. 31–32.
8. M. V. Loginov and V. N. Shrednik, Pis’ma Zh. Tekh. Fiz. **24** (11), 45 (1998) [Tech. Phys. Lett. **24**, 432 (1998)].

Translated by A. Sidorova

Technical Physics, Vol. 49, No. 7, 2004, pp. 920–926. Translated from Zhurnal Tekhnicheskoĭ Fiziki, Vol. 74, No. 7, 2004, pp. 114–120.
Original Russian Text Copyright © 2004 by Sapozhnikov, V. Mitiakov, A. Mitiakov.

EXPERIMENTAL INSTRUMENTS AND TECHNIQUES

Measurements of Nonstationary Heat Fluxes by Gradient Sensors Based on Single-Crystalline Anisotropic Bismuth

S. Z. Sapozhnikov, V. Y. Mitiakov, and A. V. Mitiakov
St. Petersburg State Technical University, ul. Politekhnicheskaya 29, St. Petersburg, 195251 Russia
e-mail: tot@pef.spbstu.ru

Received November 28, 2003

Abstract—Gradient heat flux sensors produced on the basis of anisotropic single crystals of 99.99% pure bismuth are described. Their response time is estimated at 0.05 ms. A method of control over the nonstationarity of temperature, which is measured by means of the sensors, is proposed. *© 2004 MAIK “Nauka/Interperiodica”.*

INTRODUCTION

The majority of thermal processes are characterized by time-dependent temperatures and heat fluxes with a typical variation frequency ranging from a few hertz to several kilohertz. Even in common “stationary” heat transfer problems, the thickness of the boundary layer is subjected to fluctuations, which is manifested in the oscillations of temperature and heat flux at the surface.

As a rule, the most important information on the physics of a process is associated with the nonstationary component; therefore, the measurements (with minimal distortion) of the heat flux pulsations present an interesting and significant problem. The main obstacle that hinders its solution is a limited nomenclature and the insufficient operation speed of the presently available heat flux sensors.

The classification of sensors proposed by Gerashchenko [1] includes, as a separate group, so-called “supplementary wall sensors.” Such devices have the form of a plate placed on the surface of an object or introduced into a heat-conducting medium so that the vector of the heat flux is normal to the working planes of the sensor.

In essence, the majority of these sensors are a multijunction thermocouple (Fig. 1a); the thermal e.m.f. and heat flux vectors appear to be collinear. In terms of the Mitiakov representation [2], these sensors can be classified as the longitudinal type. It is the longitudinal sensors, the best of which were elaborated in the 1960s–1970s at the Institute of Applied Thermal Physics, Academy of Sciences of the Ukr. SSR (at present, IATP NAS), which are the most often studied in Russia. The majority of their foreign analogues realize the same principle idea and have no noticeable advantages.

To improve the sensitivity of longitudinal-type sensors, one has to increase their thickness (up to 1–2 mm), which leads to two principally unavoidable drawbacks: the first is the thermal resistance of an order of 10^{-3} m^{2}K/W, which considerably distorts the temperature field in the region of measurement and, as a consequence, introduces a systematic error whose value is difficult to determine; and the second is that the high sensitivity is attained at the cost of the operation speed, so that the response times can reach 10–100 s and longer.

At St. Petersburg State Technical University, in 1996–2003, we developed a fundamentally new approach. The sensors, which were called gradient sensors, also are “supplementary-wall” devices, but the principle of their operation is quite different and they outperform longitudinal sensors in many respects.

Gradient heat flux sensors (GHFSs) are based on the transverse Seebeck effect, which consists in the appearance of thermal e.m.f. in the direction perpendicular to the vector of the heat flux; therefore, GHFSs should be considered as transverse-type sensors (Fig. 1b).

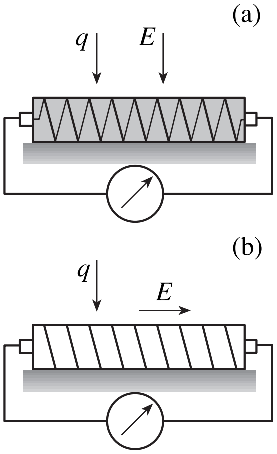

Fig. 1. Heat flux sensors of (a) longitudinal and (b) transverse types.

THEORY AND CONSTRUCTION OF GHFS

As was mentioned above, the operation principle of GHFSs involves the transverse Seebeck effect (i.e., the appearance of thermal e.m.f. with the strength vector normal to the vector of the heat flux) in media where both the thermal and electrical conductivities, as well as the thermoelectric coefficient, are anisotropic. The elementary theory of GHFSs is generalized in [3–5].

For the transverse thermal e.m.f. to appear, the heat flux vector should be off the principal axes of a crystal that is anisotropic in thermal conductivity and thermoelectric coefficients. Bismuth is an example of such a material.

Figure 2 shows a rectangular parallelepiped cut from a bismuth single crystal. The parallelepiped represents an anisotropic thermoelement, and the hatched plane is called a trigonal plane.

Because of the thermal conductivity anisotropy of the thermoelement, the heat flux vector deviates from the Z axis in any section with the exception of the *1–2–3–4* plane. This means that the difference in temperatures appears not only along the Z axis but also along the X axis and the heat flux vector in each section rotates by a certain angle with respect to the initial direction.

An external heat flux through the thermoelement gives rise to a transverse electric field with the strength

$$e_X = (\varepsilon_{33}-\varepsilon_{11})\sin\theta\cos\theta\, l\frac{\partial T}{\partial z},$$

which is proportional to the projection of the gradient or, in accordance with the Fourier law, to the heat flux density

$$e_X = \frac{(\varepsilon_{33}-\varepsilon_{11})\sin\theta\cos\theta}{\sqrt{\lambda_{33}^2\sin^2\theta+\lambda_{11}^2\cos^2\theta}}Fq_Z. \tag{1}$$

Here, ε_{11} and ε_{33} are the components of the differential thermal e.m.f. tensor, λ_{11} and λ_{33} are the components of the thermal conductivity tensor, $F = lb$ is the in-plane area of the element, and q_Z is the mean density of the external heat flux. Thus, the thermal e.m.f. e_X is a linear function of both the heat flux density q_Z and the element area F and is defined by the choice of angle θ (for bismuth, the optimal value is $\theta_{\text{opt}} = 53.4°$).

The main characteristic of such a thermoelement is its volt–watt sensitivity (V/W)

$$S_0 = \frac{e_X}{q_Z F}. \tag{2}$$

A single bismuth plate has a thickness of 0.1–0.2 mm; its in-plane area F and signal e_X appear to be small. Because of this circumstance, thermoelements are connected in series (similar to thermocouples in longitudinal sensors). The resulting stack presents the principle construction of the GHFS.

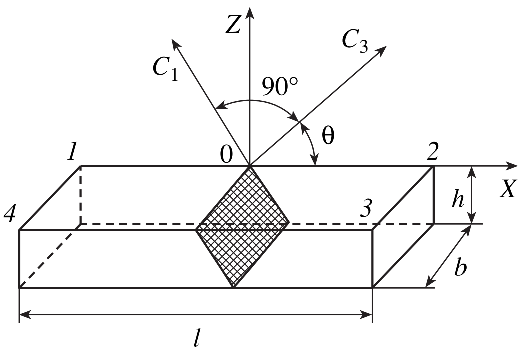

Fig. 2. Anisotropic thermoelement of size $l \times b \times h$; C_1 and C_3 are the principal crystallographic axes; θ is the angle at which the element is cut out of a single crystal.

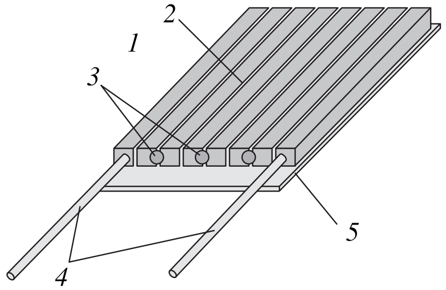

Fig. 3. Schematic of a GHFS: *1*, a plate of anisotropic bismuth; *2*, spacers; *3*, junctions; *4*, current leads; *5*, substrate.

Figure 3 shows the schematic of a GHFS assembled from bismuth plates *1*. Spatial orientation of the trigonal planes in two adjacent elements is chosen so that the finite thermal e.m.f.s of these elements are added.

The sensors are mounted on mica substrates *5*. Plates *1* are insulated from each other by thin (5 μm) Dacron spacers (*2*) and stuck to the mica substrate *5* by BF-2 glue. Junctions *3* are made with the use of pure bismuth and connect plates *1* to form a series circuit. The extreme plates are supplied with current leads *4*.

The resulting thermal e.m.f. from thus so constructed GHFS is

$$E = q_Z E S_0 n, \tag{3}$$

where n is the number of elements (plates *1*) composing the sensor.

With a thickness reduced to 0.1–0.2 mm, which is one or two orders of magnitude smaller than that of longitudinal sensors, the GHFS has a thermal resistance of 10^{-5} m^{2}K/W at an effective thermal conductivity close to 7.45 W/(m K).

In our experiments, GHFSs were fabricated on the basis of 99.99% pure bismuth single crystals, for which S_0 = 5–20 mV/W; the operation temperature ranges between 20 and 540 K (the upper limit is close to the

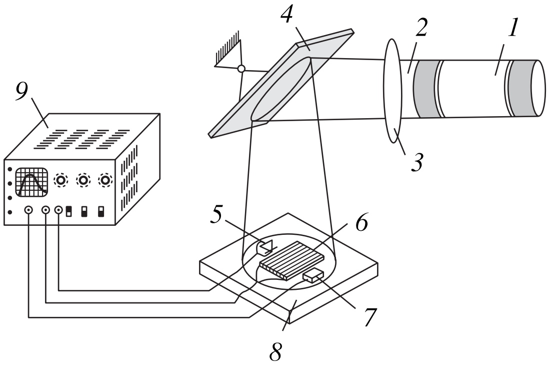

Fig. 4. Test bench for dynamical studies of GHFSs: *1*, laser; *2*, beam; *3*, optical system; *4*, mirror; *5*, photodiode; *6*, GHFS; *7*, laser radiation detector; *8*, massive aluminum substrate; and *9*, oscilloscope.

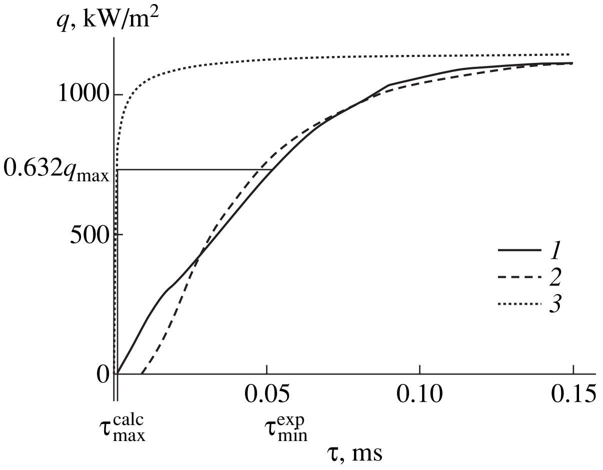

Fig. 5. Dynamical characteristics of bismuth GHFSs: (*1*) calculation by an improved model of a compound body with a defect layer, (*2*) experiment, and (*3*) calculation by the homogeneous body model.

bismuth melting point). The technique developed in [3] enables one to graduate GHFSs with reference to the Joule–Lenz heat flux with an accuracy of no worse than 1%; dependence (1) appears to be linear within 5% over the entire temperature range under pressures of up to 30 MPa. The level of thermal noise in bismuth GHFSs is comparable to that in sensors produced from other pure metals. The resistance of conventional battery-type GHFSs falls within 0.1–10 Ω, which makes it possible to detect a signal by means of devices that are typically supplied in a set with standard thermal converters.

THE DYNAMICAL CHARACTERISTICS OF GHFS

Equation (1) is obtained under the assumption that the thermal conductivity problem is stationary and the heat flux density q_Z is time-independent. However, considering nonstationary processes, one has to deal with the dynamic characteristics of the sensor, first of all, with its response time $\tau_{\min}$.

The experiments were carried out on a specially designed test bench (Fig. 4) based on a pulsed Q-switched Delta-201 laser operating at a wavelength of 1.06 μm with a pulse duration of 0.15 ms, an output power of 1250 KW/m^2, and an interval between pulses of 60 ms.

Laser *1* generates beam *2* with an initial diameter of 0.1 mm; passing through optical system *3* and mirror *4*, the beam broadens to a diameter of 15 mm. Then, beam *2* strikes photodiode *5*, GHFS *6*, and laser radiation detector *7*, which are mounted on substrate *8* by means of a heat-conducting paste and connected to storage oscilloscope *9*. Fast-response (about 1 μs) photodetector *5* was used for synchronizing the oscilloscope circuit with the laser pulse. For the independent measurement of radiation power, fast-response (1 μs) film photodetector *7* was placed near GHFS *6*.

In the first experiments, we used a GHFS with a size of 4 × 7 × 0.2 mm and a sensitivity of 9.3 mV/W. The sensor surface was coated with a special composition to a degree of blackness of 0.98. As a result, we obtained the time dependence of the GHFS signal under the irradiation by a pulsed heat flux of a constant density. Then, we considered the GHFS dynamics with a thicknesses of 0.5, 1.0, 1.5, 2.0, 2.5, and 4.0 mm; the same in-plane size (4 × 7 mm); and the same blackness degree. The results turned out to be nearly the same for all the sensors. Thus, we have obtained the first evidence of the principal difference between transverse- and the longitudinal-type sensors.

The response time of longitudinal sensors is determined by their effective thermal diffusivity *a* and thickness *h*,

$$\tau_{\min} = \frac{4}{\pi^2}\frac{h^2}{a},$$

which has a simple physical explanation: the material structure is "almost homogeneous," and the signal formation is based on the difference in the temperatures at the opposite sides of the sensor.

We assumed that a GHFS signal is determined by a thin near-surface layer of anisotropic material separated from the surface by only a 30-μm-thick region of technological etching.

Figure 5 shows the experimental (*2*) and calculated (*3*) dynamical characteristics of GHFSs obtained in [6]; the calculation implies that the GHFS is "ideal," i.e., free from the etched layer. In principle, an ideal sensor can be fabricated growing separate single-crystalline elements from melt; the response time of a such sensor presents the ultimately attainable value for anisotropic bismuth.

The calculation was carried out under the assumption that the heat flux with density $q_{\max}$ acts on the surface of semi-infinite mass. In this case, the linear theory of heat conduction gives the heat flux at depth δ_0 in the form $q(\delta_0, \tau) = q_{\max}\mathrm{erfc}0.5(a\tau/\delta_0^2)^{-0.5}$. The response time can be determined from the relation $[q_{\max} - q(\tau)]/q_{\max} = 1/\exp(1) \approx 0.368$.

Let us find the point with ordinate $(1 - 0.368)q_{\max}$ on the experimental curve *2*; the abscissa of this point defines the response time $\tau_{\min} = 0.05$ ms. The same procedure in the case of an ideal GHFS yields the limiting value $\tau_{\min}^{\mathrm{calc}} = 0.01$ ms.

The above discussion leads one to the following conclusions: (1) the sensitivity of a GHFS is divorced from its thickness (and response time); (2) in turn, the thickness is defined by only the production technology and practically lies within 0.1–0.4 mm; (3) the response time is independent of the sensor thickness and is governed by only the physical properties and the thickness of the surface (“working”) layer; and (4) the thermal resistance (and the induced distortion in the temperature field) is usually lower than that in the sensors of the longitudinal type.

THERMOMETRY OF TRANSIENT PROCESSES

Our group is concerned with the thermometry on the basis of GHFSs since 1996. The results obtained for free-convective heat transfer on a vertical plate [7], stimulated convective heat transfer in a flow past a smooth cylinder, a cylinder with turbulence stimulators [8], and a spherical hole [9], as well as for complex heat transfer in the combustion chamber of a Diesel engine [10], allowed us both to verify the workability of the method in classical cases and to gain a number of priority results.

Figure 6 shows the results of GHFS measurement of the heat flow pulsations q'_φ on the cylinder surface streamed by a transverse air flow with the heat flux density $q = q_\varphi + q'_\varphi$. The cylinder is heated by saturated water vapor, its surface temperature being close to 100°C; the air temperature is about 20°C; and the angle φ between the flow velocity vector and the radius vector to GHFS is 150°.

Of considerable interest are the measurements of heat flux in such highly nonstationary systems as waves in shock tube wind tunnels [11].

The experiments with shock tube wind tunnels were carried out at the Ioffe Physicotechnical Institute (PTI), of Russian Academy of Sciences, and at St. Petersburg State Technical University (SPSTU); both groups used GHFSs with a size of 4 × 7 × 0.2 mm and with a volt–watt sensitivity ranging from 9.4 to 9.8 mV/W.

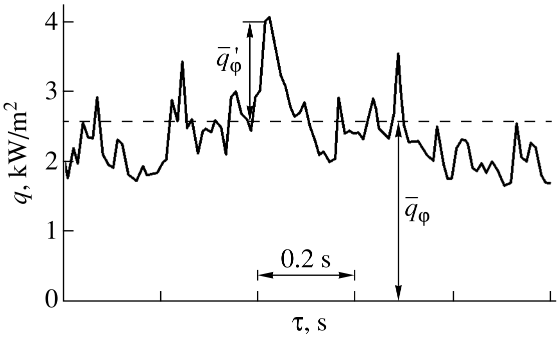

Fig. 6. Heat flux pulsation on the surface of a transversely streamlined cylinder ($\varphi = 150°$, Reynolds number Re = 5×10^4).

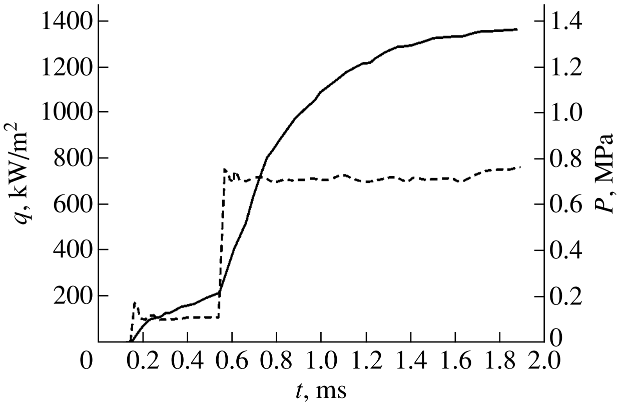

Fig. 7. Time variation of (solid curve) the heat flux and (dashed curve) pressure in xenon detected at the lateral wall of the shock tube wind tunnel at 100 mm from its end.

In the experiment performed at the PTI, xenon was heated by a shock wave with the Mach number $M = 6$. In the tube, the sensor was flush-mounted with the internal wall of the cylindrical channel at cross sections spaced 100 and 425 mm from the closed end of the tube. A piezoelectric pressure sensor with the sensitive element 4 mm in diameter was positioned in the same sections.

The results of the measurements in the cross section at 100 mm from the tube end are shown in Fig. 7. A steep rise of the sensor signal (dashed curve) is seen at the instants when the incident ($\tau = 0.15$ ms) and reflected ($\tau = 0.55$ ms) shock waves cross the section of measurement. Changes in the heat flux (solid curve) display close correlation in time with the signal of the pressure sensor. The heat flux density in the region behind the reflected shock wave (gas temperature $T \sim 7000$ K) attains 1.4 MW/m^2. Both sensors were preliminarily calibrated: the heat flux was accurate to ~2%; the pressure, no worse than 10%.

At SPSTU, the experiment took place in a shock tube wind tunnel with air ($M = 1.9$) according to the same scheme. GHFSs were positioned at the internal

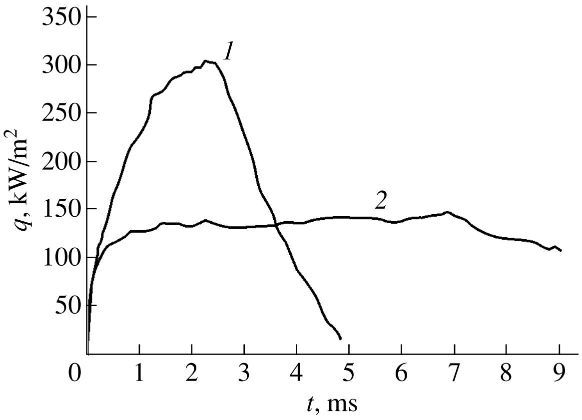

Fig. 8. Time variation of the heat flux behind the shock wave in air detected (*1*) on the lateral wall 3 m from the tube end and (*2*) on the end surface.

cylindrical wall at a distance of 3 m from the closed end and at the center of the end plug. Similar to the experiments described above, the pulse start coincides with the arrival of a shock wave at the sensors. The sensor at the lateral wall (curve *1* in Fig. 8) detects the initial increase in the heat flux induced by the incident wave with a temperature of 460 K behind its front and the following drop as soon as the cold gas from behind the contact surface reaches the cross section of measurement.

At the instant of incidence (and reflection) of the shock wave, the sensor at the end surface (curve *2*) is immediately brought into the region of stationary gas at a temperature of 900 K. In approximately 1.5 ms after the shock wave reflection, the heat flux stabilizes and remains nearly constant for up to 7 ms, when the contact surface arrives at the end surface of the tube. Attention is drawn to the more than twofold excess of the maximal heat flux to the cylindrical wall (solid curve) over that to the end (dashed curve) of the channel. This fact bears evidence of different mechanisms underlying the heat transfer at the lateral and end surfaces. Indeed, the heat transfer at the end surface occurs similar to that between two semi-infinite rods, while the heat transfer at the cylindrical wall is predominantly convective. This conclusion is confirmed by the results of measurements of the heat flux behind the reflected shock wave in the above experiments at the PTI (Fig. 7). In that study, the sensor was in the boundary layer, which was produced by the cocurrent flow behind the incident shock wave, and the reflected shock wave interacted with this layer on its way towards the cocurrent flow. Therefore, in contrast to the situation at the end of the tube, gas near the wall was not in the state of rest, thus making possible the convective heat transfer in this region.

THERMOMETRIC POTENTIAL OF GHFS

In view of the nearly linear temperature dependence of the ohmic resistance, GHFSs can be classified as resistance thermometers and used in the bridge or other standard thermometry circuits, when the thermometer as a whole is immersed in the medium being studied to avoid the effect of the transverse thermal e.m.f. In this case, the inertia of a GHFS (shaped as a plate with the thickness h) is defined by the Fourier number Fo = $a\tau/h^2$. This type of thermometry is referred to as "active," since one has to pass current from an external supply through the thermometer.

However, the ability of a GHFS to form a signal under the action of a heat flux suggests another, "passive," thermometric scheme: since the sensor itself produces a thermal e.m.f., one needs only to measure the current and the voltage drop in the circuit and to calculate the resistance by Ohm's law

$$I = \frac{E}{R_{\text{sh}} + R_0(1+\chi T)}, \tag{4}$$

where I is the current, R is the load resistance (shunt), R_0 is the resistance of the GHFS at the initial temperature (for example, at 0°C), and χ is the temperature coefficient of resistance for the GHFS material (to be determined by the calibration in the thermostat).

Thus, it will suffice only to mount the GHFS in a required position, to run wires to the place of detection, and to determine the thermal flux and the temperature by formulas (3) and (4), respectively.

Finally, we can realize a circuit for nonstationary temperature measurements. In terms of nonstationary thermometry, the true temperature in a medium is defined by

$$T_f = T_f(\tau) = T(\tau) + \tau^*_{\min}\frac{dT}{d\tau}, \tag{5}$$

where $T(\tau)$ is the reading of the inertial thermometer with the response time $\tau^*_{\min}$.

Let two GHFSs, D_1 and D_2, with thickness h each, be mounted on a massive substrate as shown in Fig. 9. We calculate temperature T from formula (4). The constant $\tau^*_{\min}$ can be determined either from experiment or again with the use of the heat conduction theory; all that remains is to calculate the derivative $dT/d\tau$. Let us use the explicit finite-difference Schmidt scheme, which suggests

$$\frac{dT}{d\tau} \approx \frac{a}{\Delta x}\left[\left(\frac{\Delta T}{\Delta x}\right)_+ - \left(\frac{\Delta T}{\Delta x}\right)_-\right], \tag{6}$$

where Δx is the thickness of the nth layer (in our case, $\Delta x = h$) and $(\Delta T/\Delta x)_+$ and $(\Delta T/\Delta x)_-$ are the finite-difference analogues of the derivatives dt/dx to the right and to the left from the middle plane of the layer, respectively (Fig. 10).

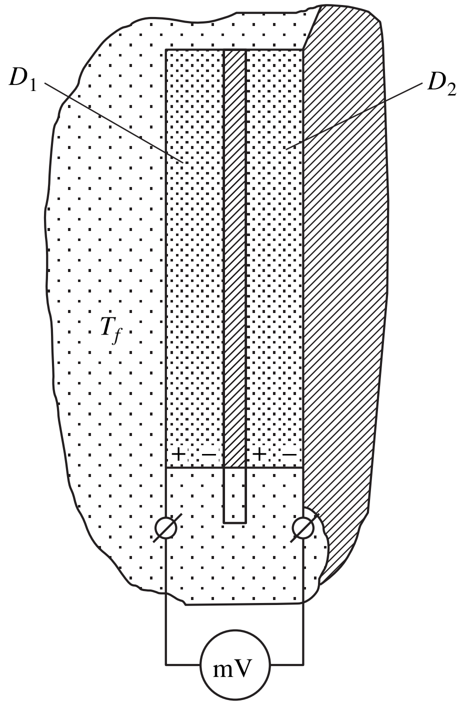

Fig. 9. The scheme of nonstationary thermometry.

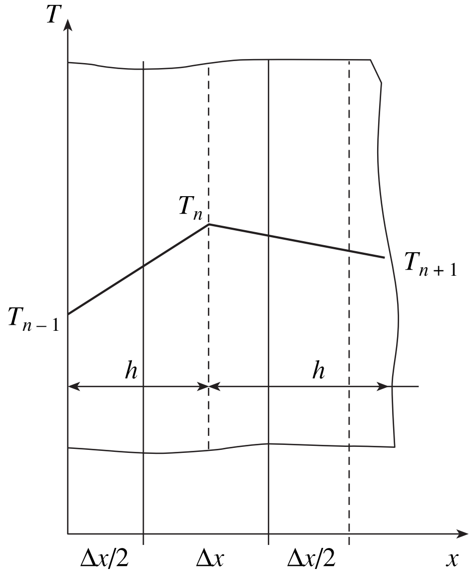

Fig. 10. Finite-difference Schmidt scheme.

Assume a linear relation of the values $(\Delta T/\Delta x)_+$ and $(\Delta T/\Delta x)_-$ to the signals E_1 and E_2 of sensors D_1 and D_2, respectively. In this case,

$$\frac{dT}{d\tau} \approx a\frac{E_2 - E_1}{hS_0F\lambda} = \frac{E_2 - E_1}{\rho cFhS_0}, \tag{7}$$

where λ, ρ, and c are the thermal conductivity, density, and the mass specific heat of the "material" of the GHFS, respectively. Finally, we calculate temperature $T_f(\tau)$ using expressions (4) and (7) in the form

$$T_f(\tau) = \frac{1}{R_0\chi}\left[\frac{E}{I} - (R_{\text{sh}} + R_0)\right] + \tau^*_{\min}\frac{E_2 - E_1}{\rho cFhS_0}.$$

Thus, GHFSs provide the possibility of control over both the heat flux and the time-dependent temperature of the material.

GHFS IN COMPARISON TO WORLD ANALOGUES

In the related literature, the data on technical characteristics of present-day heat flux sensors are scarce and, what is more, the reliability of the available data is not irreproachable. The data that we managed to derive from Internet sites are conveniently presented in Fig. 11. The characteristics of our bismuth GHFS are also shown.

It is seen that GHFSs are two or more orders of magnitude ahead of longitudinal-type sensors in response time and are second only to Vatell sensors in heat resis-

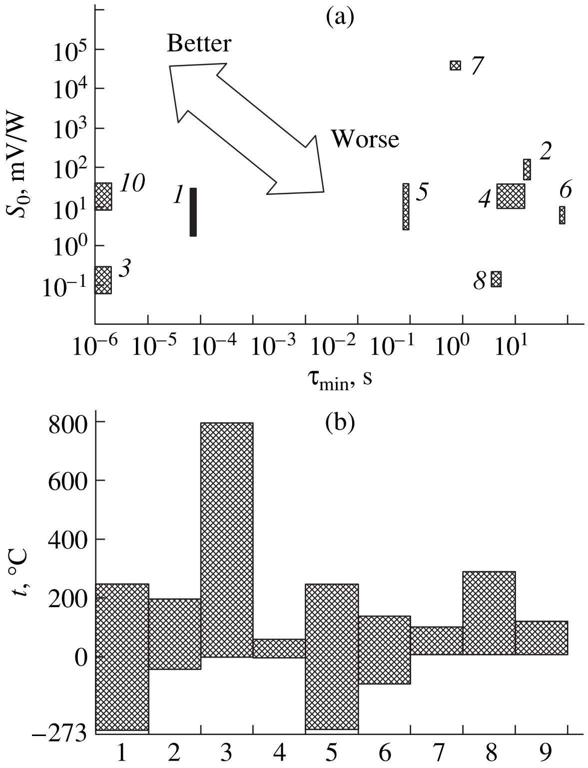

Fig. 11. (a) The sensitivity, the response time, and (b) the operation temperature range of the present-day heat flux sensors: (*1*) GHFS, sensor produced at (*2*) ITTP NAS (Ukraine), (*3*) Vatell (United States), (*4*) Wuntronic (Germany), (*5*) Captec (France), (*6*) Hukseflux (Holland), (*7*) Physical Electronics Laboratory (Switzerland), (*8*) Newport (United States), (*9*) TNO (Holland), and (*10*) FORTECH HTS (Germany).

tance. Note also that the GHFS in-plane size can be 1 × 1 mm or larger, the upper limit being placed only by the laboriousness of fabrication.

CONCLUSIONS

We proposed, developed, and elaborated to the stable technological and satisfactory technical level gradient heat flux sensors, which are measuring tools free from the principal disadvantages of longitudinal-type sensors. The experimentally determined GHFS response time was 50 μs, regardless of the device thickness, and permitted a further reduction to 10 μs. This ensures the detection of heat flux pulsations at frequencies of up to 20 kHz.

GHFSs were used in various heat exchange problems, including substantially nonstationary ones (e.g., the processes in shock tube wind tunnels). The reliability of measurements is confirmed in the standard models, and a number of priority results are obtained.

Apart from heat flux measurements, GHFSs hold promise for thermometry. The application of GHFSs allows one to avoid the use of external power supplies and provides for a correct measurement of substantially nonstationary temperatures.

In most operation parameters, GHFSs display higher performance than their present-day analogues and open new prospects in the experimental technique.

REFERENCES

1. O. A. Gerashchenko, *Fundamentals of Thermometry* (Naukova Dumka, Kiev, 1971).
2. A. V. Mitiakov, Candidate’s Dissertation (St. Petersburg. Gos. Tekh. Univ., St. Petersburg, 2000).
3. N. P. Divin, RF Inventor’s Certificate No 9959 (1998), Byull. Izobret., No. 5 (1999).
4. N. Divin and S. Sapozhnikov, in *Proceedings of the International Symposium on Power Machinery, Moscow, 1995*, pp. 79–81.
5. N. Divin, A. Kirillov, and S. Sapozhnikov, in *Proceedings of the 28th Scientific-Engineering Meeting “Messtechnik zur Untersuchung von Vorgangen in Thermischen Energieanlagen” and 6th Meeting “Messtechnik fur Energieanlagen,” Dresden, 1996*, pp. 26–28.
6. S. Z. Sapozhnikov, V. Y. Mitiakov, and A. V. Mitiakov, in *Proceedings of the 3d European Thermal Science Conference, Heidelberg, 2000*, pp. 688–690.
7. A. V. Mitiakov, S. Z. Sapozhnikov, Yu. S. Chumakov, *et al.*, Teplofiz. Vys. Temp. **40**, 669 (2002).
8. V. Y. Mitiakov, S. Z. Sapozhnikov, Y. S. Chumakov, *et al.*, in *Proceedings of the 5th World Conference on Experimental Heat Transfer, Fluid Mechanics and Thermodynamic (EXHFT-5), Thessaloniki, 2001*, pp. 111–116.
9. S. Z. Sapozhnikov, V. Y. Mitiakov, and A. V. Mitiakov, in *Proceedings of the 4th International Conference on Heat and MassTransfer, Minsk, 2000*, pp. 357–360.
10. S. Z. Sapozhnikov, V. Y. Mitiakov, and A. V. Mitiakov, Izv. Vyssh. Uchebn. Zaved. Energetich. Ob”ed. SNG, Energetika, Nos. 9–10, 53 (1997).
11. S. Z. Sapozhnikov, V. Y. Mitiakov, A. V. Mitiakov, *et al.*, Pis’ma Zh. Tekh. Fiz. **30** (2), 76 (2004) [Tech. Phys. Lett. **30**, 76 (2004)].

Translated by A. Sidorova

Technical Physics, Vol. 49, No. 7, 2004, pp. 927–928. Translated from Zhurnal Tekhnicheskoĭ Fiziki, Vol. 74, No. 7, 2004, pp. 121–122.
Original Russian Text Copyright © 2004 by Trushin, Zholudev, Markelov, Chuprunov.

BRIEF COMMUNICATIONS

Thermally Induced Adjustment of the Parameters of X-ray Diffraction Peaks from Crystals

V. N. Trushin, A. A. Zholudev, A. S. Markelov, and E. V. Chuprunov
Nizhni Novgorod State University, pr. Gagarina 23, Nizhni Novgorod, 603950 Russia
e-mail: trush@phys.unn.runet.ru

Received December 3, 2003

Abstract—The effect of nonuniform thermal action of a light beam on the parameters of a diffraction peak for a calcite crystal is studied. It is shown that the spatial intensity distribution in an X-ray beam can be corrected by controlling the thermally induced mismatch between Bragg reflections from local areas in a crystal. © *2004 MAIK “Nauka/Interperiodica”.*

One of the important problems of X-ray diffraction optics is the development and design of optical elements for controlling and correcting hard X-ray radiation. Such elements are important since they are applied in X-ray diffraction lithography, medicine, microelectronics, and other fields of engineering. This problem is difficult, since it is difficult to produce X-ray optical elements that meet certain requirements. Therefore, it is often necessary to correct the wave front of an X-ray beam. In this work, the (228) X-ray diffraction peak of a calcite ($CaCO_3$) crystal is used to study the possibility of correcting crystal parameters by the thermal effect of a light beam on the crystal surface. The experiment was performed on a two-crystal X-ray spectrometer with a high angular resolution ($\Delta d/d = 10^{-4}$) according to the scheme (n, $-n$). As a source of X-ray radiation, we applied a BSV-29 X-ray tube (Cu$K\alpha_1$ radiation, 0.4 × 8-mm focal spot). As a monochromator, we used (511) Ge cut along the (111) plane. A sample to be studied was a 20 × 15 × 4-mm plate cut at an angle of 35° to the (228) crystallographic plane; it was fixed with a sealant on the surface of the attachment, which also served as a cooler. A cooler temperature of 22°C was maintained with a thermostat. The crystal surface was heated from the diffraction side by the radiation of a projector lamp and was controlled with a thermocouple. The scheme of illumination of the sample is illustrated in Fig. 1a.

Figure 1b shows the family of rocking curves recorded at different temperatures of the left part of the sample surface. Initial rocking curve *1* (recorded without illumination) consists of two peaks, whose positions are determined by the initial disorientation of coherent domains in the crystal. The initial positions of the disoriented domains in the crystal are determined topographically (Fig. 1c, topogram *1*). Figure 1c also shows topograms *3* and *5* of the sample surface, which were taken during the illumination of the left part of the surface. When the temperature of the left part of the sample surface, which coincides with one of the two domains, increases, the rocking curve shifts as a whole toward smaller angles and the distance between the peaks on the curve decreases. The position of the light beam with respect to the disoriented domains (see Fig. 1a) was determined from the maximum change in the intensities of the rocking curves. At $t = 49$°C, both peaks in the rocking curve merge (curve *5*).

The changes in the shape of the rocking curve shown in Fig. 1b can be explained by a thermally induced mismatch in the angular displacement of the diffraction peak, which is caused by the nonuniform illumination of the sample surface, and by a change in the divergence of the X-ray beams that is related to temperature gradients [1, 2]. This dependence shows that the mismatch between the Bragg reflections from disoriented domains in the crystal can be compensated in some cases by a light beam, thus decreasing the rocking-curve width. The detected change in the shape of the rocking curve depends on the energy and geometrical position of the light beam on the crystal surface. For example, when the right part of the sample is irradiated and the light–shade boundary is retained on the sample surface, the mismatch between the Bragg reflections increases with respect to the initial mismatch.

The angular position of a diffraction peak taken from a local uniform region in a crystal that is subjected to a temperature gradient depends on the temperature of this region and its temperature gradient. The temperature dependence (without making allowance for the temperature gradient) of a Bragg reflection angle θ_{ij} for the point on the crystal surface with coordinates ij is written as

$$\theta_{ij} = \arcsin\left(\frac{\lambda}{2(d_{0ij} + d_{0ij}\alpha\Delta t_{ij})}\right), \qquad (1)$$

where θ_{ij} is the Bragg reflection angle for the (hkl) planes at the point with the coordinates ij, t_{ij} is the temperature of the crystal surface at the point with the coor-

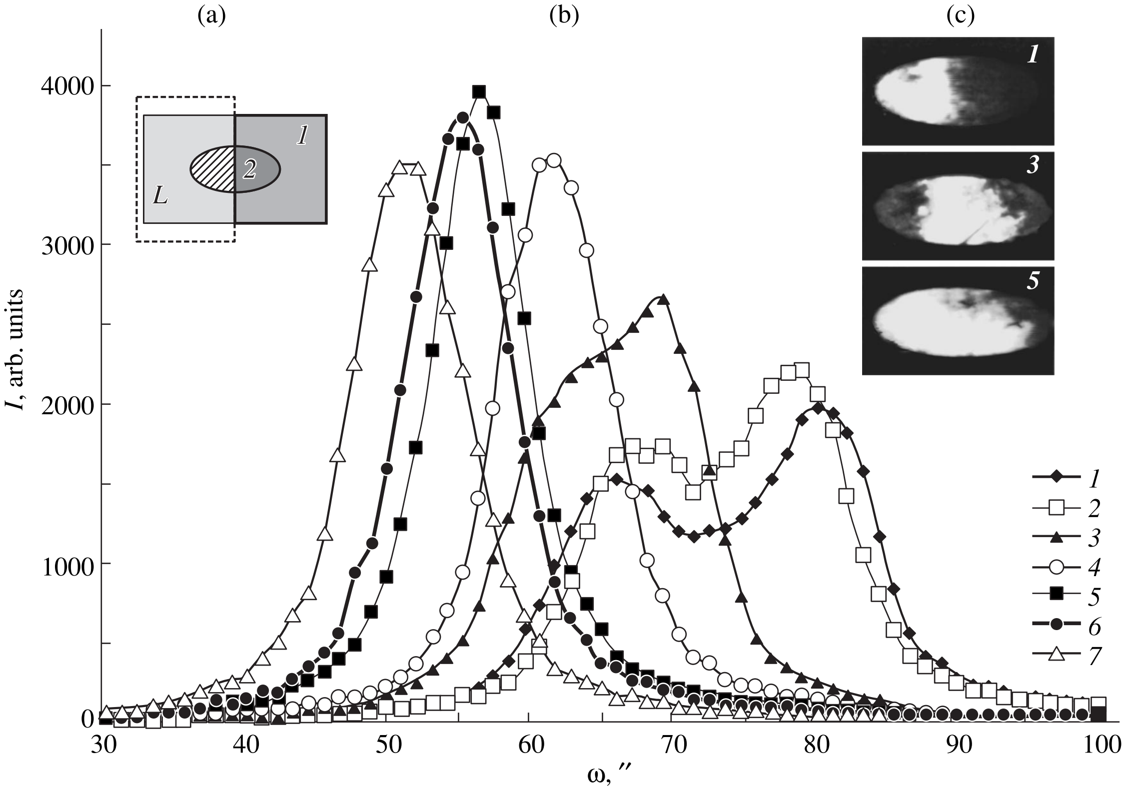

Fig. 1. (a) Schematic of the illumination of the sample surface: (*1*) sample and (*2*) diffraction area. The dotted line shows the illumination region (*L*). (b) Rocking curves recorded upon heating the left side of the sample surface to (*1*) 22, (*2*) 28, (*3*) 30, (*4*) 43, (*5*) 49, (*6*) 58, and (*7*) 72°C. (c) Topograms of a part of the sample surface taken under the illumination conditions of recording curves *1*, *3*, and *5*.

dinates *ij*, λ is the wavelength, α is the thermal expansion coefficient of the crystal along a reciprocal lattice vector, $d_{ij} = d_{0ij} + \Delta d_{ij}$, d_{0ij} is the interplanar spacing at the point on the crystal surface at a temperature t_0, t_0 is the temperature of the unexposed area in the crystal, and Δd_{ij} is the change in the interplanar spacing at the point with the coordinates *ij* that is caused by the temperature gradient Δt_{ij} at this point.

Using Eq. (1), we can qualitatively explain the disappearance of the splitting of the peaks from the two domains. To perform a quantitative estimation, it is necessary to take into account many factors, such as the thermal conductivity of the sample, heat-removal conditions, domain shapes, and the X-ray optical scheme of the experiment. Therefore, to quantitatively estimate the conditions of disappearance of the peaks from two (or several) domains, one has to introduce certain corrections related to the experimental conditions.

Thus, using the thermal effect of a light beam on the surface of a diffracting crystal, one can locally correct its parameters and control the spatial intensity distribution in an X-ray beam. The thermal effect of a light beam on the surface of a crystal can also change the angular divergence of X-ray beams within the width of a rocking curve.

This method of correcting the parameters of a diffracting crystal can be applied in X-ray diffractometry in the cases when the width of the rocking curve of the monochromator should be changed in a given manner. With this method, one can, for example, change a diffraction region in a crystal to be studied. The possibility of creating the required profile of thermal deformation at the surface of a crystal or in a multilayer structure with the help of a light beam makes it possible to control their dispersion properties, which is important in focusing optical systems.

REFERENCES

1. A. V. Mkrtchan, Izv. Akad. Nauk Arm. SSR, Fiz. **29** (6), 26 (1986).
2. V. N. Trushin, T. M. Ryzhkova, M. A. Fadeev, *et al.*, Kristallografiya **38**, 213 (1993) [Crystallogr. Rep. **38**, 542 (1993)].

Translated by K. Shakhlevich

Technical Physics, Vol. 49, No. 7, 2004, pp. 929–932. Translated from Zhurnal Tekhnicheskoĭ Fiziki, Vol. 74, No. 7, 2004, pp. 123–126.
Original Russian Text Copyright © 2004 by Uchaikin.

BRIEF COMMUNICATIONS

Fractal Walk and Walk on Fractals

V. V. Uchaikin
Ul'yanovsk State University, ul. L'va Tolstogo 42, Ul'yanovsk, 432700 Russia
e-mail: uchaikin@sv.uven.ru

Received December 25, 2002; in final form, December 4, 2003

Abstract—The one-dimensional walk of a particle executing instantaneous jumps between the randomly distributed "atoms" at which it resides for a random time is considered. The random distances between the neighboring atoms and the time intervals between jumps are mutually independent. The asymptotic ($t \longrightarrow \infty$) behavior of this process is studied in connection with the problem of interpretation of the generalized fractional diffusion equation (FDE). It is shown that the interpretation of the FDE as the equation describing the walk (diffusion) in a fractal medium is incorrect in the model problem considered. The reason is that the FDE implies that the consecutive jumps (fractal walk) are independent, whereas they are correlated in the case under consideration: a particle leaving an atom in the direction opposite to the preceding direction traverses the same path until arriving at the atom. © *2004 MAIK "Nauka/Interperiodica".*

INTRODUCTION

The term "anomalous diffusion" or, synonymously, "strange kinetics" has emerged in the last decade and been actively used in the description of the processes in which a diffusion packet spreads following the law different from the standard expression $\Delta(t) \propto t^{\gamma}$. The approximation $\Delta(t) \propto t^{1/\gamma}$ with γ differing from 1/2 is used most frequently. Among these processes are charge transfer in amorphous semiconductors and diffusion in polymeric and porous materials, turbulent and circulatory flows, the interstellar medium, rocks, etc. [1–3].

Such processes are often described analytically using the generalized diffusion equation with fractional derivatives (fractional diffusion equation (FDE)). In the one-dimensional case, it has the form

$$\frac{\partial^{\beta} p(x,t)}{\partial t^{\beta}} = -D\left(-\frac{\partial^2}{\partial x^2}\right)^{\alpha/2} p(x,t) + \frac{t^{-\beta}}{\Gamma(1-\beta)}\delta(x), \quad (1)$$

$$0 < \alpha \le 2, \quad 0 < \beta \le 1.$$

Here, $\Gamma(z)$ is the Euler gamma function,

$$\frac{\partial^{\beta} p(x,t)}{\partial t^{\beta}} = \frac{1}{\Gamma(1-\beta)}\frac{\partial}{\partial t}\int_0^t \frac{p(x,\tau)d\tau}{(t-\tau)^{\beta}}$$

is the Riemann–Liouville derivative of fractional order β, and $(-\partial^2/\partial x^2)^{\alpha/2}$ is the fractional power of the second-derivative operator [4]. The exponents α and β are related to the distributions of the particle random paths R and residence times Θ on the trap atoms by the asymptotic expressions

$$\mathrm{P}\{R > r\} \propto r^{-\alpha}, \quad r \longrightarrow \infty$$

and

$$\mathrm{P}\{\Theta > r\} \propto r^{-\beta}, \quad r \longrightarrow \infty.$$

These characteristic properties are usually interpreted in terms of medium fractality (i.e., the presence of large voids on any scale) and particle memory (i.e., the probability of a particle leaving an atom per unit time depends on the time it arrived at the atom). This work is devoted to the refinement of the first (fractal) interpretation.

ONE-DIMENSIONAL FRACTAL GAS

In [5], the random distribution $\{X_j\} = \ldots, X_{-2}, X_{-1}, X_0, X_1, X_2, \ldots$ of pointlike atoms on a line, with (1) $X_0 = 0$, (2) $X_i < X_j$ for $i < j$, and (3) $X_j - X_{j-1} = R_j$ being mutually independent similarly distributed random variables with the common distribution function $F(x)$, was called one-dimensional Lorentz gas. One can readily see that the probability distribution for the number of atoms $N_+(x)$ on the interval $(0, x]$ is expressed through the multiple convolutions of the $F(x)$ distribution as

$$W(n,x) \equiv \mathrm{P}\{N_+(x) = n\} = F_n(x) - F_{n+1}(x).$$

A similar relation holds for the distribution of the number of particles $N_-(x)$ on the interval $[-x, 0)$. The total number of atoms on a closed interval $[-x, x]$ is the sum

$$N(x) = N_+(x) + N_-(x) + 1.$$

Various models of a random medium can be obtained by choosing various distribution functions

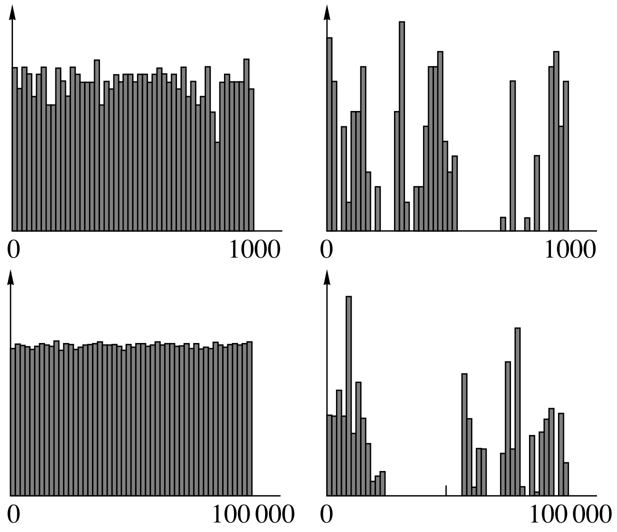

Fig. 1. (Left) regular and (right) fractal ($\alpha = 0.75$) atomic distributions on line in different scales.

$F(x)$. For instance, the Heaviside step function

$$F(x) = \mathrm{H}(x-a) \equiv \begin{cases} 0, & x < a \\ 1, & x \ge a \end{cases}$$

gives a one-dimensional determinate lattice, while the exponential distribution

$$F(x) = 1 - \exp\{-\mu x\}$$

leads to independently distributed atoms (Poisson model).

In any case, if the mathematical expectation of the random variable R is a finite value, $\langle N(x)\rangle \propto x$ and the relative fluctuation $\Delta(x)/\langle N(x)\rangle \longrightarrow 0$ for asymptotically large x. This implies that, if $f(N(x), x)$ is a smooth function of random variable N, $f(N(x), x) \longrightarrow f(\langle N(x)\rangle, x)$ at $x \longrightarrow \infty$; i.e., the self-averaging

$$\langle f(N(x), x)\rangle \longrightarrow f(\langle N(x)\rangle, x) \qquad (2)$$

occurs as the layer thickness x increases.

Let now

$$1 - F(x) \sim \frac{A}{\Gamma(1-\alpha)} x^{-\alpha}, \quad x \longrightarrow \infty, \quad \alpha < 1. \qquad (3)$$

In this case, the average interatomic distance is infinite, while the actual distances are finite for any realization of a random medium. Due to the infinite value of the mathematic expectation for R, the voids will occur alternately with concentrations (clusters) on any scales) (this property is referred to as intermittency) (Fig. 1). The use of the generalized limit theorem based on the theory of stable laws [6] gives

$$\sum_{i=1}^{n} W(i, x) \sim \int_0^z w_\alpha(z)dz, \quad x \longrightarrow \infty, \qquad (4)$$

where $z = n/\langle N(x)\rangle$ and

$$w_\alpha(z) = \frac{z^{-1-1/\alpha}}{\alpha\Gamma(1+\alpha)} g^{+}\left(\frac{z^{-1/\alpha}}{\Gamma(1+\alpha)}, \alpha\right).$$

Here, $g^{+}(z, \alpha)$ is the probability density at the positive semiaxis $z > 0$. The Laplace transform of this function is

$$\int_0^\infty g^{+}(z, \alpha)e^{-\lambda z}dz = e^{-\lambda^\alpha}.$$

One can readily see that the Lorentz gas satisfying condition (3) has the following properties: (1) all atoms are equivalent and all processes $N(X_j, X_j + x)$ are statistically equivalent $N(X_j, X_j + x) \overset{d}{=} N(x)$; the symbol $\overset{d}{=}$ indicates that all distributions of the related random variables are identical; (2) the ensemble-averaged number of atoms shows a power-law increase with increasing layer thickness counted from one of these atoms,

$$\langle N(x)\rangle \sim N_1 x^\alpha, \quad 0 < \alpha < 1;$$

and (3) relative fluctuations of the number of atoms in this layer do not decrease with increasing its thickness but remain constant.

These properties give grounds to refer to this structure as a stochastic fractal (or fractal gas), i.e., as a self-similar, in the probabilistic sense, set with fractal dimensionality α. Instead of (2), one has the following relation for the fractal gas:

$$\langle f(N(x), x)\rangle \sim \int_0^\infty f(N_1 x^\alpha z, x) w_\alpha(z)dz \qquad (5)$$

at $x \longrightarrow \infty$. Expression (5) implies that self-averaging does not occur on the fractal structures, and this is the main cause for the distinction between the walk on fractals and the walk on a regular medium.

FRACTAL MEMORY

In a similar manner, we construct the random point set $\{T_j\} = T_1, T_2, T_3, \ldots$ on the positive time semiaxis; it characterizes the random instants of time at which a particle executes jumps from one atom to another. As above, we assume that the random variables $\Theta_1 = T$, $\Theta_2 = T_2 - T_1$, $\Theta_3 = T_3 - T_2$, … are mutually independent and distributed alike with the distribution function $Q(t) = P\{\Theta < t\}$. If $Q(t) = 1 - e^{-\mu t}$ ($\mu > 0$), the random set $\{T_i\}$ forms a uniform Poisson flow. This means that the probability of a particle executing jump in the interval $(t, t + dt)$ is independent of the time of its preceding jump; in other words, the particle does not possess memory. In all other cases, the particle is said to have memory, and, if

$$1 - Q(t) \sim \frac{B}{\Gamma(1-\beta)} t^{-\beta}, \quad t \longrightarrow \infty, \quad \beta < 1,$$

one speaks about a particle with fractal memory. All the aforesaid for the $\{X_i\}$ ensemble is also true for the $\{T_i\}$ ensemble, including averaging rule (5). If $K(t)$ is the random number of jumps within a fixed interval $(0, t]$, the function $h(K(t), t)$ averaged over the statistical ensemble $\{T_i\}$ satisfies the asymptotic relation

$$\langle h(K(t), t)\rangle \sim \int_0^\infty h(K_1 t^\beta z, t) w_\beta(z) dz, \quad t \longrightarrow \infty. \quad (6)$$

WALK ON FRACTAL

Let us now consider a one-dimensional walk along the x axis. At zero time, a particle is at the origin of coordinates. After a lapse of random time $T_1 = \Theta_1$, it undergoes jump with the same probability to one of the two neighboring atoms, where it resides for a random time Θ_2, after which it again jumps to one of the neighboring atoms (among which may be the original atom from which the particle started to move).

If we use the atom number i instead of the coordinate x and the jump number j instead of time t, we obtain, according to the central limit theorem,

$$\mathrm{P}\{I < i | J = j\} \sim \frac{1}{\sqrt{2\pi j}} \int_{-\infty}^{i} e^{-x^2/2j} dx, \quad j \longrightarrow \infty. \quad (7)$$

This result is a consequence of the ensemble averaging of the random particle trajectories with fixed nodes and instants of jumps [7]. To obtain the desired distribution function, it is necessary to average expression (7) over two statistically independent ensembles $\{X_i\}$ and $\{T_i\}$, i.e., over the random values I and J of indices i and j, respectively,

$$F(x, t) = \langle\langle P\{I < i | J = i\}\rangle\rangle.$$

This averaging can be accomplished using formulas (4) and (5) to give, after some transformations,

$$F(x, t) \sim \Xi^{(\alpha, \beta)}((Ct)^{-\beta/(2\alpha)} x), \quad t \longrightarrow \infty, \quad x \longrightarrow \infty,$$

where $C = \mathrm{const}$,

$$\Xi^{(\alpha, \beta)}(x) = \int_0^\infty \Psi^{(2, \beta)}(x/y^\alpha) g^+(y, \alpha) dy,$$

and $\Psi^{(2, \beta)}(x)$ is the subdiffusional distribution derived in [8].

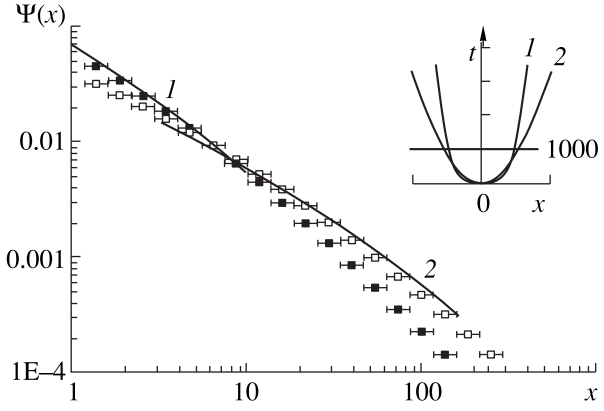

Fig. 2. Spatial distributions for a particle in the case of (*1*) walk on fractal and (*2*) fractal walk. Inset: time evolution of the width of respective diffusional packets. Exponents $\alpha = 0.5$ and $\beta = 0.25$.

The corresponding relation for the densities has the form

$$f(x, t) = (Ct)^{-\beta/(2\alpha)} \times \int_0^\infty \Psi^{(2, \beta)}((Ct)^{-\beta/(2\alpha)} y^{-\alpha}) g^+(y, \alpha) dy. \quad (8)$$

As $\alpha \longrightarrow 1$, $g^+(y, \alpha) \longrightarrow \delta(y - 1)$ and

$$f(x, t) = (Ct)^{-\beta 2} \Psi^{(2, \beta)}((Ct)^{-\beta/2}).$$

At $\beta \longrightarrow 1$, the distribution $\Psi^{(2, \beta)}$ becomes normal. If these two conditions are met simultaneously, one arrives at the Gaussian form for the density $f(x, t)$ corresponding to the conventional diffusion in a regular medium.

CONCLUSIONS

To answer the question that was posed at the beginning of the article, we present the solution to FDE (1) describing the fractal walk, i.e., a walk for which particle paths have the same distribution as the interatomic intervals in the medium considered but are independent of each other (even in the case where the walker changes its movement direction). This solution is written as

$$f(x, t) = (Ct^\beta)^{-1/\alpha} \Psi^{(\alpha, \beta)}((Ct^\beta)^{-1/\alpha} x), \quad (9)$$

where $\Psi^{(\alpha, \beta)}$ is the density, whose particular form is used in expression (8).

A comparison of spatial distribution (8) for the walk on fractal with the solution to FDE (9) (Fig. 2) suggests that, generally, the latter cannot be interpreted as the equation describing the walk on fractals; in the first case, the diffusional packet spreads following the law $\sim t^{\beta/(2\alpha)}$, while, in the second case, it spreads as $\sim t^{\beta/\alpha}$, i.e., much faster. For the walk on fractals, the exponent $\gamma =$

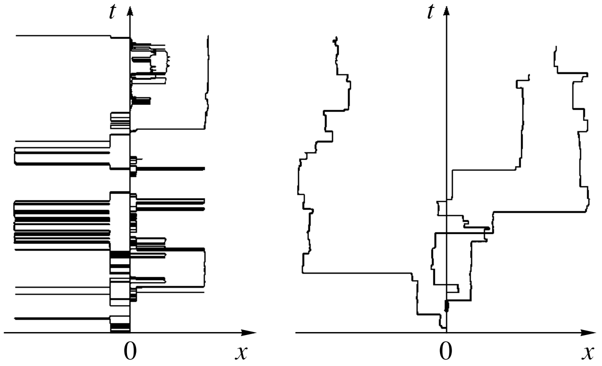

Fig. 3. Particle trajectories in the case of (left) walk on fractal and (right) fractal walk. Exponents $\alpha = 0.5$ and $\beta = 1$.

$\beta/(2\alpha)$ changes within the interval (0, 1/2), so that the superdiffusion regime ($\gamma > 1/2$) never arises. The reason for this distinction can be seen from Fig. 3; in the case of fractal walk, a particle can move far away after it leaves an atom, whereas, in the walk on fractal, it may be blocked between neighboring clusters to undergo many transitions between them.

The density distributions $\xi^{(\alpha,\ \beta)}$ and $\psi^{(\alpha,\ \beta)}$ are also different in these cases.

To summarize, it is worth noting that these conclusions are valid for a statistical ensemble of one-dimensional "frozen" atomic arrangements. With a multidimensional walk, the correlation between the consecutive paths may be weaker, so that the aforementioned distinction may be less pronounced. Moreover, the situation may radically change if the atomic arrangement changes during the characteristic residence time on one of the atoms (as is the case for the diffusion in a turbulent medium; superdiffusion has the same origin).

Nevertheless, the facts established in this work seem to be useful in the adequate understanding of the role of equations with fractional derivatives in the problem of diffusion on fractals with traps.

ACKNOWLEDGMENTS

I am grateful to V.V. Saenko for numerical calculations and E.V. Kozhemyakina for preparing the manuscript for publication. This work was supported in part by the Russian Foundation for Basic Research (project nos. 00-01-00284, 00-02-17507) and the Royal Society (grant no. gt/fSU/JP).

REFERENCES

1. J.-P. Bouchud and A. Georges, Phys. Rev. A **41**, 1156 (1990).
2. M. B. Isichenko, Rev. Mod. Phys. **64**, 961 (1992).
3. D. Ben-Avraham and S. Havlin, *Diffusions and Reactions in Fractals and Disordered Systems* (Cambridge Univ. Press, Cambridge, 2000).
4. S. G. Samko, A. A. Kilbas, and O. I. Marichev, *Fractional Integrals and Derivatives, Theory and Applications* (Nauka i Technika, Minsk, 1987; Gordon and Breach, Amsterdam, 1993).
5. E. Barkai, V. Fleurov, and J. Klafter, Phys. Rev. E **61**, 1164 (2000).
6. A. A. Borovkov, *Course of Probability Theory* (Nauka, Moscow, 1972).
7. W. Feller, *An Introduction to Probability Theory and Its Applications*, 3rd ed. (Wiley, New York, 1967; Mir, Moscow, 1967).
8. V. V. Uchaĭkin, Zh. Éksp. Teor. Fiz. **115**, 2113 (1999) [JETP **88**, 1155 (1999)].
9. V. Kolokoltsov, V. Korolev, and V. Uchaikin, *Fractional Stable Distributions* (Nottingam Trent Univ., Nottingam, 2000), No. 23/00.

Translated by V. Sakun

Technical Physics, Vol. 49, No. 7, 2004, pp. 933–934. Translated from Zhurnal Tekhnicheskoĭ Fiziki, Vol. 74, No. 7, 2004, pp. 127–128.
Original Russian Text Copyright © 2004 by Rukhadze, Yusupaliev.

BRIEF COMMUNICATIONS

On the Feasibility of the Coulomb Explosion of a Metal

A. A. Rukhadze and U. Yusupaliev
Prokhorov Institute of General Physics, Russian Academy of Sciences,
ul. Vavilova 38, Moscow, 119991 Russia
e-mail: nesu@phys.msu.ru

Received September 15, 2003; in final form, December 16, 2003

Abstract—The mechanism of the Coulomb explosion of a metal in an external pulsed electric field is discussed. In the case of a low-frequency field, when its frequency is lower than the frequency of electron collisions, it is impossible to reach the conditions of the Coulomb explosion of a metal if the field pulse duration is shorter than the time of electron energy relaxation upon elastic collisions, and the electron temperature is well above the Fermi energy and the work function. In the case of a high-frequency field, e.g., in a powerful pulse of ultraviolet laser radiation, the Coulomb explosion can occur if the field strength is well above the intraatomic field strength (i.e., when the laser power density is $\geq 10^{19}$ W/cm^2). *© 2004 MAIK "Nauka/Interperiodica".*

1. Interest in the so-called micropinches, i.e., powerful pulsed high-current discharges through thin metallic wires, has recently grown [1–3]. Such pinches can be applied in various fields, e.g., for initiating thermonuclear reactions or for creating sources of X-ray radiation and a dense hot plasma. Micropinches have attracted our attention due to the possibility of experimental observation of a very interesting phenomenon—the Coulomb explosion of a metal. This phenomenon consists in the electric explosion of a positively charged crystal when conduction electrons are rapidly removed from the bulk of the metal without significant heating of the lattice [4].

To understand the feasibility of the Coulomb explosion during electrical breakdown in a metallic wire, we conduct simple estimations. Let a voltage pulse duration τ satisfy the inequality

$$10^{-14}\ \text{s} \approx \nu_e^{-1} \ll \tau \ll (\delta\nu)^{-1} \approx 10^{-10}\ \text{s}, \tag{1}$$

where $\nu_e \approx 10^{14}$ s^{-1} is the frequency of elastic electron collisions in a metal with an electron density $n_e \approx 10^{22}$ cm^{-3} and a conductivity $\sigma \approx 10^{16}$ s^{-1}, and $\delta \approx 10^{-4}$ is the fraction of energy transferred from an electron to the lattice during an elastic collision.

Note that the electron mean free path in a metal is on the order of $L \approx v_{\text{Fe}}/v_e \approx 10^{-6}$ cm and the Debye screening length is $r_{\text{D}} \approx v_{\text{Fe}}/\omega_{\text{Le}} \approx 2 \times 10^{-8}$ cm, where $v_{\text{Fe}} \approx 10^8$ cm/s is the Fermi velocity and $\omega_{\text{Le}} \approx \sqrt{3 \times 10^9 n_e}$ is the electron Langmuir frequency.

Let a pulsed discharge current with a density j pass through a wire of radius r_0. Under condition (1), when cooling of electrons can be neglected, the electron temperature T_e (which is considered to be well above the Fermi energy $\varepsilon_{\text{Fe}} = m v_{\text{Fe}}^2/2 \approx 1$–$2$ eV) over the pulse duration τ reaches the value

$$T_e \approx \frac{j^2}{n_e\sigma}\tau = \frac{\sigma E^2}{n_e}\tau, \tag{2}$$

and the magnetic field of the current at the wire surface turns out to be

$$\frac{B^2}{8\pi} = \frac{\pi}{2c^2}j^2 r_0^2 = \frac{\pi}{2c^2}\sigma^2 E^2 r_0^2, \tag{3}$$

where E is the electric field strength in the discharge and c is the velocity of light in vacuum.

It follows from Eqs. (2) and (3) that, if $r_0 \leq 10^{-3}$ cm, the gas-kinetic pressure of the heated electron gas in the metal exceeds the pressure of the magnetic field of the current irrespective of its value even at $\tau > 10^{-11}$ s. Note also that, at this pulse duration, the electric current completely penetrates the conductor. Indeed, the time it takes for the current to penetrate a wire of radius r_0 is about

$$\tau_1 \approx \frac{\sigma r_0^2}{c^2}. \tag{4}$$

For the metal parameters given above, we have $\tau_1 \approx 10^{-11}$ s. Thus, at $\tau > 10^{-11}$ s, the current pulse completely penetrates the conductor. At shorter current pulses, the current experiences the skin effect, to say nothing of the compression of the electron gas in the metal by the magnetic field of the current.[1]

We now estimate the temperature of electrons when they are heated by a current pulse with a density $j \approx$

---

[1] Earlier [5], we showed that the Coulomb explosion of a metal cannot be realized in the stage of compression of electrons by the magnetic field of a current.

1063-7842/04/4907-0933$26.00 © 2004 MAIK "Nauka/Interperiodica"

10^{10} A/cm^2 (or in an electric field $E \approx 10^7$ V/cm at a total current $I \approx \pi r_0^2 j \approx 30$ kA) over a time $\tau \approx 10^{-11}$ s. From Eq. (2), we have $T_e \approx 100$ eV. Electrons having this energy can easily leave the wire in a time of about 10^{-11} s, which "bares" the crystal lattice and results in the Coulomb explosion of the metal. Note that all estimates agree with the experimental data [1–3]; we think that the Coulomb explosion of a metal was likely to be observed in these experiments, which dealt with the study of the *X* pinch, as a phenomenon called as a minidiode in [1].

2. Another possibility of realization of the Coulomb explosion is to irradiate a thin metallic wire by a powerful femtosecond pulse of ultraviolet radiation. If the energy of electron oscillation in the laser-radiation field is well above the Fermi energy under these conditions, the electron velocity distribution is a narrow function with a peak at a velocity that is equal to the electron oscillation velocity in the laser-radiation field [6].

However, certain conditions should be met in this case.

First, the metal must be transparent for a laser radiation with a frequency ω_0; i.e.,

$$\omega_0 > \omega_{\mathrm{Le}} \approx \sqrt{3 \times 10^9 n_e} \gg \nu_e. \tag{5}$$

For metals, this condition is met for radiation in the ultraviolet region at $\lambda < 300$ nm.

Second, the electron oscillation amplitude r_E in the laser field should exceed the half-thickness d of the metallic film:

$$r_E = \frac{eE_0}{m\omega_0^2} = \frac{v_E}{\omega_0} > d, \tag{6}$$

where E_0 is the amplitude of the electric field of the laser radiation and v_E is the amplitude of the electron oscillation velocity.

At $\omega_0 \approx 10^{16}$ s^{-1} ($\lambda_0 \approx 200$ nm) and $d \approx 10^{-6}$ cm, we have from (6) $v_E \geq 10^{10}$ cm/s and $E_0 \geq 10^{10}$ V/cm, which corresponds to a laser power density of $P_0 = cE_0^2/4\pi \geq 10^{19}$ W/cm^2. This power density of ultraviolet laser radiation has already been surpassed.

Under these conditions, the laser field penetrates a metal without attenuation and sets the electrons of the beam in oscillatory motion at an amplitude $r_E > d$; therefore, the electrons have an energy well above the work function and can easily leave the metallic foil in a time of $2\pi/\omega_0$. The crystal lattice becomes free of electrons, and heating of the metal is insignificant because of the right-hand inequality in (5). Note also that, at $E_0 \approx 10^{10}$ V/cm, the electron oscillation energy in the laser wave field is well above the Fermi energy but is still nonrelativistic (it is about 30 keV).

ACKNOWLEDGMENTS

We are grateful to the reviewer of this article for stimulating critical remarks.

This work was supported by the Scientific Program "Russian Universities," project no. UR 0102002.

REFERENCES

1. G. V. Ivannikov, A. R. Mingaleev, S. A. Pikuz, *et al.*, Fiz. Plazmy **22**, 403 (1996) [Plasma Phys. Rep. **22**, 363 (1996)].
2. S. A. Pikuz, T. A. Shelkovenkov, D. B. Sinars, *et al.*, Phys. Rev. Lett. **83**, 4313 (1999).
3. D. B. Sinars, K. M. Chendler, D. A. Hammer, *et al.*, Phys. Plasmas **8**, 216 (2001); Phys. Plasmas **8**, 1305 (2001).
4. M. Rusek, H. Lagadec, and T. Blensky, Phys. Rev. A **63**, 013203 (2001).
5. A. A. Rukhadze and U. Yusupaliev, Kratk. Soobshch. Fiz., No. 7, 36 (2003).
6. M. V. Kuzelev and A. A. Rukhadze, Fiz. Plazmy **27**, 170 (2001) [Plasma Phys. Rep. **27**, 158 (2001)].

Translated by K. Shakhlevich

Technical Physics, Vol. 49, No. 7, 2004, pp. 935–937. Translated from Zhurnal Tekhnicheskoĭ Fiziki, Vol. 74, No. 7, 2004, pp. 129–130.
Original Russian Text Copyright © 2004 by Fogelson, Likhachev.

BRIEF COMMUNICATIONS

Equation of State of a Real Gas

R. L. Fogelson and E. R. Likhachev
Voronezh State University, Voronezh, 394693 Russia
e-mail: phssd18@main.vsu.ru

Received October 27, 2003

Abstract—It is shown using 28 gases as an example that the Van der Waals equation in the form

$$\left[P + \frac{a}{(V+c)^k T^m}\right](V-b) = RT$$

correctly expresses quantitative relations between parameters P, V, and T for real gases. Here, a, b, and c are constants; k is a number close to 2; and m varies in the range 0.2–2.17 for different gases. The critical parameters of most gases calculated by this formula are found to be close in value to the experimental parameters. *© 2004 MAIK “Nauka/Interperiodica”.*

The Van der Waals equation is believed “to be just a qualitative equation expressing quantitative relations between parameters P, V, and T of real gases only approximately” [1, p. 177]. Hence, a large number of more complicated and intricate expressions were proposed as an equation of state for real gases [1, 2]. We have investigated the Van der Waals equation

$$\left(P + \frac{a}{V^2}\right)(V-B) = RT \qquad (1)$$

for various temperature and volume dependences of coefficients A and B. The investigations show that if such a dependence is chosen properly, Eq. (1) is in much better agreement with the experiment than it is generally accepted. The following form of the Van der Waals equation provides the best agreement with experiment:

$$\left[P + \frac{a}{(V+c)^k T^m}\right](V-b) = RT. \qquad (2)$$

Here, a, b, c, k, and m are constants.

The reduced equation [1, p. 150] for Eq. (2), satisfying conditions of thermodynamic stability in the critical point, is expressed by

$$\left[\pi + \frac{\alpha}{\omega^k \tau^m}\right](\alpha\omega - 1) = \frac{4k}{(k-1)^2}\tau, \qquad (3)$$

where the notation

$$\alpha = \frac{k+1}{k-1}, \quad \omega = \frac{\varphi + \nu}{1+\nu}$$

is introduced. Here, $\pi = P/P_c$, $\varphi = V/V_c$, and $\tau = T/T_c$ are the reduced parameters; P_c, V_c, and T_c are the critical parameters; and ν is the quantity appearing in Eq. (3) instead of constant c entering Eq. (2). The quantities appearing in Eq. (3) are related as

$$\frac{P_c V_c}{RT_c} = \frac{k^2-1}{4k(1+\nu)}.$$

The constants a, b, and c from Eq. (2) are related to the quantities entering Eq. (3) by the expressions

$$a = \frac{(k+1)^2}{4k}(1+\nu)^{k-1} R T_c^{m+1} V_c^{k-1},$$

$$b = \frac{k-1-2\nu}{k+1} V_c,$$

$$c = \nu V_c.$$

In this paper, Eq. (3) was used to determine constants P_c, V_c, T_c, k, m, ν by experimental data. To do that, the indicated constants were chosen in such a way that the value of P calculated by Eq. (3) was in the best agreement with the tabulated value for preset values V and T (borrowed from reference books [3–5]). Values of P, V, T were taken from reference books [3] for water, [4] for four inert gases, and [5] for other gases. The parameters for 28 gases are listed in the table. A comparison between calculated critical and experimental parameters indicated in the mentioned reference books shows that the calculated parameters are close in value to the experimental ones for most gases. The maximum difference is found for the critical volumes. This can partially be associated with the fact that an experimental critical volume is determined with the least accuracy because the substance volume changes drastically at the critical point. A considerable difference between the calculated critical and experimental parameters was obtained for three polar substances: water (of two kinds) and ammonia. The average relative deviations δ

Table

Gas	P_c, bar	V_c, 10^{-3} m^3/kg	T_c, K	k	m	ν	δ, %
Helium	2.3	15.45	5.36	2	0.2	0.175	0.35
Neon	26	2.51	45	2	0.42	0.065	0.37
Argon	50	2.23	153	1.96	0.39	0.036	0.17
Krypton	55	1.32	210	1.96	0.37	0.043	0.18
Xenon	59	1.08	292	1.93	0.33	0.032	0.25
Hydrogen	13	35	33	2	0.3	0.118	0.57
Nitrogen	35	3.8	128	1.91	0.36	0	0.3
Oxygen	52	2.75	156	1.91	0.33	–0.012	0.23
Air	33	3.98	129	1.95	0.35	0.017	0.35
Carbon monoxide	37	3.74	134	1.8	0.28	–0.091	0.63
Carbon dioxide	72	2.74	304	1.92	0.56	0.03	0.37
Methane	47	7.46	191	1.87	0.21	–0.043	0.23
Ethane	52	5.52	312	1.91	0.55	0.056	0.26
Propane	43	5.42	373	1.95	0.65	0.09	0.3
Ethylene	51	5.49	284	2.02	0.63	0.146	0.12
Acetylene	62	4.39	309	2	1.03	0.36	0.07
Benzene	50	4.22	566	2	0.46	0.071	0.05
Freon-11	44	2.09	473	2.08	1.15	0.244	0.2
Freon-12	43	1.79	385	2.03	0.94	0.322	0.42
Freon-13	42	1.97	309	1.96	0.73	0.082	0.3
Freon-21	53	2.24	455	2.02	1.08	0.18	0.12
Freon-22	54	2.01	375	2.01	1.13	0.257	0.13
FS-318	27	2.05	388	1.96	0.9	0.059	0.2
Fluorine	54	2.18	147	1.9	0.59	–0.049	0.35
Chlorine	76	2.15	418	2.02	0.52	0.144	0.2
Ammonia	203	2.61	452	1.93	1.62	0.484	0.4
Water	396	2.59	735	1.93	1.42	0.17	0.23
Heavy water	400	1.68	719	2.04	2.17	0.722	0.15

of pressures calculated by Eq. (3) are listed in the last column in the table, where

$$\delta = \frac{1}{n}\sum_{n}\left|\frac{P_{\text{exp}} - P_{\text{calc}}}{P_{\text{exp}}}\right|. \tag{4}$$

Here, P_{exp} are the experimental pressures; P_{calc} are the calculated pressures; and n is the number of values of P, V, and T used in Eq. (4). The values were taken in the range covering all the temperatures and pressures listed in the table, where the gas volume was 1–2.5 times larger than the experimental critical volume ($V_{c,\,\text{exp}}$). The smaller volume in this range relates to high pressures, while the difference between liquid and gas becomes smoothed in highly compressed medium. When calculating δ, we took $n = 50$. The value of δ gives an estimate of the agreement between calculations and experiments.

The calculated critical parameters may differ from experimental ones for yet another reason apart from the errors. It is seen from the tables of temperature and pressure dependence of viscosity given in reference books [3–5] that, at pressures higher than the critical pressure, the liquid viscosity first decreases with increasing temperature (which is typical of liquids) and then increases starting with some temperature (which is inherent in gases). Thus, a liquid is gradually transformed into a gas as the substance volume increases. When such a transformation of a “real” liquid into a “real” gas occurs, an intermediate region, where the medium is neither a liquid nor a gas yet, should exist. The presence of such a region is supported by the following fact. The volume of a medium increases drastically at the critical point, which suggests the transformation of the medium to a new state. Simultaneously, the medium viscosity continues decreasing beyond the critical point. It is well seen from the table for the viscosity of carbon dioxide in the critical region [5, p. 207]. Thus, the medium has not taken all the gas properties yet above the critical point in a certain temperature range.

The boundaries of the intermediate region can be estimated using the formulas which express the temperature and pressure dependence of any physical property of the medium. The formula for the water viscosity was obtained in [6]. The calculations by this formula show that the calculated viscosity of liquid water starts considerably deviating from the experimental viscosity at all the tabulated pressures when the liquid volume approaches $0.5V_{c,\,\mathrm{exp}}$. On the other hand, Eq. (3) of this paper is verified for a volume of water vapor of $V > (1.3–2.5)V_{c,\,\mathrm{exp}}$. It follows from the aforementioned that the critical point is in the intermediate region; hence, the experimental parameters P_c, V_c, T_c at this point may not completely obey the equation of state for the gas.

REFERENCES

1. M. P. Vukalovich and I. I. Novikov, *Equation of State of Real Gases* (Gosénergoizdat, Moscow, 1948).
2. R. C. Reid, J. M. Prausnitz, and T. K. Sherwood, *Properties of Gases and Liquids* (McGraw-Hill, New York, 1977; Khimiya, Leningrad, 1982).
3. M. P. Vukalovich, S. L. Rivkin, and A. A. Aleksandrov, *Tables of Thermal Properties of Water and Water Vapor* (Izd. Standartov, Moscow, 1969).
4. V. A. Rabinovich, A. A. Vasserman, V. I. Nedostup, and L. S. Veksler, *Thermophysical Properties of Neon, Argon, Krypton, and Xenon* (Izd. Standartov, Moscow, 1976).
5. N. B. Vargaftik, *Tables of Thermophysical Properties of Liquids and Gases* (Fizmat, Moscow, 1972; Halsted Press, New York, 1975).
6. E. R. Likhachev, Zh. Tekh. Fiz. **73** (4), 135 (2003) [Tech. Phys. **48**, 514 (2003)].

Translated by M. Astrov

Technical Physics, Vol. 49, No. 7, 2004, pp. 938–940. Translated from Zhurnal Tekhnicheskoĭ Fiziki, Vol. 74, No. 7, 2004, pp. 131–133.
Original Russian Text Copyright © 2004 by Beloshenko, Varyukhin, Shkuratov.

BRIEF COMMUNICATIONS

Production of Carbon–Nitrogen Coatings Modified by Titanium Nitride

V. A. Beloshenko, V. N. Varyukhin, and B. E. Shkuratov
Donetsk Physicotechnical Institute, National Academy of Sciences of Ukraine, Donetsk, 83114 Ukraine
e-mail: bs@hpress.dipt.donetsk.ua

Received October 28, 2003

Abstract—We offer a method of producing composite coatings based on carbon–nitrogen compounds modified by titanium nitride clusters. The structure of the material obtained is studied by transmission electron microscopy. A comparison between electron diffraction patterns from carbon–nitrogen and titanium-nitride modified coatings reveals the presence of a hexagonal syngony in the carbon–nitrogen condensate. The mechanism of the modification effect on the structure and properties of the obtained coating is discussed. *© 2004 MAIK “Nauka/Interperiodica”.*

Methods of vacuum ion-plasma sputtering find extending applications in industry since they permit the synthesis of strengthening and protective coatings on the surface of parts operating in complex technological conditions. In this connection, diamond, diamond-like, and analogous films characterized by high hardness, mechanical strength, and chemical resistance are of considerable interest. Production of diamond and diamond-like coatings on steel substrates is often associated with considerable difficulties due to the impossibility of solid-phase reaction of carbon–iron bonding [1] that does not ensure the required bond strength. The problem of improving the adhesion still persists because of the high concentration of carbon in carbon–nitrogen films.

Improving the adhesive properties of the coating and homogeneity of its structure can be achieved by modifying carbon–nitrogen condensate by introducing titanium nitride. Titanium nitride is known to have a good adhesion and a rather high hardness due to strongly pronounced asymmetry of the localized electron distribution [2]. In addition, titanium nitride is characterized by a low resistivity, reducing the effect of charge accumulation during ion-stimulated sputtering. The formation of a titanium–carbon bond [1, 3] will decrease the probability of formation of graphitelike structures. In this case, the bombardment of the film surface by noncarbonic ions also promotes etching of SP^2-hybridized carbon [4]. Shiryaev *et al.* [3] earlier reported on a three-component coating obtained by magnetron sputtering of a titanium target with carbon insets by a mixture of Ar^+ and N^+ ions. However, no information on the structure and properties of this coating was given. The authors of [5] described a composite coating which is a sandwich structure of sequentially deposited layers of titanium nitride and carbon nitride. For this reason, it radically differs from the coating suggested by us [6].

In this work, a technique for producing coatings on low-carbon steel is described. The coating is a composite based on carbon–nitrogen compounds modified by titanium nitride clusters. The results of structure investigation are also presented.

The composite films were deposited with the use of a composite cathode made of graphite and titanium in a ratio of 7 : 3. The ratio was chosen for the following reasons. At a higher content of titanium, the phase of titanium nitride will dominate, while at lower content, no improvement of the coating adhesion properties is expected.

The films were deposited on the polished surface of samples using a VNP-350-02 vacuum setup equipped with a sputter arc source. The samples made of St40 steel were of a cylindrical shape with a diameter of 5 mm and a height of 6 mm. The cathode surface was nitrided in the atmosphere of a high-energy nitrogen plasma of the arc discharge and CN_x + TiN clusters sputtered by ions could be deposited on a substrate. Extra bias (negative relative to the chamber) was applied to the substrate for providing regimes of ion precleaning and ion-stimulated deposition of a condensate.

The method for fixation of the graphite cathode plays an important role in the process of coating deposition in the setup of vacuum arc-discharge deposition. Cathode overheating increases the amount of the microdrop fraction (graphite microparticles) contaminating the condensate and leading to the formation of punctures, scabs, and other defects. Simultaneously, the vacuum in the chamber deteriorates. Methods of firm fixation of a cathode to the water-cooled base are usually used in commercial setups. However, they are not effective enough due to the difference in the thermal

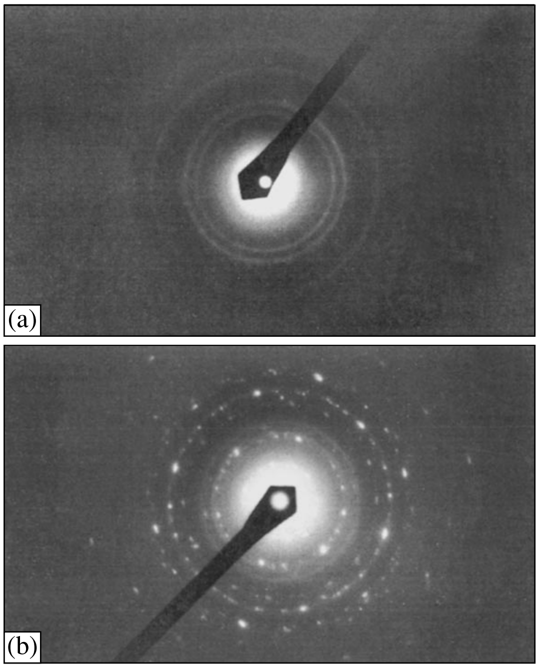

Fig. 1. CN*x* + TiN coating: electron-diffraction pattern of the composite with (a) cubic and (b) hexagonal syngony.

expansion coefficients of the materials of cathode and structure parts. We developed the method of fixation [6] in which the cathode could thermally expand freely. The cathode was made in the form of a truncated cone installed at the butt-end of the water-cooled metallic base. The centering lug prevented a radial shift. Springs provided clamping of the cathode to the base, which guaranteed a stable regime of heat removal in the contact area.

The amount of nitrogen in carbon–nitrogen condensates is known to decrease with increasing substrate temperature [7]. Hence, preliminary heating of substrates was not used. To study the structure, the samples were separated from the substrate by electrochemical etching. The composite microstructure was investigated by transmission electron microscopy (JEM 200). The microhardness of the composite was measured using a PMT-3 device.

The electron-diffraction patterns of local areas of the film modified by titanium nitride are found to consist of a halo and diffraction rings (Fig. 1), which indicates the presence of amorphous and crystalline components. The crystalline component of the film gives diffraction patterns corresponding to the cubic (Fig. 1a) and hexagonal (Fig. 1b) syngonies. A comparison of interplanar spacing of the cubic syngony of the composite obtained (see table) with the corresponding spacing for titanium nitride shows that they are rather close. The parameters of the crystal lattice of the composite calculated for the hexagonal syngony were $a = 5.27$ Å and $c = 4.87$ Å.

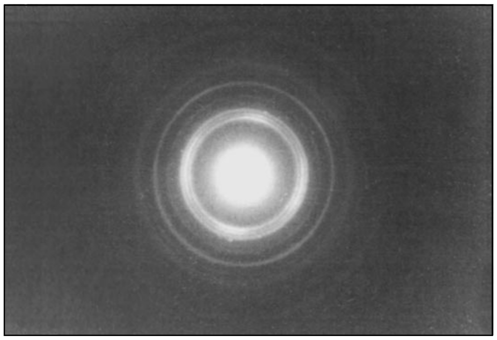

Fig. 2. CN*x* coating: electron-diffraction pattern of the local film area.

The expected low content of titanium in the modified condensate suggests that similar crystalline structures can exist in unmodified carbon–nitrogen condensate as well. Earlier, we obtained samples of carbon–nitrogen films under the same processing conditions. The main part of the electron-diffraction pattern for a local area of the carbon–nitrogen condensate (Fig. 2) can be classified as a cubic syngony with a lattice constant of $a = 4.12$ Å. Its interplanar spacing (see table) is close to the corresponding one for the structure of the titanium-modified composite. Some difference in d_{hkl} is probably due to the three-component structure of this composite. It would be difficult to identify other rings of the electron-diffraction pattern of carbon nitride, but interplanar spacing of the rings was found to correspond exactly to interplanar spacing of the hexagonal syngony of the composite (see table). Similar hexagonal crystalline structure was earlier observed in the carbon–nitrogen condensate in [7], where only one lattice parameter was given ($a = 5.3$ Å). It coincides with the parameter determined by us.

Table

CN_x + TiN				CN_x		
hexagonal syngony		cubic syngony		*d*, Å	hexagonal	cubic
d, Å	*hkl*	*d*, Å	*hkl*		*hkl*	*hkl*
4.48	100					
2.61	110					
		2.45	111	2.39		111
2.19	102			2.19	102	
		2.082	200	2.062		200
1.71	210			1.718	210	
1.516	103					
		1.483	220	1.452		220
1.322	220			1.305	220	
				1.21		222

To summarize, modification of the carbon–nitrogen compound by titanium nitride clusters resulted in some changes in the lattice parameters of the crystalline component of the obtained condensate. Parameter d_{111} of the cubic syngony was found to be two times less than the lattice constant c of the hexagonal syngony (d_{111} = 2.455 Å, c = 4.87 Å). Since plane {111} has hexagonal symmetry, the size and orientation correspondence is possible between the cubic and hexagonal syngonies.

Modification of the carbon–nitrogen condensate by titanium nitride clusters makes it possible to obtain coatings of more than 1 μm in thickness. Since in the case of carbon–nitrogen coatings we could not exceed a thickness of 0.45 μm, this fact indirectly confirms the improvement of adhesive properties of this material as a result of its modification. Microhardness was measured on different parts of the film surface. The average value of microhardness was 17.3 GPa. Only small deviations from the average value were registered, indicating a high structural homogeneity of the obtained condensate. The obtained value of microhardness is rather high, although optimization of the process of synthesis has not been carried out. This fact allows us to consider the new composite as a promising material from the viewpoint of its application as a protective coating.

REFERENCES

1. V. G. Aleshin, A. A. Smekhnov, G. P. Bogatyreva, *et al.*, *Chemistry of Diamond Surface* (Naukova Dumka, Kiev, 1990).
2. G. V. Samsonov, *Microhardness Test Method* (Nauka, Moscow, 1965).
3. S. A. Shiryaev, M. V. Atamanov, M. I. Guseva, *et al.*, Zh. Tekh. Fiz. **72** (2), 99 (2002) [Tech. Phys. **47**, 238 (2002)].
4. E. G. Spenscer, P. H. Schmidt, D. C. Joy, *et al.*, Appl. Phys. Lett. **29**, 118 (1976).
5. Dong Li, Xi Chu, Shang-Cong Cheng, *et al.*, Appl. Phys. Lett. **67**, 203 (1995).
6. B. E. Shkuratov, V. A. Beloshenko, and V. N. Varyukhin, Ukr. Patent No. 60013 A, Byull. Izobret., No. 9 (2003).
7. M. B. Guseva, V. G. Babaev, V. V. Khvostov, *et al.*, in *Proceedings of the 6th International Symposium "Thin Films in Electronics," Kherson, 1995*, Vol. 2, pp. 63–69.

Translated by M. Astrov

Technical Physics, Vol. 49, No. 7, 2004, pp. 941–943. Translated from Zhurnal Tekhnicheskoĭ Fiziki, Vol. 74, No. 7, 2004, pp. 134–136.
Original Russian Text Copyright © 2004 by Ugryumov, Shaposhnik, Voishchev.

BRIEF COMMUNICATIONS

Spectral and Static Noise Characteristics of Semiconductor Gas Sensors in Equiresistance Conditions

R. B. Ugryumov, A. V. Shaposhnik, and V. S. Voishchev
Glinka State Agricultural University, Voronezh, 394043 Russia
e-mail: asb@agrochem.vsau.ru

Received November 4, 2003

Abstract—The extent to which the resistance fluctuations in semiconductor gas sensors can be considered stationary and Gaussian, as well as the noise spectrum of these sensors in equiresistance conditions, are studied. It is shown that the extent to which the noise is stationary and Gaussian depends on gas phase composition. It is found that the spectrum of the sensor noise is qualitatively distinct in different media. On the basis of these results, it is concluded that it is possible in principle to increase the selectivity of the gas sensors by combined measurements of their resistive and noise characteristics. *© 2004 MAIK "Nauka/Interperiodica".*

Chemical adsorption substantially affects the system of the surface-state energy levels. The random character of trapping and release of charge carriers results in fluctuations of their concentration and/or mobility and, hence, in conductivity fluctuations. Modification of the energy-level system causes changes in the mean lifetime of the charged and neutral state of the surface centers and thus affects the dynamics of carrier trapping and release and, therefore, the noise in the semiconductor. Experimentally, this circumstance manifests itself in the change in the spectral and static characteristics of the current noise as the gas phase composition is changed [1, 2].

This study is concerned with the evaluation of the fundamental possibility of determining gas phase composition from noise measurements. To this end, a set of experiments was performed to measure relative noise spectral density $S(f)$ and to estimate the degree ξ to which the noise can be considered stationary and Gaussian in equiresistance conditions. The essence of the equiresistance method consists in the selection of such proportions of the oxidized and reduced components in the gas mixture at which the resistance of the sensor would be the same. This is possible because the donor effect of the reducing gases (hydrogen, carbon oxide, ethanol, etc.), which results in the decrease in the resistance, is balanced by the acceptor effect of oxygen from the air (the acceptor effect causes the increase in the resistance of an *n*-type semiconductor). In this case, the variation of the absolute noise power can be equalized due to the change in the resistance.

In order to perform the experimental part of the study, a special automated laboratory setup was assembled which allowed investigation of both sensor and noise characteristics of the gas-sensitive structures in different gas mixtures [3]. To estimate the noise spectrum, we used digital spectrum analysis. The study of the extent to which the noise was Gaussian and stationary was carried out using the technique based on the measurement of the noise intensity at the output of the bandpass filter [4, 5]. A null hypothesis that the noise is stationary and Gaussian is assumed. Then, the theoretical error of the noise power measurement is determined by the relationship $E_t^2 = 1/(t\Delta f_x)$, where Δf_x is the effective width of the filtered noise spectrum and t is the observation period. In the measurements, the experimental error, $E_e = s/(p\sqrt{N})$, is estimated, where s is the noise intensity dispersion, p is the mean value of the noise power, and N is the number of uncorrelated intensity readings. The half-width ΔE of the confidence interval for the confidence probability of 95% is calculated as the doubled relative error E_t. Then, the value $\xi = E_e/E_t - 1$ is evaluated. If $|\xi| \le \Delta E$, we assume that the input noise is stationary and Gaussian. Otherwise, at least one constraint is not fulfilled: the stationary or/and Gaussian character of the noise is violated.

The gas sensors of interest were fabricated by chemical deposition [6]. The sensor resistance in a neutral medium (argon gas) at 180°C was equal to 150 kΩ and served as a standard resistance of the gas sensor. The noise was measured in a neutral medium, as well as in air + ethanol vapor and air + CO mixtures. The CO or ethanol vapor content was adjusted so that the sensor resistance was equal to 150 kΩ. Figure 1 shows the relative noise spectral density of sensors in three media at equiresistance conditions. The relative noise spectral densities in different media at equal resistance and temperature evidently not only differ quantitatively but have qualitatively different form as well. The frequency dependence of the noise spectral density in a neutral

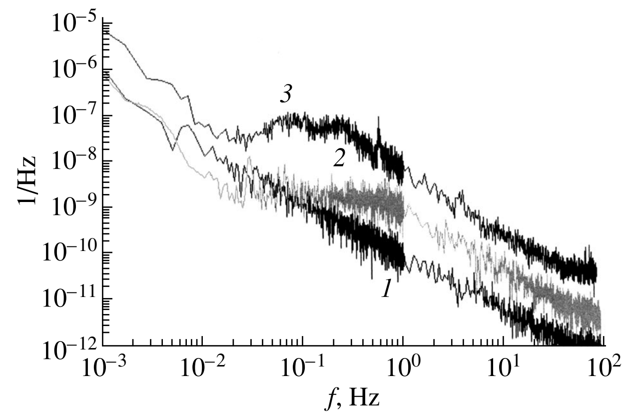

Fig. 1. Noise-power spectral density of the sensor in different gas media at a temperature of 180°C: (*1*) in argon, (*2*) in air + CO mixture (0.45%), and (*3*) in air + ethanol vapor mixture (0.33%).

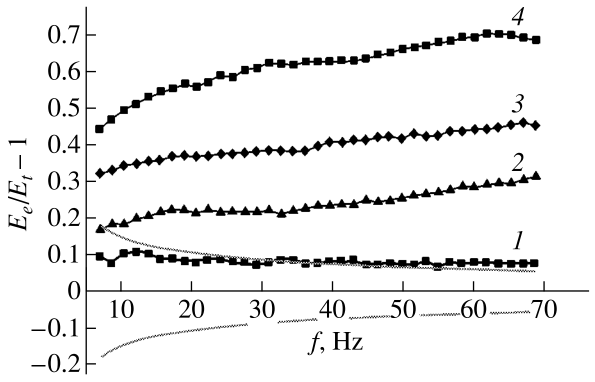

Fig. 2. Estimation of the extent to which the sensor noise is Gaussian and stationary in different gas media: (*1*) in air at 25°C, (*2*) in argon at 180°C, (*3*) in air + CO mixture (0.45%) at 180°C, and (*4*) in air + ethanol vapor mixture (0.33%) at 180°C.

medium is perfectly approximated by the reciprocal power-law dependence with the exponent close to unity. It can be seen that in a neutral medium the sensor exhibits "classical" flicker noise over almost five decades of frequency. After chemical adsorption, an appreciable nonlinearity of the frequency dependence of the noise-power spectral density appears and, moreover, its increase with frequency is observed (curve *2*). Such an increase in the noise-power spectral density cannot be explained on the basis of the model approximations where the noise is considered originating from the capture of charge carriers by traps. Such models reduce the resulting spectrum to the sum of Lorentzian spectra of independent noise-generating centers, but it is impossible to obtain the increase in the noise-power spectral density with frequency by summing these spectra. In the alcohol vapor medium (curve *3*), several broad peaks at the multiple frequencies of 0.08, 0.24, and 0.56 Hz are noticeable. The occurrence of the broad peaks in the frequency dependences of the noise-power spectral density can be related to the initiation of some self-oscillating processes, which are hardly resolved in the wideband 1/*f* noise signal. We may assume the existence of several noise-generation mechanisms that are independent of one another and give uncorrelated contributions to the total noise. These contributions can depend on such external parameters as the temperature and concentration of the active gas. The experimental data suggest the occurrence of some optimal combinations of temperature and gas concentration at which the self-oscillating processes have the highest intensity.

Figure 2 shows the dependence of estimated extent ξ (5) to which the noise is stationary and Gaussian in equiresistance conditions at different values of the filter passband. The observation period was 84 s, and the center of the filter passband was at 146 Hz. Two curves that are symmetric about zero in Fig. 2 show the confidence interval corresponding with the Gaussian stationary noise.

Curve *1* in Fig. 2 is the sensor characteristics measured in air atmosphere at room temperature. Obviously, at room temperature the estimation of ξ for the sample is close to the confidence interval; therefore, with some conditionality, it can be considered as Gaussian and stationary. Some deviation from the Gaussian and stationary character is evident as the pass-band exceeds 40 Hz. Curves *2–4* in Fig. 2 are calculated for the same conditions as curves *1–3* in Fig. 1. It is clear that, at the same resistance, the estimation for ξ is different in these three media.

The measurement of the noise-power spectral density and estimation of the extent to which the noise is Gaussian and stationary ξ in equiresistance conditions show that is basically possible to determine qualitative gas composition, which is unattainable using the conventional resistive measurements. For instance, at temperature of the sensor surface of 180°C, the alcohol with a vapor concentration of 0.33% and CO with a concentration of 0.45% cause equal relative change in conductivity and thus are indistinguishable. In contrast, the measurement of the noise characteristics makes possible the qualitative determination of the gas phase composition, since the noise characteristics depend to a greater extent on individual features of the adsorbate chemical interaction with the surface. Thus, it may be concluded that the selectivity of the gas sensors can be principally enhanced using the joint measurement of their sensor and noise characteristics.

REFERENCES

1. A. V. Titov, A. M. Gulyaev, O. B. Mukhina, and I. B. Varlashov, in *Proceedings of the Scientific–Methodical Seminar on Noise and Degradation Processes in Semiconductor Devices* (MNTORÉS im. A. S. Popova, Moscow, 2002), pp. 245–246.

2. R. B. Ugryumov, A. V. Shaposhnik, V. S. Voishchev, S. B. Ryabtsev, and A. A. Vasil'ev, in *Proceedings of the Scientific–Methodical Seminar on Noise and Degradation Processes in Semiconductor Devices* (MNTORÉS im. A. S. Popova, Moscow, 2003), pp. 245–246.
3. R. B. Ugryumov, A. V. Shaposhnik, V. S. Voishchev, P. V. Yakovlev, and D. S. Kirnov, in *Proceedings of the Scientific–Methodical Seminar on Noise and Degradation Processes in Semiconductor Devices* (MNTORÉS im. A. S. Popova, Moscow, 2003).
4. A. B. Yakimov, Izv. Vyssh. Uchebn. Zaved. Radiofiz. **40**, 1155 (1997).
5. G. Ferrante and A. B. Yakimov, in *Proceedings of the Scientific–Methodical Seminar on Noise and Degradation Processes in Semiconductor Devices* (MNTORÉS im. A. S. Popova, Moscow, 1999), pp. 177–182.
6. V. V. Malyshev and A. V. Pislyakov, Sensors, No. 1, 2 (2001).

Translated by M. Lebedev

Technical Physics, Vol. 49, No. 7, 2004, pp. 944–946. Translated from Zhurnal Tekhnicheskoĭ Fiziki, Vol. 74, No. 7, 2004, pp. 137–139.
Original Russian Text Copyright © 2004 by Koshkarev.

BRIEF COMMUNICATIONS

Optimum Ions for a Nuclear Reactor with Neutron Illumination

D. G. Koshkarev
Institute of Theoretical and Experimental Physics,
ul. Bol'shaya Cheremushkinskaya 25, Moscow, 117259 Russia
e-mail: Koshkarev@vitep1.itep.ru

Received November 4, 2003

Abstract—The main advantage of fission reactors with neutron illumination is that, owing to the neutron illumination, they operate in the subcritical mode and, hence, are safe. Neutrons required for the illumination are generated during nuclear fragmentation in a target irradiated by 1–2 GeV protons. A substantial disadvantage of this method for energy generation is the severe restriction imposed on the power of a plant. This restriction is due to the restriction imposed on the intensity of an accelerated-proton beam by the tolerances for the activation of accelerator structural elements. The substitution of heavier nuclei (from carbon to argon) for protons is shown to substantially increase the intensity of an accelerated-ion beam and to provide a commercially reasonable thermal power of ~4–6 GW. *© 2004 MAIK "Nauka/Interperiodica".*

1. In the electronuclear method of energy generation [1–3], protons are ordinarily used as ions to be accelerated, whereas the application of the nuclei of heavier atoms instead of protons can have substantial advantages. When comparing the efficiencies of using various nuclei, we take into account that the parameters of electronuclear power plants are determined by two effects: a positive effect—neutron generation under the action of accelerated ions on a target—and a negative effect—the activation of accelerator structural elements because of the illumination of the walls of a vacuum chamber in an accelerator with part of a beam. Hereafter, we assume that the mass A of accelerated ions falls in the range $1 < A < 40$, where A is the ion mass number. The ion range R in a target is determined from the expression $R \sim E/z^2$, where z is the ratio of the ion charge to the electron charge and E is the ion energy. Note that a neutron-generating target is made of the heaviest atoms, whereas accelerator structural elements are made of materials with substantially lighter nuclei, such as copper, iron, or graphite. In the energy range under study (~1 GeV/nuc.), the inelastic interaction cross sections for all ions with relatively light nuclei are virtually the same. So, we can assume that the activation of the accelerator walls induced by a single ion is proportional to the ion range $\sim R \sim E/z^2$. Hence, the optimal particle flux I_i turns out to be proportional to z^2/E, and the relation for the optimal ion flux can be written as

$$I_i = I_p z^2 E_p / E_i, \tag{1}$$

where I_p is the proton flux, E_i is the ion energy, and E_p is the proton energy.

2. In a generating target, nuclear fragmentation is caused by high-energy ions, and the generated neutrons leave the target and then, according to the standard scheme of an electronuclear power plant, enter into a subcritical nuclear reactor. The flux of the neutrons generated in the target is determined by the ion flux and the ion energy:

$$I_n = I_i E_i / \xi(E), \tag{2}$$

where $\xi(E)$ is the energy per neutron.

Combining Eqs. (1) and (2), we obtain an expression for the relative power of an electronuclear power plant in the form

$$P = P_p z^2 / \chi_i. \tag{3}$$

In Eq. (3), function χ_i is the energy per neutron for a certain ion with respect to proton; i.e.,

$$\chi_i = \xi_i(E_i)/\xi_p(E_p). \tag{4}$$

For simplicity of comparing ions with protons, we assume that protons always have an energy of 1 GeV, at which the energy per neutron is minimum and equal to 36 MeV. As follows from the data [4, 5] shown in the figure, the relation

$$\xi_i(E) \approx \xi_p(E) \tag{5}$$

holds true rather accurately for D^{1+} and He^{2+} ions and, with small errors, for C^{6+} ions in a rather wide energy range.

We can assume that Eq. (5) is valid for heavier ions as well. In this case, χ_i can be represented as $\approx 36\ \text{MeV}/\xi_p(E)$. According to the data obtained in [6, 7], this function weakly depends on the ion energy in the ion energy range from 5 to 20 GeV and falls in the range $1.5 \le \chi_i \le 2.5$. Two important conclusions can be drawn from this finding: the power of a plant depends on the charge of a chosen ion as z^2 and rather weakly depends on the potential of an ion accelerator, since this dependence is realized only through the function χ_i.

The parameters of electronuclear power plants for various ions are given in the table, where the potential of an accelerator for all ion types is taken to be the same (1 GV).

3. At a reactor safe subcritical level of ≈0.95, the reactor power increases by a factor of ≈20. When recalculating the thermal power of an electric power station, P_T, into the electric power, P_E, we used the coefficient 0.4. Note that the ratio P_L/P_E of the beam power to the electric power of an electric power station for all ion types is small and lies in reasonable limits (≤5%), varying from 2.2 to 4.8%. As an ion accelerator, we propose to apply a linear accelerator with an efficiency of energy transformation from the supply line to the beam power of ≈50%. As ion sources at the head of an accelerator, we propose to use sources [8] operating at a direct current of up to 20 mA for ions with a charge of +1, which are well known in ion implantation. After being preliminarily accelerated to ~10–40 MeV, ion beams can easily be transformed into the beams of the bare nuclei of the corresponding elements through a charge transfer in a thin target. Since this transformation can occur almost without decreasing the beam current, the limiting ion current can be $I_e \leq z20$ mA.

4. It follows from the table that the parameters are the best when nitrogen, oxygen, or neon ions are used. Indeed, the thermal powers of the plants easily fall in the optimum range 3–6 GW; the potential of a linear ion accelerator can be relatively low (≈1 GV); the powers of accelerator generators (120–200 MW) are available; and the coefficient χ, which determines the power loss as compared to the limiting gain (which is equal to z^2), is relatively low (in the range from 1.7 for nitrogen to 1.9 for neon).

Since the neutrons generated in the target have a rather high average energy ($E_n \geq 1$ MeV), as a fission reactor, one can apply a fast reactor (e.g., a Brest-type reactor) that operates on a mixture of 238 uranium and plutonium. Broadly speaking, the reactor type is of little importance.

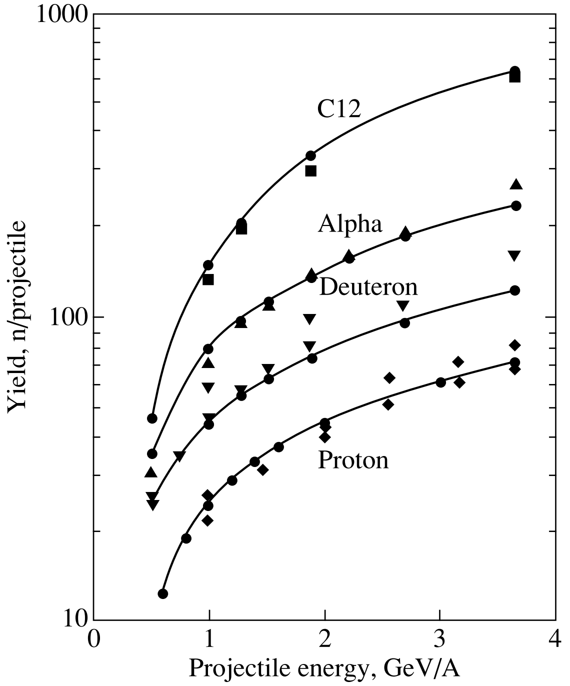

Neutron yield with an energy below 10.5 MeV from a lead target (R = 10 cm, L = 60 cm) depending on the projectile energy for protons, deuterons, and helium and carbon nuclei. Diamonds and triangles correspond to the experimental results [4], and squares, calculation using the Shield program [5].

5. The main results of this work can be derived from two theorems: (1) to a first approximation, the activation of accelerator structural elements is only determined by the accelerated-ion range in the materials of these elements and (2), to a first approximation, the neutron yield from a heavy multiplying target per incident high-energy ion is only determined by the ion energy.

However, taking into account that the conclusions following from these statements are very important for the development of nuclear power engineering, it is necessary to perform theoretical and experimental studies on light-ion beams before designing new electronuclear power plants. Note that such studies can be conducted on the novel TVN–ITEF accelerator–storage

Table

Element	I_p, mA	I_e, mA	E, GeV	$\xi(E)$, MeV	I_n, A	P_T, GW	P_E, GW	χ	P_L, MW	P_L/P_E, %
Proton	1	1	1	36	0.03	0.11	0.045	1.0	1	2.2
Carbon	6	36	6	59	0.61	2.44	0.98	1.7	36	3.7
Nitrogen	7	49	7	59	0.83	3.32	1.33	1.7	49	3.7
Oxygen	8	64	8	61	1.05	4.20	1.68	1.7	64	3.8
Neon	10	100	10	67	1.49	5.97	2.39	1.9	100	4.2
Argon	18	324	18	77	4.21	16.83	6.73	2.2	324	4.8

ring plant [9, 10], which has proper parameters and has recently been put into operation.

ACKNOWLEDGMENTS

I am grateful to Academician V.I. Subbotin for his continuous encouraging interest in the problem of electric charge.

REFERENCES

1. V. S. Barashenkov, Fiz. Élem. Chastits At. Yadra, No. 9, 871 (1978).
2. R. G. Vasil'kov, V. I. Gol'danskiĭ, and V. V. Orlov, Usp. Fiz. Nauk **139**, 435 (1983) [Sov. Phys. Usp. **26**, 228 (1983)].
3. V. I. Subbotin, Soobshch. Ob"edin. Inst. Yad. Issled., Dubna, No. R1-99-97 (1999).
4. R. G. Vasilkov and V. I. Yurevich, in *Proceedings of the 11th Meeting of International Collaboration on Advanced Neutron Sources ICANS-11, Tsukuba, 1990*, Vol. 1, p. 340 (KEK Rep. 90-25).
5. N. M. Sobolevsky and A. P. Zhukov, in *Proceedings of the 4th Workshop on Simulating Accelerator Radiation Environments SARE-4, Knoxville, 1998,* Ed. by T. A. Gabriel (ORNI, 1999), p. 283.
6. N. M. Sobolevsky, in *Proceedings of the 3rd International Conference of Yugoslav Nuclear Society YUNSC, Belgrade, 2000*.
7. A. V. Voronkov and N. M. Sobolevskiĭ, Preprint No. 78, IPM (Keldysh Institute of Applied Mathematics, Moscow, 2000).
8. K. Saadatmand, Rev. Sci. Instrum. **69**, 859 (1998).
9. D. G. Koshkarev, N. N. Alekseev, and B. Yu. Sharkov, in *Proceedings of the 15th All-Union Workshop on Charged-Particle Accelerators, Protvino, 1996*, vol. 2, pp. 319–321.
10. N. N. Alekseev, D. G. Koshkarev, and B. Yu. Sharkov, Pis'ma Zh. Éksp. Teor. Fiz. **77** (3), 149 (2003) [JETP Lett. **77**, 123 (2003)].

Translated by K. Shakhlevich

Technical Physics, Vol. 49, No. 7, 2004, pp. 947–949. Translated from Zhurnal Tekhnicheskoĭ Fiziki, Vol. 74, No. 7, 2004, pp. 140–142.
Original Russian Text Copyright © 2004 by Grigor'ev, Shiryaeva, Belonozhko, Klimov.

BRIEF COMMUNICATIONS

On the Characteristic Time for the Realization of Instability on a Flat Charged Liquid Surface

A. I. Grigor'ev, S. O. Shiryaeva, D. F. Belonozhko, and A. V. Klimov
Yaroslavl State University, ul. Sovetskaya 14, Yaroslavl, 150000 Russia
e-mail: grig@uniyar.ac.ru

Received November 24, 2003

Abstract—A nonlinear integral equation that describes the time evolution of the amplitude of a nonlinear unstable wave on the flat uniform charged surface of an ideal incompressible liquid has been derived and solved. The characteristic time for the realization of instability is found to be determined by the initial amplitude of a virtual wave initiating the instability and the supercritical increment in the Tonks–Frenkel parameter. At a zero supercritical increment, the characteristic time for the realization of instability is only determined by the initial amplitude and can be rather long (up to eight hours). This effect is characteristic of a flat charged liquid surface and does not occur in charged drops. *© 2004 MAIK "Nauka/Interperiodica".*

1. Studying the physical laws of the realization of instability on the charged flat surface of a liquid is of interest due to numerous academic, technical, and technological applications [1, 2]. However, despite a significant interest in this phenomenon, the physical mechanism of the formation of Taylor cones has not been yet studied. The cones are protrusions at the charged surface of a liquid that are formed in the nonlinear stage of the realization of its instability; an excess charge is shed from the peaks of these protrusions through the emission of highly dispersed and strongly charged droplets [1–4]. A quantitative model for the formation of such protrusions was proposed in [5]. Allen [6] tried to numerically calculate them; however, this attempt only slightly contributes to the understanding of this phenomenon. Nobody has tried to estimate the characteristic time for the formation of the Taylor cones from the onset of the realization of instability on the charged surface of a liquid. In this work, we study this problem using the scheme applied earlier to analyze the nonlinear stages of the development of a strongly charged drop [7, 8] and an uncharged drop in an external high uniform electrostatic field [9].

2. Let an ideal incompressible conducting liquid with a density ρ fill the half-space $z \le 0$ in the system of Cartesian coordinates ($\mathbf{n}_z$ is the unit vector of the z axis) in the gravity field $\mathbf{g} \parallel -\mathbf{n}_z$. Let the equilibrium flat surface of a liquid (coinciding with the xy plane) unperturbed by the wave motion be subjected to the action of surface tension forces with a coefficient γ and carry a uniformly distributed electric charge with a density σ.

In the context of the linear model [10, 11], the critical conditions for the realization of instability on this surface have the form

$$W_* = \alpha k_* + (\alpha k_*)^{-1}, \quad k_* = \alpha^{-1}, \qquad (1)$$

where W is the dimensionless Tonks–Frenkel parameter characterizing the stability of the free liquid surface with respect to the surface charge, $W = 4\pi\sigma^2/\sqrt{\rho g \gamma}$; k is the wave number; and α is the capillary constant of the liquid, $\alpha = \sqrt{\gamma/\rho g}$.

Taking into account a nonlinear correction to the frequency that appears when the profiles of nonlinear capillary waves are calculated in the third order in a small parameter $\varepsilon \equiv (a/\alpha)$, which is the ratio of the wave amplitude a to the capillary constant α, results in the appearance of the dependence of the critical value of parameter W on wave amplitude a (small parameter ε) [12]

$$W_* \approx 2 - \beta\varepsilon^2 \equiv 2 - \beta(a_0/\alpha)^2, \quad \beta = 11/8. \qquad (2)$$

We now follow the time evolution of the capillary–gravitational wave with $k_* = \alpha^{-1}$ that has lost its stability when condition (1) is met (i.e., at $W = W_* = 2$), taking into account the fact that, according to relation (2), the critical value of the Tonks–Frenkel parameter decreases with increasing wave amplitude.

The flat charged liquid surface that is unperturbed by capillary wave motion is stable at $W = 2$. Instability appears if the flat liquid surface contains a virtual wave with an arbitrary small amplitude a_0. In this case, the existing value of the Tonks–Frenkel parameter ($W = 2$) is supercritical for the wave, and, in accordance with the theory [5, 7–10], the amplitude of this wave begins to increase with time according to the exponential law $a(t) = a_0\exp(\chi t)$ with an increment χ that is proportional to the square root of the difference between the existing value $W = W_* = 2$ and the critical value for the virtual wave, which is determined by Eq. (2); that is,

$$\chi = (a_0/\alpha)\sqrt{(\beta g/\alpha)}. \tag{3}$$

This exponential growth of the wave with the increment proportional to the initial amplitude occurs only for a short time, until the increment in the initial amplitude Δa goes beyond the value determined by the condition $\Delta a \ll a_0$. Then, a_0 in Eq. (3) for the increment should be replaced by $a_0 + \Delta a$ and the exponential growth of the amplitude should be considered on the next short time interval, and so on. As a result (detailed derivation of the formula is given in the works [7–9] dealing with the study of the time evolution of drops unstable with respect to self-charges or polarization charges), we obtain the nonlinear integral equation

$$a(t) = a_0 \exp\left(\int_0^t \frac{a(t)}{\alpha}\sqrt{\beta\frac{g}{\alpha}}\,dt\right), \tag{4}$$

to find the amplitude of the unstable wave. Its solution has the form

$$a(t) = \frac{a_0}{1-(a_0/\alpha)\sqrt{\beta g/\alpha}\,t} \equiv \frac{a_0}{1-\chi t}. \tag{5}$$

It is seen from Eq. (5) that, although the entire process is essentially nonlinear, the characteristic time for the realization of instability t_*, which is defined as the characteristic time it takes for the denominator in Eq. (5) to infinitely approach zero, is completely characterized by the instability increment at the initial instant of the realization of instability, $t_* = \chi^{-1}$. Note that the meanings of χ in the nonlinear increase in the amplitude of the unstable wave with time and in the exponential increase characteristic of the linear theory are different. In the linear theory, the wave amplitude increases ~2.73 times over the time χ^{-1}, whereas it becomes infinitely high within the same time interval in the nonlinear process. The fact that law (5) of increase in the wave amplitude with time provides a higher rate of growth as compared to the exponential growth can easily be seen if we expand Eq. (5) and $\exp(\chi t)$ at $\chi t < 1$ into a power series in χt and then compare the results.

The minimum possible value of a_0 is specified by the amplitude of the capillary waves induced by the thermal motion of molecules in the liquid, $a_0 \approx \sqrt{kT/\gamma}$, where k is the Boltzmann constant and T is the absolute temperature of the liquid. The amplitude of such waves for the majority of real liquids at reasonable (from the standpoint of their existence) temperatures is about half an angstrom and, hence, the characteristic time for the development of instability is rather long. For example, at $a_0 = 10^{-8}$ cm, the characteristic time t_* for the realization of instability on a charged water surface that borders on a vacuum is about eight hours. As the initial amplitude a_0 increases, the characteristic time t_* decreases as $\sim a_0^{-1}$ and reaches several seconds even at $a_0 \approx 10^{-3}$ cm. As a result, we find that, for the characteristic time for the realization of instability on the order of several seconds, in experiment at $W = W_* = 2$, virtual waves with $k\alpha = 1$ that initiate the instability should be created artificially.

This fact means that the characteristic waiting time for the realization of instability in experiments for checking the validity of the instability criterion for a charged liquid surface [13, 14] should depend on the method of defining a virtual wave. Since this circumstance was not noted in [13, 14], we have to assume that the virtual waves in the experiments appeared because of either molecular thermal motion (in this case, the waiting time for the realization of instability should be rather long) or random vibrations of the device at uncontrolled amplitudes. However, direct evidence for the duration of the linear stage of charge preparation is given in [3]: the author noted that the event of throwing a liquid jet during the realization of instability was fixed in only one shot in about 15 m of the film used to record the experiment from the instant of voltage application. A discharge delay time was not mentioned in [14]. These facts can have another explanation: the voltage in the experiments [13, 14] exceeded the critical value, and the experiments were performed in the presence of a supercritical increment ΔW in the Tonks–Frenkel parameter as compared to the critical value $W = W_* = 2$ determined by Eq. (1), which affected the characteristic time for the realization of instability.

3. Let the Tonks–Frenkel parameter exceed the critical value for the flat liquid surface by ΔW at the initial time instant and be equal to $W_* + \Delta W$. Then, the increment of instability at the initial instant of its realization depends on both the initial amplitude of a virtual wave, a_0, and the supercritical increment ΔW and, according to the traditional concepts [1, 7–10], is specified by the relation

$$\chi = \sqrt{\frac{g}{\alpha}\left[\Delta W + \beta\left(\frac{a_0}{\alpha}\right)^2\right]}.$$

The time dependence of the amplitude of the unstable wave is determined as a solution to the nonlinear integral equation

$$a(t) = a_0 \exp\left(\int_0^t \sqrt{\frac{g}{\alpha}\left[\Delta W + \beta\left(\frac{a(t)}{\alpha}\right)^2\right]}\,dt\right),$$

whose solution has the form

$$a(t) = \frac{2\exp(\sqrt{g\Delta W/\alpha}\,t)(1+\delta)}{(1+\delta)^2 - (a_0/\alpha)^2\exp(2\sqrt{g(\Delta W/\alpha)}\,t)},$$

$$\delta \equiv \sqrt{\left(1+\left(\frac{\beta}{\Delta W}\right)\left(\frac{a_0}{\alpha}\right)^2\right)}.$$

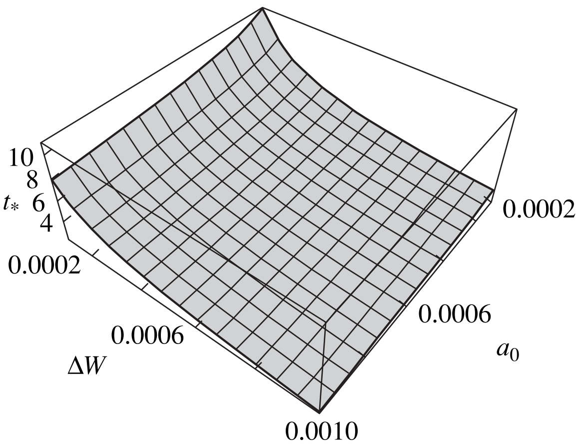

Dependence of the characteristic time for the realization of instability t_* on the initial wave amplitude a_0 changing from 10^{-4} to 10^{-3} cm and the supercritical increment in the Tonks–Frenkel parameter ΔW changing from 10^{-4} to 10^{-3}.

The characteristic time for the realization of instability that is determined by this dependence can be obtained from the condition of vanishing of the denominator in $a(t)$:

$$t_* = \sqrt{(\alpha/g\Delta W)}\ln[\delta(\alpha/a_0)]. \qquad (6)$$

As is seen from expression (6), the characteristic time for the realization of instability depends mainly on the supercritical increment ΔW in the Tonks–Frenkel parameter, and the effect of the initial amplitude a_0 of the virtual wave is weak (see figure). Taking into account the fact that the capillary constant α for most liquids amounts to several millimeters, we can find from Eq. (6) that the characteristic time for the realization of instability is several seconds even at $\Delta W \approx 10^{-3}$ irrespective of a_0. As applied to the experiments [13, 14], this behavior suggests that they were performed under the dominating effect of the supercritical increment in the Tonks–Frenkel parameter on the characteristic time for the realization of instability.

4. It is interesting to note that, when the realization of instability in drops with respect to self-charges or induced charges was studied in [7–9], the dependence of the characteristic time for the realization of instability on the amplitude of initial perturbation in an equilibrium drop shape $\zeta_0 P_2(\cos\theta)$ (here, $P_2(\cos\theta)$ is a Legendre polynomial) is masked by its strong dependence on the drop radius R, which has the form $t_* \sim (R^4/\zeta_0)$. At $R \approx 10^{-2}$ cm (the stability of drops having this radius with respect to their surface charge was experimentally studied in [2]) and $\zeta_0 \approx 10^{-8}$ cm, we have $(R^4/\zeta_0) \sim 1$. Therefore, the strong dependence of the characteristic time for the development of instability on the initial amplitude at the critical threshold of the Tonks–Frenkel parameter, which has been found in this work, is inherent in the flat charged surface of a liquid.

CONCLUSIONS

The characteristic time t_* for the realization of instability on the flat charged surface of an ideal incompressible conducting liquid is determined by the initial amplitude a_0 of a virtual wave initiating the instability and the extent of exceeding the Tonks–Frenkel parameter that is critical for the wave with a given wavelength (i.e., the supercritical increment ΔW). The effect of the supercritical increment ΔW on t_* is predominant at $\Delta W \neq 0$. At $\Delta W = 0$, the characteristic time t_* is inversely proportional to a_0 and, at sufficiently small a_0, can reach high values because of a slow increase in the amplitude at the linear stage of instability. For example, if the virtual wave is induced by molecule thermal motion in the liquid and $a_0 \approx 10^{-8}$ cm, t_* for water approaches eight hours.

ACKNOWLEDGMENTS

This work was supported by the Russian Foundation for Basic Research (project no. 03-01-00760) and grant no. MK 929.2003.01 of the President of the Russian Federation.

REFERENCES

1. M. D. Gabovich, Usp. Fiz. Nauk **140**, 137 (1983) [Sov. Phys. Usp. **26**, 447 (1983)].
2. A. I. Grigor'ev and S. O. Shiryaeva, Izv. Ross. Akad. Nauk, Mekh. Zhidk. Gaza, No. 3, 3 (1994).
3. G. I. Taylor, Proc. R. Soc. London, Ser. A **280**, 383 (1964).
4. S. I. Shevchenko, Zh. Tekh. Fiz. **60** (2), 54 (1990) [Sov. Phys. Tech. Phys. **35**, 167 (1990)].
5. L. Tonks, Phys. Rev. **48**, 562 (1935).
6. J. E. Allen, J. Phys. D **18**, 59 (1985).
7. S. O. Shiryaeva, A. I. Grigor'ev, and I. D. Grigor'eva, Zh. Tekh. Fiz. **65** (9), 39 (1995) [Tech. Phys. **40**, 117 (1995)].
8. S. O. Shiryaeva, Pis'ma Zh. Tekh. Fiz. **26** (4), 5 (2000) [Tech. Phys. Lett. **26**, 137 (2000)].
9. A. I. Grigor'ev, Pis'ma Zh. Tekh. Fiz. **24** (24), 36 (1998) [Tech. Phys. Lett. **24**, 962 (1998)].
10. Ya. I. Frenkel', Zh. Éksp. Teor. Fiz. **6**, 348 (1936).
11. A. I. Grigor'ev, D. F. Belonozhko, and S. O. Shiryaeva, Zh. Tekh. Fiz. **69** (7), 15 (1999) [Tech. Phys. **44**, 750 (1999)].
12. D. F. Belonozhko, A. V. Klimov, and A. I. Grigor'ev, Pis'ma Zh. Tekh. Fiz. **29** (24), 41 (2003) [Tech. Phys. Lett. **29**, 1031 (2003)].
13. G. I. Taylor and A. D. McIwan, J. Fluid Mech. **22**, 1 (1965).
14. A. A. Shutov, Zh. Tekh. Fiz. **72** (8), 126 (2002) [Tech. Phys. **47**, 1053 (2002)].

Translated by K. Shakhlevich